UNIVERSITY OF KENT

DOCTORAL THESIS

Supercontinuum in the practice of Optical Coherence Tomography with emphasis on noise effects

---

Author:

Michael MARIA

Supervisor:

Professor Adrian PODOLEANU

Examiners:

Professor Roy TAYLOR

Professor William WADSWORTH

Professor Chao WANG

A thesis submitted in fulfillment of the requirements for the degree of Doctor of Philosophy

in the

Applied Optics Group

School of Physical Sciences

December 13, 2018

Declaration of Authorship

I, Michael MARIA, declare that this thesis titled, "Supercontinuum in the practice of Optical Coherence Tomography with emphasis on noise effects" and the work presented in it are my own. I confirm that:

- This work was done wholly or mainly while in candidature for a research degree at this University.
- Where any part of this thesis has previously been submitted for a degree or any other qualification at this University or any other institution, this has been clearly stated.
- Where I have consulted the published work of others, this is always clearly attributed.
- Where I have quoted from the work of others, the source is always given. With the exception of such quotations, this thesis is entirely my own work.
- I have acknowledged all main sources of help.
- Where the thesis is based on work done by myself jointly with others, I have made clear exactly what was done by others and what I have contributed myself.

Signed:

Date:

""If A is success in life, then A = x + y + z. Work is x, play is y and z is keeping your mouth shut.""

Albert Einstein

University of Kent

Abstract

School of Physical Sciences

Doctor of Philosophy

Supercontinuum in the practice of Optical Coherence Tomography with emphasis on noise effects

by Michael MARIA

Optical Coherence Tomography (OCT) is an imaging modality which has proven, since the early 1990s, its incredible potential. Nowadays, numerous fields of medical investigation, such as Ophthalmology, Dermatology or Cardiovascular imaging, would not be the same without the diagnostic tools bring by OCT. This tremendous development has been supported by industry support through improvement of dedicated components such as lasers, cameras and optics.

A great example of this development is the evolution of Supercontinuum (SC) sources. Due to the extremely broad spectrum cover by SC sources, their high power density and high spatial coherence, it seems obvious to use them for driving OCT systems. However, an intensity noise issue arising from the SC sources has been reported as a limitation for OCT and needs to be addressed.

The aim of the work presented in this thesis is to create a link between the world of Optical Coherence Tomography and Supercontinuum physics in order to understand the origins and the impact of SC source intensity noise into the OCT systems. This work is of importance as it helps to optimize the usefulness of the current generation of SC sources. Also, this work is a part of the work necessary for developing a new generation of SC sources which completely addresses the intensity noise limitations. More precisely, a part of the work presented deals with an optimization of the association SC source and OCT. The second part of the results is an attempt for improving this association by using a new SC source design.

Acknowledgements

My PhD has been a three years and a half adventure. All-in-all, it was an amazing time as I had the chance to learn so much. Of course, during this period, as any young researcher I had my ups and downs. Towards this thesis, many times of struggle and frustration often made me doubt on the ending. However, and hopefully, none of those times lasted too long and here I am writing the acknowledgement section. The final success of such a long journey is always built on meeting and exchanging with other people. Therefore, I would like to thank all people that have helped me to reach this point either by their direct scientific contribution or by their indubitable support.

First of all, I would like to thank **Prof. Adrian PODOLEANU** and **Prof. Ole BANG**, my two academic supervisors, for their mentorship and support. I would like to acknowledge their constant availabilities and many advices which have contributed to all the work and results achieved. Also, I would like to thank **Dr. Thomas FEUCHTER**, **Dr. Lasse LEICK** and **Dr Peter M. MOSELUND**, my industrial supervisors, for making my time at NKT Photonics A/S as interesting as possible. A particular thanks to Peter for the nice home-made snaps tasting we had once in a while.

During the first half of my PhD, I worked at the Applied Optics Group of the University of Kent where I had the chance to meet and collaborate with numerous amazing researchers. I would like to thank **Dr. George DOBRE**, **Dr. Adrian BRADU**, **Dr. Sylvain RIVET**, **Dr. Ramona CERNAT**, **Dr. Christopher COSTA**, **Dr. Radu STANCU**, **Dr. Manuel MARQUES**, **Dr. Hannah IRONS**, **Adam EFFENBERGER** and **Yong HU**. More particularly, to Manuel, Radu and Christopher, I will always remember our sometimes "long" and "deep" talks at lunch time or our chess game!

The second half of my PhD was conducted at NKT Photonics A/S in Denmark. There, I had the chance to work with my colleagues from the UBAPHODESA project **Magalie BONDU**, **Sophie CAUJOLLE**, **Catherine CHIN** and **Felix FLEISCHHAUER** and I would like to thank them for integrating me to the small OCT group they have built there. Even though more stressful, this second half of PhD time has been enjoyable thanks to an

amazing company atmosphere, so I would like to express my gratitude to all NKT Photonics A/S employees with whom I interacted.

Many times, during my stay in Denmark, I collaborated with the research group of **Prof. Ole BANG** at the Technical University of Denmark. From there, some particular thanks go to **Dr. Niels M. ISRALESEN** and to **Ivan B. GONZALO** with whom I spent many hours working in the laboratories or simply discussing results. Also from DTU, I would like to thank **Prof. Christos MARKOS**, **Dr. Getinet WOYESSA**, **Dr. Christian R. PETERSEN**, **Dr. Kristian NIELSEN**, **Rasmus D. ENGELSHOLM**, **Manoj K. DASA**, **Kyei KWARKYE**, **Abubakar I. ADAMU**, **Mikkel JENSEN** and **Gaoyan LI**. I will always remember our fantastic improvement at "soccer" over the last few months. Also, I want to thank **Dr. Mette MOGENSEN** for her help on showing the real medical world to us physicist.

A special note for **Ludovic KERESELIDZE**, **Dr. Jean-Paul YEHOUESSI**, **Alexandre ROMPEN**, **Yanis PARRO** and **Benoit GRIFFON**. Hopefully, you will have soon to call me **Dr. Michael MARIA**.

Obviously, an immense gratitude to all my Family who has supported me throughout these moments and trusted me during my entire life.

Finally, I would like to recognize the support of one last person whom I met at the beginning of my PhD, **Xin MA**. Since the moment you came into my life, everything has become easier. The support and love you give me every day help me and keep me motivated to achieve everything I aim. I can only hope that someday, I will help you and support you as much as you did for me during this project.

Contents

List of Figures

List of Tables

List of Abbreviations

3D	**3**-**D**imensional
ANDI	**A**ll-**N**ormal **DI**spersion
CS	**C**hanelled **S**pectrum
DG	**D**iffraction **G**rating
fs	**f**emto**s**econd
FD-OCT	**F**ourier **D**omain-**O**ptical **C**oherence **T**omography
FFT	**F**ast **F**ourier **T**ransform
FWHM	**F**ull-**W**idth-**H**alf-**M**aximum
HNLF	**H**ighly **N**on-**L**inear **F**ibre
iFFT	**i**nverse **F**ast **F**ourier **T**ransform
kHz	**k**ilo**H**er**z**
MHz	**M**ega**H**er**z**
MI	**M**odulation **I**nstability
ML	**M**ode-**L**ocked
MSI	**M**aster-**S**lave **I**nterferometry
NA	**N**umerical **A**perture
ns	**n**ano**s**econd
OCT	**O**ptical **C**oherence **T**omography
OWB	**O**ptical **W**ave **B**reaking
PCF	**P**hotonic **C**rystal **F**ibre
ps	**p**ico**s**econd
PSD	**P**ower **S**pectral **D**ensity
PSF	**P**oint **S**pread **F**unction
QS	**Q**-**S**witched
RIN	**R**elative **I**ntensity **N**oise
SC	**S**uper**C**ontinuum
SD-OCT	**S**pectral **D**omain-**O**ptical **C**oherence **T**omography
SRS	**S**timulated **R**aman **S**cattering

SNR	**S**ignal-to-**N**oise **R**atio
SPM	**S**elf-**P**hase **M**odulation
SS-OCT	**S**wept **S**ource-**O**ptical **C**oherence **T**omography
TD	**T**ime-**D**omain
TD-OCT	**T**ime **D**omain-**O**ptical **C**oherence **T**omography
UHR-OCT	**U**ltra **H**igh **R**esolution-**O**ptical **C**oherence **T**omography
μs	**m**icro**s**econd
XPM	**C**ross-**P**hase **M**odulation
ZDW	**Z**ero **D**ispersion **W**avelength

Dedicated to all the people I love

Chapter 1

Introduction

1.1 Context of the Thesis

Optical Coherence Tomography (OCT) is an imaging modality used nowadays in numerous biomedical and non-biomedical applications. By measuring depth reflectivity profiles of scattering samples, OCT allows to reconstruct 3D representations of semi-transparent media. Optical coherence tomography relies on optical interference [1], which is an optical effect known for centuries. Among the first famous descriptions are the experiments of Thomas Young with his famous two slits system (1801) or the ether experiments by Michelson and Morley (1887). The first image produced using OCT [2] is however much younger and was done at the Massachusetts Institute of Technology in 1991, by the group of Professor James Fujimoto. In this first paper, they demonstrated the first cross-sectional image of a human retina based on measuring echo amplitude of a light beam compare to a known reference path. However, even though this is considered as the first demonstration of OCT, is not the earliest application of low coherence interferometry to investigate eye properties. Fercher's group at the medical University of Vienna was already measuring eye ball length using low coherence interferometry principle back in 1988 [3].

Since those first investigations, 27 years ago, OCT has followed an amazing development, which have spread among the academic and industrial world. A recent report [4] has shown the exponential growth in the number of publications related to OCT from the first paper in 1991 up to 2015. Nowadays, OCT is the main topic of an important number as large as 3000 publications a year in general and specialised peer-review journals. In terms

of industrial impact, the number of companies selling OCT systems has reached 44 companies in 2015 from countries such as United States, France, Germany and United Kingdom. This evolution has been supported by the development of Fourier Domain Optical Coherence Tomography (FD-OCT). Indeed, the earliest OCT systems were based on the Time-Domain (TD) principle. Though TD-OCT had its role, impressive at the time, it had several limitations, mainly in terms of its speed. This made the transition of OCT to clinic challenging. Most of these limitations were cleared by the improvements brought by FD-OCT, which first stones have been placed by [5, 6] in 1993 and 1995. Those experiments used a Spectral Domain-Low Coherence Interferometer as a sensor for distance investigations. A few years later, FD-OCT has been proposed using the same principle together with a lateral scanning. With FD-OCT a speed increase of more than 100 fold compared to TD-OCT has been possible [7, 8, 9]. Also, FD-OCT has brought an improvement in terms of image quality as the achievable signal to noise ratio is 20 dB higher compared to the initial TD-OCT principle [7, 8, 9].

In 2017, FD-OCT is almost always preferred to TD-OCT. Within FD-OCT, two main streams have emerged. The first one, Spectral Domain-OCT (SD-OCT) consists in using a broadband light source and a spectrometer as a detection unit. The second trend is called Swept Source–OCT (SS-OCT), where a fast tunable light source is used together with a fast photodiode as a detector. The two modalities can be applied to the same samples (eye, skin, organs, arteries . . .) but one will be preferred compared to the other depending on the expected system performance. Indeed, SD-OCT will be preferred if the main targeted parameter is the high axial resolution. This is due to the fact that only SD-OCT system can handle optical bandwidth large enough (> 200 nm) to obtain an axial resolution of a few microns. In SD-OCT, the optical bandwidth is equal to the spectral bandwidth of the source. Broadband sources such as combination of super-luminescent diodes or supercontinuum source can offer more than 300 nm within two out of the three main wavelength ranges used for OCT (800 nm, 1050 nm and 1300 nm). On the other hand, SS-OCT is the method of choice if speed is the most important factor. Tunable lasers can be swept at rates of a few hundreds of kHz up to tens of MHz. On the contrary, SD-OCT systems are limited in terms of

speed by the camera line rate used in the spectrometer, which is in the range of a few tens of kHz up to a few hundreds of kHz. However, most of tunable sources suffer from smaller optical bandwidth compared to broadband sources.

As written previously, the first image ever produced using OCT was an image of the human retina measured *in vitro* [2]. Since that point in time, the number of OCT ophthalmic applications has grown exponentially. In less than 20 years, OCT has become a tool for daily routine use by ophthalmologists. In this field, OCT helps to diagnose and understand diseases such as glaucoma [10, 11], macular degeneration [12, 13], retinal detachment [14, 15] and many others pathologies. Also, new features have been added to the original OCT. Among others, techniques like OCT-Angiography (OCTA) allows seeing the blood vessels mapping by observing a difference between the moving blood flow and the static tissue within the retina [16, 17] or Adaptive Optics-OCT (AO-OCT) [18] helps to see the retina with extreme lateral details by correcting for the eye aberration. Those new features, though not yet embedded in commercial systems as yet will for sure increase the usefulness of OCT within its clinical realm. Applications of OCT in ophthalmic environments are currently representing the largest part of the industrial market for OCT, with not less than 15 out of the 45 companies developing commercial OCT systems [4]. The value of the OCT ophthalmic market is nowadays reaching more than 500 M$ a year and it is constantly growing.

The second most important field of application for OCT, in terms of research and industrial impact, is cardiovascular imaging. The main target is the investigation of plaques within artery, which is a key criterion for understanding and preventing heart attacks [19, 20]. This field is of high importance and was the second, within all the possible OCT applications to see the release of a dedicated commercial product in 2004 [4]. Also, cardiovascular OCT applications have seen a significant improvement with the democratisation of swept sources within the OCT community. The much higher speed of operation of SS-OCT system compared to SD-OCT have helped to reduce the imaging time from minutes to almost a second for a full 3D scan of an artery area. Today, the market of cardiovascular OCT application is about

100 M$ a year shared between 5 companies [4].

A third prolific field of OCT development is dermatology. From the early stage, OCT has been considered as the equivalent of biopsy but without the need of an invasive cut. This is clearly an advantage for dermatology where many diseases concerning skin affect the superficial layers and are investigated by tissue biopsy. Indeed, the conventional procedure for dermatologists involves the analysis of a tissue biopsy under a microscope. Such procedure is costly, time ineffective and truly unpleasant for the patient. Similar results compared to biopsy can be obtained using OCT with no need for an invasive cut. Several demonstrations of OCT in skin cancer detection at have been shown over the years [21, 22]. Again, technology such as OCT angiography [23] or Optical Coherence Elastography [24] bring new useful features for cancer detection. Even though OCT is a possibly useful tool for dermatology, a certain resistance from the medical community is to be noticed to accept the technology in their daily routine. This resistance might be explained by a too important price of OCT systems and also by not enough demonstration of skin diseases diagnostic using OCT. Then, industrial development of OCT for skin imaging has been slower than for eye imaging or cardiovascular imaging. Currently, 6 companies are working on OCT for skin investigation but one of them is clearly dominating the market [4]. However, most of the companies on this market are young, less than 5 years old, so it is too early to judge either they will take-off or not.

Finally, in addition to the three main fields of OCT applications mentioned above, numerous other domains are considering the interest of bringing OCT as an imaging modality. Within the biomedical imaging community, fields that OCT has benefited are gastro-intestinal investigation [25], dentistry [26] or neurology [27]. Meanwhile, other applications in non-biomedical world have demonstrated the great potential of OCT. Among those, Art and its conservation [28], industrial quality inspection or even more recently [29], the fast-growing field of 3D-printing [30].

This non-exhaustive list proves OCT as an important imaging modality for several fields. This high interest for OCT, from both the scientific community and industry, is due to the fact that OCT is filling a gap in terms

of axial resolution versus imaging penetration. A very popular sketch, inspired from [31, 32] , is illustrating in Figure 1.1 the OCT imaging modality abilities in resolution versus imaging penetration. The main strength of OCT has been to be able to provide an intermediate modality between the Confocal Microscopy and Ultrasound Imaging.

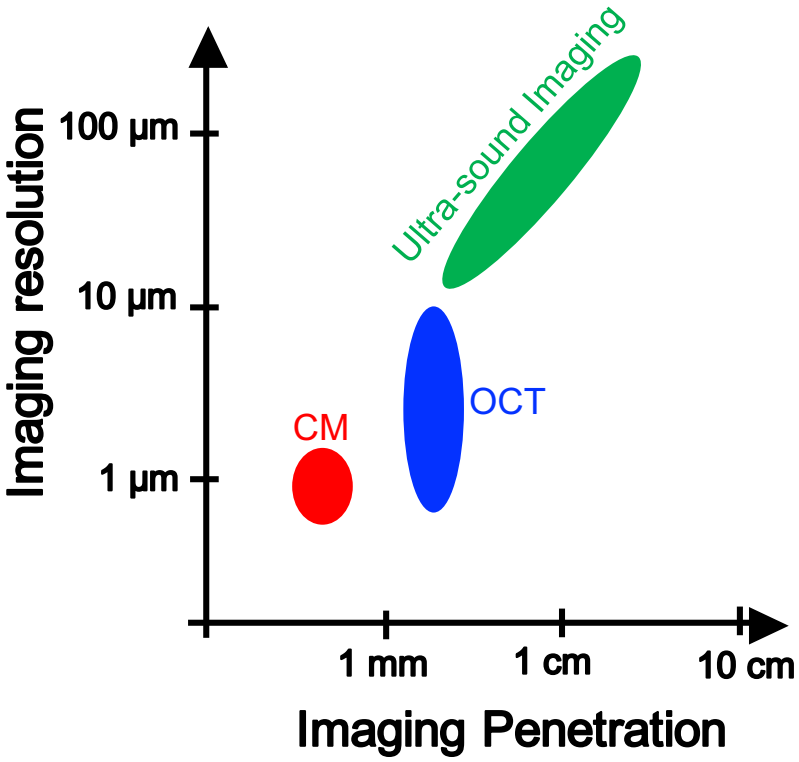

FIGURE 1.1: Representation of the imaging penetration versus axial resolution observed in medical imaging devices (Confocal Microscope, OCT: Optical Coherence Tomography). Adapted from [31, 32]

The important development of OCT finds its origins in the support and contribution from the industrial world. Many companies have developed dedicated components answering exact OCT needs. A first great example is the improvement of cameras in the Near Infra-Red region, which has led to the emergence of SD-OCT. A second important improvement for SD-OCT is the evolution of Supercontinuum (SC) light sources. A supercontinuum source is an ultra-broad optical source relying on non-linear frequency conversion, which can address the wavelength ranges used in OCT. Actually,

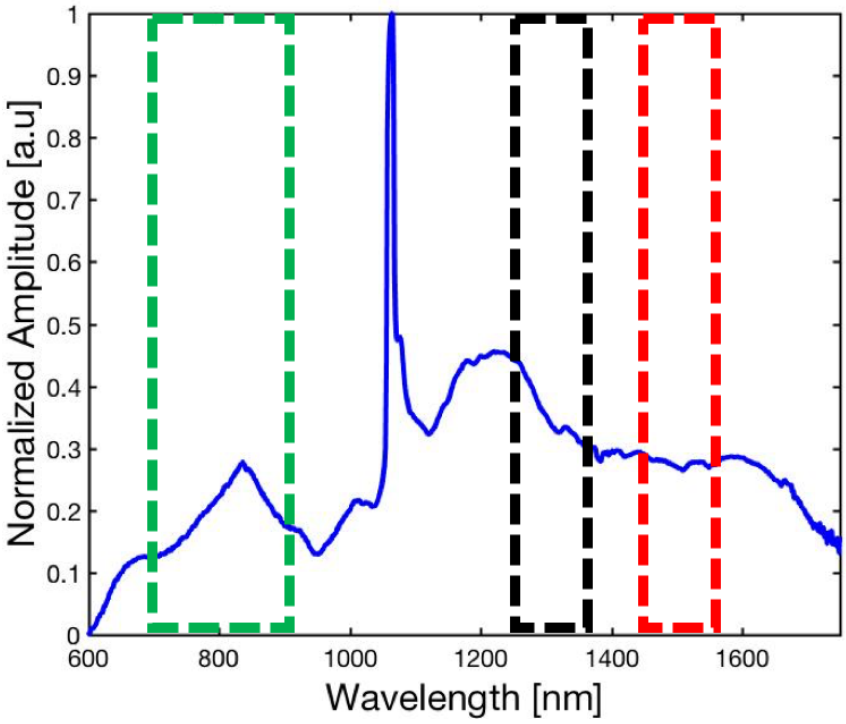

FIGURE 1.2: Example of a spectrum obtained from a SC source based on a Silica photonic crystal fibre. The dashed areas indicate the wavelength region of Titanium Sapphire laser (green), SLD at 1300 nm (black) and SLD at 1550 nm (red).

SC sources cover much broader spectral range compared to the one accessible with common spectrometers. An example of a spectrum measured from a fibre-based SC source designed for OCT is shown in Figure 1.2. This spectrum spans from around 600 nm up to beyond 1700 nm with a high average power of 4-5W. Such a spectrum is useful for OCT applications in the 800 nm range for eye imaging, in the 1300 nm region for skin imaging and at 1550 nm and 1700 nm for Non-Destructive Investigation of sample with less water content. As a comparison of spectral bandwidth covered, the dashed squares in Figure 1.2 indicate the typical bandwidth available from other sources than SC source used in OCT system. However, from the first attempts to use a SC source in OCT, a high Relative Intensity Noise (RIN) has been reported. Since then, important efforts have been dedicated by the SC scientific community and the SC industry towards reducing the noise below acceptable levels. Numerous successes of OCT using commercially

available low noise SC sources have been reported over the last 5 years.

This thesis has been written within the time-line of the project called Ultra-wide Bandwidth Photonics Devices, Source and Applications funded by the European Union (Marie Curie Actions). The aim of the project is to investigate the usefulness of SC sources for biomedical imaging applications. More particularly, the aim of the current thesis is to evaluate the usefulness of the current generation of SC sources for Ultra-High Resolution-OCT (UHR-OCT). Of particular interest, is the noise impact of a SC source on the performance of an OCT system driven by such a source.

1.2 Content of the Thesis

The present thesis is structured in three main parts. Chapter 2 and Chapter 3 are introductions for the different concepts used in the subsequent chapters. Chapter 2 is dedicated to OCT and Chapter 3 to the SC source. Then, Chapter 4 is dedicated to signal processing involved in OCT. Of particular interest is the Master/Slave Interferometry (MSI) method and its specific signal processing to ensure ultra-high resolution. Finally, Chapter 5, Chapter 6 and Chapter 7 deal with the topic of SC noise in OCT. Below is a semi-detailed description of each chapter content.

Chapter 2: Optical Coherence Tomography - Definition

This chapter defines a set of important concepts and parameters concerning SD-OCT, essential in the understanding of the thesis. Important concepts, such as white light interferometry and definitions such as the signal to noise ratio and axial resolution are introduced as they are used all along the thesis.

Chapter 3: Supercontinuum light source – Definition

Supercontinuum light sources together with OCT constitute the backbone of this thesis. Therefore, it is important to understand several definitions and parameters in order to have a good understanding of the thesis. Again, this chapter is an introduction containing some important definitions

of the supercontinuum physics. Here, the main non-linear effects involved in SC generation, such as the concept of a Photonic Crystal Fibre (PCF) or different SC generation mechanisms are presented.

Chapter 4: Signal Processing in Optical Coherence Tomography

This chapter is a description of the processing procedures required in order to analyse the raw data delivered by an OCT system. A first part describes the common SD-OCT analysis. Then, the Master/Slave Interferometry (MSI) analysis procedure is presented. By mixing mathematical description with analysis of experimental data, a clear step by step presentation is shown. Finally, a comparison of conventional SD-OCT with MSI is proposed regarding the main metric tools used by the OCT community.

Chapter 5: Optimization of supercontinuum design for noise reduction in ultra-high resolution optical coherence tomography

This chapter provides an analysis of noise from SC sources and their impact on the OCT performance. Noise from laser sources limits the achievable SNR and therefore needs to be carefully understood. This chapter proposes a method for analysing the noise in the OCT images using the hardware of an OCT system alone. This is an advantage as noise analysis of SC sources usually requires complex and expensive hardware. In addition, two parameters of SC sources are optimized. Such an analysis is useful as it helps a SC source user to optimally operate his system and it is also interesting for SC source design.

Chapter 6: Femtosecond pumped all-normal dispersion fibre supercontinuum for ultra-low noise operation

In this chapter, the initial results of an on-going study are presented, where a low-noise SC source is built and tested into an UHR-OCT system operating in the 1300 nm. This new SC source relies on the concept of pumping a PCF, with an all normal dispersion profile, using an ultra-short pulse. This new design generates a SC from several non-linear effects that are more

deterministic. Also, a discussion on possible improvements of this first prototype is presented. The initial experimental results show that such a source offers similar noise properties compared to SLD source but with broad spectral bandwidth.

Chapter 7: Q-switch pumped supercontinuum light source for ultra-high resolution optical coherence tomography – A low-cost alternative

This chapter compiles the results obtained in using a low-cost SC source for UHR-OCT. In order to reduce the total cost of an OCT system it is necessary to reduce the cost of the most expensive components. In the case of SD-OCT, the light source and the spectrometer are the most expensive components. Here, a new light source is proposed. This source is a SC source which relies on a Q-Switched laser architecture for pumping a Highly Non-Linear Fibre (HNLF). This pump laser results in a much lower cost source, less than 15 % in comparison to a conventional SC source for OCT. To demonstrate the usefulness of this source, a pulse to pulse stability analysis together with a complete OCT characterization (sensitivity + images) is proposed. Finally, it is shown that such a source can be useful if a longer exposure time, compared to current SD-OCT state of the art systems can be employed.

1.3 Results communication

Peer-reviewed articles:

- A. Bradu, N. M. Israelsen, **M. Maria**, M. J. Marques, S. Rivet, T. Feuchter and O. Bang, " Recovering distance information in spectral domain interferometry," Nature Scientific Reports 8, Articles Number 15445 (2018). https://www.nature.com/articles/s41598-018-33821-0

- M. Jensen, N. M. israelsen, **M. Maria**, T. Feuchter, A. Podoleanu and

O. Bang, "All-depth dispersion cancellation in spectral domain optical coherence tomography using numerical intensity correlations," Nature Scientific Reports 8, Articles Number 9170 (2018). https://www.nature.com/articles/s41598-018-27388-z

- N. M. Israelsen, **M. Maria**, M. Mogensen, S. Bojensen, M. Jensen, M. Haedersdal, A. Podoleanu and O. Bang, " The value of ultra-high resolution OCT in dermatology - delineating the dermo-epidermal junction, capillaries in the dermal papillae and vellus hairs," Biomed. Opt. Express 9(5), 2240-2265 (2018). https://www.osapublishing.org/boe/fulltext.cfm?uri=boe-9-5-2240&id=385739

- M. Mogensen, S. Bojesen, N. M. Israelsen, **M. Maria**, M. Jensen, A. Podoleanu, O. Bang, M. Haedersal, " Two optical coherence tomography systems detect topical gold nanoshells in hair follicles, sweat ducts and measure epidermis", J. Biophotonics 11(9) (2018). https://onlinelibrary.wiley.com/doi/abs/10.1002/jbio.201700348

- M. Dasa, C. Markos, **M. Maria**, C. Petersen, P. Moselund and O. Bang, "High-pulse energy supercontinuum laser for high resolution spectroscopic photoacoustic imaging of lipids in the 1650-1850 nm region," Biomed. Opt. Express 9(4), 1762-1770 (2018). https://www.osapublishing.org/boe/abstract.cfm?uri=boe-9-4-1762

- **M. Maria**, I. B. Gonzalo, T. Feuchter, M. Denninger, P. M. Moselund, L. Leick, O. Bang and A. Podoleanu, "Q-switch pumped supercontinuum for ultra-high resolution optical coherence tomography," Opt. Letters 42(22), 4744-4747 (2017). https://www.osapublishing.org/ol/abstract.cfm?uri=ol-42-22-4744

- S. Rivet, **M. Maria**, A. Bradu, T. Feuchter, L. Leick, and A. Podoleanu, "Complex master slave interferometry," Opt. Express 24, 2885-2904 (2016). https://www.osapublishing.org/oe/abstract.cfm?uri=oe-24-3-2885

- A. Bradu, **M. Maria** , and A. Podoleanu, "Demonstration of tolerance to dispersion of master/slave interferometry," Opt. Express 23, 14148-14161 (2015). https://www.osapublishing.org/oe/abstract.cfm?uri=oe-23-11-14148

Patent:

- A. Podoleanu, S. Rivet, A. Bradu, and **M. Maria**, "Apparatus and method for processing the signal in master slave interferometry and apparatus and method for master slave optical coherence tomography with any number of sampled depths," (2017).

Participation to peer-reviewed conferences and proceeding:

- M. Maria, M. J. M. Marques, C. Costa, A. Bradu, T. Feuchter, L. Leick, A. Gh. Podoleanu, "Broadband master-slave interferometry using a supercontinuum source", Proc. SPIE 9697, Optical Coherence Tomography and Coherence Domain Optical Methods in Biomedicine XX, 96972R (8 March 2016). (Poster presentation given by Michael MARIA).

Participation to conference and proceeding :

- A. Bradu, **M. Maria**, L. Leick, A. Gh. Podoleanu, "Novel dispersion tolerant interferometry method for accurate measurements of displacement", Proc. SPIE 9525, Optical Measurement Systems for Industrial Inspection IX, 952509 (22 June 2015). (Oral presentation given by Michael MARIA).

- **M. Maria**, I. B. Gonzalo, M. Bondu, R. D. Engelsholm, T. Feuchter, P. M. Moselund, L. Leick, O. Bang, A. Podoleanu, "A comparative study of noise in supercontinuum light sources for ultra-high resolution optical coherence tomography", Proc. SPIE 10056, Design and Quality for Biomedical Technologies X, 100560O (14 March 2017). (Oral presentation given by Michael MARIA).

-N. M. Israelsen, **M. Maria**, T. Feuchter, A. Podoleanu, O. Bang, "Non-destructive testing of layer-to-layer fusion of a 3D print using ultrahigh resolution optical coherence tomography", Proc. SPIE 10329, Optical Measurement Systems for Industrial Inspection X, 103290I (26 June 2017). (Oral presentation given by Niels Moller Israelsen).

- **M. Maria**, I. Bravo, T. Feuchter, L. Leick, P. Moselund, M. Denninger, A. Podoleanu, O. Bang, "Q-switched based supercontinuum source towards low-cost ultra-high resolution optical coherence tomography", Optics and Biophotonics in low –ressources settings IV, (2018). (Oral presentation in 2018).

- I. B. Gonzalo, **M. Maria**, R. D. Engelsholm, T. Feuchter, L. Leick, P. M. Moselund, A. Podoleanu, O. Bang, "Ultra-low noise supercontinuum source for ultra-high resolution optical coherence tomography at 1300 nm", Design and quality for biomedical technologies XI, (2018). (Oral presentation in 2018 by Ivan Bravo Gonzalo).

- N. M. Israelsen, **M. Maria**, M. Mogensen, S. Bojesen, M. Jensen, M. Haedersdal, A. Podoleanu, O. Bang, "In-vivo detection of the skin dermo-epidermal junction by ultrahigh resolution optical coherence tomography", Photonics in dermatology and plastic surgery, (2018). (Oral presentation in 2018 by Mikkel Jensen).

References

[1] Eugne Hecht. Optics - fourth edition. In *Optics - Fourth Edition*, chapter 1, pages 32–51. International Edition, 2002.

[2] D. Huang, E. A. Swanson, C. P. Lin, J. S. Schuman, W. G. Stinson, W. Chang, M. R. Hee, T. Flotte, K. Gregory, C. A Puliafito, and J. G. Fujimoto. Optical coherence tomography. *Science (New York, N.Y.)*, 254 (5035):1178–1181, 11 1991. URL http://www.ncbi.nlm.nih.gov/pmc/articles/PMC4638169/.

[3] A. F. Fercher, K. Mengedoht, and W. Werner. Eye-length measurement by interferometry with partially coherent light. *Opt. Lett.*, 13(3):186–188, Mar 1988. doi: 10.1364/OL.13.000186. URL http://ol.osa.org/abstract.cfm?URI=ol-13-3-186.

[4] E. A. Swanson and J. G. Fujimoto. The ecosystem that powered the translation of oct from fundamental research to clinical and commercial impact. *Biomed. Opt. Express*, 8(3):1638–1664, Mar 2017. doi: 10.1364/BOE.8.001638. URL http://www.osapublishing.org/boe/abstract.cfm?URI=boe-8-3-1638.

[5] A. F. Fercher, C. K. Hitzenberger, G. Kamp, and S.Y. El-Zaiat. Measurement of intraocular distances by backscattering spectral interferometry. *Optics Communications*, 117(1):43 – 48, 1995. ISSN 0030-4018. doi: https://doi.org/10.1016/0030-4018(95)00119-S. URL http://www.sciencedirect.com/science/article/pii/003040189500119S.

[6] S. Taplin, A. G. Podoleanu, D. J. Webb, and D. A. Jackson. Displacement sensor using channelled spectrum dispersed on a linear ccd array. *Electronics letters*, 29(10):896–897, 5 1993. ISSN 0013-5194. doi: 10.1049/el:19930598.

[7] R. Leitgeb, C. K. Hitzenberger, and A. F. Fercher. Performance of fourier domain vs. time domain optical coherence tomography. *Opt. Express*, 11(8):889–894, Apr 2003. doi: 10.1364/OE.11.000889. URL http://www.opticsexpress.org/abstract.cfm?URI=oe-11-8-889.

[8] J. F. de Boer, B. Cense, B. H. Park, M. C. Pierce, G. J. Tearney, and B. E. Bouma. Improved signal-to-noise ratio in spectral-domain compared with time-domain optical coherence tomography. *Opt. Lett.*, 28(21):2067–2069, Nov 2003. doi: 10.1364/OL.28.002067. URL http://ol.osa.org/abstract.cfm?URI=ol-28-21-2067.

[9] M. A. Choma, M. V. Sarunic, C. Yang, and J. A. Izatt. Sensitivity advantage of swept source and Fourier domain optical coherence tomography. *Opt. Express*, 11(18):2183–2189, Sep 2003. doi: 10.1364/OE.11.

002183. URL http://www.opticsexpress.org/abstract.cfm?URI=oe-11-18-2183.

[10] F. A. Medeiros, L. M. Zangwill, C. Bowd, R. M. Vessani, R. Susanna, and R. N. Weinreb. Evaluation of retinal nerve fiber layer, optic nerve head, and macular thickness measurements for glaucoma detection using optical coherence tomography. *American Journal of Ophthalmology*, 139(1):44 – 55, 2005. ISSN 0002-9394. doi: https://doi.org/10.1016/j.ajo.2004.08.069. URL http://www.sciencedirect.com/science/article/pii/S0002939404010815.

[11] D. C. Hood. Improving our understanding, and detection, of glaucomatous damage: An approach based upon optical coherence tomography (OCT). *Progress in Retinal and Eye Research*, 57(Supplement C):46 – 75, 2017. ISSN 1350-9462. doi: https://doi.org/10.1016/j.preteyeres.2016.12.002. URL http://www.sciencedirect.com/science/article/pii/S1350946216300702.

[12] M. A. Wirth, F. Freiberg, M. Pfau, J. Wons, M. D. Becker, and S. Michels. Optical coherence tomography angiography in age-related macular degeneration: persistence of vascular network in quiescent choroidal neovascularization. *Acta Ophthalmologica*, 95(4):428–430, 2017. ISSN 1755-3768. doi: 10.1111/aos.13226. URL http://dx.doi.org/10.1111/aos.13226.

[13] L. Toto, E. Borrelli, R. Mastropasqua, L. Di Antonio, E. Doronzo, P. Carpineto, and L. Mastropasqua. Association between outer retinal alterations and microvascular changes in intermediate stage age-related macular degeneration: an optical coherence tomography angiography study. *British Journal of Ophthalmology*, 101(6):774–779, 2017. ISSN 0007-1161. doi: 10.1136/bjophthalmol-2016-309160. URL http://bjo.bmj.com/content/101/6/774.

[14] R. N. Louzada, T. E. de Carlo, M. Adhi, E. A. Novais, M. K. Durbin, E. Cole, M. Lane, O. Moghimi, M. Arya, M. B. Filho, A. J. Witkin,

C. R. Baumal, M. Ávila, J. S. Duker, and N. K. Waheed. Optical coherence tomography angiography artifacts in retinal pigment epithelial detachment. *Canadian Journal of Ophthalmology / Journal Canadien d'Ophtalmologie*, 52(4):419 – 424, 2017. ISSN 0008-4182. doi: https://doi.org/10.1016/j.jcjo.2016.12.012. URL http://www.sciencedirect.com/science/article/pii/S0008418216301727.

[15] T. Sato, T. Wakabayashi, N. Shiraki, and H. Sakaguchi. Retinal thickness in parafoveal subfields and visual acuity after vitrectomy for macula-off rhegmatogenous retinal detachment repair. *Graefe's Archive for Clinical and Experimental Ophthalmology*, 255(9):1737–1742, Sep 2017. ISSN 1435-702X. doi: 10.1007/s00417-017-3716-8. URL https://doi.org/10.1007/s00417-017-3716-8.

[16] J. P. Venugopal, H. L. Rao, R. N. Weinreb, Z. S. Pradhan, S. Dasari, M. Riyazuddin, N. K. Puttiah, D. A. S. Rao, S. Devi, K. Mansouri, and C. A. B. Webers. Repeatability of vessel density measurements of optical coherence tomography angiography in normal and glaucoma eyes. *British Journal of Ophthalmology*, 2017. ISSN 0007-1161. doi: 10.1136/bjophthalmol-2017-310637. URL http://bjo.bmj.com/content/early/2017/07/23/bjophthalmol-2017-310637.

[17] R. Mastropasqua, L. Toto, E. Borrelli, L. Di Antonio, P. A. Mattei, A. Senatore, M. Di Nicola, and C. Mariotti. Optical coherence tomography angiography findings in stargardt disease. *PLOS ONE*, 12 (2):1–11, 02 2017. doi: 10.1371/journal.pone.0170343. URL https://doi.org/10.1371/journal.pone.0170343.

[18] R. S. Jonnal, O. P. Kocaoglu, R. J. Zawadzki, Z. Liu, D.T. Miller, and J. S. Werner. A review of adaptive optics optical coherence tomography: Technical advances, scientific applications, and the future. *Investigative Ophthalmology & Visual Science*, 57(9):OCT51–OCT68, 07 2016. URL http://dx.doi.org/10.1167/iovs.16-19103.

[19] J. Hu, F. Rivero, R. A. Torres, H. Loro Ramírez, E. M. Rodríguez, F. Alfonso, J. García Solé, and D. Jaque. Dynamic single gold nanoparticle visualization by clinical intracoronary optical coherence tomography. *Journal of Biophotonics*, 10(5):674–682, 2017. ISSN 1864-0648. doi: 10.1002/jbio.201600062. URL http://dx.doi.org/10.1002/jbio.201600062.

[20] E. Tenekecioglu, F. N. Albuquerque, Y. Sotomi, P. Zeng, Y.and Suwannasom, R. Tateishi, H.and Cavalcante, Y. Ishibashi, S. Nakatani, J.and Bourantas C. Abdelghani, M.and Dijkstra, C. Collet, A. Karanasos, M. Radu, A. Wang, U. Muramatsu, T.and Landmesser, T. Okamura, E. Regar, G. Räber, L.and Guagliumi, R. T. Pyo, Y. Onuma, and P. W. Serruys. Intracoronary optical coherence tomography: Clinical and research applications and intravascular imaging software overview. *Catheterization and Cardiovascular Interventions*, 89(4):679–689, 2017. ISSN 1522-726X. doi: 10.1002/ccd.26920. URL http://dx.doi.org/10.1002/ccd.26920.

[21] T. Gambichler, A. Orlikov, R. Vasa, G. Moussa, K. Hoffmann, M. Stücker, P. Altmeyer, and F. G. Bechara. In vivo optical coherence tomography of basal cell carcinoma. *Journal of Dermatological Science*, 45(3):167 – 173, 2007. ISSN 0923-1811. doi: https://doi.org/10.1016/j.jdermsci.2006.11.012. URL http://www.sciencedirect.com/science/article/pii/S0923181106003501.

[22] T. Gambichler, P. Regeniter, F. G. Bechara, A. Orlikov, R. Vasa, G. Moussa, M. Stücker, P. Altmeyer, and K. Hoffmann. Characterization of benign and malignant melanocytic skin lesions using optical coherence tomography in vivo. *Journal of the American Academy of Dermatology*, 57(4):629 – 637, 2007. ISSN 0190-9622. doi: https://doi.org/10.1016/j.jaad.2007.05.029. URL http://www.sciencedirect.com/science/article/pii/S0190962207008985.

[23] V. Sigsgaard, L. Themstrup, P. Theut Riis, J. Olsen, and G. B. Jemec. In vivo measurements of blood vessels' distribution in non-melanoma

skin cancer by dynamic optical coherence tomography — a new quantitative measure? *Skin Research and Technology*, pages n/a–n/a. ISSN 1600-0846. doi: 10.1111/srt.12399. URL http://dx.doi.org/10.1111/srt.12399.

[24] B. F. Kennedy, X. Liang, S. G. Adie, D. K. Gerstmann, B. C. Quirk, S. A. Boppart, and D. D. Sampson. In vivo three-dimensional optical coherence elastography. *Opt. Express*, 19(7):6623–6634, Mar 2011. doi: 10.1364/OE.19.006623. URL http://www.opticsexpress.org/abstract.cfm?URI=oe-19-7-6623.

[25] John A. Evans, John M. Poneros, Brett E. Bouma, J. Bressner, E. F. Halpern, M.Shishkov, G. Y. Lauwers, M. M. Kenudson, N. S. Nishioka, and G. J. Tearney. Optical coherence tomography to identify intramucosal carcinoma and high-grade dysplasia in barrett's esophagus. *Clinical Gastroenterology and Hepatology*, 4(1): 38 – 43, 2006. ISSN 1542-3565. doi: https://doi.org/10.1016/S1542-3565(05)00746-9. URL http://www.sciencedirect.com/science/article/pii/S1542356505007469.

[26] L. O. Fernandes, C. Cristina Mota, L. S. A. de Melo, M. U. S. da Costa Soares, and A. S. L. da Silva Feitosa, D.and Gomes. In vivo assessment of periodontal structures and measurement of gingival sulcus with optical coherence tomography: a pilot study. *Journal of Biophotonics*, 10(6-7):862–869, 2017. ISSN 1864-0648. doi: 10.1002/jbio.201600082. URL http://dx.doi.org/10.1002/jbio.201600082.

[27] A. Lichtenegger, D. J. Harper, M. Augustin, P. Eugui, M. Muck, J.Gesperger, C. K. Hitzenberger, A. Woehrer, and B. Baumann. Spectroscopic imaging with spectral domain visible light optical coherence microscopy in alzheimer's disease brain samples. *Biomed. Opt. Express*, 8(9):4007–4025, Sep 2017. doi: 10.1364/BOE.8.004007. URL http://www.osapublishing.org/boe/abstract.cfm?URI=boe-8-9-4007.

[28] H. Liang, M. Mari, C. S. Cheung, S. Kogou, P. Johnson, and G. Filippidis. Optical coherence tomography and non-linear microscopy

for paintings; a study of the complementary capabilities and laser degradation effects. *Opt. Express*, 25(16):19640–19653, Aug 2017. doi: 10.1364/OE.25.019640. URL http://www.opticsexpress.org/abstract.cfm?URI=oe-25-16-19640.

[29] D. Stifter. Beyond biomedicine: a review of alternative applications and developments for optical coherence tomography. *Applied Physics B*, 88(3):337–357, Aug 2007. ISSN 1432-0649. doi: 10.1007/s00340-007-2743-2. URL https://doi.org/10.1007/s00340-007-2743-2.

[30] N. M. Israelsen, M. Maria, T. Feuchter, A. Podoleanu, and O. Bang. Non-destructive testing of layer-to-layer fusion of a 3d print using ultrahigh resolution optical coherence tomography. volume 10329, pages 10329 – 10329 – 7, 2017. doi: 10.1117/12.2269807. URL http://dx.doi.org/10.1117/12.2269807.

[31] W. Drexler and J. G. Fujimoto. Introduction to optical coherence tomography. In *Optical coherence tomography - Technology and applications*, chapter 1, pages 32–51. Springer, 2015.

[32] B. Bouma and G. Tearney. Introduction. In *Handbook of optical coherence tomography*, chapter 1, pages 32–51. Cambridge University Press, 2001.

Chapter 2

Optical Coherence Tomography – Definition and Theory

2.1 Introduction

Optical Coherence Tomography (OCT) is an imaging modality based on the optical effect called interference [1]. Even though OCT is a relatively young field with its first report in the year 1991 [2], it represents nowadays a very hot topic for academia and industry with thousands of reports a year [3]. The current chapter aims to introduce the required background for understanding this thesis. It starts with the introduction of low coherence interferometry and shows how is possible to use it to infer distances. Then, important concepts related to OCT and more specifically to Spectral-Domain-OCT (SD-OCT) are presented.

2.2 White Light Interferometry

2.2.1 Concept of temporal coherence

White light interferometry, also called low coherence interferometry, is a metrology tool which uses the property of temporal coherence of a light source [4]. Temporal coherence refers to the phase relationship which exists when considering the electric field from a source at two distinct points in time. In case of a completely temporally incoherent source, no phase relationship is kept between two instants t_1 and t_2 and the electric field expression is unpredictable. On the contrary, if considering a coherent source, the

electric field is deterministic and its expression at t_2 can be inferred from its expression at t_1 (assuming $t_2 > t_1$). An intermediate status exists between coherent and incoherent, which is partially coherent. A partially coherent source maintains a deterministic electric field over a relatively short period in time and then experiences a random phase change [4].

Mathematically, the coherence property of a light source is described through the temporal coherence function $G(\tau)$ of the source electric field as

$$G(\tau) = \langle E^*(t)E(t+\tau)\rangle, \tag{2.1}$$

where $<>$ denotes the time averaging, τ is the correlation lag variable and $*$ the complex conjugate notation. Then from Equation 2.1, the coherence time τ_c can be calculated as

$$\tau_c = \int_{-\infty}^{+\infty} |g(\tau)|^2 \, \mathrm{d}\tau, \tag{2.2}$$

where the ratio $g(\tau) = G(\tau)/G(0)$ is the complex degree of coherence. The complex degree of coherence is a parameter with absolute values between 0 and 1. An ideal perfect coherence corresponds to $|g(\tau)| = 1$ while an incoherent source corresponds to $|g(\tau)| = 0$. The coherence time τ_c is linked to the coherence length of the source l_c through

$$l_c = c\tau_c, \tag{2.3}$$

where c is the speed of light in vacuum.

Finally, a very important property regarding the temporal coherence of a light source is the link between temporal coherence function and Power Spectral Density (PSD). The two functions are conjugate variables by Fourier Transform (FT) operation

$$S(\nu) = \int_{-\infty}^{+\infty} G(\tau)e^{-2i\pi\nu} \, \mathrm{d}\tau, \tag{2.4}$$

where ν is the optical frequency variable.

Equation 2.4 is important as it establishes a connection between the extension of the two functions along their coordinates. Thus, the broader the

source PSD, the shorter its coherence length. This property is key in the high axial resolution selection of OCT systems along the optical path coordinate, where high resolution is achievable by using a broadband optical source.

2.2.2 White Light Interferometry Definition

Figure 2.1 represents an amplitude-splitting interferometric system in its simplest form. Light is supplied by a polychromatic light source, characterized by its spectral shape $S(\omega)$, central frequency ω_0 and frequency bandwidth $\Delta\omega$. The light is split into two paths by a splitting device BS. The lengths of the two paths are L and $L + \delta l$. After free space propagation, the light along each path is reflected back towards BS by the mirrors M_1 and M_2. The two fields are superposed on the detector. Interference takes place only when δl is shorter than a certain path interval, called the coherence length of the source. Following a similar formalism as in [5] and adapted to a simpler

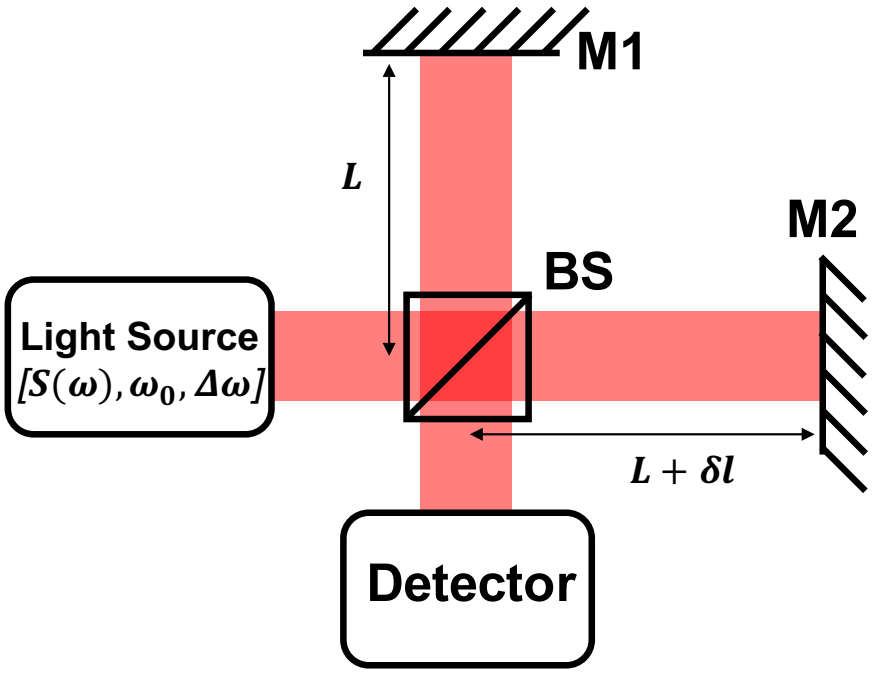

FIGURE 2.1: Simplified sketch of an amplitude-splitting interferometer based on a light source, two mirrors and a detector.

situation, the light from the optical source can be described by its electric

field as

$$E_{source} = E_0(\omega) \times e^{i(kz-\omega t)}, \tag{2.5}$$

where k is the wavenumber of the light, ω is the frequency of the light, and for simplification we consider the wave propagation confined along the z direction, with z the path travelled. t is the time variable and E_0 is the amplitude of the electric field. For ease of identification, let the electric field E_R be the so-called reference field, travelling along a round trip reference path, from BS to mirror $_1$ and back towards the BS, of length $2L$. Let us also consider the field in the sample arm, as sample field, characterized by a E_S, travelling from BS towards mirror M_2 and back towards the BS, along a round trip optical path of length $2(L + \delta l)$. Also, let the BS splitting ratio be 0.5. Considering R_R and R_S as the power reflectivities of mirrors placed in the reference and sample arm respectively, E_R and E_S can be written as:

$$E_R(\omega) = \frac{E_0(\omega)}{\sqrt{2}} \times \sqrt{R_R} \times e^{i(kL-\omega t)}, \tag{2.6}$$

and

$$E_S(\omega) = \frac{E_0(\omega)}{\sqrt{2}} \times \sqrt{R_S} \times e^{i(k(L+\delta l)-\omega t)}. \tag{2.7}$$

For simplicity, let us assume that there are no losses in the reference path, in which case $\sqrt{R_R} = 1$. Let us also assume that there are no losses in the sample arm and that the scattering centre in the sample is replaced by a mirror of reflectivity $R_S = 1$. Later will return to considering the sample with its own reflectivity.

It is important to mention that considering k as a constant in Equation 2.6 and Equation 2.7 is equivalent to assuming no dispersive effects in the interferometer paths. A more accurate representation should be to consider $k_R(\omega)$ and $k_S(\omega)$. A more complete description will be presented in section 2.7.1.

Detectors used in low coherence interferometry are sensitive to the optical intensity and not to the electric field. The link between optical intensity and electric field can be approximated by

$$I(\omega) \propto |E(\omega)|^2. \tag{2.8}$$

The detector is exposed to the superposition of the two electric fields E_R and E_S, which are both function of ω, recombined at the splitting device and it is integrating over a given time (brackets denote time averaging). Then, the signal per pixel is

$$I_{Detector}(\omega) \propto \langle (E_R(\omega) + E_S(\omega))^2 \rangle = \langle (E_R(\omega) + E_S(\omega)) \times (E_R(\omega) + E_S(\omega))^* \rangle. \tag{2.9}$$

By combining Equation 2.9 with the expressions from Equation 2.6 and Equation 2.7:

$$I(\omega) \propto \langle (E_R^2(\omega) + E_S^2(\omega) + E_R(\omega)E_S^*(\omega) + E_S(\omega)E_R^*(\omega)) \rangle. \tag{2.10}$$

This can be simplified to:

$$I(\omega) \propto S(\omega) \times (1 + \cos(2\beta\delta l)). \tag{2.11}$$

Equation 2.11 describes the fact that the signal detected at the output of the interferometer is a modulated version of the source spectrum where the modulation periodicity is governed by the mismatch in length between the reference and sample paths. Low coherence interferometry principle is at the heart of OCT technology as it allows to locate the position in depth in the sample of scattering centres along the optic axis oriented along OZ.

2.2.3 Measuring depth reflectivity profile using white light interferometry

The above description of Low coherence interferometry, concluding with Equation 2.11, has been built from an interferometer with a mirror as the reflector in the sample path. A sample can be approximated by a series of discrete reflectors distributed along the depth dimension. This leads to a modification of the expression for the electric field E_S, if assuming N scattering centres along the axis OZ, each of reflectivity $R_{Sn}$and located at a

distance $(L + \delta l_n)$ from BS:

$$E_S(\omega) = \frac{E_0(\omega)}{\sqrt{2}} \times \sum_{n=1}^{N} \sqrt{R_{Sn}} \times e^{i(2\beta(L+\delta l_n)-\omega t)}. \tag{2.12}$$

Considering the sample path electric field and repeating a similar process as in section 2.2.2, the detected signal at the output of the interferometer can be written as:

$$\begin{aligned} I_{Detector}(\omega) \propto \quad & S(\omega) \times \left[R_r + \sum_{n=1}^{N} R_{Sn} \right] \\ & + S(\omega) \times \sum_{n=1}^{N} \sqrt{R_R R_{Sn}} \times \cos\left(2\beta\delta l_n\right) \\ & + S(\omega) \times \sum_{n\neq m=1}^{N} \sqrt{R_{Sm} R_{Sn}} \times \cos\left(2\beta(\delta l_n - \delta l_m)\right) \end{aligned} \tag{2.13}$$

Equation 2.13 can be separated into 3 terms:

- $S(\omega) \times \left[\sum_{n=1}^{N} R_{Sn}\right]$ represents a DC signal which is a summation of contributions from all reflectors along a line in depth within the sample plus a contribution due to the mirror in the reference path.

- $S(\omega) \times \sum_{n=1}^{N} \sqrt{R_R R_{Sn}} \times \cos\left(2\beta\delta l_n\right)$ represents the interference between the light from the reference path and the light reflected by all reflectors within the sample. This term, called interference term, is the useful part of the signal for OCT analysis. Its amplitude is large compared to the auto-correlation term as R_R is much larger than R_S.

- $S(\omega) \times \sum_{n\neq m=1}^{N} \sqrt{R_{Sm} R_{Sn}} \times \cos\left(2\beta(\delta l_n - \delta l_m)\right)$ is a term which described the interferences occurring between light back-scattered by all the scattering centres along a line in depth within the sample. The amplitude of such a signal is relatively small as R_{Sn} is small inside the sample. Usually, samples such as eye and skin present power reflectivity in the range of 10^{-3} to 10^{-5} [5]. This term is called the auto-correlation term or self-interference term.

Similarly, to the previous section, the signal detected at the output of the interferometer, given by Equation 2.13, provides information on the

depth positions of the scattering centres in the sample. Also, from Equation 2.13, not only the positions can be inferred but also the strengths of the reflected signals are accessible through R_{Sn}. All R_{Sn} coefficients are mixed together because the power reflectivities of the sample reflective centres are assumed to be very small. Then, it is fair to consider that the optical power incident on the sample is not decrease from reflective centre to the next one over the 1 mm depth of the imaging system capabilities. The power reflectivities R_{Sn} are governed by local variations of the index of refraction within the sample investigated [6].

2.3 Low coherence interferometry + Scanning sample = OCT

2.3.1 Optical Coherence Tomography Definition

Optical coherence tomography is an imaging modality obtained by the association of a low coherence interferometry system and a lateral scanning device [2]. As shown by section 2.2.3, the positions and the power reflectivities of each reflective centres can be measured using low coherence interferometry (Equation 2.13). With the addition of lateral scanning device, a 3-dimensional representation of a sample can be obtained by measuring low coherence interferometry signal along two lateral dimensions.

Two sub-categories of OCT systems exist. Time-Domain-OCT (TD-OCT) and Fourier Domain-OCT (FD-OCT). The first one, TD-OCT, is the original method presented in [2], where the sample reflectivity profile $r_s = \sqrt{R_{Sn}}$ is built by scanning the reference arm of the interferometer, which means that the depth reflectivity profile is measured depth point by depth point. Then, similar axial scans are acquired at several lateral locations on the sample. The characteristic components of a TD-OCT system are a broadband light source, an interferometer and a photodiode as a detection unit. In

the last 15 years, TD-OCT was almost replaced by Fourier domain (FD)-OCT, methods that are much faster and present better sensitivity than TD-OCT [7]. The second sub-category of OCT technology, Fourier Domain-OCT (FD-OCT), is nowadays the most spread technique within the community. Within FD-OCT, two trends have emerged, Spectral Domain-OCT (SD-OCT) and Swept-Source OCT (SS-OCT). Both methods are based on the fact that depth-domain and the wavenumber-domain are conjugate variable by Fourier Transform (FT) operation. Spectral domain-OCT relies on a broad-band source and a spectrometer while SS-OCT relies on fast tunable laser and a photodiode. Both methods offer much higher image quality and acquisition speed than TD-OCT [8, 9, 10].

However, TD-OCT has an important advantage in comparison with the FD-OCT system in terms of lateral resolution. TD-OCT is compatible with adjusting the focus position for each depth investigated, a procedure termed as dynamic focusing [11].

This thesis is dedicated to the use of supercontinuum light source in SD-OCT. Therefore, the following parts of this chapter are dedicated to describe particular features of SD-OCT. Some of the concepts are also applicable to SS-OCT and even to TD-OCT.

2.3.2 Optical Coherence Tomography terminology (A-scan, B-scan, en-face or C-scan)

When considering images obtained from an OCT system (FD-OCT and TD-OCT), it is usual to use a particular set of denominations describing the dimensions represented by the image. Let x, y, z be a 3-dimensional referential with x and y axes oriented along the lateral dimensions and z along the depth dimension. Data obtained from an OCT system is a measure of the depth information profile of the sample at a given lateral location. Then, this corresponds to a reflectivity measurement at $x =$ constant and $y =$ constant with the information along the z-axis. Such 1-dimensional scan along depth is called an A-scan. An example of an A-scan measured from a skin sample is presented in Figure 2.2 (b). Then, the beam can be scanned along either the x or y dimension. By recording and stitching A-scans acquired along a

lateral direction, a 2-dimensional view of the sample can be obtained. Such a 2D transverse representation is called a B-scan. Figure 2.2 (c) is an example of B-scan, made of 500 A-scans, measured from a skin sample. Finally, it is possible to record a volume by moving the beam along both a fast and a slow axis. Here, the fast axis corresponds to the acquisition of B-scan as previously and the slow axis is perpendicular along the fast direction. In that case, the volume is made of an assembly of B-scans. From such a volume, it is possible to extract an image which corresponds to a slice of the sample at a given depth. This particular view is called a C-scan or *en-face* view. Figure 2.2 (d) is an example of C-scan extracted from a volume representing a skin sample.

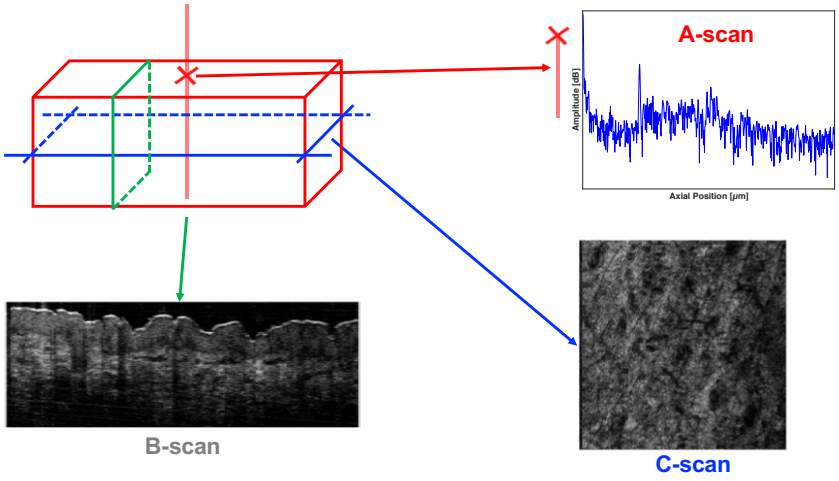

FIGURE 2.2: Definition of the scanning terminology depending on the coordinate axes represented in an image.

The data acquisition sequence is an important parameter of an OCT system. Nowadays, with additional features such as OCT-Angiography or Spectroscopic-OCT, it is common for certain applications that a C-scan is the most effective way to analyse an image. In that situation it is necessary to acquire and process a full volume of data to obtain this representation. This is time-consuming as most of the processed data are not used for displaying a single C-scan. A good example in this respect is the *en-face* view of the retinal blood vessel distribution [12, 13] which is extremely useful for ophthalmologists. Then, it is interesting to develop alternative techniques for modifying the imaging sequence. This topic will be discussed in Chapter 4.

2.3.3 Spectral-Domain OCT (SD-OCT)

Spectral domain OCT allows creating three-dimensional representation of a scattering sample by using a broadband optical source and a spectrometer as a detection unit. Sources such as Super-Luminescent Diode (SLD), Supercontinuum (SC), Solid State Laser (SSL) can be used considering that one of the main criteria of SD-OCT is the optical bandwidth of the source. The detection unit is a spectrometer that accomplishes the operation of diffracting (dispersing) the spectrum onto the array of pixels of a linear camera. This highly reduces the contribution of shot noise, leading to a much higher Signal to Noise Ratio (SNR) compared to TD-OCT [5]. Typically, a SNR improvement of around 20-30 dB is observed from TD-OCT to SD-OCT. Optimally, a spectrometer dedicated to SD-OCT should be built with a good balance between spectral resolution and spectral bandwidth. The different parameters of the source and detection unit are discussed in section 2.8 and section 2.6 of this Chapter 2.

The main advantage of SD-OCT compared to TD-OCT is that it is a single shot interrogation method. Using SD-OCT, no depth scanning of the reference path is required. This means that a single interrogation of the sample is enough to build a complete depth reflectivity profile at a given lateral position. This advantage, in comparison with TD-OCT, offers a speed increase of around 100 folds when using a system operation with line-rate of few tens of kHz [8, 9, 10]. Even more, SS-OCT systems, due to the fast laser wavelength swept, can operate up to the MHz regime. This increase in speed is one the two reasons why FD-OCT (SD-OCT and SS-OCT) are nowadays much more used in comparison to TD-OCT.

A typical SD-OCT system is sketched in Figure 2.3, in a bulk configuration and in a fibre-based configuration. The light from a broadband source is split into two paths by either a bulk beam splitter (BS) or a directional coupler (DC). The first path, commonly called the reference path, consists in a fixed-length free-space propagation of light. The second path, called the sample path, is made of a free space part, a scanning system and a lens acting as an objective for focusing the light beam onto the sample. Then, the light reflected by the reference mirror and the sample recombine at the

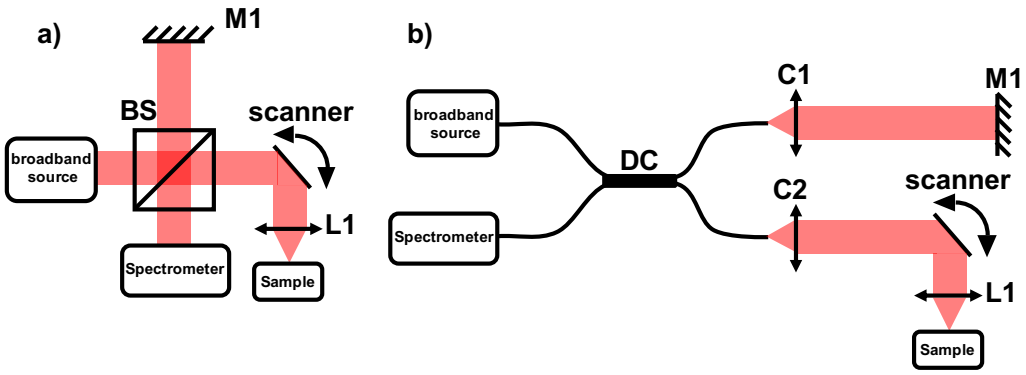

FIGURE 2.3: Typical configuration of a SD-OCT system. Bulk configuration (a) and fibre-based configuration (b).

splitting device and their spectral interference is translated by the spectrometer into a modulated signal. The interference signal consists of a DC signal superposed with a modulated signal corresponding to different scattering centres within the sample (see Equation 2.11 and Equation 2.13).

2.4 Noise definition in OCT and Signal-To-Noise Ratio

A SD-OCT system is affected by different sources of noise, which can limit the achievable Signal to Noise Ratio (SNR). The SNR is a measure of the contrast between the useful information within the image compared to the background noise. Limiting the SNR has the direct consequence of reducing the final image quality obtained from the OCT system. Image quality reduction leads to lower visual contrast. Then, it is important to properly control the different parameters within the system which might play a role in the overall noise behavior of the system.

2.4.1 Source of noise in SD-OCT

There are several noise sources in an SD-OCT system as described in [14] and summarized below:

Read (r) and detector (d) noise σ^2_{r+d}: It is due to the different electronic components used in the SD-OCT system. In the notation, the (r) denotes the noise added when reading the signal. Read noise can be seen as noise created at the digitization stage of the analogous signal. The second letter of the notation (d) represents the detector noise, the noise created within the camera of the spectrometer. In such detectors, the thermal fluctuations can randomly transfer electrons from the valence band to the conduction band of the semiconductor material.

Shot noise $\sigma^2_{shotnoise}$: It is due to the random arrival of photons at the detector. This random arrival leads to a random temporal generation of photo-electrons in the detector. Shot noise can be expressed as

$$\sigma^2_{shotnoise} = \frac{\rho\eta\tau}{h\nu_0} \times \frac{P_0}{N} \times \left(\alpha_s\gamma_s R_s + \alpha_r\gamma_r R_r\right), \tag{2.14}$$

where ρ is the spectrometer efficiency, η is the quantum efficiency of the camera, τ is the camera exposure time, h is the Planck constant, ν_0 is the central frequency of the light source, P_0 is the optical power at the interferometer input, N is the number of pixel on the camera, α_s and α_r are the ratios of the light coupling back into the fibre while returning from respectively the sample and the reference mirror, γ_s and γ_r are the fraction of the total power P_0 in respectively the sample path and the reference path of the interferometer, R_s and R_r are the power reflectivities of the sample and the reference mirror respectively. Commonly, when using a SC light source which provides high average power, R_r is the total reflectivity of a system consisting of a mirror and a neutral density filter. The neutral density filter is necessary to avoid saturation of the detector. Shot noise is the less limiting operation regime for an SD-OCT system and corresponds to a maximum SNR. Ideally, any imaging modality should operate under shot noise limited detection.

Relative Intensity Noise σ^2_{RIN}: It is characterizing the excess noise in the system. Mainly the excess noise is dominated by RIN which is due to the

light source intensity fluctuations in time. Similarly, to the shot noise expression, RIN can be expressed:

$$\sigma^2_{RIN} = \frac{(1+\Pi^2)}{2} \times \left(\frac{\rho\eta}{h\nu_0}\right)^2 \times \frac{N}{\Delta_{eff}} \times \frac{\tau P_0^2}{N^2} \times (\alpha_s\gamma_s R_s + \alpha_r\gamma_r R_r)^2 , \quad (2.15)$$

with Π is the degree of polarization of the light source and $\Delta\nu_{eff} = \sqrt{\frac{\pi}{2\ln(2)}} \times \frac{c\Delta\lambda}{\lambda_c^2}$ is the source effective line-width with c the speed of light, λ_c^2 is the light source central wavelength and $\Delta\lambda$ is the light source optical bandwidth. It is assumed for this definition of RIN that the system is free from what could be described as environmental RIN. Environmental RIN would include noise contributions such as mechanical instability of the components in the system and temperature fluctuations. Such variations lead to variation of the coupling of light into the interferometer and therefore create additional intensity fluctuations.

2.4.2 Signal to noise ration in SD-OCT

It is common to assume that the power returning from the sample back into the interferometer is much smaller compared to the power considered in the reference path. Then, if similar coupling coefficients α_s and α_r are considered,

$$\alpha_s\gamma_s R_s + \alpha_r\gamma_r R_r \approx \alpha_r\gamma_r R_r. \quad (2.16)$$

The tool for noise consideration, not only in SD-OCT but also in SS-OCT and TD-OCT, is the SNR. For ease of identification let's denote $P_{sample} = P_0\gamma_s$ and $P_{ref} = P_0\gamma_r$. Then, the SNR of an SD-OCT can be expressed as

$$SNR_{SD-OCT} = \frac{\langle S^2_{SD-OCT}\rangle}{\sigma^2_{total}} = \frac{\frac{1}{N^2}\left(\frac{\rho\eta\tau}{h\nu_0}\right)^2 \times \alpha_s P_{sample} R_s \times \alpha_r P_{ref} R_r}{\frac{1}{N}\left(\sigma^2_{r+d} + \frac{\rho\eta\tau}{h\nu_0}\frac{P_{ref}R_r}{N} + \frac{(1+\Pi^2)}{2}\left(\frac{\rho\eta}{h\nu_0}\right)\frac{N}{\Delta_{eff}}\frac{\tau P^2_{ref}R_r}{N^2}\right)} \quad (2.17)$$

2.4.3 Consideration for optimal noise SNR of an SD-OCT

As described above, noise in SD-OCT has different origins. The different contributions are not equal in amplitude and might affect the SNR

with various impacts. Since the early stage of SD-OCT, important technological improvements have led to a generation of highly sensitive detectors which show low detector noise [15, 16]. Thanks to such low noise detectors, SD-OCT systems are nowadays able to achieve shot noise limited detection. Nevertheless, if a source with high intensity fluctuations is used, the system might be within the RIN limited regime. It has been shown in many reports that the optimal regime for maximizing the SNR is shot noise [17, 18]. This is achieved when the conditions of Equation 2.18 and Equation 2.19 are fulfilled:

$$\frac{\sigma^2_{shotnoise}}{\sigma^2_{r+d}} = \frac{\rho\eta\tau}{h\nu_0}\frac{\alpha_r P_{ref} R_r}{N} > 1, \tag{2.18}$$

and

$$\frac{\sigma^2_{shotnoise}}{\sigma^2_{RIN}} = \frac{h\nu_0}{\rho\eta}\frac{2}{1+\Pi^2}\frac{\Delta_{eff}}{\alpha_r P_{ref} R_r} > 1. \tag{2.19}$$

Under those conditions, the expression of the SNR can be simplified as a shot noise limited expression:

$$SNR^{shotnoise}_{SD-OCT} = \frac{\frac{1}{N^2}\left(\frac{\rho\eta\tau}{h\nu_0}\right)^2 \times \alpha_s P_{sample} R_s \times \alpha_r P_{ref} R_r}{\frac{1}{N}\frac{\rho\eta\tau}{h\nu_0}\frac{P_{ref} R_r}{N}}. \tag{2.20}$$

As a conclusion regarding noise in SD-OCT, it is crucial to understand that not all SD-OCT configurations can fulfill Equation 2.18 and Equation 2.19 for shot noise limited SNR. Indeed, a system driven by a noisy optical source will have high RIN from the source, leading to an SNR below the shot noise limited regime. This is the case when using supercontinuum lasers as sources in OCT. This problem is addressed in Chapter 5, Chapter 6 and Chapter 7 of this thesis.

2.5 OCT characteristic values

As with any scientific field, the OCT community has a list of parameters and definitions which are essential to understand. It often happens that peer review papers use these without recalling their complete definitions. This section provides a description of the required terms for understanding this thesis and other documents in the literature.

2.5.1 Sensitivity

The first parameter of this list is the so-called Sensitivity. Sensitivity represents the ability for an OCT system (TD-OCT or FD-OCT) to image weak signals within the sample. Signals returning back from the sample are potentially weak, both due to the limit of optical power applied to the sample and also because of the light attenuation while propagation into the sample. The physical definition of Sensitivity is the attenuation value to consider in the sample path of the interferometer, given a mirror as the sample, in order to achieve a SNR equal to 1 [5]. However, this measurement is not straightforward to implement as the typical minimum reflectivity measurable is around 100 dB. A popular way of estimating the Sensitivity is by measuring a SNR, using a mirror in the sample path, where a given attenuation has been added to avoid camera saturation. Then, the sensitivity S can be obtained has

$$\text{S[dB]} = \text{SNR[dB]} + \text{Attenuation [dB]}. \tag{2.21}$$

Several parameters can cause a decrease in Sensitivity. For example, a non-optimized collection of the light returning from the sample path. However, if considering carefully the different hardware issues, the main limiting factor of Sensitivity is the noise in the system. The optimal working point of an OCT system is shot noise dominated regime as it is the only regime which see the SNR increases while P_{Ref}increases. Any other regime such as electronics noise dominated regime or RIN dominated regime leads to non-optimal Sensitivity values. The shot noise limited Sensitivity, for a given power applied on sampled P_{Sample}, is deduced from Equation 2.20 and Equation 2.21 as

$$\text{S[dB]} = 10 \times \log\left[\frac{\rho\eta\tau}{h\nu_0} \times \alpha_s P_{sample} R_s\right] + \text{Attenuation [dB]}. \tag{2.22}$$

2.5.2 Axial resolution in SD-OCT

Optical Coherence Tomography relies on low coherence tomography and therefore offers one main advantage compared to conventional microscopy

techniques. This advantage is the disconnection between axial and lateral resolution. Indeed, while the microscopy resolutions, in all dimensions, are linked to the objective Numerical Aperture (NA), only the transverse resolution of an OCT system is linked to the objective NA. For low coherence interferometry based systems, the resolution in depth is governed by the coherence length of the optical source.

The OCT system axial resolution corresponds to the width of the point spread function (PSF) in the z-domain and is equal to half the coherence length of the source. As described by Equation 2.4, temporal coherence and PSD are linked via a FT operation. Then, the axial resolution Δz of an SD-OCT system is calculated as

$$\Delta z = \frac{l_c}{2} = \text{FWHM}\left[\text{iFFT}\left[S(k)\right]\right], \tag{2.23}$$

where FWHM[.] represents an operator measuring the Full Width at Half Maximum, iFFT is the inverse Fourier Transform operation and $S(k)$ is the source PSD.

From the early stage of OCT, Super-Luminescent Diode (SLD) sources have been used in OCT systems as they are relatively cheap with a smooth Gaussian spectrum and with broad spectrum (few tens of nanometres). In such a case, the Fourier relation between the spaces z and k leads to a relation as described in [5]

$$S(k) = \frac{1}{\Delta k\sqrt{\pi}} \times e^{-\left[\frac{(k-k_0)}{\Delta k}\right]^2} \Leftrightarrow \gamma(z) = e^{-z^2\Delta k^2}, \tag{2.24}$$

with $\gamma(z)$ is called the coherence function and its width at half maximum is related to the coherence length of the source. Within this assumption of a Gaussian PSD, Δz the axial resolution can be calculated as

$$\Delta z = \frac{l_c}{2} = \frac{2\ln(2)}{\pi} \times \frac{\lambda_c^2}{\Delta\lambda} = \frac{2\sqrt{\ln(2)}}{\Delta k}, \tag{2.25}$$

where λ_c is the central wavelength of the PSD and $\Delta\lambda$ is the source spectral bandwidth. Even though the two expressions of Equation 2.25 are correct,

it is much more common to obtain the wavelength information from an optical source rather than the wavenumber one. The term $\sqrt{\ln(2)}$ comes from the estimation of the FWHM of $\gamma(z)$.

When discussing an axial resolution in SD-OCT, it is important to understand that since the early days of OCT technology the number of sources available have dramatically increased. Nowadays, the list of sources includes super-luminescent diodes, solid state lasers or SC sources. The large bandwidth made available by several new concepts has created a new OCT field referred to as Ultra-High Resolution-OCT (UHR-OCT) [19]. In some cases, the source spectrum is so broad that it exceeds the spectrometer bandwidth. In such cases, the axial resolution of the SD-OCT system is less than that determined by the coherence length of the source, it is instead determined by the spectrum width utilized by the spectrometer. An overview of the sources available for SD-OCT is presented in section 2.8.

2.5.3 Lateral resolution consideration in OCT

As described above in section 2.5.2, the lateral or transverse resolution of an OCT system depends on the objective numerical aperture. The equations governing the lateral resolution are those established for confocal microscopy or conventional optical microscopy [20]. The lateral resolution is then linked to the spot size (along the lateral direction) of the focused Gaussian beam. The expression of the lateral resolution Δx of an OCT system is given by

$$\Delta x = \frac{2\lambda_c}{\pi} \times \frac{1}{NA}, \tag{2.26}$$

where NA $= D/2f$ is the numerical aperture of the objective with D the diameter of the beam on the objective and f the focal length of the objective lens. The NA of an objective is an indication of the capacity for the objective to collect light from a point source. The higher the NA, the larger the maximum angle from a point source from which the objective can collect photons. As shown in Equation 2.26, the higher the NA the better the OCT lateral resolution. However, it is important to consider a second parameter called the Depth of Focus.

The depth of focus is a measure of the distance around the minimum beam waist position, where the beam waist is smaller than twice its minimum value. Physically, it characterizes the length where a tight focus is maintained. Mathematically, it is calculated as twice the Rayleigh length z_r and can be expressed as

$$\text{DoF} = 2z_r = \frac{\pi \Delta x^2}{2\lambda_c} = \frac{2\lambda_c}{\pi} \times \frac{1}{NA^2}. \tag{2.27}$$

It is noticeable that the DoF varies with the inverse square of the objective NA. Then, using high NA objective leads to a reduction of the DoF of the objective. While designing an OCT system, there is a balance to consider regarding the choice of the objective between lateral resolution and depth of focus. The better the lateral resolution of the system, the smaller the distance out of which the lateral resolution is maintained. A popular sketch inspired from [5] describes this effect in Figure 2.4.

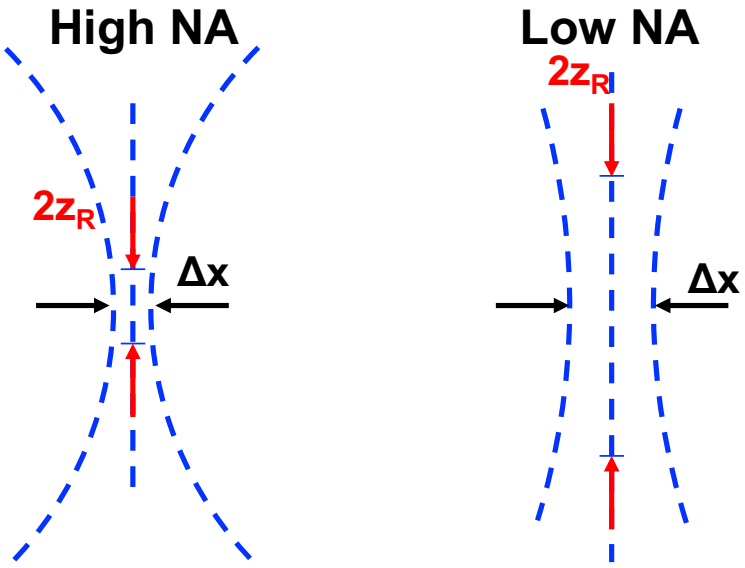

FIGURE 2.4: Schematic of the balance between Rayleigh length and lateral resolution for high and low numerical aperture of the objective lens. Adapted from [5]

2.6 Spectrometer for SD-OCT

2.6.1 Spectrometer concept

A spectrometer is a detection unit used for measuring the spectral intensity distribution of light. The physical effect behind the spectrometer principle is diffraction. By diffracting the light before detection, the spectral shape of the input light is accessible. A spectrometer is composed from five elements. The first is the slit and is placed at the input port of the spectrometer. The second element is the collimation lens. The third is the diffraction grating. The focal length of the collimation lens is chosen in such a way that, together with the Numerical Aperture (NA) of the fibre (the fibre core is acting as the slit), a parallel beam illuminates as many lines as possible on the diffraction grating. It is important to illuminate as much lines as possible on the grating in order to ensure a spectral resolution as small as possible and therefore an optimal imaging range (see section 2.6.4). The diffraction grating is the element of the spectrometer responsible for diffracting the light. A diffraction grating can be either in transmission or reflection. Assuming a monochromatic beam, the angle at which the light exits the diffraction grating follows the rule given by Equation 2.28 and Equation 2.29 (according to the sketch shown in Figure 2.5).

$$d \times [\sin(\theta_m) - \sin(\theta_i] = m\lambda, \tag{2.28}$$

which gives the exiting angle θ_m as:

$$\theta_m = \sin^{-1}\left[\frac{m\lambda}{d} + \sin(\theta_i)\right], \tag{2.29}$$

where θ_i is the angle of incidence of the beam on the diffraction grating, θ_m is the exiting angle at diffraction order m, λ is the wavelength of the light, m is the order of diffraction consider and d is the distance between two lines within the grating usually called grating spacing. Commonly, if using non-blazed grating, spectrometers in OCT operate with the first order of diffraction as higher orders have weaker intensities. The fourth element of the spectrometer is the focusing lens which focuses the light on the detector.

A telescope system is created by the collimation lens and the focusing lens. When designing the spectrometer, it is important to ensure that the image of the input slit of the spectrometer by the telescope is smaller than the pixel size on the detector. Pixel intensity leakage can significantly reduce the efficiency of the spectrometer. Finally, the last element of the spectrometer is the camera. In a conventional SD-OCT system, this camera is a line-scan camera. A line-scan camera is a detector using a single line of pixels, which is read at a rate of a few tens of kHz to a few hundreds of kHz. Considering OCT typical wavelength, silicon detectors are used from 600 to 900 nm while InGaAs detectors are used from 1000 to 2000 nm. A typical pixel size of 5 - 10 µm is achieved in Silicon camera and 20 - 30 µm for InGaAs cameras. Nowadays, the number of pixels are generally of 4096 - 8192 for silicon cameras and 2048 - 4096 for InGaAs cameras [15, 16].

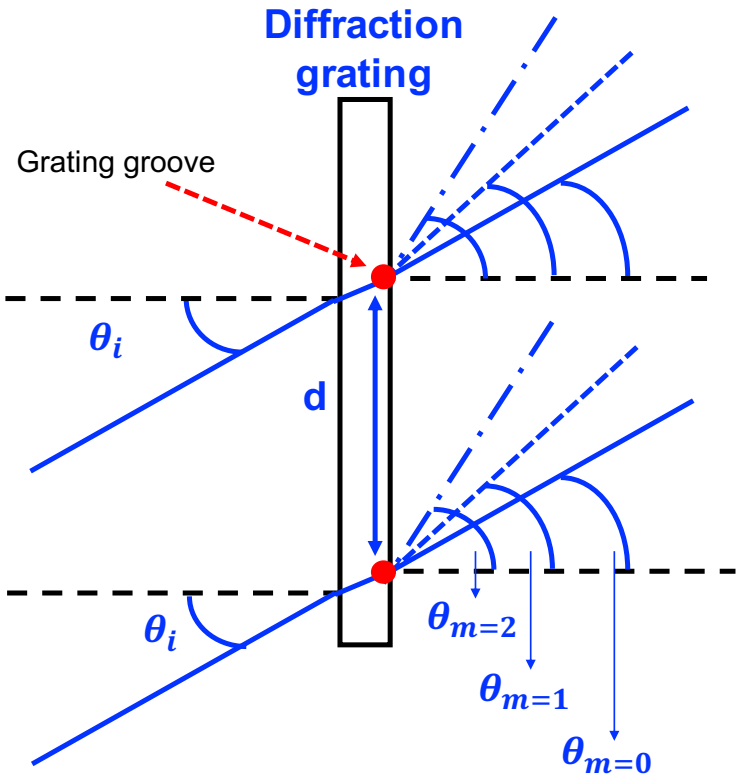

FIGURE 2.5: Sketch of light diffraction by a diffraction grating for a monochromatic light at wavelength λ.

A typical transmission diffraction grating based spectrometer designed for OCT application is presented in Figure 2.6. Commonly, an OCT interferometer is based on a fibre coupler in order to divide and recombine the light. Assuming this fibre-based configuration, the slit of the spectrometer is the core of the optical fibre connected to the input of the spectrometer. Most of the time this will be a single mode fibre as a homogeneous illumination is required on the grating. This fibre is placed at a distance corresponding to the focal length of the collimation lens in order to obtain a parallel beam of diameter D. The diameter D is influenced by the focal length f_1 and the fibre NA. It is important to ensure a beam diameter large enough to illuminate a large number of lines on the DG [21]. Therefore, as the NA is fixed for a given fibre, the focal length of the collimation lens need to be chosen for maximizing the illumination of the grating. The limitation in beam diameter for a spectrometer is the dimension of the grating effective area. The grating effective area is the area of the grating over which the manufacturer ensures the grating line density within a small margin. The expression for D (in air) is given by the NA expression as:

$$NA = sin(\theta_f) = \frac{D}{2f_1}. \tag{2.30}$$

Then, the collimated beam hits the DG and the light is diffracted according to Equation 2.29. The focusing lens L_2 is placed at an intermediate distance to the grating in order to collect the light contained in the first order of diffraction. This intermediate distance is a balance between the lens diameter and the diameter of the beam after the DG. However, it is important to consider the problem of intensity leakage from pixel to pixel due to defocusing of the beam on the camera caused by geometrical aberrations. Indeed, geometrical aberrations degrade the focusing properties of the lens, especially if the edges of the lens are used. Finally, the last element, the line-scan camera, detects the light and provides a measure of the intensity which is a representation of the intensity per non-equally spaced wavelength slot. The choice of the components of the spectrometer is done in consideration of the

expected specifications and requirements of the imaging system. For example, in the case of UHR-OCT, where large optical bandwidth are considered, one would prefer to use mirrors for collimation and focusing instead of lenses in order to obtain low chromatic effects. Also, reflection based grating would be preferred compared to transmission based one for if very high efficiency is required.

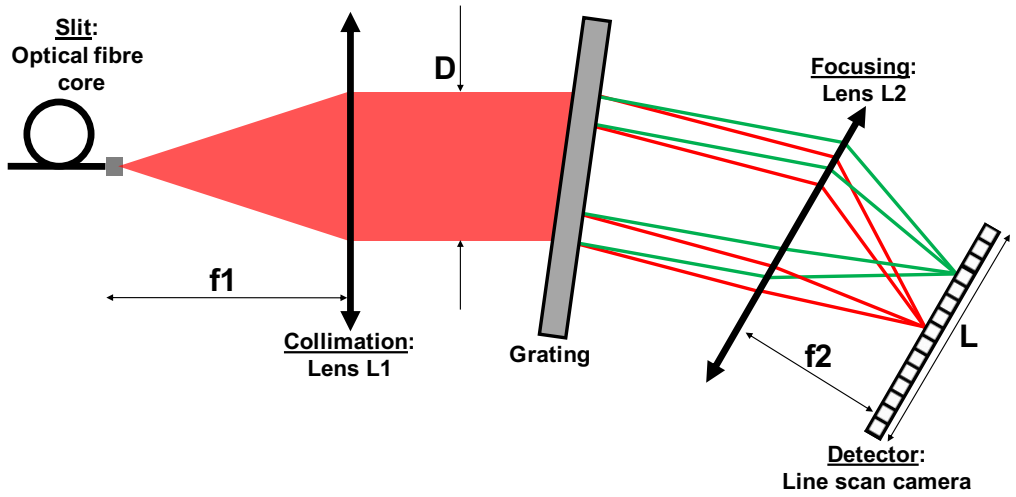

FIGURE 2.6: Configuration of a transmission DG-based spectrometer commonly used in SD-OCT.

Such a spectrometer is characterized by several parameters. The basic ones are:

- Spectrometer Efficiency: It represents the power efficiency of the spectrometer. Due to the different lenses and the different orders of diffraction, a spectrometer involves a certain amount of losses.

- Spectral Bandwidth: It is the span of wavelengths which is detected by the spectrometer. Ideally, this bandwidth has to be equal to the source bandwidth or smaller. Operating with a spectrometer bandwidth larger than the source bandwidth will lead to a limited imaging range for the SD-OCT system (see section 2.6.3).

- Spectral Resolution: It describes the sampling properties of the spectrometer and also influences the imaging range (see section 2.6.3) of the SD-OCT system.

2.6.2 Issue of spectrometer non-uniformity in k

As mentioned above, the data from the spectrometer are measured along the pixel line of the camera. The wavelength distribution along the pixel line can be deduced through the grating Equation 2.29 and geometrical optics considerations [22]. Then, considering the parameters of Figure 2.5 and Figure 2.6, the wavelength distribution is:

$$\lambda_j = d\left[\sin(\theta_i + \sin\left(\sin^{-1}\left(\frac{\lambda_c}{d} - \sin(\theta_i)\right) + \tan^{-1}\left(\frac{w \times j - x_c}{f_2}\right)\right)\right], \tag{2.31}$$

with w the pixel size, j is the pixel position, x_c the distance between the first pixel to the middle of the pixel line and f_2 the focal length of the focusing lens L2. Such distribution is non-uniform in wavelength. However, SD-OCT relies on the conjugate link between axial position (or depth) and wavenumber. It is then required that the signal is converted in wavenumber units through the hyperbolic relation $k = 2\pi/\lambda$. As the data are initially non-uniform in wavelength, the wavenumber distribution is also non-uniform and needs to be corrected before FFT. The direct consequence of the data non-uniformity in wave-number is observed within the phase of the interference equation (Equation 2.13). The wavenumber non-uniformity makes the interference phase non-linear in wave-number and leads to a non-Transform limited PSF for the SD-OCT system [23].

Numerous techniques have been proposed in order to correct for this non-uniform distribution of wave-number. Hardware modifications of conventional spectrometer designs [24, 25] have shown encouraging results. However, the most popular method is based on phase extraction and extrapolation of data [17]. A complete description of this procedure is proposed in section 4.4.4. By using a calibration procedure prior to imaging, complete correction of the non-uniformity can be achieved and transform limited PSF is obtained. In addition, dispersive effects can also alter the phase linearity. This point is discussed in section 2.7.1 of this chapter.

2.6.3 Sensitivity decay with depth

When using a spectrometer in SD-OCT, a discrete vector is built which represents the spectral shape of the interference signal. The discrete nature of this vector comes from the pixel line of the camera. Each pixel on the line is detecting a slot of frequency/wavelength equivalent to more or less the spectrometer resolution. Due to the finite slot dimension and the Gaussian beam illuminating the spectrometer, a sensitivity decay of the SD-OCT system is observed with depth [26]. This decay, or fall-off, $R(z)$ can be expressed as

$$R(z) = \text{sinc}^2(\psi) \times e^{-\frac{p^2}{2ln(2)}\psi^2}, \tag{2.32}$$

where $\psi = \frac{\pi}{2}\left(\frac{z}{z_{max}}\right)$ and $p = \delta_s\lambda/\Lambda$. z denotes the depth dimension and Λ is the spacing between pixels. The sensitivity decay with depth corresponds in wavenumber domain to a drop of the fringes visibility at large depths (fast modulation frequency). It is necessary to consider the decay carefully while designing a spectrometer. Large spectrometer bandwidth leads to large spectrometer resolution and important sensitivity decays. Then, a clear analysis of the SD-OCT spectrometer together with the overall imaging requirement is necessary to fully optimize the system performance.

2.6.4 Imaging depth of an SD-OCT

As introduced by section 2.5, a SD-OCT system uses a spectrometer in order to measure an interferogram. In the case of SD-OCT, it is a discrete vector where the interferogram is encoded in the pixel line of the detector. Due to this discrete nature and due to the fact that OCT is a modulation decoding problem, the Nyquist theorem [27] needs to be considered. Then, for a given sampling resolution $\delta_s\lambda$ of the signal, the maximal and minimal imaging depth achievable (in air) by an SD-OCT system is

$$\pm\, z_{max} = \pm\frac{\lambda_c^2}{4\delta_s\lambda}. \tag{2.33}$$

Such description of the imaging depth is valid only for a correctly designed spectrometer, more precisely for a spectrometer which uses a large

number of lines on the diffraction grating. Indeed, if the number of lines used is too low, it will become the dominant effect on the imaging range calculations.

It was mentioned in section 2.6.1 that the spectral bandwidth has to be ideally equal to the source bandwidth or smaller but not larger. This requirement can be explained through the imaging depth $\pm z_{max}$. Indeed, if considering a spectrometer bandwidth larger than the source bandwidth, the spectrometer resolution $\delta_s\lambda$ is larger compared to small bandwidth case. Then, the imaging depth is limited compared to what could be achieved for a given source bandwidth. However, when designing a spectrometer, two additional parameters need to be considered. The first one, is the spectrometer sensitivity decay with depth discussed in section 2.6.3. The second one is related to the sample under investigation. As an example, the light can penetrate through skin up to 2 mm. In this situation, an imaging range much larger than 3 mm seems not well suited. Similarly, spectrometers in the 800 nm region allow an imaging range around 1 mm while the retina thickness is less than 300 µm. If a very long imaging range is required, a SS-OCT system would be more suited as an imaging range within the cm scale is easily achievable [28, 29]. This is because the equivalent parameter to spectral resolution in SS-OCT is the light source line-width which can be within a few pm compared to a few tens of pm for the best spectrometer.

2.7 Other important aspects of SD-OCT

2.7.1 Dispersion issue in SD-OCT

Dispersion is a well-known effect arising in optical system due to the frequency dependence of the index of refraction of any material. Due to this dependency, wavelengths propagate at different group velocities and follow slightly different optical paths[30]. Within an OCT system dispersion effects can cause significant degradation of the axial resolution by broadening the PSF [14]. Such degradation is even more problematic if UHR is targeted as larger optical bandwidths are used. This degradation manifests as a chirping effect on the CS modulation. Mathematically, the chirp corresponds to

a non-linearity within the phase of the CS modulation. It is common to observe the effect of dispersion by decomposing the propagation constant term into a Taylor series [14] as

$$\beta(\omega) = \beta(\omega_0) + \left.\frac{\partial\beta}{\partial\omega}\right|_{\omega_0}(\omega-\omega_0) + \frac{1}{2}\left.\frac{\partial^2\beta}{\partial\omega^2}\right|_{\omega_0}(\omega-\omega_0)^2 + \ldots + \frac{1}{n!}\left.\frac{\partial^n\beta}{\partial\omega^n}\right|_{\omega_0}(\omega-\omega_0)^n. \tag{2.34}$$

Within this decomposition each order has a particular influence on the axial resolution of the OCT system [14]

- $\beta(\omega_0)$ adds a constant phase term which does not influence the PSF.
- $\frac{\partial\beta}{\partial\omega}$ modifies the coherence length as $l_{c,Dispersion} = \frac{l_c}{n_G}$ where $n_G = \left(\frac{\partial\beta}{\partial\omega}\right)^{-1}$ is the group index. The first order term shift the position of the coherence function and decreases its width.
- The second order term $\frac{\partial^2\beta}{\partial\omega^2}$ is responsible for Group Velocity Dispersion (GVD) in the system which broadens the PSF. The chirping effect mentioned earlier is due to this second order term. Also, due to the energy conversation principle between CS in the k-domain and axial profile in the z-domain, a SNR reduction is observed due to GVD.
- High orders of dispersion (>2), contribute much less to the distortion of the PSF. However, if targeting UHR-OCT, it is important to compensate for such terms. Typical UHR-OCT reports consider dispersion compensation up to the $6-7^{th}$ orders.

Over the years, numerous methods have been proposed to compensate or cancel dispersion in OCT systems. A first consideration is to analyse the factors responsible for dispersion effects, originating from the system itself or from the sample investigated or from both.

When dispersive effects are only due to mismatch of material in the interferometer itself (propagation through glass such as lenses or fibre of the OCT system), several methods can be used for dispersion compensation. The easiest one is certainly the duplication of elements on each path of the interferometer. Doing so, dispersive effects become negligible, but such solution can be expensive. An alternative to this initial solution is to measure the material mismatch between the sample and reference paths

and to insert a block of glass corresponding to the same mismatch. However, even though hardware dispersion compensation solutions are available, they have been overtaken regarding efficiency by software-based solutions. Indeed, dispersion effects act as a non-linear term within the phase of the interference signal. Then, a proper corrective term can be added to the phase of the CS in order to cancel non-linearity due to dispersion. This principle is shown on section 4.5.4. Such methods are now popular and have shown that transform limited PSF can be obtained [23, 31].

In the case of dispersion arising from both the sample and the interferometer, it is complicated to obtain an accurate compensation. In that case, most of the time, the compensation consists in a correction of an average of the dispersion by optimizing a metric function [23]. Recently a report proposed to assume a linear evolution of the dispersion within layered structured such as skin and obtained satisfactory correction [32].

Finally, a different method is that where the dispersion is not compensated but simply cancelled. This is achieved for system dispersion by using Master-Slave Interferometry (MSI) [33] (see Chapter 4). Also, quantum-optical coherence tomography [34] and intensity correlation optical coherence tomography [35] have been proposed for complete cancellation of dispersion from both the sample and the system.

2.7.2 Mirror terms issue

Earlier in this chapter, Equation 2.13 has been used to describe the signal at the output of a low coherence interferometry system. In that case, a sample consisting of N reflective centres at axial positions δ_n were considered. Let's assume now that the sample consists of only two reflective centres at axial positions $\pm\delta$ and with a power reflectivity R_{S1} and R_{S2}. Also, it is considered here only the interference term so no DC term neither autocorrelation term. Then,

$$I_{Detector} \propto S(\omega)\times\sqrt{R_r R_{S1}}\times\cos\left(2\beta\delta l\right)+S(\omega)\times\sqrt{R_r R_{S2}}\times\cos\left(-2\beta\delta l\right). \quad (2.35)$$

After dedicated signal processing described in Chapter 4, the depth reflectivity profile is obtained by iFFT of the interference signal. It is important

to notice here the even nature of the cosine function. The Fourier Transform (FT) of a cosine function is

$$\frac{1}{2}\left(\delta(z+\delta l)+\delta(z-\delta l)\right) \Leftrightarrow cos(k\delta l). \tag{2.36}$$

After iFFT operation of Equation 2.35:

$$I_{Detector} \propto \frac{1}{2}\left(\sqrt{R_R R_{S1}}+\sqrt{R_R R_{S2}}\right)\times\delta(z+\delta l)+\frac{1}{2}\left(\sqrt{R_R R_{S1}}+\sqrt{R_R R_{S2}}\right)\times\delta(z-\delta l). \tag{2.37}$$

Due to the parity of the cosine function, it is not possible to differentiate, within the depth reflectivity profile, between signal arising from negative or positive path difference. From Equation 2.37, the signal from each reflector contributes to the positive and negative delta functions. This effect results in operating the SD-OCT signal using only half of the imaging range available (either the positive side or the negative side). This results in the situation described by Figure 2.7, where the zero-axial position has to be placed outside the sample of investigation. If not, overlaps between positive and negative axial positions create of false representation of the sample.

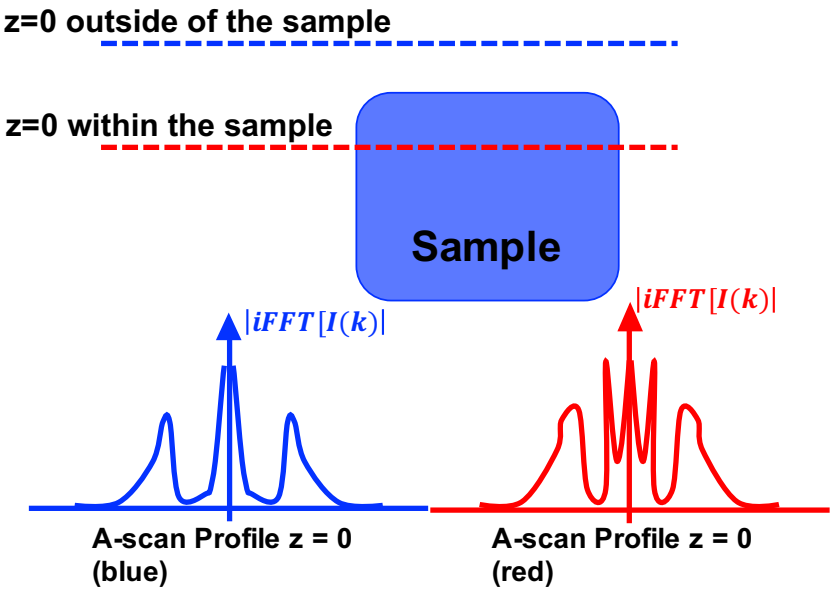

FIGURE 2.7: Illustration of the mirror term effect and the requirement for the positioning of the zero-axial position outside of the sample.

2.8 Light sources for SD-OCT

2.8.1 Super-Luminescent Diodes

SLDs are one for the simplest source for OCT. An super-luminescent diode is basically a laser diode without a lasing cavity. Then, the stimulated emission regime is never reached and the light emitted is only based on Amplified Spontaneous Emission (ASE) [36]. SLDs are available for the three main wavelength ranges for SD-OCT applications (800 nm, 1050 nm and 1300 nm). Semiconductor alloys such as Indium-Phosphide (InP), Gallium-Arsenide (GaAs) or Gallium-Nitride (GaN) are commonly used. Typically, super-luminescent diode bandwidth are limited by the gain of the material [36], leading to maximal bandwidth around 100-120 nm. The total output power can be from few mWs to several hundreds of mWs. In order to overcome the bandwidth limitation of super-luminescent diode, it has been shown that stitching 3 to 4 spectra from different SLDs can be used as an ultra-broad source for UHR-OCT [37].

2.8.2 Solid State Lasers

Solid state laser is a denomination for a type of laser which relies on pumping a bulk crystal (doped or not) using a high-power laser [38]. This category, when considering application to OCT, comprises laser such as Titanium Sapphire source and Chromium based source. Solid state lasers for OCT are available in the 800 nm and 1300 nm wavelength range. In the 800-nm region, Titanium sapphire laser is certainly the best option. Titanium sapphire lasers are centered around 800 nm with bandwidth as large as 300 nm together with high power (>100s mW), very high spatial coherence and low intensity noise. Alternative sources exist for this wavelength region which are based on chromium crystal but proposed less interesting parameters. The first UHR-OCT proposed by [19] used a Titanium sapphire laser. In the 1300 nm region, many options based on pumping a Chromium type crystal exist. The broadest solid state laser for OCT in the 1300 nm range is a chromium based source called Cr4+: Forsterite [38] which covers several hundreds of nm around 1280 nm. The total output power is larger than 100

mW. All solid state lasers offer very interesting properties for OCT and have attracted interest due to the need of large optical bandwidth. However, solid state lasers are bulk, complex and very expensive laboratory equipment. A few of those mentioned here have been proposed as a reliable commercial product. Even more, none have been implemented into commercial OCT system.

2.8.3 Fibre-based source

Broad light source can be obtained by pumping optical fibre with intense short pulse. Such source is often called Supercontinuum (SC) light source, though it is an inaccurate denomination. Supercontinuum is a general description for any spectral broadening occurring due to non-linear effects in material including bulk material, optical fibres, liquid and gases [39]. A more accurate denomination would be fibre-based SC. Most of the time, fibre-based SC relies on pumping a Highly Non-Linear Fibre (HNLF) using a short optical pulse with pulse length in the ps or ns regime [40]. Typically, in the practice of OCT, the HNLF is a Photonic Crystal Fibre (PCF) made of silica. Fibre-based SC sources have been used in the early stage of SD-OCT. However, their pulse to pulse fluctuations have significantly limited their usefulness [41]. Since these first attempts, important progresses have been made in understanding the mechanism of SC generation in fibre and several low noise SC sources have been proposed. Concepts such as tapering the optical fibre or increasing the pulse repetition rate have been investigated. Since then, SC source have been used successfully in numerous OCT applications [17, 18]. Supercontinuum light sources exist as commercial turn key product with repeatable and robust design [42, 43].

2.9 Conclusion

This chapter aims was to introduce a number of concepts and parameters of importance when discussing OCT technology. Most of them are used along the thesis without new definition. However, a short summary

is sometime proposed, at the beginning of a chapter, regarding a particular topic to help the reader.

References

[1] E. Hecht. Brief history. In *Optics - Fourth Edition*, chapter 1. International Edition, San Francisco, 2002.

[2] D. Huang, E. A. Swanson, C. P. Lin, J. S. Schuman, W. G. Stinson, W. Chang, M. R. Hee, T. Flotte, C. A. Gregory, K.and Puliafito, and J. G. Fujimoto. Optical coherence tomography. *Science (New York, N.Y.)*, 254 (5035):1178–1181, 11 1991. URL http://www.ncbi.nlm.nih.gov/pmc/articles/PMC4638169/.

[3] E. A. Swanson and J. G. Fujimoto. The ecosystem that powered the translation of oct from fundamental research to clinical and commercial impact. *Biomed. Opt. Express*, 8(3):1638–1664, Mar 2017. doi: 10.1364/BOE.8.001638. URL http://www.osapublishing.org/boe/abstract.cfm?URI=boe-8-3-1638.

[4] B. E. A. Saleh and M. C. Teich. In *Fundamentals of Photonics - Second Edition*, chapter 11. Wiley, New York, NY, 2007.

[5] W. Drexler and J. G. Fujimoto. Theory of optical coherence tomography. In *Optical Coherence Tomography - Technology and Applications*, chapter 2. Springer, Basel, 2015.

[6] E. Hecht. Wave motion. In *Optics - Fourth Edition*, chapter 11. International Edition, San Francisco, 2002.

[7] A. Podoleanu. Optical coherence tomography. *Journal of Microscopy*, 247(3):209–219, 2012. ISSN 1365-2818. doi: 10.1111/j.1365-2818.2012.03619.x. URL http://dx.doi.org/10.1111/j.1365-2818.2012.03619.x.

[8] R. Leitgeb, C. K. Hitzenberger, and A. F. Fercher. Performance of fourier domain vs. time domain optical coherence tomography. *Opt. Express*, 11(8):889–894, Apr 2003. doi: 10.1364/OE.11.

000889. URL http://www.opticsexpress.org/abstract.cfm?URI=oe-11-8-889.

[9] J. F. de Boer, B. Cense, B. H. Park, M. C. Pierce, G. J. Tearney, and B. E. Bouma. Improved signal-to-noise ratio in spectral-domain compared with time-domain optical coherence tomography. *Opt. Lett.*, 28 (21):2067–2069, Nov 2003. doi: 10.1364/OL.28.002067. URL http://ol.osa.org/abstract.cfm?URI=ol-28-21-2067.

[10] M. A. Choma, M. V. Sarunic, C. Yang, and J. A. Izatt. Sensitivity advantage of swept source and fourier domain optical coherence tomography. *Opt. Express*, 11(18):2183–2189, Sep 2003. doi: 10.1364/OE.11.002183. URL http://www.opticsexpress.org/abstract.cfm?URI=oe-11-18-2183.

[11] M. R. N. Avanaki and A. Podoleanu. En-face time-domain optical coherence tomography with dynamic focus for high-resolution imaging. *Journal of Biomedical Optics*, 22:22 – 22 – 10, 2017. doi: 10.1117/1.JBO.22.5.056009. URL http://dx.doi.org/10.1117/1.JBO.22.5.056009.

[12] V. J. Srinivasan, D. C. Adler, Y. Chen, I. Gorczynska, R. Huber, J. S. Duker, J. S. Schuman, and J. G. Fujimoto. Ultrahigh-speed optical coherence tomography for three-dimensional and en face imaging of the retina and optic nerve head. *Investigative Ophthalmology & Visual Science*, 49(11):5103–5110, 11 2008. URL http://dx.doi.org/10.1167/iovs.08-2127.

[13] D. Ferrara, K. J. Mohler, N. Waheed, M. Adhi, J. J. Liu, I. Grulkowski, M. F. Kraus, C. Baumal, J. Hornegger, J. G. Fujimoto, and J. S. Duker. En face enhanced-depth swept-source optical coherence tomography features of chronic central serous chorioretinopathy. *Ophthalmology*, 121(3):719–726, 2014. doi: https://doi.org/10.1016/j.ophtha.2013.10.014. URL http://www.sciencedirect.com/science/article/pii/S0161642013009147.

[14] J. G. Fujimoto and W. Drexler. In *Optical Coherence Tomography Technology and Applications*, chapter 4. Springer, 2008.

[15] Camera teledyne. https://www.e2v.com/markets/medical-science/opthalmology-imaging/, . Accessed: 2017-10-23.

[16] Camera sensor unlimited. http://www.sensorsinc.com/products/linescan-cameras/,. Accessed: 2017-10-23.

[17] X. Yao, Y. Gan, C. C. Marboe, and C. P. Hendon. Myocardial imaging using ultrahigh-resolution spectral domain optical coherence tomography. *Journal of Biomedical Optics*, 21(6):061006, 06 2016. doi: 10.1117/1.JBO.21.6.061006. URL http://www.ncbi.nlm.nih.gov/pmc/articles/PMC4814547/.

[18] W. Yuan, J. Mavadia-Shukla, J. Xi, W. Liang, X. Yu, S. Yu, and X. Li. Optimal operational conditions for supercontinuum-based ultrahigh-resolution endoscopic oct imaging. *Opt. Lett.*, 41(2):250–253, Jan 2016. doi: 10.1364/OL.41.000250. URL http://ol.osa.org/abstract.cfm?URI=ol-41-2-250.

[19] W. Drexler, U. Morgner, R. K Ghanta, F. X. Kärtner, J. S. Schuman, and J. G. Fujimoto. Ultrahigh-resolution ophthalmic optical coherence tomography. *Nature medicine*, 7(4):502–507, 04 2001. doi: 10.1038/86589. URL http://www.ncbi.nlm.nih.gov/pmc/articles/PMC1950821/.

[20] J. G. Fujimoto and W. Drexler. In *Optical Coherence Tomography - Technology and Applications*, chapter 9. Springer, 2015.

[21] A. Bradu and A. Podoleanu. Attenuation of mirror image and enhancement of the signal-to-noise ratio in a talbot bands optical coherence tomography system. *Journal of Biomedical Optics*, 16:16 – 16 – 11, 2011. doi: 10.1117/1.3598446. URL http://dx.doi.org/10.1117/1.3598446.

[22] B. H. Park, M. C. Pierce, B. Cense, S. H. Yun, M. Mujat, G. J. Tearney, B. E. Bouma, and J. F. de Boer. Real-time fiber-based multi-functional spectral-domain optical coherence tomography at 1.3 µm. *Opt. Express*, 13(11):3931–3944, May 2005. doi: 10.1364/OPEX.13.

003931. URL http://www.opticsexpress.org/abstract.cfm?URI=oe-13-11-3931.

[23] M. Wojtkowski, V. J. Srinivasan, T. H. Ko, J. G. Fujimoto, A. Kowalczyk, and J. S. Duker. Ultrahigh-resolution, high-speed, fourier domain optical coherence tomography and methods for dispersion compensation. *Opt. Express*, 12(11):2404–2422, May 2004. doi: 10.1364/OPEX.12.002404. URL http://www.opticsexpress.org/abstract.cfm?URI=oe-12-11-2404.

[24] Z. Hu and A. M. Rollins. Fourier domain optical coherence tomography with a linear-in-wavenumber spectrometer. *Opt. Lett.*, 32(24):3525–3527, Dec 2007. doi: 10.1364/OL.32.003525. URL http://ol.osa.org/abstract.cfm?URI=ol-32-24-3525.

[25] G. Lan, G.and Li. Design of a k-space spectrometer for ultra-broad waveband spectral domain optical coherence tomography. 7:42353 EP –, 03 2017. URL http://dx.doi.org/10.1038/srep42353.

[26] J. G. Fujimoto and W. Drexler. In *Optical Coherence Tomography - Technology and Applications*, chapter 5. Springer, 2015.

[27] M. W. Maciejewski, H. Z. Qui, I. Rujan, M. Mobli, and J. C. Hoch. Nonuniform sampling and spectral aliasing. *Journal of Magnetic Resonance*, 199(1):88–93, 2009. doi: https://doi.org/10.1016/j.jmr.2009.04.006. URL http://www.sciencedirect.com/science/article/pii/S1090780709001037.

[28] F. B. Lazarow, G. S. Ahuja, A. Chin Loy, E. Su, T. D. Nguyen, G. K. Sharma, A. Wang, J. Jing, Z. Chen, and B. J. F. Wong. Intraoperative long range optical coherence tomography as a novel method of imaging the pediatric upper airway before and after adenotonsillectomy. *International Journal of Pediatric Otorhinolaryngology*, 79(1):63–70, 2015. doi: https://doi.org/10.1016/j.ijporl.2014.11.009. URL http://www.sciencedirect.com/science/article/pii/S0165587614006077.

[29] S. Song, J. Xu, and R. K. Wang. Long-range and wide field of view optical coherence tomography for in vivo 3d imaging of large volume object based on akinetic programmable swept source. *Biomed. Opt. Express*, 7(11):4734–4748, Nov 2016. doi: 10.1364/BOE.7.004734. URL http://www.osapublishing.org/boe/abstract.cfm?URI=boe-7-11-4734.

[30] B. E. A. Saleh and M. C. Teich. In *Fundamentals of Photonics - Second Edition*, chapter 5. Wiley, 2007.

[31] X. Wu and W. Gao. Dispersion analysis in micron resolution spectral domain optical coherence tomography. *J. Opt. Soc. Am. B*, 34(1):169–177, Jan 2017. doi: 10.1364/JOSAB.34.000169. URL http://josab.osa.org/abstract.cfm?URI=josab-34-1-169.

[32] L. Pan, X. Wang, Z. Li, X. Zhang, Y. Bu, N. Nan, Y.Chen, X. Wang, and F. Dai. Depth-dependent dispersion compensation for full-depth oct image. *Opt. Express*, 25(9):10345–10354, May 2017. doi: 10.1364/OE.25.010345. URL http://www.opticsexpress.org/abstract.cfm?URI=oe-25-9-10345.

[33] A. Bradu, M. Maria, and A. Podoleanu. Demonstration of tolerance to dispersion of master/slave interferometry. *Opt. Express*, 23(11):14148–14161, Jun 2015. doi: 10.1364/OE.23.014148. URL http://www.opticsexpress.org/abstract.cfm?URI=oe-23-11-14148.

[34] M. B. Nasr, B. E. A. Saleh, A. V. Sergienko, and M. C. Teich. Demonstration of dispersion-canceled quantum-optical coherence tomography. *Phys. Rev. Lett.*, 91:083601, Aug 2003. doi: 10.1103/PhysRevLett.91.083601. URL https://link.aps.org/doi/10.1103/PhysRevLett.91.083601.

[35] T. Shirai and A. T. Friberg. Intensity-interferometric spectral-domain optical coherence tomography with dispersion cancellation. *J. Opt. Soc. Am. A*, 31(2):258–263, Feb 2014. doi: 10.1364/JOSAA.31.000258. URL http://josaa.osa.org/abstract.cfm?URI=josaa-31-2-258.

[36] V. R. Shidlovski and J. Wei. Superluminescent diodes for optical coherence tomography. volume 4648, pages 4648 – 4648 – 9, 2002. doi: 10.1117/12.462650. URL http://dx.doi.org/10.1117/12.462650.

[37] M. A. Shousha, V. L. Perez, J. Wang, T. Ide, S. Jiao, Q. Chen, V. Chang, N. Buchser, S. R. Dubovy, W. Feuer, and S. H. Yoo. Use of ultra-high-resolution optical coherence tomography to detect in vivo characteristics of descemet's membrane in fuchs' dystrophy. *Ophthalmology*, 117(6):1220–1227, 2010. doi: https://doi.org/10.1016/j.ophtha.2009.10.027. URL http://www.sciencedirect.com/science/article/pii/S0161642009012226.

[38] J. G. Fujimoto and W. Drexler. In *Optical Coherence Tomography - Technology and Applications*, chapter 19. Springer, 2015.

[39] R. Alfano. In *The Supercontinuum Laser Source, Fundamentals with updated references - Second editions*, chapter 12. Springer, 2006.

[40] J. M. Dudley, G. Genty, and S. Coen. Supercontinuum generation in photonic crystal fiber. *Rev. Mod. Phys.*, 78:1135–1184, Oct 2006. doi: 10.1103/RevModPhys.78.1135. URL https://link.aps.org/doi/10.1103/RevModPhys.78.1135.

[41] W. J. Brown, S. Kim, and A. Wax. Noise characterization of supercontinuum sources for low-coherence interferometry applications. *J. Opt. Soc. Am. A*, 31(12):2703–2710, Dec 2014. doi: 10.1364/JOSAA.31.002703. URL http://josaa.osa.org/abstract.cfm?URI=josaa-31-12-2703.

[42] NKT Photonics A/S. http://www.nktphotonics.com/. Accessed: 2017-10-23.

[43] Leukos. http://www.leukos-systems.com/spip.php?rubrique23. Accessed: 2017-10-23.

Chapter 3

Fibre-based Supercontinuum - Introduction

3.1 Introduction

A Supercontinuum (SC) light source is a broad optical source based on non-linear frequency broadening caused by an intense wave propagating into a non-linear medium. The first demonstration of a SC light source was reported on 1970 [1] where a ps pulse broadened over the entire visible range into a borosilicate glass. This first demonstration was based a bulk glass as the non-linear medium, however nowadays SC can be generated in many different ways by pumping gases, liquids or glass. The limitation regarding the medium used is that material with low non-linearities will require pumping at much higher peak power.

A major revolution in SC generation was to use optical fibre as the non-linear medium. Due to the confinement of light within the small fibre core, long length of interaction is achieved. Even more, the use of Photonic Crystal Fibre (PCF) for SC generation was a game changing [2] because of the dispersion engineering. Nowadays, PCF-based SC sources are available as robust and reliable commercial products which are use in many different applications such as material processing [3, 4] or medical imaging [5, 6].

This Chapter 3 aims to provide a short introduction to the concepts of PCF, SC generation mechanisms and optical non-linear effects in fibre. This Chapter 3 remains relatively simple as it is just introducing the concepts used in other Chapter of the thesis which are discussing how SC sources are used into OCT systems.

3.2 Optical fibre - Definition

An optical fibre is a dielectric waveguide which presents a circular symmetry. In a first approximation, the physical principle behind an optical fibre can be seen using a geometrical description. Figure 3.1 is a simplified representation of the optical fibre concept. A material of refractive index n_1 (red) is surrounded by a second material of index of refraction n_2 (grey). The material with refractive index n_1 is called the fibre core and the material with refractive index n_2 is called the fibre cladding. Usually, the two materials of the fibre core and the cladding are similar and the refractive index difference is obtained by doping the material of the fibre core in order to increase its refractive index. The refractive index difference is measured using the refractive index change as $\Delta \approx (n_1 - n_2)/n_1 \ll 1$. As an example, for silica based fibre Δ is typically within 0.001 to 0.02. The light guidance occurs through total internal reflection inside the fibre core only if $n_1 > n_2$. Also, a condition exists regarding the maximum input angle at the fibre facet. If assuming an external medium with unity refractive index (n_{ext}=1).The maximum angle θ_i for total internal reflection is defined as

$$\sin(\theta_i) = \frac{\sqrt{n_1^2 - n_2^2}}{n_{ext}} = \sqrt{n_1^2 - n_2^2}. \tag{3.1}$$

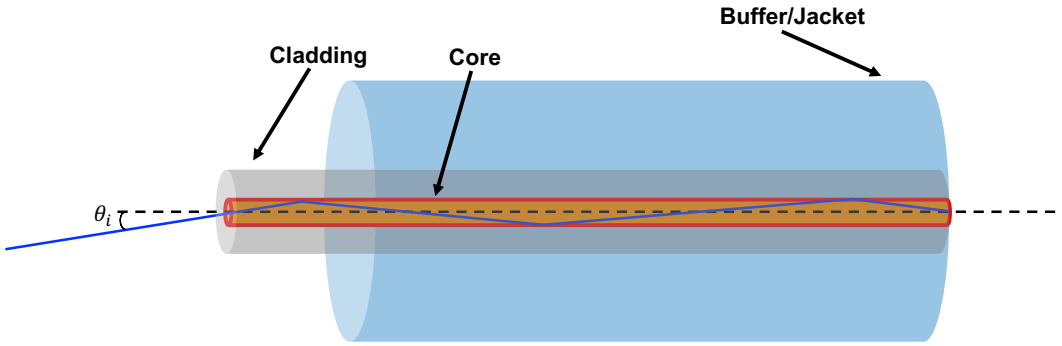

FIGURE 3.1: Geometrical description of light propagation into an optical fibre based on trapping the light within the fibre core using slightly larger index of refraction for the core material.

The simple geometrical model proposed above is enough to introduce the basic concept of an optical fibre. For a more complete description, one would prefer to use the electromagnetic wave guided model. This model uses Maxwell's equations to determine the electric and magnetic field expressions within the fibre. Then, the light propagation is described using a modal formalism. In that case by solving the Helmholtz equation [7], each solution of the equation is called an optical mode. A mode can be described as an electric field distribution which intensity profile does not varies while propagating into the fibre. The number of modes N allowed to propagate in the core of the fibre (considering a step index fibre) is :

$$N \approx \frac{V^2}{2} \quad \text{with} \quad V \approx \frac{1}{2} \times \frac{2\pi}{\lambda} a \sqrt{n_1^2 - n_2^2}, \tag{3.2}$$

with V is the normalized frequency characterising the fibre, λ is the light wavelength and a the fibre core radius. For $V \leq 2.405$, an optical fibre an optical fibre can supports one mode per polarization.

Operating with single mode behavior ($N = 2$, one mode per polarization) in fibre used in imaging is often important to avoid important losses of power but also exploiting the spatial coherence properties of light.

3.3 Photonic crystal fibre

Supercontinuum generation requires a balance between dispersion and strong non-linear effects [8]. As mentioned above, optical fibres are ideal for SC generation due to the long interaction length inside the small fibre core. In addition, PCF fibres are well suited because of the dispersion tailoring described below. All the SC sources used during this thesis are fibre-based and rely on pumping a Highly Non-Linear Fibre (HNLF), commonly a Photonic Crystal Fibre (PCF), with an intense relatively short optical pulse.

In the case of a PCF, the confinement and guidance of light within the core of the fibre can be obtained by two mechanisms. The first one is the photonic band gap effect [9]. In that situation, the guidance of light is ensured by forbidding the light to propagate through the fibre cladding. The

photonic band gap effect is used in hollow core fibres where the light is confined within an air hole based core [10]. The second effect used for light guidance in PCF is the effective index mechanism [11]. This effect relies on creating a total internal reflection, similar to the one used in conventional step index fibres but using a pure glass. This is obtained by creating a refractive index difference between the solid core of a PCF and the air holes structure of the cladding. If the diameter d of the air holes is much smaller than the wavelength of the light, the effective index of refraction is only the average of the material and the air structure. However, if the holes diameter is within the dimension of the wavelength of the light then the effective refractive index is equal to the average refractive index between air and silica. During the research described in the thesis, the SC sources used are based on solid core PCF which uses the effective index guidance mechanism where the holes diameter is in the same range as the wavelength of light ($d \approx \lambda$).

Figure 3.2 is a representation of a fibre facet appearance of a solid core PCF (b) in comparison with a step index fibre (a). The solid core PCF is based on a hexagonal air-hole structure characterised by the holes diameter d and the pitch Λ (distance between the centre of two holes). One hole is missing at the centre of the structure in order to create a high index of refraction position which is then acting as the core of the fibre.

Both fibre concepts rely on the refractive index difference between core and cladding in order to guide the light. Then, the light is well guided only if the core has a higher refractive index compared to the cladding. An illustration of the index of refraction profile of a solid core PCF together with a step index fibre is presented in Figure 3.3. In the case of the PCF, the air-holes structure creates a effective index of refraction lower compared to the central point of the fibre (missing hole position).

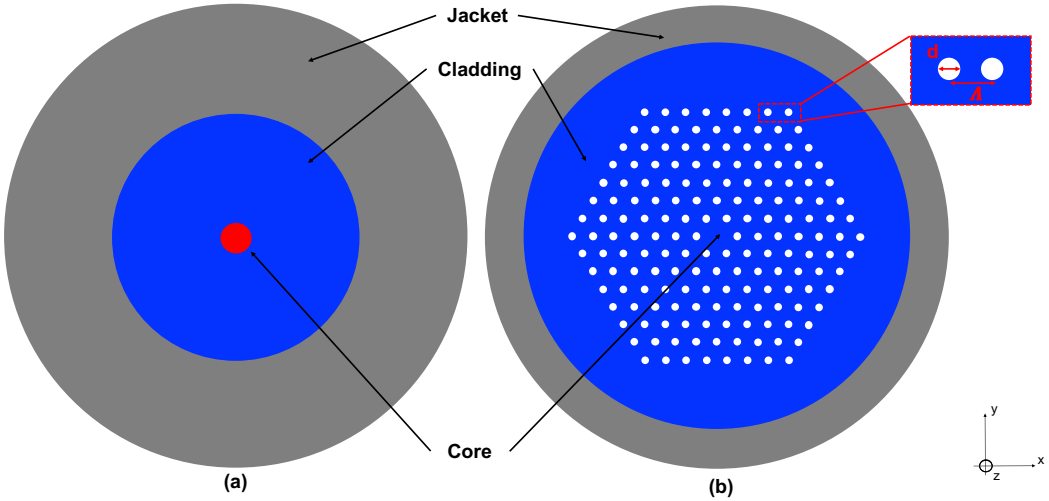

FIGURE 3.2: Sketch of a fibre facets for a conventional step index fibre with (n_{core}>$n_{cladding}$) (a) and a solid core PCF with ($n_{core} = n_{silica}$>$n_{cladding} = n_{effective}$) (b).

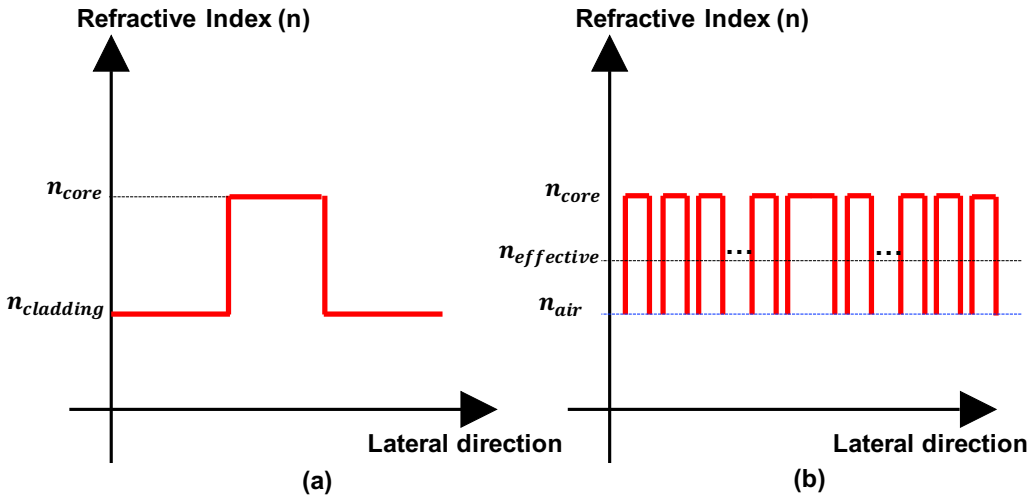

FIGURE 3.3: Refractive index profile for a step index fibre (a) and a solid core PCF (b).

3.4 Optical effects (Linear and non-linear)

3.4.1 Dispersion

Dispersion is a linear effect occurring in any material and is related to the variation of the index of refraction which is frequency dependent [12]. It is common to describe the propagation constant $\beta(\omega)$ as a Taylor series as:

$$\beta(\omega) = \beta(\omega_0) + \left.\frac{\partial\beta}{\partial\omega}\right|_{\omega_0}(\omega-\omega_0) + \left.\frac{1}{2}\frac{\partial^2\beta}{\partial\omega^2}\right|_{\omega_0}(\omega-\omega_0)^2 + ... + \left.\frac{1}{n!}\frac{\partial^n\beta}{\partial\omega^n}\right|_{\omega_0}(\omega-\omega_0)^n . \tag{3.3}$$

Within Equation 3.4 several terms can be extracted and identified as $\beta_1 = \left.\frac{\partial\beta}{\partial\omega}\right|_{\omega_0} = \frac{n_g}{c} = v_g^{-1}$ is the inverse group velocity and $\beta_2 = \left.\frac{1}{2}\frac{\partial^2\beta}{\partial\omega^2}\right|_{\omega_0} = \frac{\partial v_g^{-1}}{\partial\omega}$ is the Group Velocity Dispersion (GVD).

The measured of dispersion within an optical system is generally done through the GVD which is denoted with two parameters, D (with unit is ps.nm^{-1}.km^{-1}) and β_2 (with units s^2.m^{-1}), where both parameter are linked as:

$$D(\lambda) = -\frac{2\pi c}{\lambda^2} \times \beta_2(\lambda) \tag{3.4}$$

with c the speed of light, λ the wavelength of light.

Dispersion in a single mode optical fibre can be divided into two contributions, the material dispersion and the waveguide dispersion. The material dispersion is defined by the material used for the fibre (Silica, chalcogenide glass, ...). The waveguide dispersion is linked to the geometry of the fibre. Step index fibre, graded index fibre or PCF do not show the same waveguide dispersion [11]. Depending on the value of D two regimes exist, the normal and anomalous regime. The normal regime corresponds to $D < 0$ and the anomalous regime corresponds to $D > 0$.

An interesting property of a PCF is that the dispersion profile can be engineered. As stated above, in the case of a holes diameter similar to the wavelength of the light, the effective index is dependent on the optical field distribution. Short wavelengths are more confined than longer wavelengths which lead to a smaller index of refraction difference between cladding and core for short wavelengths (the effective index of the cladding is decreasing with wavelengths). Then, the diameter of the core can be tuned to control

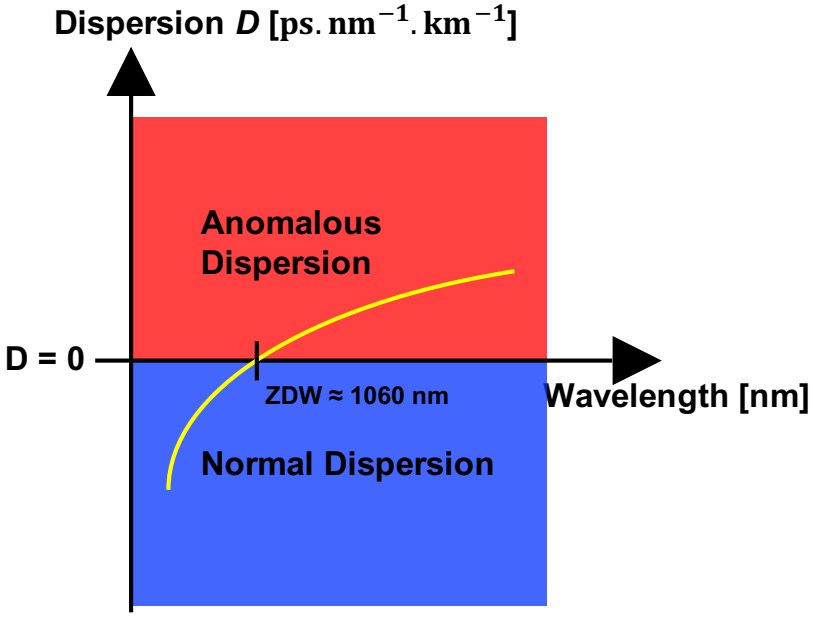

FIGURE 3.4: Dispersion regime definition versus wavelength with a sketch of dispersion curve of a PCF used for SC generation around 1060 nm.

the dispersion profile of the fibre. Doing so, the Zero Dispersion Wavelength (ZDW) can be shift to different wavelength (from 1300 nm up to 780 nm). The key advantage of shifting the ZDW is the availability of high peak power lasers at wavelength around 1060 nm or 1550 nm which is important for efficient non-linearities within the fibre. Supercontinuum generation is possible if a good balance exists between non-linear effects and dispersion within the HNLF. High dispersion leads to fast broadening of the optical pulse and then weak non-linear interactions. So, close to zero dispersion is necessary around the wavelength of the pump laser of the SC source.

3.4.2 Losses

Losses in optical fibre can be categorized into three contributions, the scattering losses, the absorption losses and the confinement losses [13]. Then, the power at the fibre output which is a function of the fibre length L can be calculated as:

$$P_{output}(L) = P_{input} \times exp\left[-\left(\alpha_{scattering} + \alpha_{absorption} + \alpha_{confinement}\right) L\right] \quad (3.5)$$

The first type of losses, the scattering losses, are to be attributed to the interaction of light with particle within the fibre. First, the Rayleigh scattering is a linear optical phenomenon which happens due to interaction of the light with particles which are much smaller than the wavelength of light. Rayleigh scattering losses vary with $\frac{1}{\lambda^4}$. A second type of scattering in fibre is the Mie scattering which is caused by imperfections within the fibre with size similar or larger compared to the wavelength. Confinement losses are the losses caused by leaking of the optical mode into the cladding of the fibre.

3.4.3 Self Phase Modulation / Cross-Phase Modulation

While propagating into a medium, for example silica glass in the case of the optical fibres considered in the thesis, an intense optical pulse locally modifies the index of refraction. If considering the effect of a strong optical radiation, the index of refraction can be re-written as:

$$n\left(\omega, I(\omega)\right) = n_{linear}(\omega) + n_{non-linear} I(\omega) \tag{3.6}$$

where $n\left(\omega, I(\omega)\right)$ is the index of refraction considering its linear and non-linear term and $I(\omega) \propto |E(\omega)|^2$ is the pulse intensity at a given frequency. The additional contribution to the index of refraction leads to a local modification of the phase of the pulse. Such an effect is called Self Phase Modulation (SPM) [13, 14, 15]. Under normal dispersion regime, SPM is responsible for a symmetric spectral broadening of the optical field around its central frequency. This broadening has the advantage to be highly coherent (low noise). In the case of anomalous dispersion, SPM participates to the creation of Solitons.

So far, only a monochromatic radiation of frequency ω has been considered. In reality, the lasers used for SC generation are spectrally broad (few nm to few tens of nm). In that case, it is possible that the light at a frequency ω_1 influences the light at a frequency ω_2 through a non-linear effect called Cross-Phase Modulation (XPM). In that case, the phase modification of the light at ω_2 is caused by the light at ω_1 and vice-versa.

3.4.4 Modulation Instability

Modulation Instability (MI) is a non-linear effect which consist in a break-up of a continuous or quasi continuous optical radiation into a train of ultra-short pulses [13, 16] . It arises in optical fibre due to the inherent noise present into any light source. Such noise leads to local variation of the pulse spectral shape which can trigger local SPM effect and spectral broadening. Under normal dispersion regime such local maxima are not of an issue as they are rapidly broadened leading to a smoother spectral shape. However, under anomalous dispersion condition those local maxima are compressed and hence create some SPM effect. This leads to a break-up of the initial radiation into a train of ultra-short pulses with duration in the tens of femtosecond. This train of ultra-short pulse is responsible for a spectral broadening of the initial radiation. Modulation instability is naturally considered as a noisy effect due to its origin (amplification from quantum noise).

3.4.5 Optical Wave Breaking

Optical Wave Breaking (OWB) is a non-linear effect occurring under normal dispersion regime. It is due to the superposition in time of different frequency components of the pump pulse [17, 18]. It is cause by the chirp induced by SPM while an intense pulse propagate through the PCF. Optical Wave Breaking contributes to the spectral broadening of a SC generated using coherent effect as described by section 3.5.2. Similarly to SPM, OWB is a coherent process which can be used for low noise SC generation.

3.4.6 Raman Scattering

Raman Scattering is an inelastic optical effect which can be simply described as an energy transfer from a light beam to the material by the creation of an optical phonon (vibration of the crystal lattice) in which the light is propagating [19]. This energy transfer is due to the scattering of the light by the material inhomogeneity. This energy transfer leads to a wavelength

shift of the light towards longer wavelength (lower energy). Raman scattering is responsible for the spectral shift of solitons so it plays an important role in SC generation.

3.4.7 Solitons

A soliton is a type of wave which is created through the balance of anomalous dispersion and SPM [20]. While anomalous dispersion tends to shift the long wavelength towards the rear of the impulse and the short wavelength to the front, SPM is doing the exact opposite. Then, the two effects are balanced into a stable or periodically stable solution (along the propagation) called solitons. Solitons correspond to analytic solutions of the propagation equation of a pulse into the fibre (Non-Linear Schrödinger Equation). Solitons have the particularity to propagate inside the fibre core with either no temporal broadening or with periodical broadening and compression pattern depending on the solitons number. The solitons number N_s can be calculated as:

$$N_s^2 = \frac{\gamma P_0 T_0^2}{|\beta_2|} \tag{3.7}$$

with γ is the non-linearity parameter of the fibre, P_0 is the optical peak power, T_0 is the input pulse length (FWHM) assuming a Gaussian shape and β_2 is the second order term of the dispersion Taylor expansion. A fundamental soliton, which can propagate infinitely with no spectral or temporal change (if neglecting other effects such as losses and Raman scattering), has a soliton number $N = 1$. If N is larger than one, this corresponds to higher order soliton which have periodical pattern of compression/broadening during their propagation into the fibre.

Solitons are responsible for the broadening of the SC towards infra-red wavelengths. The short pulse length (< 100 fs), large spectral bandwidth and high peak power of solitons permit some energy exchanges between wavelength of the soliton itself through Raman Scattering effect. Basically, this can be understand as a shift of the solitons short wavelengths energy towards the longer wavelengths. In addition, it is noticeable that solitons behave chaotically so that they collide, interact and exchange energy which then all together also contribute to the energy exchange within the soliton

wavelengths energy transfers. This tends to contribute to the high pulse to pulse fluctuations of SC source based on solitons [8, 21]. Also, this creates higher noise at the red-edge of the generated supercontinuum which can be problematic if used in a system such as OCT.

3.4.8 Dispersive Waves

A dispersive wave is a generated when the spectral extension of a soliton (generally close to the ZDW of the fibre) reaches the normal dispersion regime and if a phase matching relation exists between the solitons wavelength and shorter wavelength located within the normal dispersion regime. Under this condition an overlap exists between the solitons wavelength and the shorter wavelength which leads to energy transfer from the soliton to the shorter wavelength wave as they are group velocity matched [13]. Dispersive waves generation efficiency is influenced by the same parameters that influence the soliton creation. So, it is influenced by several parameters such as the peak power of the solitons, the pulse length of the solitons and the central wavelength of the soliton. In parallel to the Solitons red-shift effect through Raman Scattering, dispersive waves are blue-shifted [13]. Dispersive waves are important in SC generation as they are responsible for the blue extension of the SC. This portion of the SC source is the one used when considering OCT at 800 nm or in the visible range.

3.5 Fibre-based SC generation mechanism

When considering fibre-based SC generation, two important parameters are to be considered, the optical fibre and the pump laser. The optical fibre is modifying the SC generation mechanism and SC output through its dispersion profile. The dispersion profile can be either normal, anomalous or both depending on the wavelength considered and the optical bandwidth of the pump laser. The pump laser is also influencing the SC generation mechanism and SC output through the achievable peak power and the pump wavelength. For example, a SC can be generated by pumping an optical fibre nearby its Zero Dispersion Wavelength (ZDW) if the fibre

possesses one. In that case, the pump wavelength can be either within the normal or anomalous regime. Also, the driving mechanisms will be different depending on the pump pulse duration (fs, ps, ns or even continuous wave pumping). If a fibre with an all-normal dispersion profile is used, a SC can be generated and its noise properties will be affected by the pump pulse duration. Low noise operation is obtained only if short pulse are used, in the case of long pulse Raman scattering might raised the noise level [22].

In the course of this thesis two types of SC source have been used. The first one is a SC source where the pump is a 1064 nm mode-locked laser with a pulse duration in the range of 10 ps. In that case, the fibre used is a PCF with a ZDW located around 1040 nm. Below the ZDW the fibre shows a normal dispersion and above the ZDW an anomalous dispersion. The second SC source used during the course of the research is a source based on a fs-laser with a wavelength of 1064 nm and a tunable pulse duration as short as 170 fs. For this second type of SC, the fibre is a PCF with an all normal dispersion profile. The two mechanisms describing the SC generations mentioned above are presented next.

3.5.1 ps pumped and fibre with ZDW

The first type of SC source relies on pumping a PCF nearby its ZDW with a ps-long high intensity pulse [8]. The SC generation is initiated by MI which breaks up the pump pulse into a train of Solitons. Then, those solitons experience a complex dynamic which tends to red-shift them towards longer wavelength though Raman Scattering [23**?**]. The frequency shift experienced by each soliton is governed by their instantaneous peak power, central wavelength and pulse duration. In addition, the speed of the red-shift of each soliton is related to its own peak power. Then, high peak power solitons shift faster (central wavelength shift) and crash back into slower, low peak power, solitons. Those solitons collisions are responsible for high power solitons taking away power from lower power solitons. In parallel of the solitons dynamics and as described above, dispersive waves are generated by solitons on the blue side of the pump and through dispersive waves trapping effect are shifted towards shorter wavelengths [23**?**]. In addition to those different process, losses due to propagation in the PCF

have to be considered. Finally, the red spectral extension of such SC source when considering a silica based PCF is stopped at a wavelength around 2.3 µm to 2.4 µm as the silica losses there become too high. The corresponding blue edge reached is around 500 - 600 nm which corresponds to the GV match of the longest wavelength reach on the red side of the SC.

3.5.2 fs pumped and ANDi fibre

The second type of SC source used in the course of the thesis is based on pumping a PCF which dispersion is measured in the normal regime over a wavelength range spanning from around 600 nm up to more than 1400 nm. The pump laser used is a femtosecond laser with variable pulse length from 170 fs to 1 ps. Considering this SC source design, the spectral broadening is initiated by the SPM effect triggered by the high intensity pulse from the femtosecond laser [22]. Then, OWB effect is triggered and contributes to additional spectral broadening. Such SC source spans from 700 - 800 nm up to 1450 nm [22]. The red-edge of the SC is at much shorter wavelengths compared to the first SC source described in section 3.5.1 because the confinement losses of the ANDi fibre are very high after 1450 nm. This SC source is generated only through coherent and deterministic effects which makes it potentially very interesting for OCT applications. Chapter 7 is dedicated to investigate the usefulness of such SC source for OCT application.

3.6 Conclusion

This Chapter was dedicated to give a short introduction to important concepts regarding optical fibre, non-linear effects and SC generation. Similarly to the previous Chapter about OCT theory, small summaries are provided at the beginning of each Chapter when required.

References

[1] R. R. Alfano and S. L. Shapiro. Emission in the region 4000 to 7000 å via four-photon coupling in glass. *Phys. Rev. Lett.*, 24:584–587, Mar

1970. doi: 10.1103/PhysRevLett.24.584. URL https://link.aps.org/doi/10.1103/PhysRevLett.24.584.

[2] J. K. Ranka, R. S. Windeler, and A. J. Stentz. Visible continuum generation in air–silica microstructure optical fibers with anomalous dispersion at 800 nm. *Opt. Lett.*, 25(1):25–27, Jan 2000. doi: 10.1364/OL.25.000025. URL http://ol.osa.org/abstract.cfm?URI=ol-25-1-25.

[3] Material processing using sc source - note 1. https://www.nktphotonics.com/wp-content/uploads/sites/3/2016/09/surface-texturing-application-note-01-14.pdf/, . Accessed: 2018-02-01.

[4] Material processing using sc source - note 2. https://www.nktphotonics.com/wp-content/uploads/sites/3/2016/09/tco-application-note-05-11.pdf/, . Accessed: 2018-02-01.

[5] J. Yi, Q. Wei, W. Liu, V. Backman, and H. F. Zhang. Visible-light optical coherence tomography for retinal oximetry. *Optics letters*, 38(11): 1796–1798, 06 2013. URL http://www.ncbi.nlm.nih.gov/pmc/articles/PMC3986589/.

[6] W. M. Harmening, W. S. Tuten, A. Roorda, and L. C. Sincich. Mapping the perceptual grain of the human retina. *The Journal of Neuroscience*, 34(16):5667–5677, 04 2014. doi: 10.1523/JNEUROSCI.5191-13.2014. URL http://www.ncbi.nlm.nih.gov/pmc/articles/PMC3988416/.

[7] A. W. Snyder and W. R. Young. Modes of optical waveguides. *J. Opt. Soc. Am.*, 68(3):297–309, Mar 1978. doi: 10.1364/JOSA.68.000297. URL http://www.osapublishing.org/abstract.cfm?URI=josa-68-3-297.

[8] J. M. Dudley, G. Genty, and S. Coen. Supercontinuum generation in photonic crystal fiber. *Rev. Mod. Phys.*, 78:1135–1184, Oct 2006.

doi: 10.1103/RevModPhys.78.1135. URL https://link.aps.org/doi/10.1103/RevModPhys.78.1135.

[9] P. Yeh, A. Yariv, and E. Marom. Theory of bragg fiber. *J. Opt. Soc. Am.*, 68(9):1196–1201, Sep 1978. doi: 10.1364/JOSA.68.001196. URL http://www.osapublishing.org/abstract.cfm?URI=josa-68-9-1196.

[10] P. J. Roberts, F. Couny, H. Sabert, B. J. Mangan, D. P. Williams, L. Farr, M. W. Mason, A. Tomlinson, T. A. Birks, J. C. Knight, and P. St.J. Russell. Ultimate low loss of hollow-core photonic crystal fibres. *Opt. Express*, 13(1):236–244, Jan 2005. doi: 10.1364/OPEX.13.000236. URL http://www.opticsexpress.org/abstract.cfm?URI=oe-13-1-236.

[11] T. A. Birks, J. C. Knight, and P. St. J. Russell. Endlessly single-mode photonic crystal fiber. *Opt. Lett.*, 22(13):961–963, Jul 1997. doi: 10.1364/OL.22.000961. URL http://ol.osa.org/abstract.cfm?URI=ol-22-13-961.

[12] E. Hecht. Electromagnetic Theory, Photons, and Light. In *Optics - Fourth Edition*. International Edition, San Francisco, 2002.

[13] P. M. Moselund. *Long-pulse Supercontinuum Light Sources*. PhD thesis, Chapter 2 - 2009. URL http://orbit.dtu.dk/files/5030320/Peter%20Moselund.pdf.

[14] Y. R. Shen and G.Z. Yang. Theory of Self-Phase Modulation and Spectral Broadening. In *The Supercontinuum Laser Source*, chapter 1, pages 1–32. Robert R Alfano - Springer, 2006.

[15] A. Boucon. *Modulation instability and supercontinuum generation for a quasi continuous-wave pumping in highly non linear and microstructured fibers*. PhD thesis, Chapter 1 - 2008.

[16] P. L. Baldeck, P. P. Ho, and R. R. Alfano. Cross-Phase Modulation. In *The Supercontinuum Laser Source*, chapter 4, pages 117–183. Robert R Alfano - Springer, 2006.

[17] W. J. Tomlinson, R. H. Stolen, and A. M. Johnson. Optical wave breaking of pulses in nonlinear optical fibers. *Opt. Lett.*, 10(9):457–459, Sep 1985. doi: 10.1364/OL.10.000457. URL http://ol.osa.org/abstract.cfm?URI=ol-10-9-457.

[18] C. Finot, B. Kibler, L. Provost, and S. Wabnitz. Beneficial impact of wave-breaking for coherent continuum formation in normally dispersive nonlinear fibers. *J. Opt. Soc. Am. B*, 25(11):1938–1948, Nov 2008. doi: 10.1364/JOSAB.25.001938. URL http://josab.osa.org/abstract.cfm?URI=josab-25-11-1938.

[19] E. Hecht. Modern Optics: Lasers and Other Topics. In *Optics - Fourth Edition*, chapter 13, pages 581–648. International Edition, 2002.

[20] J. C. Travers, M. H. Frosz, and J. M. Dudley. Non-linear fibre optics overview. In *Supercontinuum generation in optical fibres*, chapter 3, pages 32–51. J.M. Dudley, J.R. Taylor - Cambridge University Press, 2010.

[21] U. Møller, S. T. Sørensen, C. Jakobsen, J. Johansen, P. M. Moselund, C. L. Thomsen, and O. Bang. Power dependence of supercontinuum noise in uniform and tapered pcfs. *Opt. Express*, 20(3):2851–2857, Jan 2012. doi: 10.1364/OE.20.002851. URL http://www.opticsexpress.org/abstract.cfm?URI=oe-20-3-2851.

[22] I. Bravo Gonzalo, R. D. Engelsholm, M. P. Sørensen, and O. Bang. Polarization noise places severe constraints on coherence of all-normal dispersion femtosecond supercontinuum generation. *Scientific Reports*, 8 (1):6579, 2018. doi: 10.1038/s41598-018-24691-7. URL https://doi.org/10.1038/s41598-018-24691-7.

[23] S. T. Sørensen. *Deep-blue supercontinuum light sources based on tapered photonic crystal bres*. PhD thesis, 2013.

Chapter 4

Signal processing in optical coherence tomography

4.1 Introduction

Optical Coherence Tomography (OCT) and Ultra-High Resolution-OCT (UHR-OCT) are based on the physical phenomenon called interference (section 2.2.1). Then, OCT is equivalent to a problem of frequency decomposition/identification. The frequencies of the interference fringes are linked to the position of scattering centres within the sample (decomposition) and the amplitudes of the fringes are linked to the power reflectivities of the scattering centres. The OCT processing can be divided into three blocks. The first block is the pre-processing of the raw data towards the frequency analysis. It comprises processing steps such as noise and background correction, apodization and optional processing such as resampling and dispersion compensation. The second block is the frequency analysis itself which can be done using Fast Fourier Transform (FFT) or correlation. Finally, the third block is the data displaying generally obtained using logarithmic representation.

In this Chapter, a description of the mathematical processing used in OCT and UHR-OCT is proposed. Two processing methods are described, the conventional FFT based Spectral Domain-OCT (SD-OCT) algorithm and the Master/Slave Interferometry (MSI) based OCT algorithm. In both case, the mathematical description is supported by experimental data in order to show step-by-step the status of the processing.

4.2 OCT system definition

A typical SD-OCT system relies on three main parts. The first one is the broad optical source. If considering UHR-OCT, it is required that the axial resolution is within few microns, therefore it is required to operate with bandwidth $\Delta\lambda$ as large as possible (see section 2.5.2). Typically, in the 800 nm range, a bandwidth of at least 300 nm is required [1]. In the 1300 nm range, due to the variation of the axial resolution with the central wavelength the bandwidth needs to be larger to achieve UHR ($\Delta\lambda > 300$ nm)[1]. The bandwidth increase requirement while the central wavelength increase comes from the fact that axial resolution in OCT scales with bandwidth in wavenumber units. The second element constituting the SD-OCT system is the interferometer. Again, if UHR-OCT is targeted, it is important that the component involved are able to operate with a bandwidth of a few hundred of nanometres. In that case, the directional coupler and the optics need to be chosen accordingly. For example, it is wise to use reflective elements such as parabolic collimators instead of transmissive elements such as lenses. Finally, the last element is the spectrometer. As described in section 2.6, the spectrometer is used to disperse the broad signal into a line of photo-detectors.

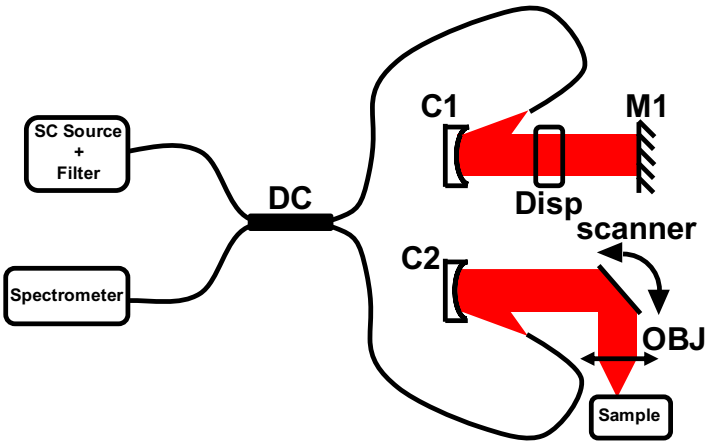

FIGURE 4.1: Sketch of the SD-OCT used for the results presented in the thesis: C1, C2: Parabolic collimators; Disp: Dispersion compensation block; M1: Flat mirror; OBJ: Objective; DC: Directional coupler.

Figure 4.1 is a sketch representing the UHR-OCT system used during the word described in this thesis. The SD-OCT system is Michelson interferometer with an ultra-broadband 50/50 directional coupler (DC) splitting the light, from a Supercontinuum (SC) source filtered around 1270 nm (NKT Photonics A/S) [2], into a reference path and a sample path. The splitting ratio of the DC coupler is maintained between 45 % and 55 % over the entire wavelength range of the system. The reference path consists of a reflective collimator ($C2$ – Thorlabs $RC04APC-P01$), a dispersion compensation block (Thorlabs $LSM02DC$), and a flat mirror ($M1$). The sample arm consists of a reflective collimator ($C1$ - Thorlabs $RC04APC-P01$), a set of galvanometer-based XY-scanners (Thorlabs $GVSM002/M$) and a scan-lens. All the optics described here are selected for optimal operation with large optical bandwidth centered around 1300 nm, then they are either based on reflective components or using special coating for this wavelength region. The spectrometer is a Cobra 1300 (Wasatch Photonics) which is a reflective based grating spectrometer[3] with an optical bandwidth covering from 1070 nm to 1470 nm based on a line-scan camera (Sensor unlimited GL-2048) [4] operating at a maximum line-rate of 76 kHz.

Figure 4.2 is an example of the data obtained at the output of the SD-OCT system described by Figure 4.1. Such signal is often call a channelled spectrum (CS). Each spectrometer readout $I(p)$ consists in a one dimensional discrete vector of length P with A_p is the amplitude in counts of pixel p.

$$I_p \equiv [A_1, A_2, A_3, ..., A_p]\,. \tag{4.1}$$

4.3 General considerations

The amplitude A_p of Equation 4.1 is representation of the photo-current that is proportional to the intensity of the light detected by the pixel p to which corresponds a wavenumber value k_p. When considering raw data from the spectrometer, the spacing in wavenumber units between two pixels is not necessarily identical along the pixel line. Considering a mirror in the

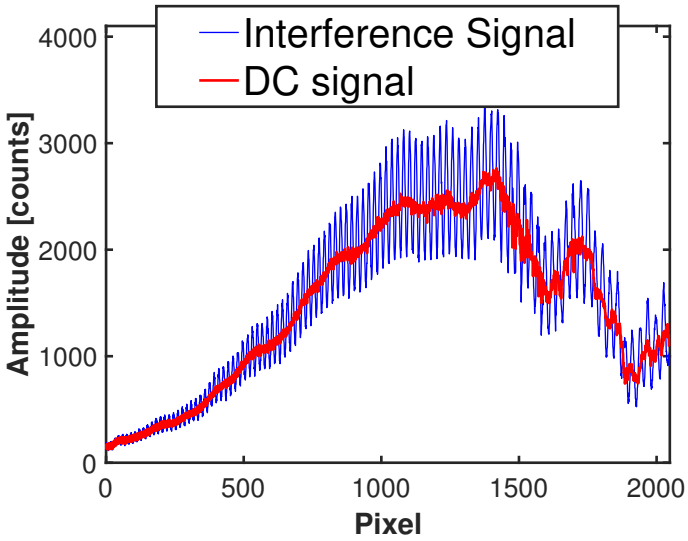

FIGURE 4.2: Example of the typical readouts measured by the spectrometer considering a DC signal and a signal with interference.

reference path of the interferometer with a power reflectivity R_R and an object in the sample path with n reflective centres of power reflectivities R_{Sn}. The spectrometer readout can be expressed as shown by Equation 4.2

$$\begin{aligned} I(k_p) \propto & \left[S(k_p) \times \left[R_R + \sum_{n=1}^{N} R_{Sn}\right]\right] \\ & + \left[S(k_p) \times \sum_{n=1}^{N} \sqrt{R_R R_{Sn}} \times cos\left(k_p \times 2\left(Z_R - Z_{Sn}\right) + \Phi_{disp}(k_p)\right)\right] \\ & + \left[S(k_p) \times \sum_{n \neq m=1}^{N} \sqrt{R_{Sn} R_{Sm}} \times cos\left(k_p \times 2\left(Z_{Sn} - Z_{Sm}\right) + \Phi_{disp}(k_p)\right)\right], \end{aligned} \tag{4.2}$$

where $S(k_p)$ is the discrete power spectral density, Z_R is the length of the reference path of the interferometer, Z_{Sn} and Z_{Sm} are the lengths of the sample path considering the reflective centres n and m respectively. The additional term $\Phi_{Disp}(k_p)$ in the phase of the cosine functions is accounted for the dispersive effects in the system.

In order to simplify the description and the comprehension of the processing steps, a system where the sample is a mirror placed at a distance Z_S from the fibre facet is considered. Then, the processing steps will be applied on a simplified version of Equation 4.2, given by:

$$I(k_p) \propto [S(k_p)\,[R_R + R_S]] + [S(k_p) \times cos\,(k_p \times 2 \times z_0 + \Phi_{Disp}(k_p))]\,, \quad (4.3)$$

with $z_0 = Z_R - Z_S$ is the optical path difference between the reference path and the sample path of the interferometer. Also, in that context, the autocorrelation term disappears as the sample consists in a single reflective centre.

4.4 Conventional OCT dedicated processing

In this section, the step-by-step signal processing algorithm required to plot an axial reflectivity profile (A-scan) is presented. This algorithm is dedicated to a conventional UHR-OCT system which relies on Fast Fourier Transform (FFT) operation. It includes compulsory steps such as resampling and dispersion compensation and also some highly-recommended steps such as apodization and background subtraction. Figure 4.3 is a flow chart of the steps required for a FFT based A-scan.

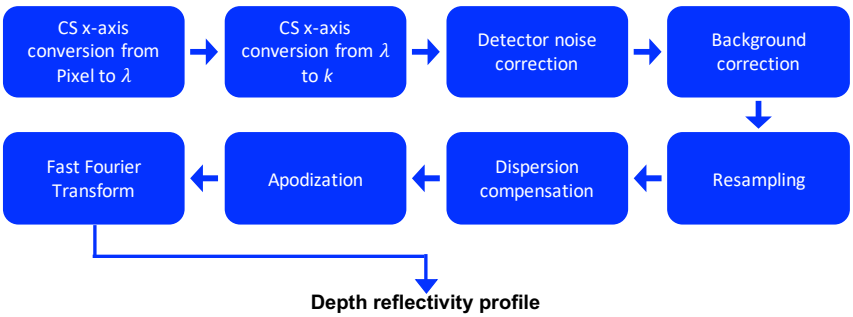

FIGURE 4.3: Step by step signal processing procedure required for FFT based SD-OCT.

4.4.1 Axis conversion from pixel position to non-uniform wavelength and non-uniform wavenumber distribution

Equation 4.3 is a function of k_p as OCT relies on the Fourier conjugation between wavenumber space and axial position space. However, spectrometers are often designed and characterised using wavelengths. As described in section 2.6.2 of the thesis, the pixel distribution corresponds a non-uniform distribution of wavelength $\tilde{\lambda}$ (the tilde notation describes the non-uniform nature of the distribution). Several methods are available to map the wavelength distribution along the pixel line of the spectrometer. Among them the spectral calibration using multiple laser lines is one the easiest. This method relies on using a series of narrow laser lines in order to map the wavelength distribution along the pixel line of the spectrometer. Then, a polynomial fit is used to describe continuously the wavelength as a function of the pixel position. The spectrometer used in the course of this thesis has been characterized by the manufacturer (Wasatch Photonics - United States) using a series of 8 narrow laser lines. Equation 4.4 is the resulting pixel to wavelength polynomial function as

$$\tilde{\lambda}(p) = C_0 \times p^0 + C_1 \times p^1 + C_2 \times p^2 + C_3 \times p^3, \tag{4.4}$$

with $C_0 = 1.06789 \times 10^3$ [nm], $C_1 = 2.04954 \times 10^{-1}$ [nm], $C_2 = -2.02466 \times 10^{-6}$ [nm] and $C_3 = -1.16410 \times 10^{-9}$ [nm]. It is important to notice that the wavelength distribution is non-linear with the pixel number (see section 2.6.2).

The data need to be expressed as a function of wavenumber, instead of wavelength, before FFT operation. The relation between wavelength and wavenumber is $\tilde{k} = 2\pi/\tilde{\lambda}$. The distribution $\tilde{k}$ is non-uniform due to the non-uniformity of $\tilde{\lambda}$ and Equation 4.3 can be re-written as

$$I\left(\tilde{k}\right) \propto \left[S(\tilde{k}) \times [R_R + R_S]\right] + \left[S(\tilde{k}) \times cos\left(2 \times \tilde{k} \times z_0 + \Phi_{Disp}(\tilde{k})\right)\right]. \tag{4.5}$$

4.4.2 Detector noise correction

The processing of section 4.4.1 has led to Equation 4.5 which described the spectrometer readout in the wavenumber space. Section 2.4 has described the different noise contributions within the SD-OCT system which are within any OCT signal. The first contribution to compensate for is the detector noise. This source of noise includes several types of noise such as the dark noise and the electronic noise. The first one, dark noise is to be attributed to random generation of electrons within the detector due to thermal fluctuations. The second type of noise, the electronic noise, is the noise generated at the digitization of the analogous signal through the different electronic components within the detecting unit.

As any source of noise, the detector noise cannot be cancelled but only approximately compensated for. Thermal control of the detection unit reduces it but is not simple to implement. A digital minimization of its effect can be obtained by subtracting an estimation value from the spectrometer readout. The detector noise can be measured by operating the detection unit at room temperature with no light (optical source off) and recording a series of spectra. In this case, the detector noise estimation per pixel can be approximated as the standard deviation of the time series of spectra:

$$\sigma^2_{Detector}(\tilde{k}) = \sigma_{I_{NoLight}(\tilde{k})}. \tag{4.6}$$

Then, after correction of detector noise

$$I_{Detector}(\tilde{k}) = I\left(\tilde{k}\right) - \sigma^2_{Detector}(\tilde{k}). \tag{4.7}$$

Figure 4.4 is showing an example of detector noise signal recorded at an exposure time of 20 µs (green). Also on Figure 4.4, a spectrometer readout with and without detector noise correction are shown. The corrected readout lies a few counts below the uncorrected values as the detector noise values are relatively small for short exposure time such as 20 µs.

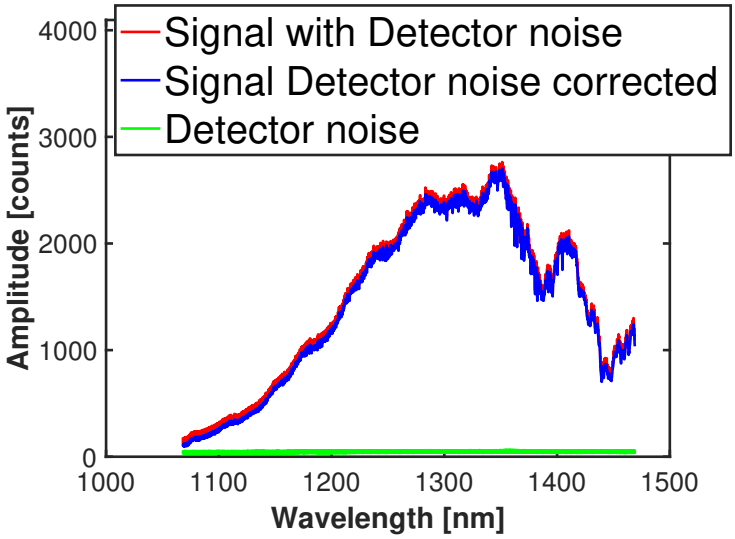

FIGURE 4.4: Example of detector noise signal (green) and the effect of its correction on a spectrometer readout (blue and red).

4.4.3 Background correction

While considering OCT imaging conditions using white light interferometry, it is important to understand that there is a large amplitude difference between the signal returning from the reference path of the interferometer and the signal returning from the sample path of the interferometer. This difference is to be attributed to the difference in power reflectivity of the mirror in the reference path (R_R) and the power reflectivities to investigate in the sample path (R_{Sn}). Most of the time, it is assumed that $R_R >> R_{Sn}$. Then, the first term from Equation 4.5 can be simplified as

$$S\left(\tilde{k}\right) \times R_R \gg S\left(\tilde{k}\right) \times R_S => S\left(\tilde{k}\right)[R_R + R_S] \approx S\left(\tilde{k}\right) \times R_R. \quad (4.8)$$

Equation 4.8 assumes that within a spectrometer readout, recorded from a real sample, the signal amplitude is dominated by the signal returning from the reference path of the interferometer. This contribution is seen as a DC component which need to be corrected in order to better exploit the dynamic range of the OCT system. Regarding this DC signal, it is fair to assume that it is quite stable. This means that the signal is not varying in

time except for noise within the system. It is then possible to compensate for the background signal by a subtracting an approximated reference signal $I_{reference}(\tilde{k}) = S(\tilde{k}) \times R_R$. Similarly, to the detector noise compensation, an average of few hundreds of readouts, acquired from the reference path of the interferometer only, is a good approximation for $I_{reference}(\tilde{k})$. The background corrected signal can be calculated as

$$I_{BackgroundCorrected}(\tilde{k}) = I_{DectectorCorrected}(\tilde{k}) - I_{Reference}(\tilde{k}). \tag{4.9}$$

This background subtraction modified Equation 4.5, if considering also the detector noise correction, as

$$I_{BackgroundCorrected}(\tilde{k}) \propto S(\tilde{k}) \times cos\left(2 \times \tilde{k} \times z_0 + \Phi_{Disp}(\tilde{k}\right). \tag{4.10}$$

Figure 4.5 is an example the reference signal measured as an average of 500 readouts measured from the reference path of the interferometer (red). Also, shown in Figure 4.5, are the readouts with and without the background correction. The corrected signal (thick blue line) shows a reduced DC component as it is almost centred around 0 counts.

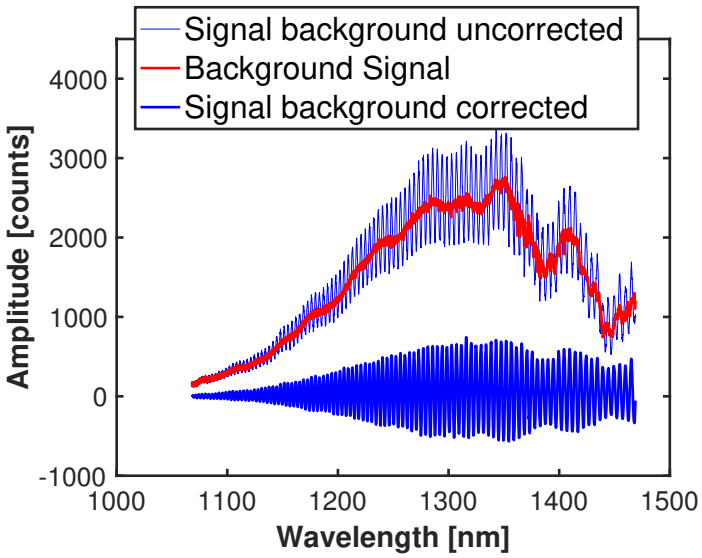

FIGURE 4.5: Example of reference signal (red) and the effect of its correction for a given readout (blue: uncorrected – blue thick: corrected).

4.4.4 Resampling

From Figure 4.3, the next step in the processing algorithm is the one called resampling. Resampling is a re-organization of the readout array, originally non-uniformly distributed in wavenumber ($\tilde{k}$), into a uniformly distributed array . This non-uniformity is expected due to the design of the spectrometer [5]. If operating with non-uniform $\tilde{k}$ distribution, the OCT will experience a broaden and varying axial resolution with the axial position [6].

Several methods have been proposed to obtain a uniform wavenumber distribution prior to FFT operation. From hardware point of view, spectrometer with linear in wavenumber output have been proposed [7]. Also, completely new techniques which do not rely on FFT operation for frequency analysis exist. Among those is the Master/Slave Interferometry (MSI) described later on this chapter in section 4.6 or the non-uniform discrete Fourier Transform technique [8]. Nevertheless, the most popular method available is the digital correction. The method used during the thesis is described below. It relies on measuring the spectrometer wavenumber distribution during a calibration step prior to imaging followed by an interpolation step.

The present method is based on phase analysis of readout and interpolation within spectrometer readout. The first step is to acquire two readouts, at two axial positions z_1 and z_2, separated by few hundreds of µm using a mirror as the sample. The two interference signals $I_{1,2,bc,dc}\left(\widetilde{k_{rel}}(p)\right)$ after detector correction (DC), background correction (BC) and assuming power reflectivity for the mirror $R_n = R_1 = 1$ can be expressed as

$$I_1\left(\widetilde{k_{rel}}(p)\right) \propto S\left(\widetilde{k_{rel}}(p)\right)\left[cos\left(2 \times \widetilde{k_{rel}}(p) \times z_{S1} + \Phi_{Disp}(p)\right)\right], \qquad (4.11)$$

and

$$I_2\left(\widetilde{k_{rel}}(p)\right) \propto S\left(\widetilde{k_{rel}}(p)\right)\left[cos\left(2 \times \widetilde{k_{rel}}(p) \times z_{S2} + \Phi_{Disp}(p)\right)\right], \qquad (4.12)$$

where $\widetilde{k_{rel}}(p)$ is the non-uniform distribution of wave-number along the pixel line of the camera. $\widetilde{k_{rel}}(p)$ is different from $\tilde{k}$ previously mentioned in

this chapter. $\widetilde{k_{rel}}(p)$ is measured with no prior knowledge of the wavelength distribution while $\tilde{k}$ is calculated from the manufacturer wavelength calibration of the spectrometer. This is an advantage of the resampling method proposed, which also includes a spectrometer wavenumber calibration. Using a Hilbert transform operation on the two readouts, their phases can be extracted and the phase difference is expressed as

$$\left(\phi_{I_1(\widetilde{k_{rel}}(p))} - \phi_{I_2(\widetilde{k_{rel}}(p))}\right)(p) = 2\widetilde{k_{rel}}(p)\Delta z, \tag{4.13}$$

where $\phi_{I_1(\widetilde{k_{rel}}(p))}$ and $\phi_{I_2(\widetilde{k_{rel}}(p))}$ are the phase of $I_{1,bc,dc}\left(\widetilde{k_{rel}}(p)\right)$ and $I_{2,bc,dc}\left(\widetilde{k_{rel}}(p)\right)$ respectively. With $\Delta z = z_{s1} - z_{s2}$ is the axial position difference. Figure 4.6 is showing the phases of $I_{1,bc,dc}\left(\widetilde{k_{rel}}(p)\right)$ and $I_{1,bc,dc}\left(\widetilde{k_{rel}}(p)\right)$, together with the phase difference calculated from Equation 4.13.

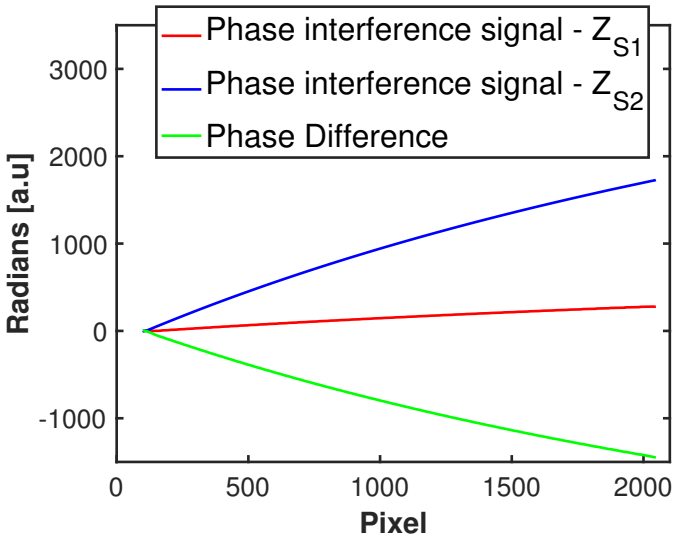

FIGURE 4.6: Extracted phase of the readout measured at z_{S1} (red) and z_{S2} (blue) together with the calculated phase difference (green).

Using a single narrow laser or a narrow band-pass filter, it is possible to obtain a wavelength value (λ_{known}) characterising a single pixel within the pixel line. Then, the wavenumber distribution can be calculated for the entire pixel line using the expression of $\widetilde{k_{rel}}(p)$ from Equation 4.13 as

$$\tilde{k}(p) = \frac{2\pi}{\lambda_{known}} + \widetilde{k_{rel}}(p). \tag{4.14}$$

It is interesting to see that the dispersion term has been cancelled by the phase difference calculation. Then, the resampling step is addressing only the non-uniformity induced due to the spectrometer design.

Figure 4.7 is a plot the wavenumber distribution obtained using the proposed resampling method and the data obtained from the spectrometer manufacturer (Equation 4.4). The difference between the two distribution is calculated as

$$\epsilon_k(p) = 100 \times \left[\tilde{k} - \frac{2\pi}{\tilde{\lambda}(p)} \Big/ \frac{\tilde{k} + \frac{2\pi}{\tilde{\lambda}(p)}}{2} \right]. \tag{4.15}$$

The two wavenumber distributions are relatively close. The difference $\epsilon_k(p)$ along the pixel line between the two methods is always smaller than 0.5 %. The largest difference is observed at the beginning of the pixel line where the signal is the weakest. Weak signals make the phase reading less accurate and therefore weaken the method accuracy.

This first step is concluded with an estimation (relatively accurate) of the wavenumber distribution along the pixel line of the camera. Such distribution is still non-linear (the spacing of wavenumber from pixel to pixel is not the same along the pixel line). Then, the second step of the calibration procedure consists in an interpolation of point within the phase of the readout at equidistant wavenumber positions. The new uniform wavenumber distribution is

$$k(p) = \tilde{k}_{LastPixel} + \left[\frac{\tilde{k}_{LastPixel} - \tilde{k}_{FirstPixel}}{N} \right] \times (p-1). \tag{4.16}$$

From Equation 4.16, an interpolation within the spectrometer readout can be performed at each $k(p)$. Numerous interpolation methods can be used and will differ in terms of speed versus efficiency. Typical software used in

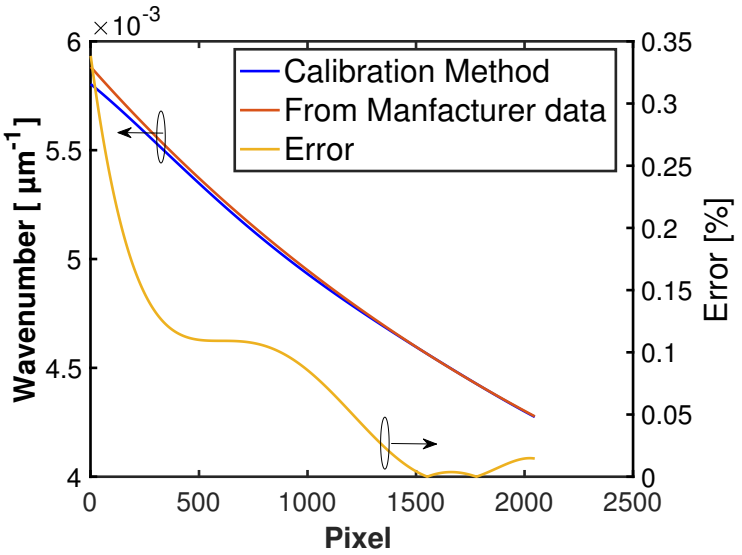

FIGURE 4.7: Wave-number distribution obtained from experimental calibration (blue) and manufacturer data (red) also with the computed error (green).

the OCT community such as Matlab or LabVIEW include interpolation possibilities such as spline, nearest, linear or cubic. Within this thesis, a spline interpolation method is used as it represents an interesting compromise between efficiency and speed. The resampled readout can be expressed as

$$I_{Resampled}(k) \propto S(k) \times cos\left(2 \times k \times z_0 + \Phi_{Disp}(k)\right). \tag{4.17}$$

As described in section , From Equation 4.17, the depth reflectivity profile can be obtained by calculating the inverse FFT of $I_{Resampled}(k)$ as

$$I(z) \propto \text{Real}\left[\text{iFFT}\left[I_{resampled}(k)\right]\right] \propto \left|\text{FFT}\left[S(k)\right]\right| \otimes \delta\left(z \pm z_0\right). \tag{4.18}$$

The resampling step is crucial for FFT based OCT. A depth reflectivity profile with relatively good precision can be obtained after resampling. The accuracy of such depth reflectivity profile depends on the amount of dispersion left uncompensated within the system. Figure 4.8 is an example of a depth reflectivity profile obtained after iFFT of a readout characterising

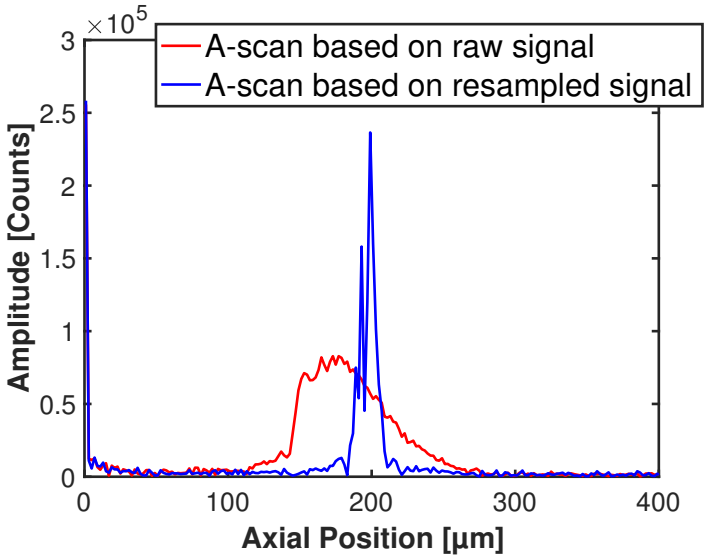

FIGURE 4.8: Depth reflectivity profile obtained from a readout corresponding to a mirror located at an axial position of 200 m before (red) and after resampling (blue).

a mirror placed at an axial position of 200 µm. It is clear that the resampling procedure followed by a conventional FFT operation has narrowed the width of the peak in the z-domain compared to the case of direct FFT of raw data. As described by section 2.5.2, the OCT axial resolution is characterised by the width of the Point Spread Function (PSF) obtained by imaging a mirror. In the present example, the peak width is around 10 -15 µm, which is far above the Fourier Transform limit expected value from an OCT system driven by a SC source. From Figure 4.5, the FWHM of the PSD seems to be around 200 nm centred around 1300 nm which corresponds to a FT limited width around 5 µm (in air). The large difference between the expected PSF width and measured width indicates the presence of dispersion within the system. A FT limited PSF can be obtained only after dispersion compensation.

4.4.5 Dispersion compensation - System dispersion

As described in the previous section, resampling only is not enough to achieve Fourier Transform limited PSF. A part of the non-linearity within the interference fringes phase is indeed due to dispersive effects within the

OCT system. The dispersion within the system is arising from two sources, the interferometer dispersion and the sample dispersion. Equation 4.17 can be written as

$$I_{Resampled}(k) \propto S(k) \times cos\left(2 \times k \times z_0 + \Phi_{Disp-int}(k) + \Phi_{Disp-sample}(k,z)\right), \tag{4.19}$$

where $\Phi_{Disp-int}(k)$ is the constant dispersion in depth arising from the interferometer and $\Phi_{Disp-sample}(k,z)$ is the depth dependent dispersion arising from the sample. In the case considered in this chapter, with a mirror as the sample, the sample dispersion is non-existent and only a constant dispersion need to be compensated for. Similarly, to the resampling phase analysis, the phase of the Equation 4.11 or Equation 4.12 can be extracted using a Hilbert transform and is written as

$$\phi_{I_{1,2}(\widetilde{k_{rel}}(p)} = 2 \times \widetilde{k_{rel}}(p) \times z_{S_{1,2}} + \phi_{Disp-int}(p). \tag{4.20}$$

Then, using the expression of $\widetilde{k_{rel}}(p)$ of Equation 4.13, the dispersion term can be calculated as:

$$\phi_{Disp-int}(p) = \phi_{I_{1,2}(\widetilde{k_{rel}}(p)} - 2 \times \widetilde{k_{rel}}(p) \times z_{S_{1,2}}. \tag{4.21}$$

This operation is possible only if the axial positions of the mirror $z_{S_{1,2}}$ are known. So far only the difference between the two positions was used. To obtain the axial position of each position, it requires a simple measurement done while acquiring each signal. First, one needs to approximate the position of the null axial position which can be measured while the interference fringes disappear (the cosine function of Equation 4.3 almost equal 1) by using a micro-metric translation stage to match the reference path and the sample path. Then, the two signal required for resampling are recorded with an estimation of their axial position.

Finally, the expression of Equation 4.21 is fitted with a j^{th} order polynomial function $\sum_{i=1}^{j} c_j k^j$ and subtracted to the phase of the resampled readout as

$$I_{Resampled}(k) \propto S(k) \times cos\left(2 \times k \times z_0 + \Phi_{Disp-int}(k) - \sum_{i=1}^{j} c_j k^j\right). \quad (4.22)$$

Figure 4.9 is showing the depth reflectivity profile, considered in the previous sections, obtained after resampling and dispersion compensation. The Fourier transform limited PSF, calculated as the $iFFT$ of the source PSD (section 2.5.2), is also displayed. The width of the peak of Figure 4.9 is close to its Fourier Transform limited value. A difference in the range of 500 nm is obtained between measured width and its limited value. Such difference falls within the accuracy of the resampling error (Figure 4.7) or the system configuration changes (temperature, polarisation, ...) affecting the interference fringes.

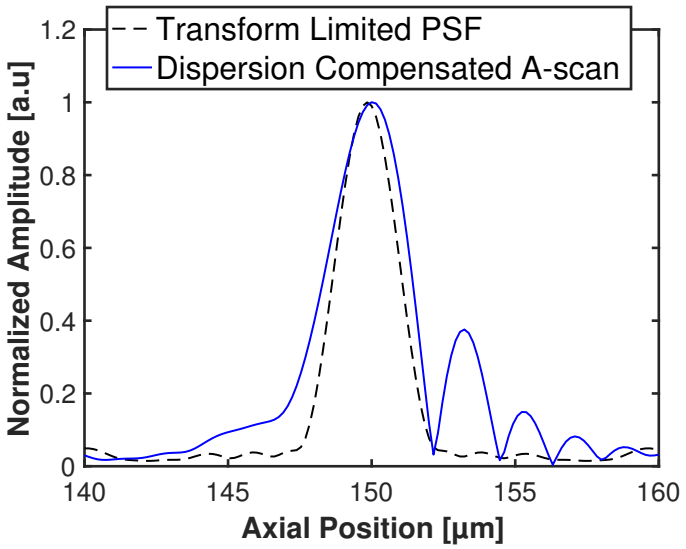

FIGURE 4.9: Depth reflectivity profile obtained from a readout corresponding to a mirror located at an axial position of 200 µm after dispersion compensation (blue continuous) and the FT limited PSF (black dashed).

It is noticeable that after the dispersion compensation the peak has been shifted in the z-domain. It appeared initially (before dispersion compensation) at an axial position of 200 µm and shifts to an axial position of 150 µm.

This shift is due to the first order dispersion Taylor expansion term added to the phase of the spectrometer readout. Such a shift is expected because of the dispersion effect on the system (section 2.7.1) and also it is not a problem for the following step of the processing as all eventual peaks within the imaging range would shift by the same 50 µm. Also, as shown by Figure 4.9, the PSF is not symmetric with important side lobes. This is due to the non-smooth spectral shape of the source PSD (Figure 4.5) and also because the two edges of the PSD are not equal to 0 (see figure 4.5).

4.4.6 Windowing

As described in the previous section, the ultra-broad spectrum comes with a non-smooth spectral shape leading to side lobes on the PSF. Of course, a hardware solution can be used for spectral shaping of the source PSD. However, such correction is hard to implement due to the particular filters required. Then, the most common technique for correcting the non-Gaussian spectral shape is to apply digitally a window function on the spectrometer readout prior to FFT operation. Numerous options exist such as Hanning, Hamming or Tukey. The window function is applied by simply multiplying the readout by the window expression. Then, Equation 4.22 is modified as

$$I_{Windowed}(k) \propto W(k) \times S(k) \times cos\left(2 \times k \times z_0\right), \tag{4.23}$$

where $W(k)$ is the expression of the window function.

During the thesis, two window functions have been widely used. The first one is the Hanning window and the second one the Tukey window. Equation 4.23 and Equation 4.24 are representing the respective expression of a Hanning window and a Tukey window

$$W_{hanning}(k) = \frac{1}{2} \times \left(1 - cos\left(\frac{2\pi}{N}\right)\right), \tag{4.24}$$

$$W_{Tukey} = \begin{cases} \frac{1}{2} \times \left[cos\left(\pi \times \left(\frac{2n}{\alpha N} - 1 \right) \right) \right] \ for\ 0 < n \leq \frac{\alpha N}{2} \\ 1\ for\ \frac{\alpha N}{2} \leq n \leq N \times \left(1 - \frac{\alpha}{2} \right) \\ \frac{1}{2} \times \left[1 + cos\left(\pi \times \left(\frac{2n}{\alpha N} - \frac{2}{\alpha} + 1 \right) \right) \right] \ for\ N\left(1 - \frac{\alpha}{2} \right) < n \leq N, \end{cases} \tag{4.25}$$

where N is the length (equal to the number of pixel of the readout) of the window W. Figure 4.10 is showing the effect of a Hanning window function applied on the previous readout after dispersion compensation. The side lobes effect previously observed in Figure 4.9 are no longer affecting the PSF.

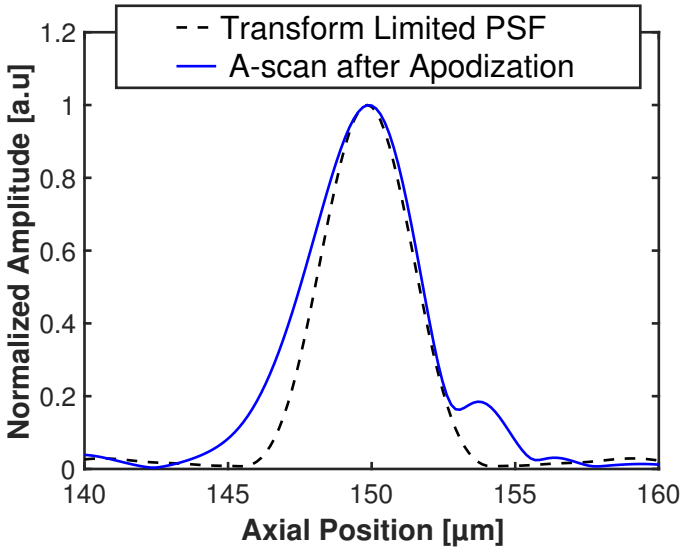

FIGURE 4.10: Normalized depth reflectivity profile obtained, from a readout corresponding to a mirror located at an axial position of 200 µm after Hanning windowing and its FT limited PSF.

An important parameter to consider while applying a window function is that the bandwidth will be reduced as the window function must be narrower than the source PSD. Then, an increase of the axial resolution value is to be expected as shown if comparing Figure 4.9 and Figure 4.10. After windowing, the measured width is broader by around $1\ \mu m$ compared to the FT limited width.

4.5 Complex Master-Slave UHR-OCT dedicated processing

This section is supported by Appendix A, which is an open access paper published during the PhD. This paper is describing the theoretical background for understanding MSI and CMSI. It is also explaining the reason for switching from MSI to CMSI.

This section is dedicated to the method called Complex Master/Slave Interferometry (CMSI). The CMSI is an extension of the Master/Slave Interferometry (MSI) first proposed in [9]. The new denomination "Complex" comes from the fact that CMSI uses complex formalism in opposition to the original MSI which uses only real number. The idea behind the MSI principle is to avoid the FFT operation required in conventional FD-OCT. The FFT operation is used in FD-OCT as a decomposition/identification tool for the interference fringes at the output the interferometer. Such decomposition/identification can also be obtained using a comparison operator. Indeed, each axial position within the imaging range of the interferometer is associated with a certain frequency of the fringes oscillations. Then, it is possible to compare the inference fringes with a set of oscillations describing discretely all the axial positions which can be imaged with the OCT system. If there is a match between a frequency of the interference signal with the oscillations describing the imaging range, the comparison signal will be high at the matching position. In opposition, if no match is detected the comparison signal will remains low at all axial positions.

A parallel can be made between the conventional FD-OCT and the MSI principle. In FFT based OCT, the interference signal measured by the interferometer has to be decomposed on a basis of single frequency sine and cosine functions which represent the frequency kernel of the system. The single frequency condition comes from the fact that wavenumber k and axial position z are direct conjugate variables by Fourier Transform operation. As shown in section 2.6.2 a readout from the interferometer is non-uniformly distributed in wave-number and needs to be resampled before FFT operation. In the case of the MSI based system, the idea is to operate with a kernel of sine and cosine function which represent the non-uniform wavenumber

distribution of the OCT system. In that situation, the cosine and sine functions are no longer single frequency function but chirped functions. Then, MSI based OCT can be described as a FD-OCT modality which is using an adapted kernel for frequency decomposition/identification. By operating with a kernel made of non-uniform functions, MSI allows to skip some of the processing steps required from the algorithm of section 4.4, namely the dispersion compensation from the interferometer and the resampling of data into equal wavenumber slots. Master/Slave Interferometry belongs to the group of FD-OCT as it does not require any scanning of the interferometer reference path in depth during imaging. However, in opposition to common FD-OCT, the depth reflectivity profile is not obtained after a single FFT operation but after a series of N comparison operations.

The original MSI method relied on comparing the interference signal with a series of pre-measured spectra. Those spectra were acquired prior to imaging using a mirror at the sample position [8, 9, 10, 11, 12, 13, 14]. In the numerous reports on MSI, those spectra are called Masks. From an experimental point of view, the Masks are acquired by translating the reference mirror by micro-metric steps using a translation stage and then saved on a computer. The maximal distance separating two Masks has to be smaller than half the coherence length of the source [9]. However, it is more interesting to use smaller steps in order to ensure a correct sampling of the peaks in the z-domain.

The new CMSI method is based on a similar concept of comparison of shapes used in MSI. Nonetheless, instead of experimental Masks a set of theoretical Masks is used [15, 16]. The Mask set is generated by measuring the system properties affecting the interference signal uniformity. The CMSI Masks generation procedure involves the measurement of the spectrometer wavenumber distribution and the dispersion effect arising in the interferometer. This new way of Mask generation has solved numerous drawbacks of the original MSI as described in Appendix A.

Both MSI and CMSI show a certain number of advantages compared to FFT based OCT. First, the most important point is that MSI and CMSI do not require the resampling of data in equal wavenumber slots. Indeed,

resampling is the computation time bottleneck of SD-OCT system. The second advantage of MSI and CMSI is the tolerance to dispersion arising from the interferometer [13]. The dispersion from the system is affecting both the readout measured with a sample and the Masks. Then, the comparison operation is tolerant to the chirping effect caused by dispersion. A third advantage is the computation methodology used to obtain a depth reflectivity profile. In the case of FFT based OCT, the entire imaging range is computed and processed while the sample might occupy only a fraction of it. In the MSI principle, each point of the depth reflectivity profile is obtained separately. It is then possible to compute only the imaging range required for a given sample. It is also noticeable that such property is ideal for parallel computing and GPU processing. Finally, due to this depth by depth processing, an *en-face* image can be produced with no need for processing a full volume as in SD-OCT.

The MSI and CMSI principle have been proposed in multiple FD-OCT configuration such as SD-OCT [13, 15], Swept source OCT [9, 10, 11, 12, 14, 15] and Full field-OCT [8]. Also, recent demonstrations of application of the CMSI based OCT have been reported [16, 17, 18].

4.5.1 Mathematical summary

It is proposed in here a short summary of the mathematical definition of the MSI and CMSI mathematical background. A complete description is proposed in Appendix A.

Master Slave Interferometry

Following a similar formalism compared to section 4.4 and demonstrated in Appendix A, the MSI depth reflectivity profile is approximated as

$$MSI(z) \propto \mathrm{Max_K}\left[\int_{-\infty}^{+\infty} I\left(\tilde{k}\right) M\left(\tilde{k}+K, z\right) d\tilde{k}\right], \tag{4.26}$$

where $\mathrm{Max_K}$ is an operator measuring the maximum value of the integral along the lag variable axis, z is the axial position, $\tilde{k}$ is the non-uniform

wavenumber distribution of light along the pixel line, $I(\tilde{k})$ is the interference signal describing the sample reflectivity profile, $M\left(\tilde{k}+K,z\right)$ is the mask characterizing the axial position z and K is the correlation lag variable. The latest reports on MSI used the dot product operation, which is the calculation of the correlation only at its maximum value (K=0), to approximate the MSI signal so Equation 4.26 is calculated as

$$MSI(z) \propto \int_{-\infty}^{+\infty} I\left(\tilde{k}\right) M\left(\tilde{k},z\right) d\tilde{k}. \tag{4.27}$$

Equally to section 4.4 and also described in Appendix A the depth characterization of an OCT system is a convolution between the system depth PSF with the sample complex reflectivity profile. If considering as a sample a flat mirror located at an axial position z_0, the MSI signal is equivalent to

$$MSI(z) = \text{Real}\left[\delta\left(z-z_0\right) \otimes \text{FT}\left[|A\left(\tilde{k}\right)|^2 \times \frac{\text{d}\left(\tilde{k}^{-1}\right)}{\text{d}\tilde{k}}\right]\right], \tag{4.28}$$

with $A\left(\tilde{k}\right) \propto E_0^2$ corresponds to the interference envelope and $\tilde{k}^{-1}$ corresponds to the inverse function of the distribution $\tilde{k}$.

As shown by Equation 4.28 and described in Appendix A, the original MSI allows to measure the depth reflectivity profile of a sample with no resampling and no interferometer dispersion compensation. However, such measurement is not perfect as the PSF is not FT limited as $\text{FT}\left[|A\left(\tilde{k}\right)|^2 \times \frac{d\left(\tilde{k}^{-1}\right)}{d\tilde{k}}\right] \neq \text{FT}\left[A\left(\tilde{k}\right)\right]$. Operating with a PSF broader than its transform limited value corresponds to wasting some of the source optical bandwidth.

Complex Master Slave Interferometry

The CMSI has been developed in order to address the drawbacks of the original MSI. However, CMSI has to keep the advantages such as no need for data resampling, tolerance to dispersion from the interferometer and customized sampling possibilities. To do so, the Masks set has to be modified in order to obtain a FT limited PSF. The experimental Masks leading to

Equation 4.28 can be model as

$$M_{experimental}\left(\tilde{k},z\right)=S(\tilde{k})\times exp\left[i\times\left(2\times\tilde{k}\times z+\phi_{Disp}\left(\tilde{k}\right)\right)\right]. \tag{4.29}$$

The new expression for the synthesised Masks at an axial position z is then (see Appendix A)

$$M_{experimental}\left(\tilde{k},z\right)=\frac{\partial\tilde{k}}{\partial k}\times exp\left[i\times\left(2\times\tilde{k}\times z+\phi_{Disp}\left(\tilde{k}\right)\right)\right]. \tag{4.30}$$

Similarly, if considering a dot product operation as the comparison operator and if using the Masks of Equation 4.30, Equation 4.28 becomes

$$MSI(z)\propto \text{Real}\left[\delta\left(z-z_0\right)\otimes \text{FT}\left[A(\tilde{k})\right]\right]. \tag{4.31}$$

From Equation 4.31, the depth reflectivity profile is now obtained with a FT limited PSF. The expression of Equation 4.31 can be identified to the one of 4.4 with a convolution product between reflectivity profile of the sample and the Fourier transform of the source PSD.

4.5.2 CMSI Flowchart

The CMSI processing necessary to obtain a depth reflectivity profile can be divided into two steps. The first one, called Master step, is dedicated to the generation of a chosen number of Masks from a set of a few experimental measurements. This step occurs prior to imaging, so the computing time used is not affecting the OCT imaging rate. Those Masks are generated based on a procedure described in section 4.5.3. The second step of the CMSI procedure, called the Slave step, is the imaging step itself. This imaging step includes the acquisition of readouts by the spectrometer and the comparison operation for frequency analysis. A flow chart describing the CMSI procedure is proposed in Figure 4.11.

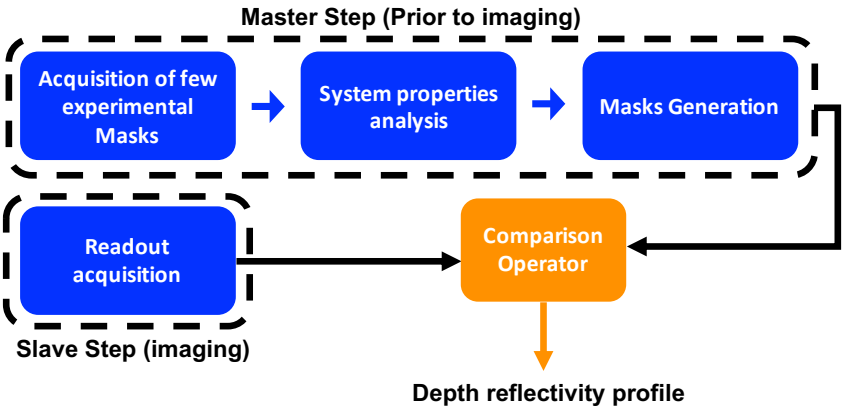

FIGURE 4.11: Flowchart of the CMSI procedure for generating a depth reflectivity profile.

4.5.3 Theoretical generation of adequate Masks

The first step of the CMSI procedure is the generation of Masks. The Masks generation starts with a phase analysis of several experimental readouts recorded at several axial positions using a mirror as a sample. Examples of two experimental Masks are shown in Figure 4.12.

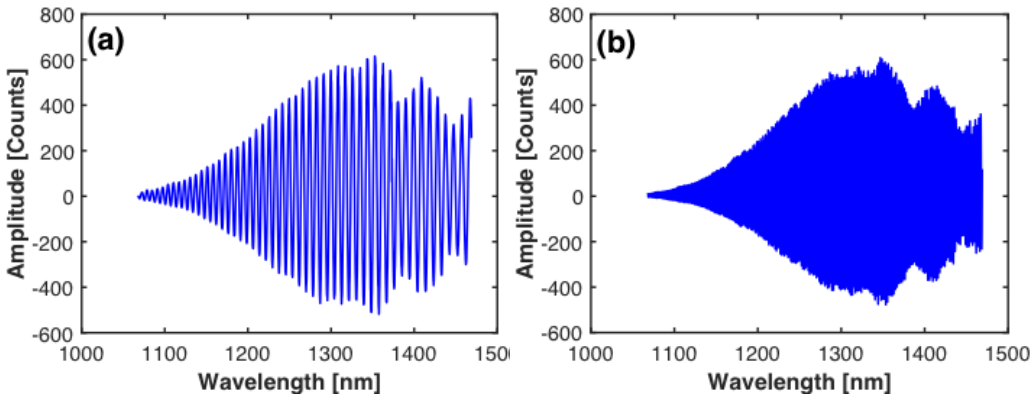

FIGURE 4.12: Example of experimental Masks recorded at axial positions of 100 µm (a), 500 µm (b).

The masks generation is based on reading the phase of few experimental readouts in order to infer the non-uniformity induced by the spectrometer and also the non-uniformity induced by dispersive effects within the interferometer. In order to read the phase of those experimental readouts,

an algorithm based on complex formalism is used. Following a similar formalism as before, the readouts shown in Figure 4.12, can be mathematically approximated as

$$I\left(\tilde{k}\right) = S\left(\tilde{k}\right) \times cos\left(2 \times \tilde{k} \times z + \phi_{rand}\left(z\right) + \phi_{Disp}\left(\tilde{k}\right)\right), \tag{4.32}$$

where $\phi_{rand}\left(z\right)$ is an additional phase term representing the eventual changes occurring in the system when recording the readouts. This additional phase term has been added to the readout expression because of the original MSI procedure described in Appendix A. Indeed, the MSI method relied only on experimental Masks which are recorded during several tens of minutes. During such a long-time frame, vibrations or temperature fluctuations have to be taken into account in the readouts expression.

The conversion from real formalism to complex formalism is obtained using a FFT operation, a filtering technique and then an inverse FFT operation of the readout. The real part of the FFT of the readout leads to the representation shown in Figure 4.13 (a). This is the typical representation of an axial profile obtained if considering a non-uniform distribution of wavenumber. The axial profile is symmetric around the zero-axial position but the peak localization is very poor due to the broadness of the peak. The filtering step consists in zeroing $FFT\left[I\left(\tilde{k}\right)\right]$ for the entire negative side of the axial position axis and also a small part of the positive side in order to cancel the DC components. The effect of the filtering technique is illustrated on Figure 4.13 (b). Finally, the inverse FFT operation is applied to the filtered signal. The complex Masks can be expressed as:

$$I\left(\tilde{k}\right) = \text{iFFT}\left\{\begin{array}{l} 0 \text{ for axial position} < 0 \\ 0 \text{ for } 0 \leq \text{axial position} \leq DC_{cut} \\ \text{FFT}\left[I\left(\tilde{k}\right)\right] \end{array}\right]. \tag{4.33}$$

From Equation 4.33, the phase extracted of a readout can be approximated as

$$\phi_{experimental\ masks}\left(\tilde{k}, z\right) = 2 \times \tilde{k} \times z + \phi_{rand}(z) + \phi_{Disp}\left(\tilde{k}\right). \tag{4.34}$$

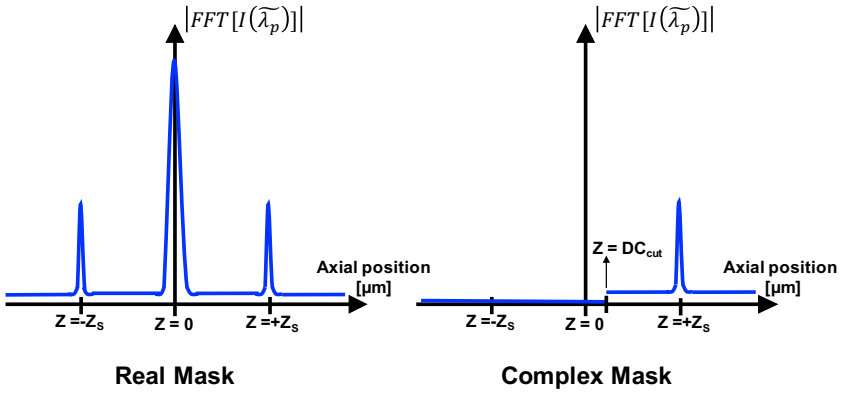

FIGURE 4.13: Illustration of the conversion from real formalism to complex formalism by using FFT operation and filtering.

For ease of notation and in order to match the notation of Appendix A, let's denote $g\left(\tilde{k}\right) = 2 \times \tilde{k}$, $h\left(\tilde{k}\right) = \phi_{Disp}\left(\tilde{k}\right)$. Then, Equation 4.34 is the sum of three functions. Two of them $g\left(\tilde{k}\right)$ and $h\left(\tilde{k}\right)$ vary with $\tilde{k}$ while the last one $\phi_{rand}(z)$ is independent of $\tilde{k}$. Due to the fact that $\phi_{rand}(z) \neq f\left(\tilde{k}\right)$, the derivative of Equation 4.34 according to $\tilde{k}$ can be written:

$$\frac{\partial \phi_{experimental\ masks}\left(\tilde{k}, z\right)}{\partial \tilde{k}} = \frac{\partial g\left(\tilde{k}\right)}{\partial \tilde{k}} \times z + \frac{\partial h\left(\tilde{k}\right)}{\partial \tilde{k}}. \tag{4.35}$$

The derivative operation of the phase according to $\tilde{k}$ has cancelled the contribution of the random phase term $\phi_{rand}(z)$. Also, a linear relation is established between the phase derivative and the axial position. Figure 4.14 shows the phase derivative evolutions versus the axial position for different pixel positions on the camera.

As shown in Figure 4.14, the evolutions of the phase derivative with the axial positions are effectively linear (expected from Equation 4.35). This behaviour is very well demonstrated for pixels 500, 1000 and 1500. However, the linear evolution is not clear regarding the pixel 100. A large variation occurs at axial position of 600 µm, which is due to the weak signal amplitude at this position on the pixel line (see Figure 4.12). Such weak signal tends to make the phase analysis less accurate.

For each pixel, a linear fit is applied on the phase derivative evolution

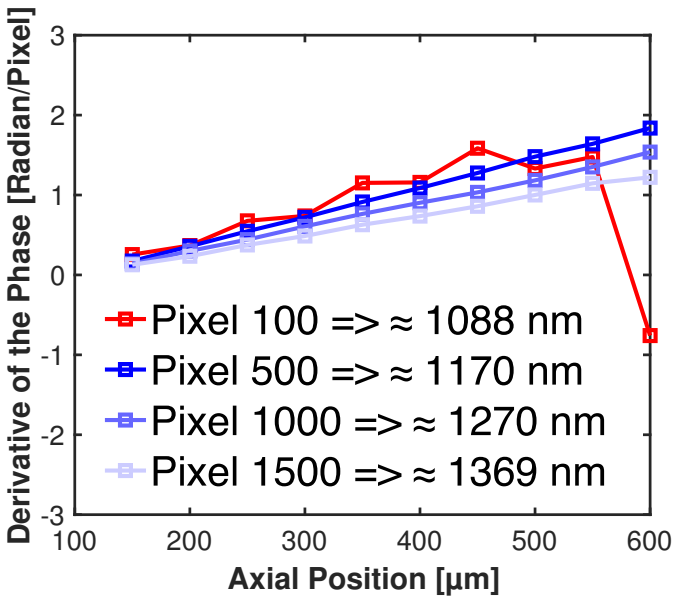

FIGURE 4.14: Phase derivative evolution versus the axial position considering four different pixels

with the axial position. The linear fits can be described for the pixel position i as

$$y_i\left(\tilde{k}\right) = a_i\left(\tilde{k}\right) \times z + b_i\left(\tilde{k}\right). \tag{4.36}$$

By identification of terms in Equation 4.35 and Equation 4.36, the gradient $a_i\left(\tilde{k}\right)$ of the fit functions represent an estimation of $\frac{\partial g\left(\tilde{k}\right)}{\partial \tilde{k}}$ and the y-axis crossing point $b_i\left(\tilde{k}\right)$ is an estimation of $\frac{\partial h\left(\tilde{k}\right)}{\partial \tilde{k}}$. Then, by integrating $a_i\left(\tilde{k}\right)$ and $b_i\left(\tilde{k}\right)$ according to $\tilde{k}$, the functions $g\left(\tilde{k}\right)$ and $h\left(\tilde{k}\right)$ can be retrieved. Figure 4.15 (top) and Figure 4.15 (bottom) display the functions $g\left(\tilde{k}\right)$ and $h\left(\tilde{k}\right)$ obtained after numerical integration.

It is noticeable that both functions $g\left(\tilde{k}\right)$ and $h\left(\tilde{k}\right)$ display irregular variations at short wavelengths. Those non-regularities are due to the weak signal amplitude (red plot of Figures 4.15).

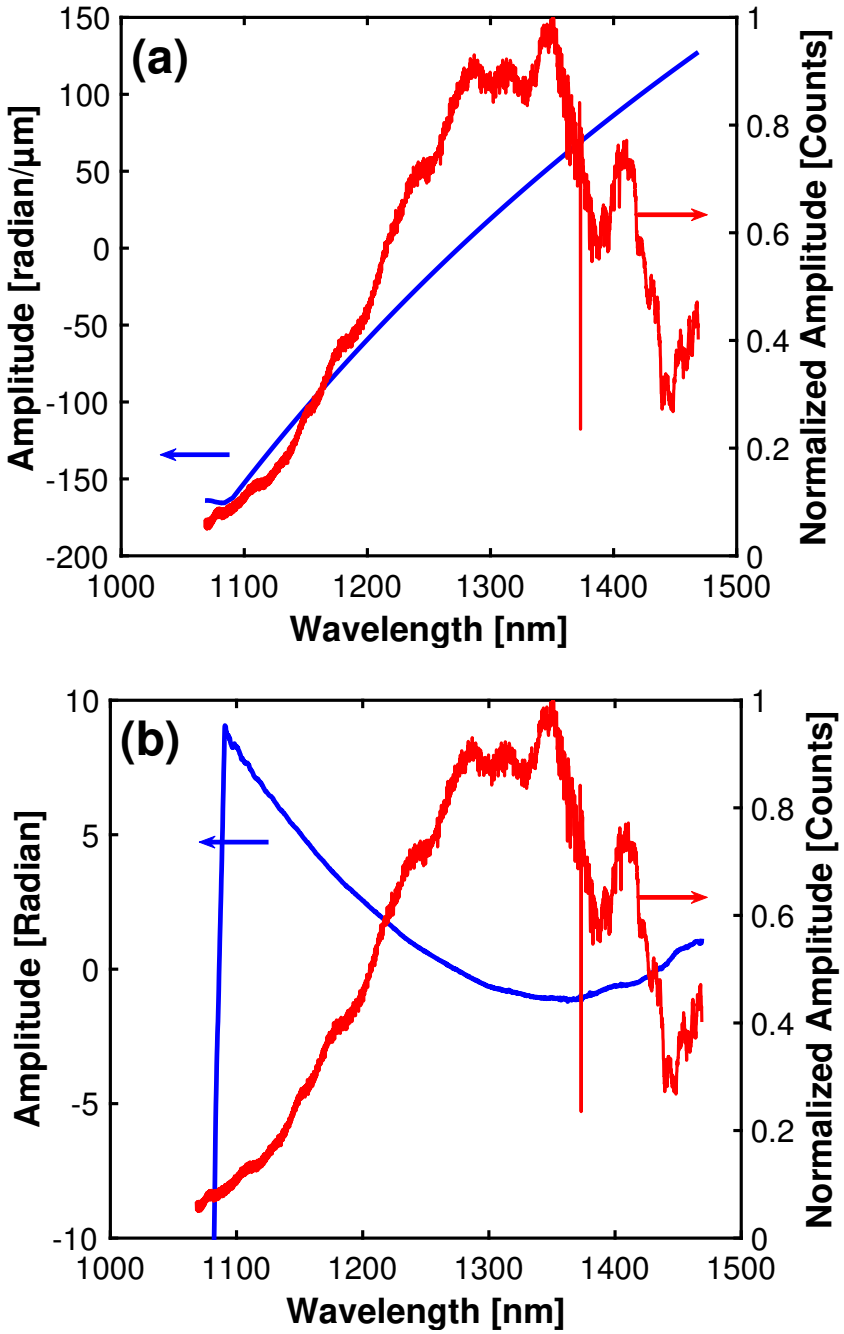

FIGURE 4.15: Representation of the functions $g\left(\tilde{k}\right)$ (a) and $h\left(\tilde{k}\right)$ (b) obtained after numerical integration of the phase derivative.

Using the two functions $g\left(\tilde{k}\right)$ and $h\left(\tilde{k}\right)$, a Mask at any axial position z can be built free from the effects of the random phase term and free from the source PSD:

$$M_{synthesised}\left(\tilde{k},z\right)=\frac{\partial g\left(\tilde{k}\right)}{\partial\tilde{k}}\times exp\left[i\times\left(g\left(\tilde{k}\right)\times z+h\left(\tilde{k}\right)\right)\right]. \tag{4.37}$$

The Masks built from Equation 4.37 are ideally matching the system properties and therefore represents the ideal kernel for the frequency analysis of the imaging step of the CMSI based OCT. In addition, the spectral shape has been completely cancelled leading a FT limited PSF as the CMSI signal depend on FT $\left[A\left(\tilde{k}\right)\right]$ instead of FT $\left[|A\left(\tilde{k}\right)|^2\right]$. Finally, the axial position is no longer a discrete experimental parameter but a mathematical variable.

Figure 4.16 (b) shows the synthesised Mask corresponding to the axial position 100 µm compared to the experimental Mask recorded at an axial position of 100 µm (Figure 4.15 (a)). A Hanning window function has been applied to both Masks.

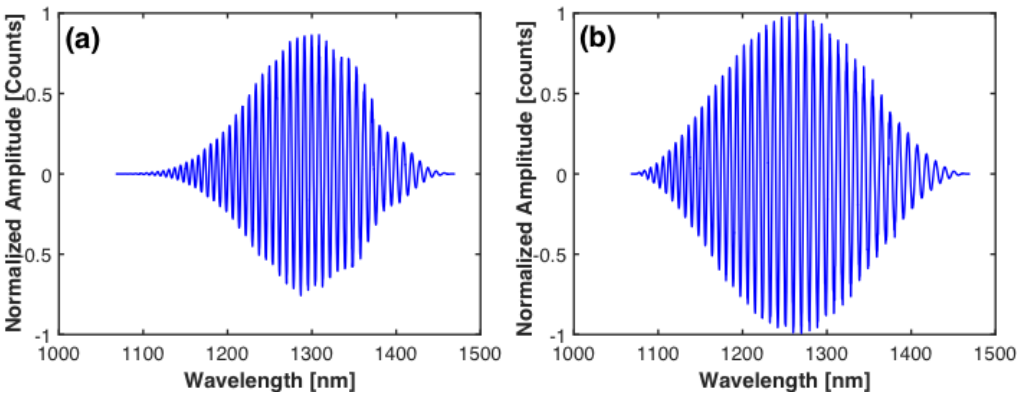

FIGURE 4.16: (a) Experimental Mask measured at an axial position of 100 µm, (b) Theoretical Mask generated corresponding to the axial position 100 µm.

4.5.4 Depth reflectivity profile calculation using CMSI

Similarly, to the original MSI (Equation 4.26), a depth reflectivity profile based on CMSI can be calculated using the Masks produced with the protocol of section 4.5.2. Then, the depth reflectivity profile, using a dot product operator for comparison, is computed as

$$MSI\,(z) \propto \int_{-\infty}^{+\infty} I\left(\tilde{k}\right) \times M_{synthesised}\left(\tilde{k}, z\right) d\tilde{k}. \tag{4.38}$$

Assuming the same situation of section 4.4.6 where the sample considered is a mirror located at an axial position of 200 µm, a CMSI based A-scan is shown in Figure 4.17:

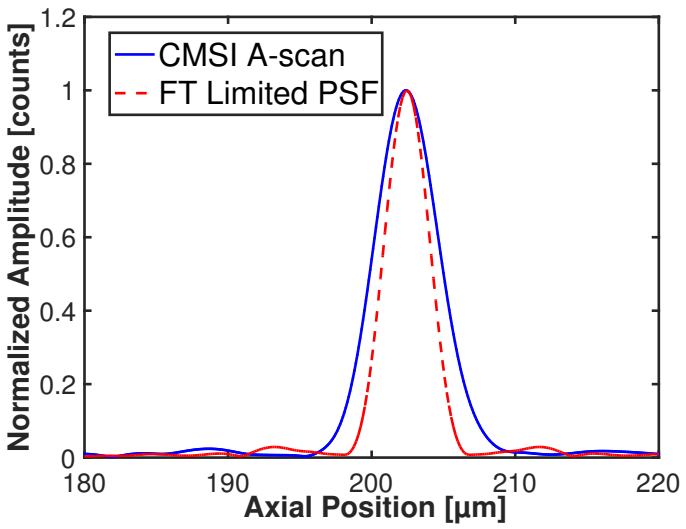

FIGURE 4.17: CMSI based A-scan considering a mirror located at an axial position of 200 µm. (blue): Measured PSF, (red) FT Limited PSF.

The CMSI based A-scan shows a peak located at an axial position around 200 µm as expected from the mirror location. The peak width is however broader compared to the FT limited width. This indicates that the current CMSI algorithm used for Masks generation is not yet optimal and needs to be improved.

4.6 Comparison between conventional OCT and MSI - Discussion

A first metric which can be used to compare CMSI based OCT and FFT based OCT is the Sensitivity. As described in section 2.5.1, the sensitivity is a metric related to the ability for a system to image weak signals from the sample. Considering that an identical set of readouts is used for comparing the sensitivity obtained using the CMSI and the FFT based A-scans, any difference has to be attributed to the method itself. Figure 4.18 is a comparison of the Sensitivity decays with axial positions measured with the two methods for an exposure time of 20 µs and 4 mW of optical power on the sample. Both methods show a Sensitivity value around 95 dB at shallow axial positions. This is a few dB below the theoretical values achievable under those conditions (Theoretical Sensitivity, calculated as in [19], around 100 dB). No particular differences are observable, the CMSI based decay seems a bit higher than the FFT based one at shallow axial position and then the trend is inverted at larger axial positions. However, the differences are very small so it is hard to conclude on the advantage of one method. The fact that the two methods are concluding equally, when using the exact same data, regarding the system sensitivity is important as it informs on the fact that the comparison approach used for the CMSI is equally good regarding the noise behavior.

The second metric which is important to conclude on when comparing two OCT techniques is the axial resolution. The axial resolution obtained using FFT based OCT is described by Figure 4.10 and the measured axial resolution, corresponding to the peak FWHM, after resampling and dispersion compensation is 4.2 µm (in air). As illustrated in Figure 4.10, this axial resolution value is very close to the FT limited value, with a difference smaller than 500 nm. In the case of the CMSI technique, the axial resolution is illustrated in Figure 4.17 and the FWHM is approximately 5.3 µm (in air). The axial resolution measured using CMSI is broader by around 1.5 µm compared to the FFT limited values. This difference can be explained by errors within the Mask generation during the CMSI procedure. It is important to consider that the CMSI Masks generation is a protocol applied to a

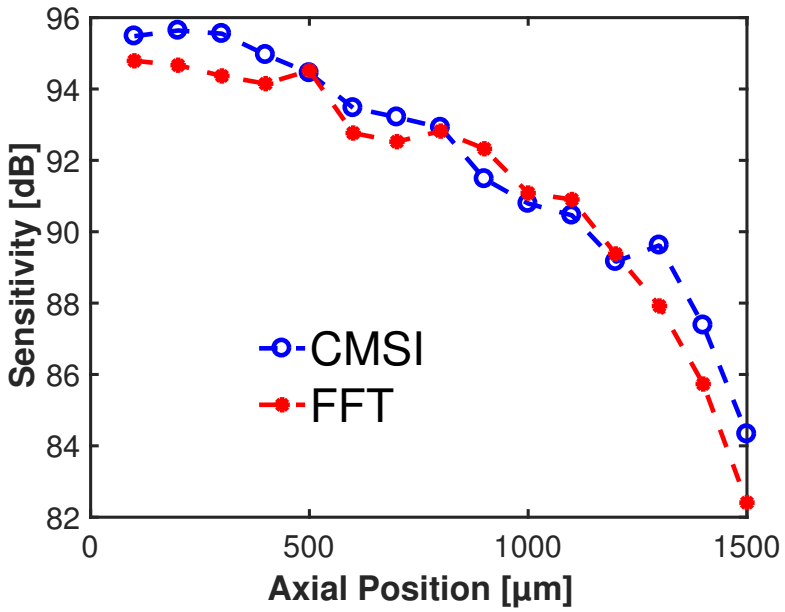

FIGURE 4.18: Sensitivity versus axial position measured using FFT based OCT procedure and CMSI based OCT procedure.

set of experimental readouts with no optimization. No optimization means that the Masks generation is done without adjustments. In opposition, the FFT based procedure includes an optimization at the dispersion compensation step where the order of the polynomial function is set iteratively to obtained a PSF as close as possible compared to the FFT limited PSF. Also, an optimization is done at the calculation of $\widetilde{k_{rel}}(p)$ where the parameter Δz is adjusted to optimise the resampling effectiveness. Finally, the results presented in this chapter are based on the early development of the CMSI procedure and therefore might not be optimal. However, a difference of 30 % between measured axial resolution and theoretical axial resolution is still encouraging if considering that no resampling neither dispersion compensation has been used.

Finally, a clear difference is observed regarding the time for computing the axial profiles using the two procedures. The study of the exact timing difference has not been conducted during this investigation. However, when simply comparing the time for computing a single depth reflectivity profile, a clear advantage is demonstrated for the FFT based technique. When using the same computer, the same data and the software Matlab,

the time for the calculation of a single FFT based A-scan is shorter than a second. In the case of the CMSI based A-scan the time is above a few seconds. This can be simply explained by the fact that the FFT based A-scan is based on built-in function such as FFT operation or Spline interpolation and therefore is relatively fast to compute. In the other hand, the CMSI based A-scan is built using conventional numerical integration which are not optimized for fast computation. A recent report on CMSI has investigated the computation speed of both CMSI and FFT method [16]. The conclusion of the study is that CMSI can be as fast or even faster compared to FFT based method. This is obtained if particular care is taken regarding the number of points considered in the A-scan and the use of optimized processing tool (matrices based computation).

4.7 CMSI continuation

The idea behind this chapter was to introduced the methods called CMSI and to compare it to the gold standard of FFT based OCT. As mentioned above, the CMSI is relatively new and requires some more work in order to be fully equivalent to the FFT based processing. Two types of work need to be completed regarding the CMSI.

The first category includes tasks related to establish a clear equivalence between the CMSI results with the FFT based ones. To do so, the first task is to confirm that the CMSI procedure is dealing similarly with noise compared to the FFT based one. A second task is to investigate why the proposed CMSI algorithm displays a broader PSF compared to the FFT based procedure. Certainly, this broader PSF is due to the Masks generation. Error such as integration errors or cancellation of the random phase term by phase differentiation needs to be investigated. Finally, the CMSI method relies on a set of few experimental readouts, so it is necessary to study the influence of those readouts on the CMSI accuracy. For example, an investigation on parameters such as the minimal number of experimental readouts, the distance between those readouts, the required signal amplitude for correct phase reading need to be conducted.

The second category of work which have to be done to pursue the CMSI project is to validate the possibility of functional CMSI based OCT. Currently, OCT angiography, Spectroscopic OCT and Doppler OCT are very common within the OCT community. Then, it is important for the CMSI to be able to be used for the same type of applications.

4.8 Conclusion

In this chapter, the signal processing procedures for computing an SD-OCT A-scan are described. Two methods are detailed: FFT based OCT and CMSI based OCT. Using the FFT based procedure, a well localized A-scan with high signal to noise ratio and narrow width is obtained. The resulting axial resolution is very close to the theoretical limit determined by the FT of the source PSD. Considering the CMSI procedure, a well localized A-scan with high SNR is obtained. However, the axial resolution is not FT limited. More work is required to establish a correct correspondence between CMSI and FFT. However, recent reports on the CMSI procedure have shown encouraging application possibilities using the advantages of the CMSI procedure such as the tolerance to dispersion and the custom sampling in depth.

References

[1] W. Drexler. Ultrahigh-resolution optical coherence tomography. *Journal of Biomedical Optics*, 9:9 – 9 – 28, 2004. doi: 10.1117/1.1629679. URL http://dx.doi.org/10.1117/1.1629679.

[2] NKT Photonics A/S, howpublished = http://www.nktphotonics.com/lasers-fibers/en/product/superk-oct-broadband-sources-optical-coherence-tomography/, note = Accessed: 2017-11-30.

[3] Wasatch photonics. http://wasatchphotonics.com/product-category/optical-coherence-tomography/cobra-oct-spectrometers/. Accessed: 2017-11-30.

[4] Sensor unlimited. http://www.sensorsinc.com/products/detail/gl2048-ingaas-linescan-camera. Accessed: 2017-11-30.

[5] B. H. Park, M. C. Pierce, B. Cense, S. H. Yun, M. Mujat, G. J. Tearney, B. E. Bouma, and J. F. de Boer. Real-time fiber-based multi-functional spectral-domain optical coherence tomography at 1.3 µm. *Opt. Express*, 13(11):3931–3944, May 2005. doi: 10.1364/OPEX.13.003931. URL http://www.opticsexpress.org/abstract.cfm?URI=oe-13-11-3931.

[6] X. Yao, Y. Gan, C. C. Marboe, and C. P. Hendon. Myocardial imaging using ultrahigh-resolution spectral domain optical coherence tomography. *Journal of Biomedical Optics*, 21(6):061006, 06 2016. doi: 10.1117/1.JBO.21.6.061006. URL http://www.ncbi.nlm.nih.gov/pmc/articles/PMC4814547/.

[7] G. Lan and G. Li. Design of a k-space spectrometer for ultra-broad waveband spectral domain optical coherence tomography. *Scientific Reports*, 7:42353 EP –, 03 2017. URL http://dx.doi.org/10.1038/srep42353.

[8] J. Wang; A. Bradu; G. Dobre and A. Podoleanu. Full-field swept source master-slave optical coherence tomography. *IEEE Photonics Journal*, 7(4), 2015. ISSN 1943-0655. doi: 10.1109/JPHOT.2015.2461571. URL http://ieeexplore.ieee.org/stamp/stamp.jsp?arnumber=7169502.

[9] A. Podoleanu and A. Bradu. Master–slave interferometry for parallel spectral domain interferometry sensing and versatile 3d optical coherence tomography. *Opt. Express*, 21(16):19324–19338, Aug 2013. doi: 10.1364/OE.21.019324. URL http://www.opticsexpress.org/abstract.cfm?URI=oe-21-16-19324.

[10] A. Bradu and A. Podoleanu. Calibration-free b-scan images produced by master/slave optical coherence tomography. *Opt. Lett.*, 39(3):450–453, Feb 2014. doi: 10.1364/OL.39.000450. URL http://ol.osa.org/abstract.cfm?URI=ol-39-3-450.

[11] A. Bradu and A. Podoleanu. Imaging the eye fundus with real-time en-face spectral domain optical coherence tomography. *Biomed. Opt. Express*, 5(4):1233–1249, Apr 2014. doi: 10.1364/BOE.5.001233. URL http://www.osapublishing.org/boe/abstract.cfm?URI=boe-5-4-1233.

[12] A. Bradu, K. Kapinchev, F. Barnes, and A. Podoleanu. On the possibility of producing true real-time retinal cross-sectional images using a graphics processing unit enhanced master-slave optical coherence tomography system. *Journal of Biomedical Optics*, 20:20 – 20 – 9, 2015. doi: 10.1117/1.JBO.20.7.076008. URL http://dx.doi.org/10.1117/1.JBO.20.7.076008.

[13] A. Bradu, M. Maria, and A. Podoleanu. Demonstration of tolerance to dispersion of master/slave interferometry. *Opt. Express*, 23(11):14148–14161, Jun 2015. doi: 10.1364/OE.23.014148. URL http://www.opticsexpress.org/abstract.cfm?URI=oe-23-11-14148.

[14] A. Bradu, K. Kapinchev, F. Barnes, and A. Podoleanu. Master slave en-face oct/slo. *Biomed. Opt. Express*, 6(9):3655–3669, Sep 2015. doi: 10.1364/BOE.6.003655. URL http://www.osapublishing.org/boe/abstract.cfm?URI=boe-6-9-3655.

[15] S. Rivet, M. Maria, A. Bradu, T. Feuchter, L. Leick, and A. Podoleanu. Complex master slave interferometry. *Opt. Express*, 24(3):2885–2904, Feb 2016. doi: 10.1364/OE.24.002885. URL http://www.opticsexpress.org/abstract.cfm?URI=oe-24-3-2885.

[16] A. Bradu, S. Rivet, and A. Podoleanu. Master/slave interferometry – ideal tool for coherence revival swept source optical coherence tomography. *Biomed. Opt. Express*, 7(7):2453–2468, Jul 2016. doi: 10.1364/BOE.7.002453. URL http://www.osapublishing.org/boe/abstract.cfm?URI=boe-7-7-2453.

[17] R. Cernat, A. Bradu, N. M. Israelsen, O. Bang, S. Rivet, P. A. Keane, D. G. Heath, R. Rajendram, and A. Podoleanu. Gabor fusion master slave optical coherence tomography. *Biomed. Opt. Express*, 8(2):

813–827, Feb 2017. doi: 10.1364/BOE.8.000813. URL http://www.osapublishing.org/boe/abstract.cfm?URI=boe-8-2-813.

[18] S. Caujolle, R. Cernat, G. Silvestri, M. J. Marques, A. Bradu, T. Feuchter, G. Robinson, D. K. Griffin, and A. Podoleanu. Speckle variance oct for depth resolved assessment of the viability of bovine embryos. *Biomed. Opt. Express*, 8(11):5139–5150, Nov 2017. doi: 10.1364/BOE.8.005139. URL http://www.osapublishing.org/boe/abstract.cfm?URI=boe-8-11-5139.

[19] J. F. de Boer, B. Cense, B. H.Park, M. C. Pierce, G. J. Tearney, and B. E. Bouma. Improved signal-to-noise ratio in spectral-domain compared with time-domain optical coherence tomography. *Opt. Lett.*, 28 (21):2067–2069, Nov 2003. doi: 10.1364/OL.28.002067. URL http://ol.osa.org/abstract.cfm?URI=ol-28-21-2067.

Chapter 5

Optimization of SC source design for noise reduction in UHR-OCT

5.1 Introduction

Nowadays, Supercontinuum (SC) are more than interesting laboratory laser systems. Commercially available turn-key systems exist, customized on: (i) low noise, (ii) enhanced optical density within a given wavelength region or (iii) overall spectral flatness [1, 2]. With an ultra-broad spectrum covering often more than what a spectrometer can detect, together with a high-power density and good beam quality, SC sources are ideal for UHR-OCT in the visible or near infra-Red region. This is despite the fact that initially, the relatively large intensity fluctuations have led to too much noise in the OCT system. The large intensity noise from SC source has limited the usefulness of the SC source in OCT applications. However, in the last couple of years, a resurgence of interest in the SC sources for OCT applications is recorded. Low noise SC sources have been applied successfully to produce ocular images [3], dermal images [4] and internal organ images [5]. This has been possible through important progresses and understanding of noise sources in the SC generation mechanism.

In this chapter, an analysis of noise from SC sources is performed using conventional SD-OCT hardware. First, the method used is described by showing that a shot noise limited detection regime is achievable, when using a SC source for UHR-OCT in the 1300 nm range. This is done by carefully adjusting the signal in the reference path of the interferometer. Then, SC parameters are varied, such as the peak power at the Highly Non-Linear

Fibre (HNLF) and the pump laser repetition rate. Doing so, it is shown how a SC source can be optimized for reducing its noise impact into the OCT system.

5.2 Summary of Noise in UHR-OCT

A complete description of noise and related issues for OCT applications is provided in section 2.4. However, in order to facilitate the understanding of this chapter, a brief summary is presented below.

Noise in OCT can be separated into 4 main contributions [6]. The first one is the electronic noise arising from the digitization of the analogue signal measured by the spectrometer. The second type of noise is the dark noise, which is due to the generation of electrons through random thermal fluctuations within the camera quantum well. Later in this chapter, these two contributions will be assembled into one and denoted detector noise. The third type of noise is the so-called shot noise, arising in the system because of the random arrival of photons into the detector. Finally, the last contribution is the Relative Intensity Noise (RIN), which is attributed to the intensity fluctuations of the optical source in time. Other source of intensity fluctuations can cause similar effect than RIN in the system. Variations of parameters such as light coupling from free space to fibre, polarization of the light, mechanical stability of the system lead to variation of the light intensity detected by the OCT detector. However, it is assumed here that such variations are negligible.

An interesting point to remember when discussing sources of noise in SD-OCT is that their evolution is dependent on the optical intensity. Table 5.1, based on [6], describes the evolution of the different types of noise with the optical power. A and A' are two constants including several parameters such as the detector quantum efficiency, the exposure time, the central frequency of the source and other parameters. A complete description of the parameters involved is provided in section 2.4.1. P_0 is the optical power at the input of the interferometer, N is the number of pixels of the detector, R_s and R_r are the power reflectivities of the object placed in the sample path and reference path of the interferometer. γ_s and γ_r are the fractions of

power in the sample path and reference path of the interferometer respectively and finally Δ_{eff} is the effective bandwidth of the detection unit. The first contribution, the detector noise is not linked to the optical power. This is expected as it is attributed to the thermal fluctuations and digitization of the analogue signal. On the other hand, shot noise and RIN vary with the optical power, linearly for the shot noise and with the square of the optical power for the RIN. The different evolution with the optical power are at the centre in what follows.

TABLE 5.1: Dependence of the different noise contributions to the optical power.

Noise Type	Theoretical expression	Link to the optical power
$\sigma^2_{detector}$	$\sigma^2_{electronics} + \sigma^2_{dark}$	$\neq f(P_0)$
$\sigma^2_{shotnoise}$	$A \times P_0 \times (\gamma_s R_s + \gamma_r R_r) \setminus N$	$\propto P_0$
σ^2_{RIN}	$A' \times P_0^2 \times (\gamma_s R_s + \gamma_r R_r)^2 \times N \setminus (N^2 \Delta_{eff})$	$\propto P_0^2$

5.3 Shot noise detection using a SC source in the 1300 nm range

The method used for noise analysis consists first in evaluating the existence of a regime where the shot noise dominates over the other sources of noise. Then, the second part of the analysis is to characterize the portion of the camera dynamic range over which such regime exists. An ideal OCT system should operate within a regime dominated by shot noise [7], as this would correspond to a maximized Signal to Noise Ratio (SNR). A similar method was used to investigate an optimal working regime for any OCT system [7, 8]. However, those reports assumed a noise independent on the wavelength. Conventional optical sources such as Super-Luminescent Diodes (SLDs) present RIN properties that are independent on wavelength. This is not the case for the SC sources. Supercontinuum sources offer such a broad spectrum that different non-linear effects are responsible for the intensity fluctuations. For example, in the 1300 nm wavelength range ,used

for the OCT experiments presented in this chapter, three effects are responsible for the SC broadening and therefore for the amplitude fluctuations [9]. Close to the pump wavelength, around 1060 nm, the amplitude fluctuations are principally caused by the pump laser amplitude fluctuations. Then, around 1100 nm, the Modulation instability (MI) dominates. Modulation instability is an amplification of quantum noise symmetrically around the pump wavelength. Finally, towards longer wavelengths, the broadening is due to solitons red-shifting by Stimulated Raman Scattering (SRS) and solitons chaotic interactions. A description of these non-linear effects is presented in section 3.4. To overcome the wavelength dependency of the noise, the analysis is performed in the z-domain (depth domain) instead of the k-domain, which means that the analysis is performed after Fourier transform of the OCT signals.

The noise characterization consists in evaluating the standard deviation measured within the noise floor of a series of axial profiles. Figure 5.1 is a representation of the principle of the noise measurement. The first step is the Fourier transform of a full frame, containing 500 readouts from the camera, that determines a given signal level. This leads to a frame of axial profiles as shown in Figure 5.1(b). Then, the standard deviation is measured along the position in the frame for a set of pixels within the noise floor of the axial profiles. This leads to a vector of standard deviation values, whose coordinates are σ_1, σ_2, $\sigma_3 \ldots$ σ_N. Finally, the total noise measured is an average of those standard deviation values.

The spectral shape of the SC sources used in this chapter can be described as the upper part of a Gaussian curve centred within the spectrometer pixel line. Then, all along this chapter, the maximum of this Gaussian like curve, situated around pixel 1024 on the array detector, will be used as the level indicator of signal on the camera as described by Figure 5.1(a). For example, a maximum reference path signal of 3000 counts means that the signal contained in the reference path of the interferometer has its maximum (located around pixel 1024) at a value of 3000 counts. Also, in this chapter, only signal in the reference path of the interferometer are considered. Indeed, it is assumed that the signal in the reference path of the interferometer is much stronger than the signal in the sample path (when

considering imaging conditions). This is a correct assumption as when considering imaging conditions, the power reflectivity of the sample is smaller by several order of magnitude compared to the power reflectivity of the reference mirror. Therefore, any optical noise in the system is mainly due to the power fluctuations in the reference path of the interferometer.

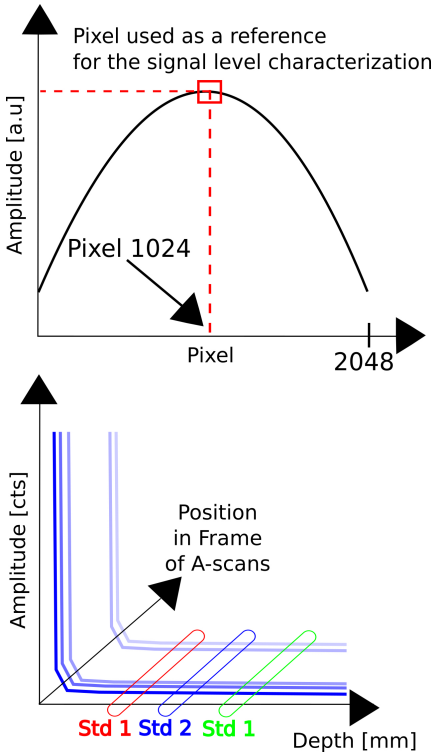

FIGURE 5.1: Conceptual sketch for noise measurements methodology: (a) Definition of reference path signal definition, (b) Definition of region of interest within a frame of A-scans for calculation σ_{Total}.

Figure 5.2 shows the evolution of the total noise measured within a frame of axial profiles while increasing the signal in the reference path of the interferometer by steps of few hundreds of counts. Each point corresponds to a given signal level on the camera. Both axis have been converted to dB scale for ease of identification of regime. As stated above, the different sources of noise evolve differently with the optical power, mainly linearly for the shot noise and with the square of the power for the RIN. If considered in dB scale, a linear evolution in linear scale, will be represented linearly with a slope of 0.5. Similarly, if considered in dB scale, a squared

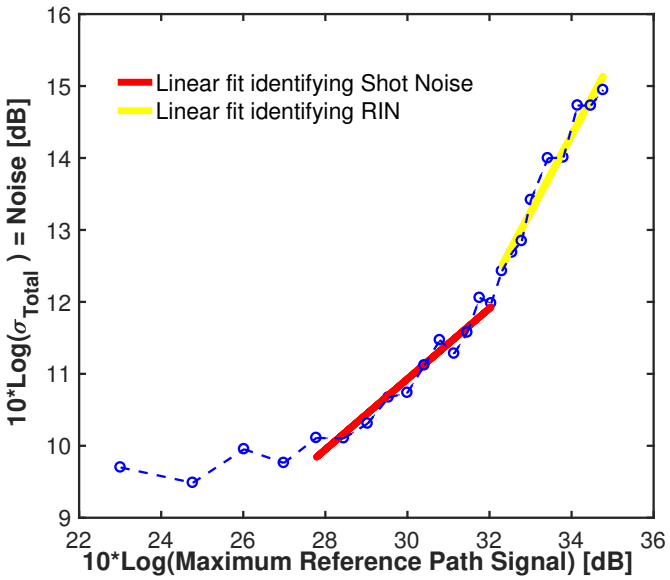

FIGURE 5.2: Representation of the total standard deviation versus the maximum of the reference path signal. Red fit identifies the shot noise dominated regime (slope = 0.5) and the yellow fit identifies the RIN dominated regime (slope = 1.0).

evolution will be represented linearly with a slope of 1. Two linear fits can be identified in Figure 5.2, the red fit located in the middle of the dynamic range and the yellow fit located at the end of the dynamic range. Equation 5.1 and Equation 5.2 are the equations describing the two linear fits as

$$Red\ linear\ fit : y_1 = 0.51 \times x - 4.35, \tag{5.1}$$

and

$$Yellow\ linear\ fit : y_2 = 1.00 \times x - 9.17, \tag{5.2}$$

Those two linear fits are obtained by an iterative procedure where, for each case, the fit with the closest slopes compare to 0.5 and 1 are selected respectively. The red fit, with a slope of 0.51 shows a goodness (R-square) of fit of 0.94 while the yellow fit with a slope of 1.0 shows a goodness (R-square) of fit of 0.93. High values of the goodness of fits clearly confirm that different regimes exist when the signal level on the camera varies. The last area on the dynamic range, located at the beginning of the x-axis, seems almost flat. This indicates that the detector noise is dominating the total

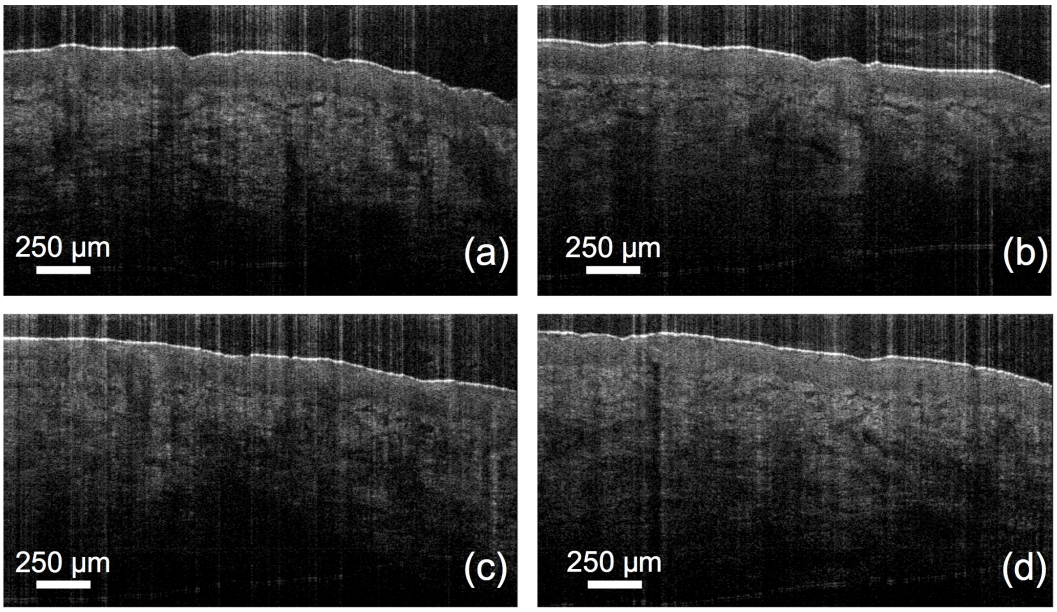

FIGURE 5.3: Example of B-scans measured from the forearm skin of a healthy volunteer (power on sample of 4 mW). (a - b - c - d) B-scans measured with a maximum of the reference arm signal (signal level on the camera) of 500, 1000, 2000 and 3000 respectively.

noise.

In order to demonstrate the impact of the concept of noise regime when varying the signal on the reference path of the interferometer, a B-scans comparison together with a contrast analysis is shown in Figure 5.3 and Table 5.2. Figure 5.3 represents a set of B-scans acquired from the fore-arm of a healthy volunteer using 4 mW of optical power on the sample and an exposure time of 20 µs. Within the set of images of Figure 5.3, the signal on the reference path of the interferometer is set to 500 counts (a), 1000 counts (b), 2000 counts (c) and finally 3000 counts (d). The signal in the reference path of the interferometer is controlled using a variable neutral density filter which does not alter the spectral shape of the source. All B-scans show similar structural information. Different layers can be identified, such as the stratum corneum and the epidermis. In case of high values of the reference path signal, cases (c-d) of Figure 5.3, the backgrounds of the images seem whiter, leading to a reduction of the visual contrast. Table 5.2 summaries the calculated Michelson C_M contrast from each B-scan. The Michelson contrast

TABLE 5.2: Michelson contrast measured within the B-scans of skin in Figure 5.3 when varying the signal in the reference arm of the interferometer (Exposure time 20 µs – Power on sample arm = 4 mW - Source: SuperK Extreme EXR9-OCT Repetition Rate of 320 MHz.

$S_{reference\ arm}\ [cts]$	C_M
500	0.36
1000	0.37
2000	0.33
3000	0.32

is calculated as

$$C_M = \frac{I_{max} - I_{min}}{I_{max} + I_{min}}, \tag{5.3}$$

where I is the intensity signal of each pixel within the image, and where I_{max} and I_{min} are calculated as an average of the 50 first highest and respectively 50 first lowest intensity pixels within the image. This modification of the original Michelson contrast is required for calculating a realistic contrast value. Indeed, if the real minimum and maximum of the image are considered, a contrast of 0.99 is obtained which is unrealistic. All calculated contrast values are comprised between 0.37 ($S_{ReferenceArm} = 1000$ counts) and 0.32 ($S_{ReferenceArm} = 3000$ counts), which show that setting the signal in the reference path of the interferometer too high on the dynamic range can impair the image quality. Setting the signal too high, around 3000 counts, clearly places the system into the RIN dominated regime (see Figure 5.2) and then corresponds to the lowest contrast value of 0.32. To the contrary, placing the signal too low can also lead to a non-ideal image quality. In the present case, a value of 500 counts is close to the transition between detector noise dominated regime and shot noise dominated regime. Considering only the noise plot of Figure 5.2 can lead to an uncertainty regarding the noise regime, therefore a contrast analysis helps to select the best working point for the system. In this study, a reference path signal of 500 counts offers a contrast of 0.36 while a signal of 1000 counts offers a slightly better contrast of 0.37. Ideally, an OCT system should operate far from the transition point between noise regime in order to ensure optimal operation.

So far in this chapter, the existence of noise dominating regimes (Shot

noise and RIN) have been demonstrated for an OCT system driven by a SC source used in the 1300 nm. Knowing that such regime exists can be used as a noise measurement tool where the metric is the extension of each regime over the dynamic range of the camera. The larger the extension of the shot noise dominated regime the lower the RIN arising from the source is affecting the system performance. Therefore, under similar operating conditions one can compare light sources for OCT using this principle. An interesting way of using this tool is to study the impact of the SC source parameters on the overall noise evolution into the OCT system. Then, the noise analysis can be used for comparing SC sources. Using it to compare SC sources is interesting as it relies on the UHR-OCT hardware only, i.e. on an interferometer and a spectrometer. Usually, noise analysis of SC sources relies on fast electronics and complex hardware [10, 11] in order to track the pulse to pulse fluctuations within different wavelength bands. The method presented is also interesting compared to traditional methods for SC noise characterization as it is a single shot interrogation of the noise impact into the OCT. The more traditional methods are characterizing the source noise itself without linking it to the impact in the OCT system. In the next two parts of this chapter, two parameters of SC source design will be optimized using the just presented method.

5.4 Optimizing the SC source pump peak power

As described in section 3.1, a SC source is made of two main elements; the pump laser and the Highly Non-Linear Fibre (HNLF). The second of those two, the HNLF is a passive component with specific parameters of pitches and holes dimension controlling the dispersion profile of the fibre [12, 13] (see section 3.2). The fibre properties determine the spectral broadening of the SC through the launched peak power from the pump laser before reaching the power damage threshold [14]. Off course, the material also influences the extension of a given SC as material losses have to be considered. It has been shown that a peak power as high as possible is required when generating the SC, not only for extending the broadening but also to reduce the intensity fluctuations [15]. This is due to the fact that the

spectral edges of a SC are noisier than the central part, nearby the pump wavelength. To understand this phenomenon it is necessary to remember the SC generation steps described in section 3.4.

Initially, the high peak power pulse from the pump laser is split into solitons by MI in the fibre. Then, the remaining broadening occurs through the red-shifting of solitons by Stimulated Raman Scattering (SRS) and the chaotic interactions solitons. From this initial number of solitons, it is easy to understand that the higher initial number of solitons, the larger the number of interactions and therefore the further away the red-edge of the SC in the NIR. The spectral edge of the SC source in the IR side is then noisier in comparison to the central part of the spectrum as it is generated from rare interactions of solitons, at those long wavelengths, where the number of solitons becomes low. It is then necessary to get the SC red-edge far away for the wavelength range of use in the OCT system.

Figure 5.4 (a) describes the spectrum emitted by a SC source from 1200 nm to 2200 nm while the pump peak power is increased, from 10 % to 100 % of the available peak power. This characterization consider only the red-side of the SC as it is obtained using an Optical Spectrum Analyser sensitive from 1200 nm to 2600 nm. The SC red-edge clearly shifts towards longer wavelengths while increasing the peak power. Figure 5.4 (b) shows the position of the red-edge, measured at a level of -75 dB, for peak power varying from 10 % to 100 % (as the source used offer a power control scaled in percentage). Table 5.3 is an indication of the conversion rate between percentage and optical power. The red-edge varies from 1550 nm at 10 % peak power to 1950 nm at 100 % peak power. The position of the red edge does not evolve linearly with the peak power because of the silica material losses increase non-linearly toward long wavelengths. The longer wavelength achieved for 100 % peak power is around 1950 nm. This is because the peak power is not large enough, however further increase of peak power would lead to very high average power and possible damage of the fibre.

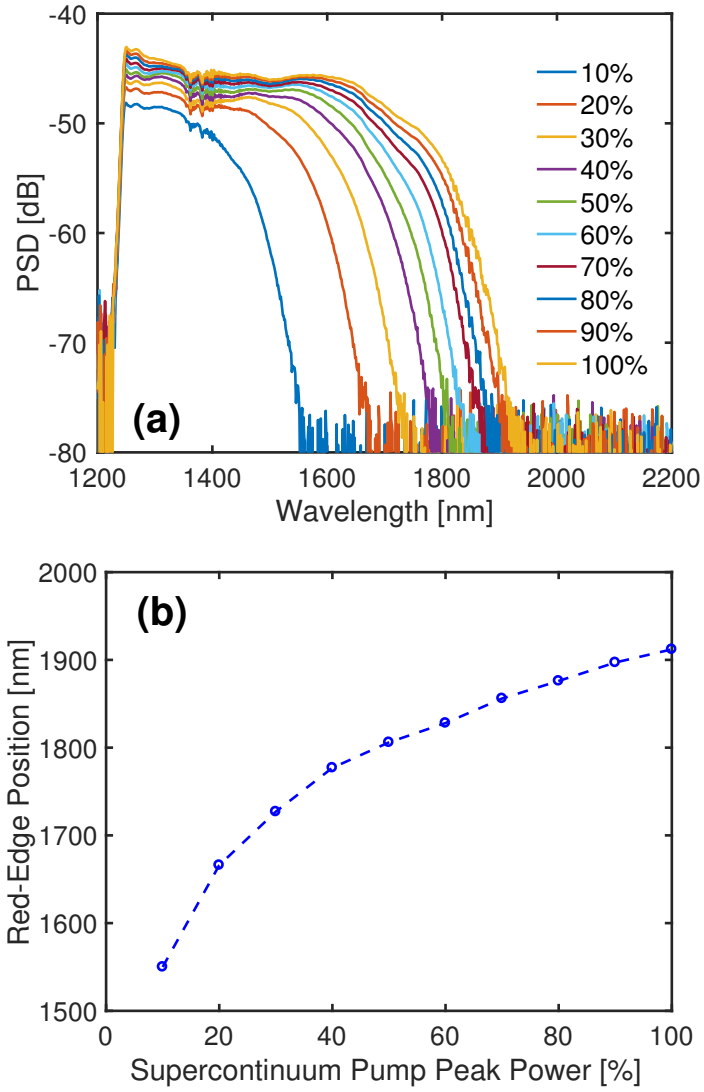

FIGURE 5.4: (a) Measured Infra-red side of a SC source (Type SuperK Extreme EXR9 – R= 320 MHz) using an OSA and an integrating sphere (A filter has been used to filter the wavelengths below 1200 nm). (b) Evolution of the red-edge position (measured at -75 dB) versus the peak power of the pump (measured in percentages).

TABLE 5.3: Percentage to estimated values in kW conversion of the pump peak power.

Values from SC source interface [%]	Estimated Peak Power [kW]
20	0.3
40	0.6
60	0.9
80	1.2
100	1.5

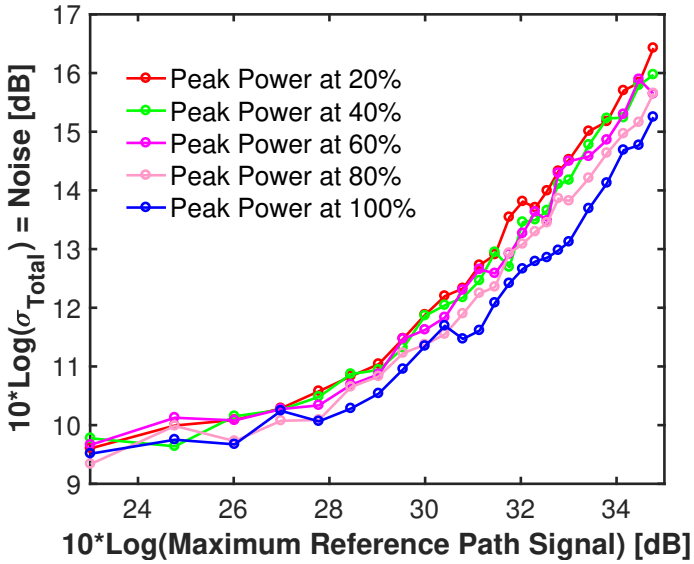

FIGURE 5.5: Total Standard Deviation versus the maximum reference arm signal for several pump peak powers.

The previously introduced method for noise analysis (see section 5.2) is applied to the pump peak power case study. The parameter which was varied was the pump peak power presented in percentages with the estimated correspondence of Table 5.3. Figure 5.5 is the total noise (in dB) versus the maximum of the signal contained in the reference path of the interferometer. As previously, the exact definition of the horizontal axis is the maximum value (in dB) of the reference path signal measured in the central part of the pixel line. From Figure 5.5 only, it is not obvious to see an improvement in terms of noise. Though, it seems that a trend can be observed where the noise decreases while increasing the peak power. The blue and pink curve, representing respectively 100 % and 80 %, are clearly below the red curve

which is the 20 % case. However, when considering the fit extractions used to identify the dynamic range area where the shot noise dominates over the other sources of noise, a clear trend can be seen. Figure 5.6 (a) is the plot where only the fits of the shot noise dominated regime are displayed for each peak power case. It is noticeable that the extent, in terms of camera dynamic range, is increasing when the peak power increases. Starting all from around 27 dB (500 counts - in linear scale). It is expected that all shot noise fits start at the same location on the dynamic range as it is the transition from detector noise dominated regime to shot noise dominated regime. However, all the shot noise fits terminate at a different positions, locating the transition between shot noise and RIN dominated regime differently. In the case of 20 % peak power, the transition is located at 30 dB (1000 counts), while it is moving up to 31.7 dB (1500 counts) in the case of the 100 % peak power. There is a difference of around 500 counts available for shot noise limited operation if considering carefully the signal on the reference path of the interferometer and the peak power at the HNLF. This represents a higher SNR achievable in the high peak power configuration. Figure 5.6 (b) is the complementary plot of Figure 5.6 (a), where only the RIN fits are plot. Similar conclusions can be done from this plot, if the peak power increases then the RIN dominated regime extension is limited. It is also interesting to notice the difference in terms of the amplitude of the total noise measured for the different peak powers. The method is measuring the total noise and then inform about which source of noise is dominating over a certain area of dynamic range. However, while shot noise is dominating there is still a certain contribution of RIN, which means that a higher RIN case, such as the 20 % peak power will show a slightly higher total noise compared to the 100 % peak power. In the present study, a difference of 1 dB can be observed between the two extreme configurations (peak power at 20 % and 100 %).

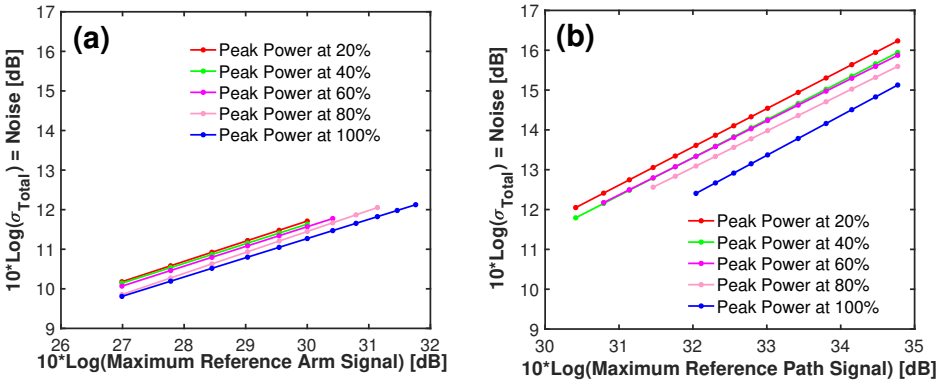

FIGURE 5.6: Extracted linear fits describing, for several pump peak powers, the part of dynamic range where the system is under the shot noise dominated regime (a) or the RIN dominated regime (b).

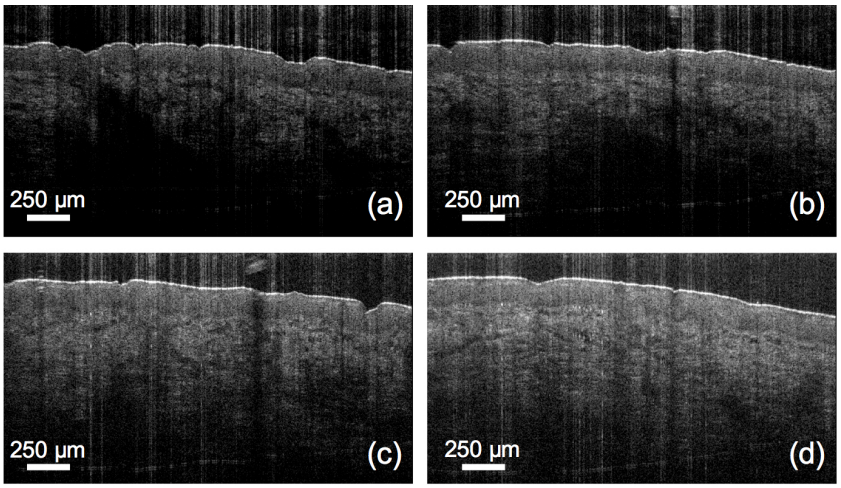

FIGURE 5.7: Example of B-scans measured from the forearm skin of a healthy volunteer (power on skin of 4 mW). (a – b – c – d) B-scans measured with a pump peak power of 20 %, 40 %, 80 % and 100 % respectively.

The influence of the peak power at the HNLF on the RIN level into the OCT system can be evaluated through a noise analysis method but also by direct B-scans comparison. Figure 5.7 shows a set of B-scans measured from the fore-arm skin of a healthy volunteer. A power of 4 mW is used in each case. The total output power of the SC source is higher than 100 mW even for the 20 % peak power case, therefore a neutral density filter is used to control the optical power injected into the OCT system. Four peak powers are considered here, 20 % (a) - 40 % (b) - 80 % (c) and 100 % (d). The signal level in the reference path of the interferometer is set to deliver a signal of around 1400 counts. This places the system in a regime where the 20 % and 40 % cases should be RIN dominated while the 80 % and 100 % cases should be shot noise dominated. The four B-scans display similar structural information without obvious differences neither structural nor visual . A contrast analysis is required to conclude on an effective noise improvement. Table 5.4 is a summary of the measured Michelson contrast (C_M) within the set of images. All four contrasts are similar, varying by less than 5 % which prevent to conclude on the real impact of such a small noise improvement. Nevertheless, it is important to consider that the Silica material loss increases around 2.4 µm, and the current SC source red-edge is at maximum at a position of 1.95 µm. Then, for a Silica HNLF, it is still possible to increase the pump peak power to push the red-edge to longer wavelengths. Then, the difference in the total noise increases in comparison to its current value of 1 dB (total noise difference between 20 % and 100 % cases). In this case, the influence of the pump peak power can be of importance . Also, some techniques in OCT literature rely on the direct image SNR, for example Speckle Variance OCT [16]. For such application, it is crucial to operate within shot noise dominated regime in order not to disturb the variance measurements due to large RIN.

TABLE 5.4: Michelson contrast measured within the B-scans of skin in Figure 5.7, when varying the pump peak power (exposure time 20 µm – Power on sample arm = 4 mW - Source: SuperK Extreme EXR9-OCT 320 MHz.

Pump Peak Power [%]	C_M
20	0.38
40	0.39
80	0.4
100	0.4

5.5 Optimization of SC source repetition rate

The second optimization proposed in this study is achieved via the investigation of the pump laser repetition rate importance for noise reduction in OCT system. Commonly, the high peak power required for SC generation is obtained through Mode-Locked (ML) lasers, which can provide from few kWs to hundreds of kW peak power at repetition rates of hundreds of MHz to GHz [17]. Other types of lasers can be used as pumps for SC generation, such as Q-Switched lasers or continuous wave lasers. When designing a pulsed laser, it is important to keep in mind the need of a balance between peak power and average power. Optical components such as optical fibres have a limit on acceptable average power before reaching a non-reversible damaged threshold [14]. Therefore, if a very high peak power is required, a limit has to be placed on the repetition rate in order to operate below the damage threshold in average power. In the opposite, a peak power limit needs to be set if very high repetition rate is considered. Regarding SC generation, this balance is crucial as the peak power it related to the spectral broadening of the SC source. The higher the peak power, the further in the infra-red the SC spectrum can be extended. This last point imposes a limit on the repetition rate of a SC source. Currently, commercially available SC sources use peak power within few kWs and repetition rates in the range of 20 MHz to 320 MHz [18, 19]. Then, the present study proposes to compare 4 SC sources, with repetition rates of 20, 40, 80 and 320 MHz, in terms of noise into an OCT system operating in the 1300 nm range.

Figure 5.8 represents the total noise measured by the spectrometer when varying the signal on the reference path of the interferometer for the 4 SC

sources considered in this study. This measurement is similar to that used in sections 5.2 and 5.3. Here, comparatively to the previous analysis of peak power influence, a very clear trend is shown. The higher the repetition rate the lower the total noise. A difference of up to 5 dB is obtained at large signals in the reference path of the interferometer (2500 to 3000 counts). By using the linear fit procedure described earlier in this chapter, Figure 5.9 (a) displays the extension of the shot noise dominated regime for each SC source. As a first comment, there is no shot noise dominated regime in the case of a 20 MHz SC source, which means that the RIN is the always the dominant noise except for the detector noise regime (located at low signal level around 200 – 300 counts). This is the worst-case scenario for an OCT system. Then, when increasing the repetition rate, the total noise drops significantly and the shot noise limited regime takes over. Though, it is very limited at 40 MHz repetition rate, with an extension of only 2 dB (200 counts). Only the 80 MHz and 320 MHz repetition rates SC sources offer a reasonable shot noise limited regime that starts from around 25 dB (400 counts) up to 30 dB (1000 counts) and 32 dB (1600 counts) respectively. This noise improvement obtained by increasing the repetition rate comes from the available number of pulses detected per readout of the spectrometer's camera (see Table 5.5). When doubling or quadrupling the repetition rate, the number of pulses which are detected during a camera readout is also multiplied. This increase of number of pulse from 400 (20 MHz) to 6400 (320 MHz) leads to an averaging of the intensity fluctuation from the SC source and therefore a drop of the RIN contribution in the OCT system by around 3 to 4 dB on the total noise measured.

TABLE 5.5: Number of pulses per camera readout, considering an exposure time of 20 µs, for 4 different SC source repetition rates.

Repetition Rate $[MHz]$	*Pulses per camera readout*
20	400
40	800
80	1600
320	6400

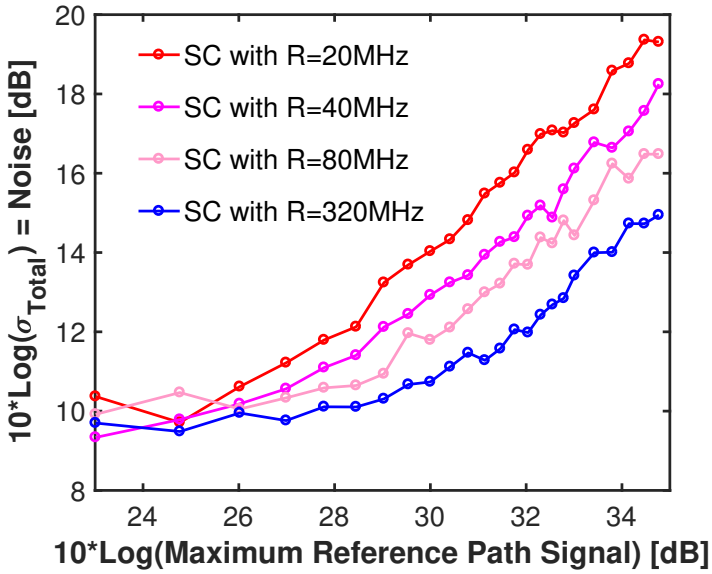

FIGURE 5.8: Total standard deviation versus the maximum of the reference path signal for different pump repetition rates.

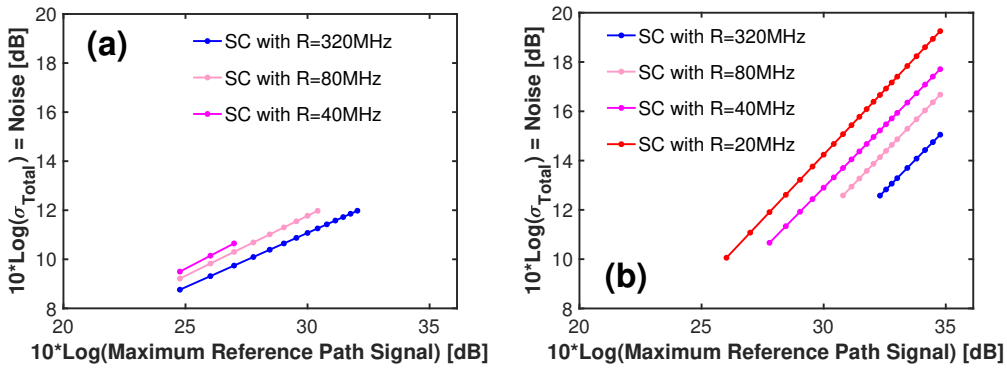

FIGURE 5.9: Extracted linear fits describing, for several pump peak powers, the part of dynamic range where the system is under the shot noise dominated regime (a) or the RIN dominated regime (b).

To complete this noise analysis, similarly to the previous study, a comparison of 4 B-scans is presented in Figure 5.10. Each B-scan is acquired with a different SC source from the set previously mentioned. Each B-scan is acquired from the forearm of a healthy volunteer using 4 mW power on skin and using an exposure time of 20 µs. The comparison of the 4 images highlight the importance of the repetition rate of the SC source in reducing the

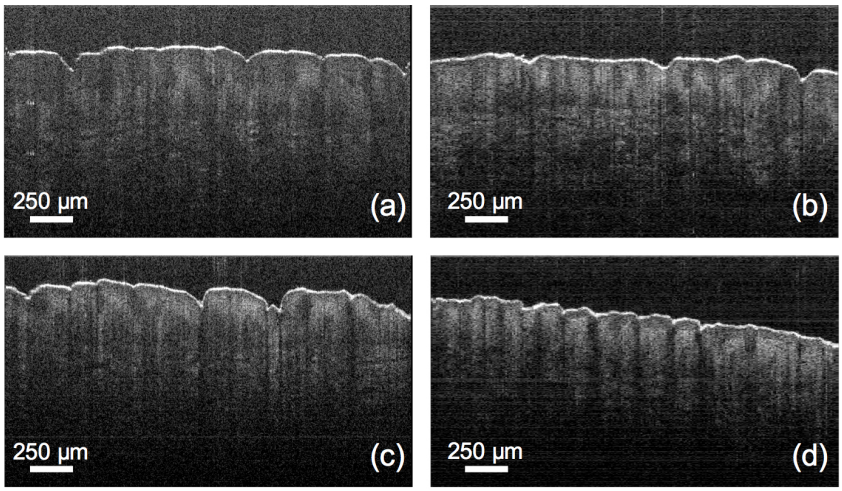

FIGURE 5.10: Example of B-scans measured from the forearm skin of a healthy volunteer (power on skin of 4 mW). (a - b - c -d) B-scans measured with a pump repetition rate of 20 MHz, 40 MHz, 80 MHz and 320 MHz respectively using an exposure time of 20 µs.

RIN impact into the OCT system. When all images are displayed using the same encoding of grey level, a direct difference in the background darkness can be seen. The 20 MHz based image shows a much whiter background compared to the images obtained at other repetition rates. In that case, the background is almost as white as structure within the sample. At this repetition rate, the noise is so important that it affects the structural information of the OCT image. In opposition, the 320 MHz presents a quasi-black background with this grey level encoding, leading to a clear contrast between the sample and the background. Table 5.6 shows the calculated Michelson contrast for the 4 B-scans of Figure 5.10. The same precaution as in section 5.2 is taken regarding the minimum and maximum number calculations. Again, differences between high and low repetition rates are observed for the contrast values, with an improvement of 0.09 point for the contrast between the extreme cases of 20 MHz and 320 MHz, corresponding to almost 20 % (from 0.49 to 0.58). The two intermediate measurements (40 MHz and 80 MHz) are at an equal contrast of 0.54. This equality can be attributed to the time separation of the two images. Indeed, it is complicated to set the system in exact same configuration except for the repetition rate. Small changes in optical power, angle of incidence on the sample or sample itself might explain

the non-varying contrast issue. This type of uncertainty confirms that the noise measurement method is complementary to a contrast analysis.

TABLE 5.6: Michelson contrast measured within the B-scans of skin in 5.10 when varying the pump repetition rate (exposure time 20 µs – Power on sample arm = 4 mW.

$Repetition\ Rate\ [MHz]$	C_M
20	0.49
40	0.54
80	0.54
320	0.58

5.6 Comparison of Noise Analysis method

Commonly, Sensitivity is the metric used to analyse OCT system quality when considering optical noise. Sensitivity represents the ability for a system to measure weak signal which are generally coming from deep positions into the sample. A comprehensive definition of sensitivity is provided in section 2.5.1. A relatively simple method to measure the sensitivity of a system consists in replacing the sample to image by a Neutral Density Filter (NDF) together with a mirror and measure the SNR obtained when the injection is optimized. The sensitivity is then calculated as the summation of the SNR and the optical density of the neutral density filter. This metric has been used to compare optical sources used in OCT, however an important drawback is that it relies on a non fixed parameter. Indeed, the injection into the interferometer of the back-reflected light from the sample can vary over time. This parameter makes the comparison sometimes inaccurate as the system status varies from measurement to measurement.

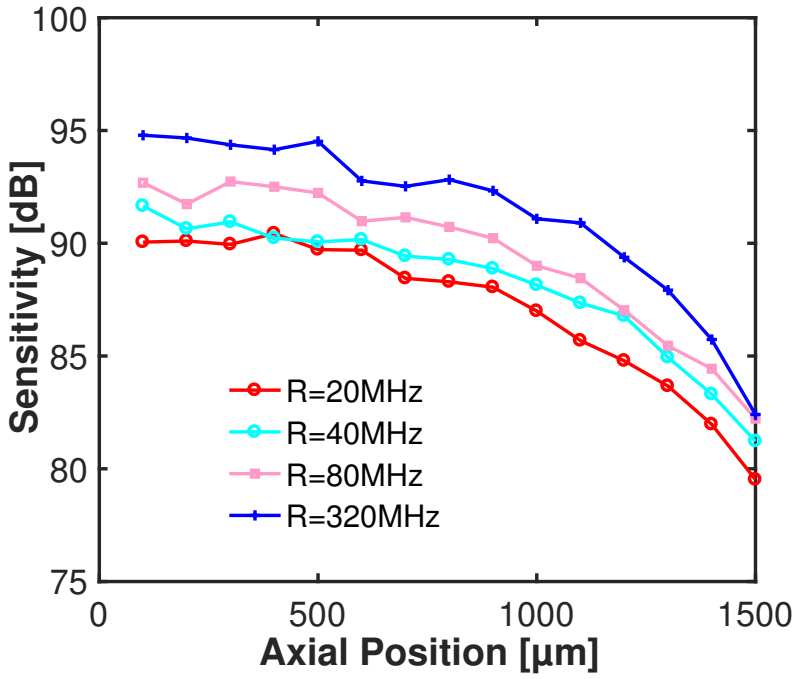

FIGURE 5.11: Sensitivity measured for 4 SC sources used in the repetition rate study (P_{sample} = 4.5mW - Exposure Time 20 µs).

Interestingly, the proposed noise measurement method concludes on similar differences in noise compared to a sensitivity analysis with each SC source. However, it is not involving any optimization of injection making it reliable, repeatable and much faster. Figure 5.11 is the sensitivity versus axial positions obtained for the 4 SC sources used in the repetition rate case study with an optical power of 4.5 mW on the sample. An NDF with and attenuation of OD = 2 is used in a Michelson interferometer, corresponding to a total attenuation of 40 dB. Sensitivity measured for all 4 SC sources are around 90 dB or higher. In order to measure the sensitivities , the signal in the reference path of the interferometer have been placed around 70 % of the dynamic range (3000 counts). The maximal difference observed between the 20 MHz and the 320 MHz is 5 dB, which is similar to the noise difference presented in Figure 5.8.

5.7 Discussion

A first important point is that the noise method proposed in this chapter is qualitative. It relies on measurements of the total noise recorded by the spectrometer and then on identifying intervals of dynamic range where a single source of noise dominates, either shot noise or RIN. When SC sources are compared using this method, it is important to consider that all noise curves are acquired under given conditions. So, it might happen that the system configurations were not identical on each measurement step. This has been observed in the previous section where the quantitative evaluation of the Michelson contrast deviates from the qualitative shot noise regime extension. Therefore, the noise measurement is useful in observing the trend in the noise variation and not for quantitative noise evaluation. However, the important aspect when dealing with noise in OCT is to be able to identify that the system operates under shot noise dominated regime while at the same time operating with large power in the reference path of the interferometer. This is important as detector noise is dominating at lower reference path power.

Several times in this chapter, fitting procedures have led to conclusions in terms of the noise regime (either shot noise or RIN dominated). Though, it seems crucial to operate under shot noise dominated regime for SNR optimization. It is also good to observe that the difference between the two regimes (shot noise and RIN) lies within small total noise difference. Relative Intensity Noise and shot noise regimes can be considered similar condition for imaging. Indeed, by extrapolating the fit of the shot noise obtained for higher dynamic range value in Figure 5.9 (a) for example, for the case of 320 MHz SC source, the total noise will reach a value of 13 to 14 dB which is only 1 to 2 dB lower compared to the RIN regime. Then, an OCT system will see its SNR value increased by few dBs only if operating in shot noise regime instead of RIN dominated regime. Such a small difference might not impact the OCT image. Along the same interpretation, no significant difference can be seen by simple visual inspection of images acquired at different peak powers at the HNLF (see section 5.3) even though the measured total noise indicates that they should be different. This few dBs higher noise

might be tolerable for applications where other optical sources cannot offer similar broad spectrum or high optical power.

Images and contrast analysis have been used in this chapter and sometimes contradict the total noise measurement by showing unexpected contrast variations. Such a behaviour is not abnormal, measuring the contrast can be an inaccurate modality for direct comparison of images. The contrast varies with the noise, which is the parameter we investigate, but also with the signal returned by the sample. Therefore, changes on the sample, for example changes in incident power or angle of incidence might affect the signal backscattered and then the contrast calculated from the image. Still, observing in parallel the total noise measurement and the contrast provide information on how a noise improvement really contributes to the overall image quality.

The results shown in this chapter help the design of SC sources dedicated to OCT applications. By optimizing the peak power at the HNLF together with the pump repetition rate, complete shot noise limited detection regime becomes possible. Such a source will be ideally suited for UHR-OCT as it can offer the SC broadband advantage in conjunction with stability similar to that of an SLD or a titanium sapphire lasers [7, 20]. To design this ideal source, it is important to understand the connection between repetition rate and peak power. Currently, the peak power used for the pump leaves some room for improvement as the red-edge of the SC source is located 500 nm before the material losses of silica which are problematic around 2.4 µm. Increasing the peak power might move the red-edge further away from the OCT wavelength range of 1300 nm. This modification of peak power corresponds to an increase of the number of solitons created at the ignition of the SC. This can reduce the noise into the OCT system but it requires to consider carefully the average power into the HNLF in order to avoid fibre damages. On the other hand, an increase of the repetition rate is also possible but with the same consideration of average power maximum. Then, a possible option could be to play with the balance repetition rate and peak power in a non-obvious way. So far, only increasing the peak power have been proposed. But, from Figure 5.5 and Figure 5.8, it is noticeable that the

pump peak power and repetition rate do not provide the same noise improvement. Increasing the repetition rate seems to be more advantageous compared to increasing the peak power. Then, a solution where the peak power is reduced together with an increase of the repetition rate seems interesting. Indeed, increasing the repetition rate while decreasing the peak power can lead to a large noise reduction and also to a decrease in the peak power, avoiding fibre damages. Reducing the average power is not a problem for OCT, as the current average power is much higher than what is required for OCT.

5.8 Conclusion

In this chapter a method for noise analysis in SD-OCT is proposed. This method relies on identifying the part of the camera dynamic range over which the shot noise or the RIN is dominating the total noise.

Then, the methods is used for comparing SC sources and observe the impact of the pump laser peak power and repetition rate on the RIN contribution. It is shown that the higher the peak power, the larger the extension of the shot noise limited regime and therefore the lower the impact of the noise arising from the source. Also, the effect of increasing the repetition rate of the pump laser on the noise is demonstrated. High repetition rates correspond to better averaging per readout leading to a decrease of the RIN contribution to the total noise into the OCT system.

Each comparison of SC source parameters using the noise analysis method is supported by images and contrast analysis. The two analysis agree on the optimization parameters most of the time. Though, it seems that the methods based on images and contrast are sometimes less accurate than the noise measurements. This is due to the fact that they can be affected by several parameters including the SC noise but also by the system configuration or the sample conditions.

Such a noise analysis method is interesting as it is based on the SD-OCT hardware only, i.e. a spectrometer as the detection unit. In the case of analysis of SC source noise this is an important advantage. Usually, SC

noise measurement requires fast electronics (fast photo-diodes and fast oscilloscopes), which can be costly.

References

[1] Supercontinuum NKT Photonics A/S (Denmark). http://www.nktphotonics.com/lasers-fibers/product-category/supercontinuum-lasers/, . Accessed: 2017-08-06.

[2] Supercontinuum Leukos (France). http://www.leukos-systems.com/spip.php?rubrique28, . Accessed: 2017-08-06.

[3] J. Yi, S. Chen, V. Backman, and H. F. Zhang. In vivo functional microangiography by visible-light optical coherence tomography. *Biomed. Opt. Express*, 5(10):3603–3612, Oct 2014. doi: 10.1364/BOE.5.003603. URL http://www.osapublishing.org/boe/abstract.cfm?URI=boe-5-10-3603.

[4] W. C. Kuo, Y. M. Kuo, and S. Y. Wen. Quantitative and rapid estimations of human sub-surface skin mass using ultra-high-resolution spectral domain optical coherence tomography. *Journal of Biophotonics*, 9(4):343–350, 2016. ISSN 1864-0648. doi: 10.1002/jbio.201400153. URL http://dx.doi.org/10.1002/jbio.201400153.

[5] K. K. Chu, C. U., T. N. Ford, D. Cui, R. W. Carruth, K. Singh, L. Liu, S. E. Birket, G. M. Solomon, S. M. Rowe, and G. J. Tearney. In vivo imaging of airway cilia and mucus clearance with micro-optical coherence tomography. *Biomed. Opt. Express*, 7(7):2494–2505, Jul 2016. doi: 10.1364/BOE.7.002494. URL http://www.osapublishing.org/boe/abstract.cfm?URI=boe-7-7-2494.

[6] R. Leitgeb, C. K. Hitzenberger, and A. F. Fercher. Performance of fourier domain vs. time domain optical coherence tomography. *Opt. Express*, 11(8):889–894, Apr 2003. doi: 10.1364/OE.11.000889. URL http://www.opticsexpress.org/abstract.cfm?URI=oe-11-8-889.

[7] W. Yuan, J. Mavadia-Shukla, J. Xi, W. Liang, X. Yu, S. Yu, and X. Li. Optimal operational conditions for supercontinuum-based ultrahigh-resolution endoscopic oct imaging. *Opt. Lett.*, 41(2):250–253, Jan 2016. doi: 10.1364/OL.41.000250. URL http://ol.osa.org/abstract.cfm?URI=ol-41-2-250.

[8] X. Yao, Y. Gan, C. C. Marboe, and C. P. Hendon. Myocardial imaging using ultrahigh-resolution spectral domain optical coherence tomography. *Journal of Biomedical Optics*, 21(6):061006, 2016. doi: 10.1117/1.JBO.21.6.061006. URL http://dx.doi.org/10.1117/1.JBO.21.6.061006.

[9] J. M. Dudley, G. Genty, and S. Coen. Supercontinuum generation in photonic crystal fiber. *Rev. Mod. Phys.*, 78:1135–1184, Oct 2006. doi: 10.1103/RevModPhys.78.1135. URL https://link.aps.org/doi/10.1103/RevModPhys.78.1135.

[10] M. Klimczak, G. Soboń, R. Kasztelanic, K. M. Abramski, and R. Buczyński. Direct comparison of shot-to-shot noise performance of all normal dispersion and anomalous dispersion supercontinuum pumped with sub-picosecond pulse fiber-based laser. 6:19284 EP –, 01 2016. URL http://dx.doi.org/10.1038/srep19284.

[11] T. Godin, B. Wetzel, T. Sylvestre, L. Larger, A. Kudlinski, A. Mussot, A. Ben Salem, M. Zghal, G. Genty, F. Dias, and J. M. Dudley. Real time noise and wavelength correlations in octave-spanning supercontinuum generation. *Opt. Express*, 21(15):18452–18460, Jul 2013. doi: 10.1364/OE.21.018452. URL http://www.opticsexpress.org/abstract.cfm?URI=oe-21-15-18452.

[12] P. Russell. Photonic crystal fibers. *Science*, 299(5605):358–362, 2003. ISSN 0036-8075. doi: 10.1126/science.1079280. URL http://science.sciencemag.org/content/299/5605/358.

[13] A. Hartung, A. M. Heidt, and H. Bartelt. Design of all-normal dispersion microstructured optical fibers for pulse-preserving supercontinuum generation. *Opt. Express*, 19(8):7742–7749, Apr 2011. doi:

10.1364/OE.19.007742. URL http://www.opticsexpress.org/abstract.cfm?URI=oe-19-8-7742.

[14] M. Bondu, C. Brooks, C. Jakobsen, K. Oakes, P. M. Moselund, L. Leick, O. Bang, and A. Podoleanu. High energy supercontinuum sources using tapered photonic crystal fibers for multispectral photoacoustic microscopy. *Journal of Biomedical Optics*, 21(6):061005, 2016. doi: 10.1117/1.JBO.21.6.061005. URL http://dx.doi.org/10.1117/1.JBO.21.6.061005.

[15] U. Møller, S. T. Sørensen, C. Jakobsen, J. Johansen, P. M. Moselund, C. L. Thomsen, and O. Bang. Power dependence of supercontinuum noise in uniform and tapered PCFs. *Opt. Express*, 20(3):2851–2857, Jan 2012. doi: 10.1364/OE.20.002851. URL http://www.opticsexpress.org/abstract.cfm?URI=oe-20-3-2851.

[16] N. U. Patarroyo, M. Villiger, and B. E. Bouma. Quantitative technique for robust and noise-tolerant speed measurements based on speckle decorrelation in optical coherence tomography. *Opt. Express*, 22(20):24411–24429, Oct 2014. doi: 10.1364/OE.22.024411. URL http://www.opticsexpress.org/abstract.cfm?URI=oe-22-20-24411.

[17] M. E. Fermann and I. Hartl. Ultrafast fibre lasers. *Nat Photon*, 7(12):1006–1006, 12 2013. URL http://dx.doi.org/10.1038/nphoton.2013.319.

[18] Supercontinuum NKT Photonics, link = http://www.nktphotonics.com/lasers-fibers/product/superk-extreme-supercontinuum-lasers/, note = Accessed: 2017-08-06, .

[19] Supercontinuum thorlabs, link = https://www.thorlabs.com/newgrouppage9.cfm?objectgroup_id=10819, note = Accessed: 2017-08-06, .

[20] W. J. Brown, S. Kim, and A. Wax. Noise characterization of supercontinuum sources for low-coherence interferometry applications. *J.*

Opt. Soc. Am. A, 31(12):2703–2710, Dec 2014. doi: 10.1364/JOSAA.31.002703. URL http://josaa.osa.org/abstract.cfm?URI=josaa-31-12-2703.

Chapter 6

Femtosecond pumped with all normal dispersion fibre SC source for ultra-low noise operation

6.1 Introduction

In the previous chapter of this thesis, it has been shown that current commercially available Supercontinuum (SC) sources are suitable for Ultra-High Resolution Optical Coherence Tomography (UHR-OCT) at 1300 nm, achieving shot noise limited detection under particular conditions. In terms of applications, the use of SC for UHR-OCT has been demonstrated by numerous reports over the last 5 years [1, 2, 3]. However, Relative Intensity Noise (RIN) is still an issue for some highly demanding applications [4], where achieving shot noise limited detection is essential. Indeed, such applications rely on intensity fluctuations and therefore are affected by intensity noise. Due to their ultra-broad spectral bandwidth, SC sources represent an ideal choice for ultra-high axial resolution OCT. Therefore, over the years, important efforts have been made within the SC community to address the issue of high intensity fluctuations of SC sources. Several directions have been investigated, such as tapering the Highly Non-Linear Fibre (HNLF) for increasing the non-linearity of the fibre [5] or pumping in different dispersion regime in order to modify the SC generation mechanism. Also, it has been shown that increasing the source repetition rate of the pump laser might not reduce the RIN of the source itself but could reduce its impact on the OCT system performance[6, 7] . More recently, it

has been proposed to use a completely different SC generation mechanism in order to avoid noise effects such as Modulation Instability and Solitons dynamics [8, 9]. This concept relies on using an ultra short pulse to pump a fibre with a dispersion profile located in the normal dispersion regime ($\beta < 0$). Normal dispersion regime corresponds to a regime where the fibre dispersion is negative regardless of the wavelength. Ideally, such a source can offer an ultra-broad spectrum together with a level of stability comparable to that of Super-Luminescent Diode (SLD) making it the ideal source for UHR-OCT. In this chapter, a SC source based on an All-Normal Dispersion (ANDI) fibre is assembled for application to UHR-OCT in the 1300 nm wavelength range. A noise analysis using the ratio of OCT signal over the noise and quality assessment of images is presented. Then the noise properties of the newly developed source are compared with those of the current state of the art SC sources for biomedical imaging application.

6.2 Supercontinuum generation summary

Chapter 3 of this thesis is entirely dedicated to describe the process of SC generation and the different non-linear effects involved. Below, a short summary of the two SC generation principles used in this chapter is presented.

The first SC generation principle presented here is the most commonly used in fibre based SC source. It relies on pumping a HNLF, a Photonic Crystal Fibre (PCF), with a relatively long high peak power optical pulse whose pulse width can be from a few ps to ns. The PCF is used due to the easy control of the dispersion profile of the fibre. The PCF is designed in such a way that its Zero Dispersion Wavelength is placed nearby the pump laser wavelength. This is done in order to balance the non-linear effects and the dispersive effects. A too high dispersion can indeed stretch the pulse too quickly, leading to a quick drop of optical peak power and therefore less effective non-linear effects. In the present case, the pump is at 1064 nm and the ZDW of the fibre is at around 1040 nm. While considering the red side of the SC, the mechanisms responsible for the broadening are first the modulation instability (which breaks the initial pulse into a train of solitons) and

then a chaotic shift/interaction of solitons. Modulation Instability is an amplification of noise from the side bands around the pump wavelength [9]. Solitons are analytical solutions of the Non-Linear Schroedinger Equation, their physical meaning corresponds to a short pulse which propagates into the fibre seeing the dispersive effects and the non-linear effects compensating themselves [10]. A more extensive description of such effects is given in section 3. Then, these solitons are red shifted through Stimulated Raman Scattering effect and solitons chaotic dynamics. Typically, when using silica fibre as the HNLF, the SC red edge can be pushed towards wavelengths as long as 2.4 µm. Beyond this point, the silica losses become very high and the SC generation stops. The principle presented here is the type of SC source used in chapter 5 and in other attempts of using SC sources for OCT systems. Most of the early reports of UHR-OCT using SC light sources have been done using such a SC source design. Then, the old conclusion of SC source being too noisy for OCT is linked to these MI/Solitons based generation.

The novel SC generation method relies on a HNLF with a dispersion in the normal regime regardless of the wavelength considered. Such a dispersion property is obtained by ensuring a particular dimension for holes and pitches distribution during the PCF manufacture. The pump laser used in this low noise design is a femtosecond laser. Then, the non-linear effects responsible for the broadening are no-longer MI and solitons but Self-Phase Modulation (SPM) and Optical Wave Breaking (OWB). As mentioned above, MI and solitons are responsible for the noise properties of conventional SC sources. This is due to the fact that these effects are based on amplification of noise. On the contrary, SPM and OWB are deterministic, not based on any random amplification. Self-Phase Modulation is an effect created by the time varying phase delay induced by the pulse intensity through a Kerr effect phenomenon [10]. Optical Wave Breaking corresponds to frequency generation through four waves mixing effects occurring when different frequencies overlap in time during the pulse propagation into the HNLF [11]. The proposed source concept has been demonstrated using a pump at 1550 nm. Femtosecond lasers with extremely short pulse length have been developed at this wavelength for telecommunication system. At

1064 nm, though femtosecond lasers are available, the achievable pulse length is longer and their cost is high.

6.3 Supercontinuum Sources

In this study, two SC sources are considered. The first one is a commercially available SC source called SuperK Extreme (EXR9-OCT). This source is based on the principle of pumping a HNLF nearby the ZDW, following the design presented in Figure 6.1. Later in this chapter, this SC source is denoted ZDW-SC. Due to industrial secrecy considerations, it is not possible to show the exact dispersion profile of the fibre in this manuscript. However, Figure 6.2(a) displays a dispersion profile similar to that used for the ZDW-SC. The ZDW is located around 1040 nm and the pump laser is at a wavelength of 1064 nm. This means that the pumping occurs in the anomalous dispersion regime. In opposition of normal dispersion, anomalous dispersion characterizes a regime where the dispersion of the fibre is anomalous. A length of 10 ms of HNLF is used. The HNLF possesses a mode field diameter of 4 to 4.5 µm. The pump laser is a Mode-Locked (ML) laser operating at a repetition rate of 80 MHz with a pulse length of 10 ps. The repetition rate of the pump is quadrupled using a pulse dividing scheme creating a 320 MHz repetition rate. The ML laser itself provides several mW of optical power at 1064 nm, which are then amplified through several stages of fibre based amplification. Then, the pump delivers 4 W average power at the input of the HNLF. The peak power used for SC generation is around a few kW. An example of spectrum generated by the ZDW-SC is presented in Figure 6.3 (red). Typically, the generated SC from the ZDW-SC spans from 500-600 nm up to 1950 nm. The Power Spectral Density (PSD) shows a locally flat spectrum, which is interesting for UHR-OCT as this would minimize the need for spectral shaping. Indeed, such spectral shape are easy to correct using pure digital processing like windowing of the spectrum.

The second SC source used in this experiment is based on the principle of pumping a HNLF with all-normal dispersion profile using an ultra-short pulse within the femtosecond regime. Later in this chapter, this SC source is

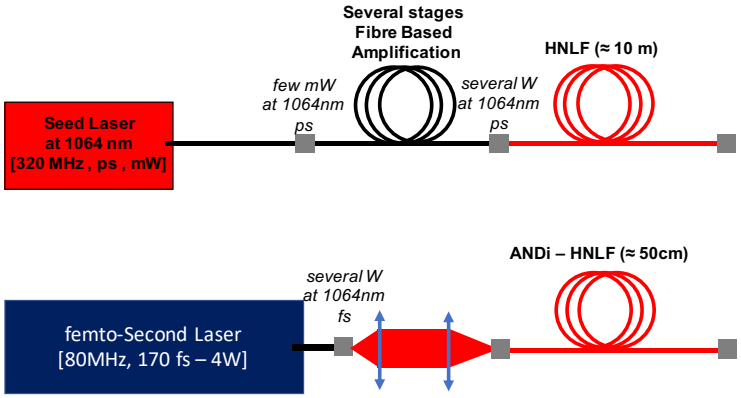

FIGURE 6.1: Simplified description of the two SC sources: ZDW-SC (upper sketch) and ANDI-SC (lower sketch).

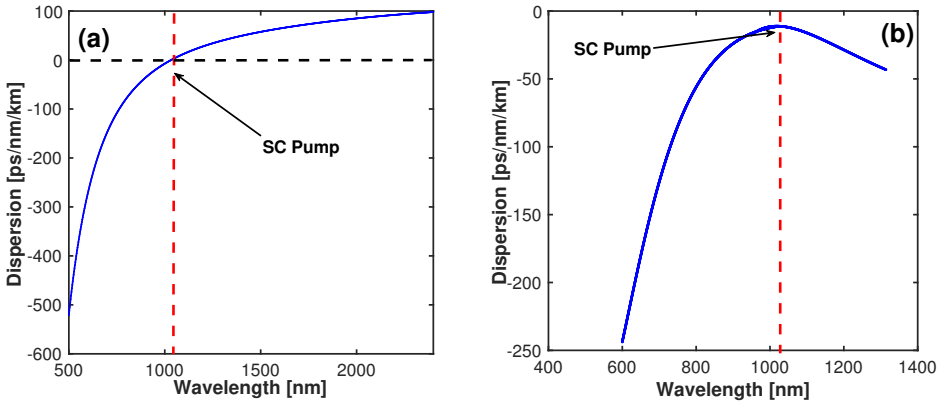

FIGURE 6.2: Dispersion profile of the HNLF for: (a) ZDW-SC and (b) ANDI-SC.

denoted ANDI-SC. This SC source is made of two components, both commercially available through the company NKT Photonics A/S (Denmark), but which have not been designed for this specific application. Therefore, this SC source is an attempt to demonstrate the potential low noise operation of such a configuration as described in different reports coming from the SC community [8, 9, 12] and using it into an UHR-OCT system in the 1300 nm wavelength region. The HNLF is a 50 cm silica PCF with an all-normal dispersion profile as shown in Figure 6.2(b). The fibre has a mode field diameter of 2 to 2.5 µm. The pump laser is again at 1064 nm. The pump laser is a commercially available femtosecond laser from NKT Photonics A/S (Denmark). It is a ML laser operating at a repetition rate of 80

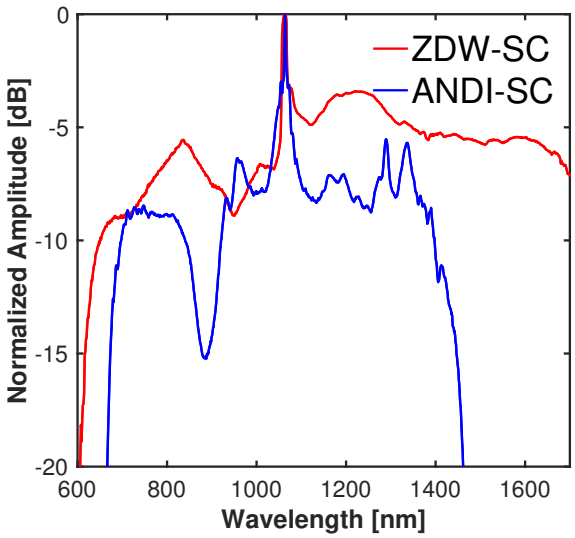

FIGURE 6.3: Normalized PSD of the ZDW-SC and the ANDI-SC measured using an integrating sphere coupled to photo-detector and an oscilloscope.

MHz. A bulk compression is used that offers after compression a variable pulse-width within the fs regime from 170 fs to 1 ps. The maximal average output power is around 4 W, leading to possible peak powers of a few tens of kW for pumping the HNLF. The generated SC exhibits a relatively non smooth PSD with many variations over the wavelength range of the spectrometer, making it slightly uneasy to work with in UHR-OCT. Indeed, such local variations of the spectral shape can distort the Point Spread Function (PSF) shape leading to a lower axial resolution compared to what can be expected from the spectral bandwidth. Using this particular HNLF, the longest achievable wavelength for the SC in the Near Infra-Red is located around 1400 nm as the confinement losses become too important after this wavelength (see Figure 6.4). Confinement losses are losses which can be described as a propagation of the optical mode within the core and the cladding of the fibre. By propagating into the cladding instead of the fibre core, the mode experiences higher losses compared to a well confined mode.

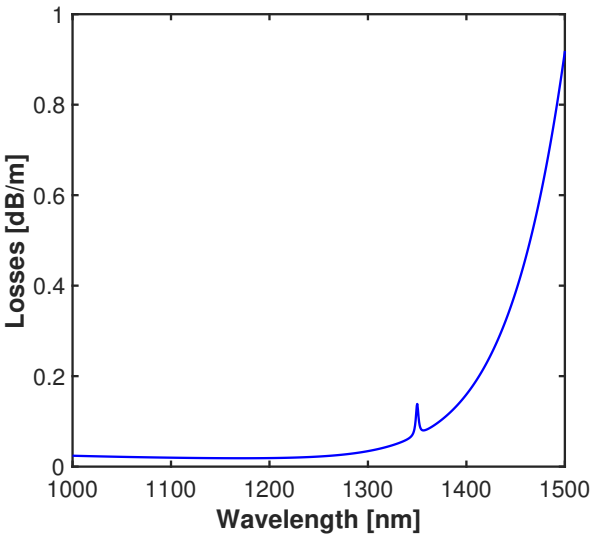

FIGURE 6.4: Confinement losses of the ANDI fibre versus wavelength.

6.4 Influence of pump peak power on the spectral broadening

When considering a SC light source for OCT, and more especially for UHR-OCT, the spectral extension of the SC is a key parameter. The larger the available optical bandwidth the higher the achievable axial resolution. The spectral shape of the optical source is also to be considered as it influences the shape of the PSF, which is related to the Fourier Transform (FT) of the source PSD. The influence of these parameters is discussed in detail in Section 2.5.2.

The SC broadening is governed by the peak power injected into the HNLF, regardless of the type of SC (ZDW-SC or ANDI-SC). Higher peak power corresponds to broader SC, which are however limited by light confinement losses or material losses [13]. Table 6.1 summarises the peak power experimentally estimated, for the two SC sources mentioned above, at given measured average power. To calculate the peak power, it is assumed that the ZDW-SC pump has a Gaussian pulse shape while the ANDI-SC pump has a sech^2 pulse shape. The peak power of the SC source pump is calculated

according to:

$$P_{Peak} = \left\{ \begin{array}{c} 0.94 \text{ if Gaussian pulse shape} \\ 0.88 \text{ if sech}^2 \text{ pulse shape} \end{array} \right\} \times \frac{P_{average}}{\tau_p \times R}, \tag{6.1}$$

where P_{Peak} is the pulse peak power, P_{avg} is the average power, τ_p is the pulse length and R is the laser repetition rate. The factors 0.94 and 0.88 are different from one pulse shape to the other as they are linked to the evaluation of the Full Width at Half Maximum of the pulse. The two SC sources operate with quite different pulse peak power with a factor of twenty times higher for the ANDI-SC. However, it is important to remember that the processes involved for the two sources are completely different and the higher peak power of the ANDI-SC is only due to the shorter pulse length.

TABLE 6.1: Calculated peak power of the pump lasers from measured average power for the ZDW-SC and the ANDI-SC.

$ZDW-SC$		$ANDI-SC$	
$\tau_p = 10\ ps$		$\tau_p = 170\ fs$	
$R = 320\ MHz$		$R = 80\ MHz$	
$P_{average}\ [mW]$	$P_{peak}\ [kW]$	$P_{average}\ [mW]$	$P_{peak}\ [kW]$
4000	1.5	850	55
3200	1.2	780	49
1600	0.6	515	33
800	0.3	450	29

The ZDW-SC used in this study is a commercial product dedicated to OCT at 800 nm and 1300 nm, which has been built in order to provide a variable output average power while maintaining a broad spectral shape. Then, the available pump peak power variation range ensures that the spectral extension is large for the different available pump peak power. Figure 6.5 shows the ZDW-SC spectral shape measured with a spectrometer sensitive from 1070 nm to 1470 nm for peak power at 0.3 kW, 0.6 kW, 1.2 kW and 1.5 kW. While varying the peak power the signal on the camera is adjusted in order to avoid saturation, then all signal level on camera look similar regardless the peak power. These peak powers represent respectively 20 %, 40 %, 80 % and 100 % of the maximum peak power available the ZDW-SC.

From those spectrometer measurements, no noticeable changes can be identified on the spectral shape. A measurement of the ZDW-SC used for this study, obtained with an Optical Spectrum Analyser (OSA) covering 1200 nm to 2400 nm, is presented in Section 5.4. It is shown there that the higher the peak power, the broader the SC generated, with a shift of the red-edge position from 1550 nm at 20 % of the maximal peak power up to 1950 nm for the 100 % maximal peak power.

In the case of the ANDI-SC source, the spectral shape behaviour is more complicated. Indeed, low peak powers create SC in a regime where only SPM is used for frequency broadening. This leads to the spectral shape presented in Figure 6.6(a-b) with large local variations in shape and amplitude. Those shapes deviate from conventional OCT requirements of Gaussian like intensity distribution. A direct consequence of the non-optimal spectral shape is a distorted PSF in the Fourier domain resulting in a poor axial resolution. In addition, Figure 6.6 shows the spectral shape at a given point in time, but large time fluctuations are also observed when low peak power are used, making conventional spectral shape compensation technique almost unusable. Such fluctuations are due to the fact that while using lower peak powers, the dominant effect is SPM. However, SPM is directly depending on the input power which is not perfectly constant. Even more due to the current design of the injection into the PCF the large coupling instability causes this SPM fluctuations to be very problematic. When the peak power is increased, Figure 6.6(c-d), the spectral shapes become smoother and stable. In Figure 6.6(c-d), the peak power varies from 49 kW to 55 kW but the red-edge is still located at 1.4 µm. This is due to the increase of confinement loss of the ANDI fibre as shown by Figure 6.4. Further increase of the peak power cannot increase anymore the broadening but can improve the average power. Though, it is important to keep in mind that too high average power might damage the fibre.

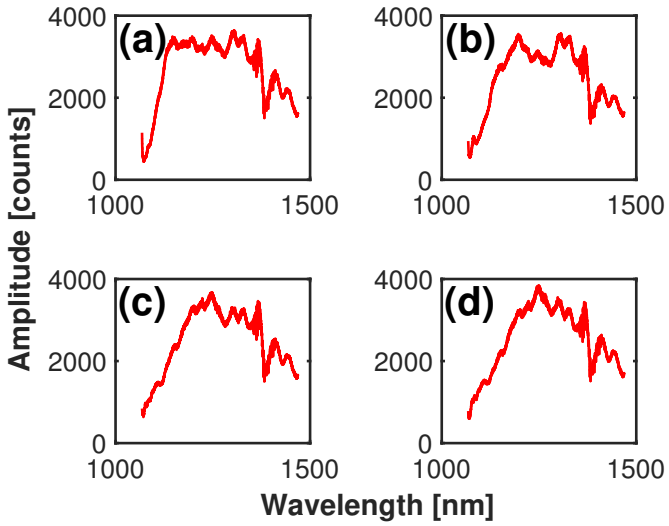

FIGURE 6.5: ZDW-SC adjusted spectral shape evolution, seen by the spectrometer, for different pump laser power level: (a) 800 mW, (b) 1600 mW, (c) 3200 mW and (d) 4000 mW corresponding to peak powers of 0.3 kW, 0.6 kW, 1.2 kW and 1.5 kW respectively.

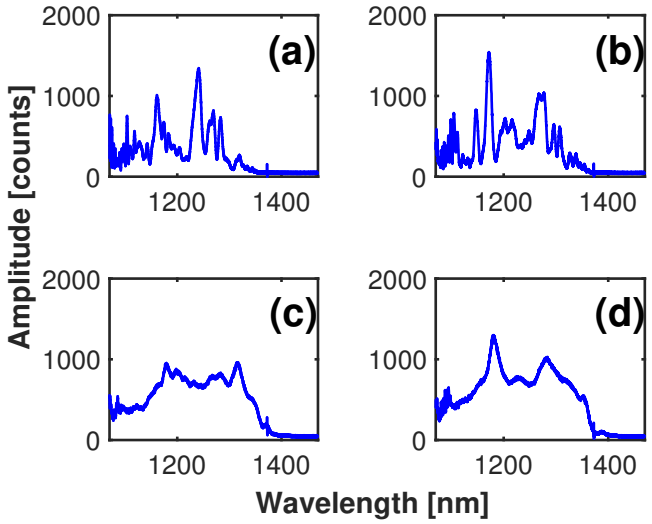

FIGURE 6.6: ANDI-SC adjusted spectral shape evolution, seen by the spectrometer, for different pump laser power level: (a) 450 mW, (b) 515 mW, (c) 780 mW and (d) 850 mW corresponding to peak powers of 29 kW, 33 kW, 49 kW and 55 kW respectively.

6.5 Self-Phase Modulation issue

Self-Phase Modulation is a non-linear effect which occurs when an intense short pulse propagates into a material. The high intensity of the pulse modifies locally the index of refraction of the material and induces a modification of the pulse phase. This phase change tends to blue-shift the wavelengths a the back of the pulse and red-shift the wavelengths at the front part of the pulse creating a frequency broadening of the optical spectrum [14]. The advantage of such a broadening, compared to other mechanism, is its high coherence (temporal stability) [8, 9]. However, even though SPM broadening is a deterministic effect (low noise, highly coherent), it also comes with an important spectral modulation of the intensity depending on the wavelength considered [14]. This spectral modulation of the light intensity is attributed to interferences between similar frequencies of the pulse experiencing different time delays.

Depending on the periodicity of such intensity modulation in wavenumber, a problem might appear when using such SC source in an OCT system. Indeed, if the modulation frequency of the SPM fringes is within a similar frequency range compared to the OCT modulation, which characterizes the depth information profile of the sample, corrupting peaks appear into the OCT image. No distinction is possible between the SPM effects and the useful signals arising from interference between sample and reference light. In addition, the SPM intensity modulation highly depends on the stability of the pump laser. Any fluctuations in intensity of the pump, due to laser instability or coupling into the HNLF, create a modification of the SPM modulation frequency and amplitude. Then the corruption is no longer a single peak into the A-scan profile but a wide area that corrupts a part of the imaging range. This is equivalent to an increase in the noise floor when considering the SC source and the OCT system association.

To illustrate the effect of SPM into an OCT image, Figure 6.7 shows a particular configuration of the ANDI-SC source where the SPM effect is dominant. To isolate the effect of SPM only, a spectrum is acquired by

pumping the ANDI fibre with a relatively short pulse of 370 fs. The spectrum is measured without passing through the interferometer, so this modulation is only due to non-linear effect in the HNLF. The pulse length of the pump laser is chosen longer than its minimal value in order to reduce the peak power. Therefore, the broadening is dominated by SPM only and not by a mix of SPM and OWB as described in Section 6.2. It would have been possible to reduce the power (average and peak) using a neutral density filter and reach the same SPM only broadening mechanism. Figure 6.7(a) shows that the intensity modulation obtained from SPM is similar, in terms of frequency, to that of a channelled spectrum modulation at the interferometer output with an approximate optical path difference close to 100 µm. Then, if analyse with conventional OCT processing tool (FFT based), a peak will appear at a depth matching the modulation frequency. However, the power within the HNLF is not constant due to both fluctuations of the pump laser and coupling into the HNLF, therefore instead of seeing a single peak in the z-domain (at a single depth), a portion of the imaging range seems corrupted. This is due to a washing out effect of the fringes due to constant variations of periodicity and amplitude of the SPM modulation that lead to an overall increase of the noise floor of the A-scan profile as shown in Figure 6.7(b), which is an average over 500 readouts from the spectrometer.

Such a corruption is dramatic for an OCT system as the most important part of the dynamic range is not usable for imaging. Indeed, due to the inevitable effect of sensitivity decay with density of the modulation of channelled spectra (see Section 2.6.3), the part of the imaging range with the highest sensitivity is unusable. During the time attributed to this study on the topic of low noise SC source, no solution has been found to eliminate the SPM corruption effect. However, an optimization can be done to minimize its effect. As described above, at relatively low peak power, SPM dominates the broadening mechanism. In case of higher peak power, a second non-linear effect called OWB needs to be considered. Then, the generated spectrum becomes smoother as the fringes due to SPM disappear as shown by the spectral shape evolution of Figure 6.6. Nevertheless, this high peak power idea used for spectrum smoothing allows only to reduce the part of

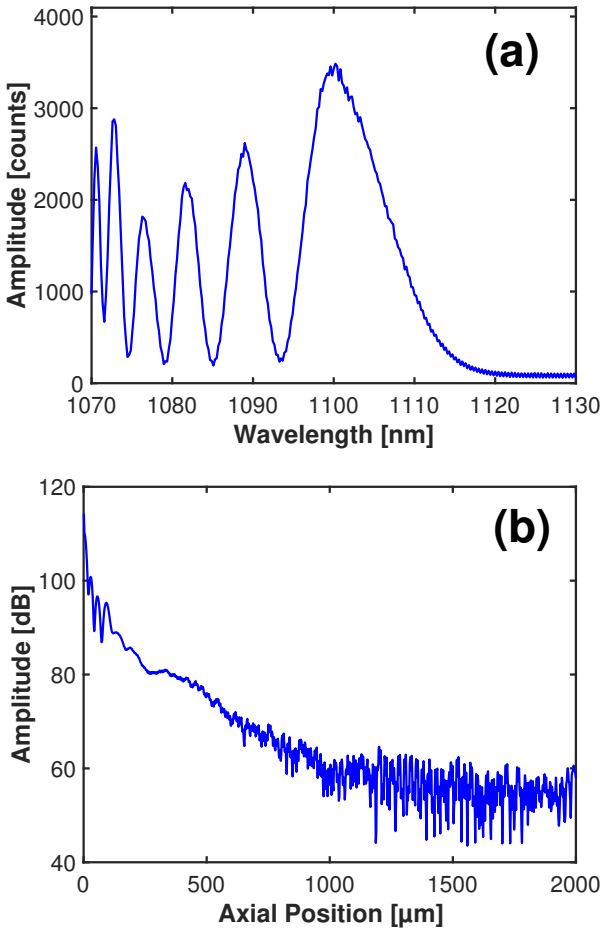

FIGURE 6.7: Illustration of the SPM fringes image corruption. (a) Spectrum measured by the spectrometer for a SC generated using a pump pulse length of 370 fs. (b) Average of the FFT for 500 spectra similar to (a) (dB scale).

the image corrupted and not to completely cancel the SPM corruption effect. Also, using high peak power around $50\ kW$ creates an average power of almost 1 W into the HNLF, which is close to the damage threshold at the injection point. Figure 6.8 is an example of the corruption effect, on the background of an OCT image compared to a non-corrupted image obtained from a commercial SC source (ZDW-SC) in Figure 6.8 top. The ZDW-SC source based image shows a homogeneous black background while the ANDI-SC based image has a white portion from 0 to 150 µm depth range. Even though, a SPM corruption is still observed, it is not covering an important part of the dynamic range and permits to use the ANDI-SC source

for OCT.

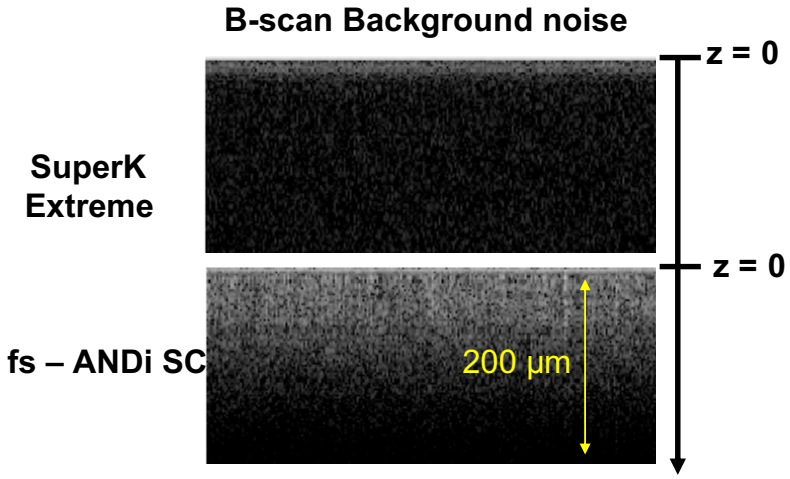

FIGURE 6.8: Illustration of the SPM corruption effect on the upper part of an OCT B-scan.

6.6 Supercontinuum usefulness for optical coherence tomography

So far, it has been shown that a SC source based on the principle of pumping a HNLF with an all-normal dispersion profile and using a short optical pulse (fs regime) can generate a SC covering a spectral range broad enough for UHR-OCT. The results below describes a comparison between the ZDW-SC and the ANDI-SC when used into an OCT system operating at 1300 nm.

Conventional signal processing procedure for OCT, applied to raw channelled spectra (CS) data, includes a dark signal correction, a subtraction of the reference path signal, a normalization step, a linearisation of the data in k-space, a dispersion compensation and finally an apodization or windowing. A description of these steps is done in the Chapter 3. All these steps are done in order to achieve an optimal SNR after Fast Fourier Transform (FFT) of the processed data. After signal pre-processing, ideally only the modulated signal due to interferences should remain. This signal is centred

and symmetric around zero and its edges (shortest and longest wavelength detected) should be at zero. Figure 6.9 is an example of CSs acquired and processed, from a mirror located at an axial position of 500 µm, using the ZDW-SC (red) and the ANDI-SC (blue).

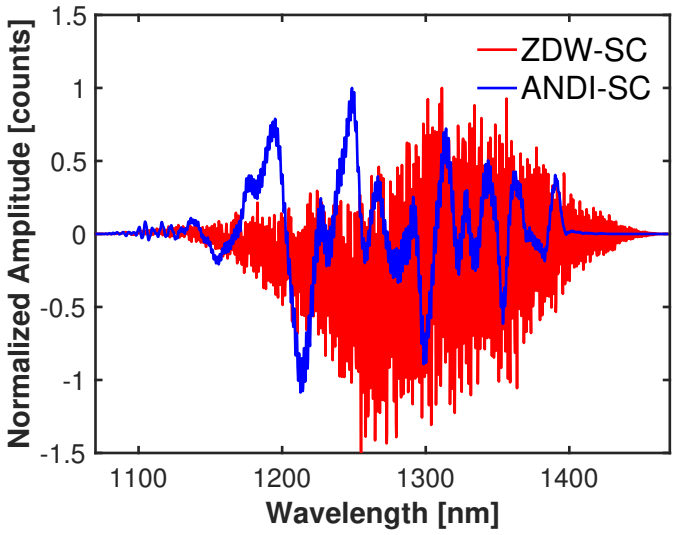

FIGURE 6.9: Measured spectra, processed with dark correction, reference subtraction, normalization, resampling and apodization, for the ZDW-SC and the ANDI-SC, with a mirror at an axial position of 500 µm.

The two CSs after processing have a completely different shape. The ZDW-SC based CS (red) shows the expected behaviour of a modulated signal centred and almost symmetric around zero and with edges at 0 counts. The asymmetry of the modulation is due to small variation of the spectral shape in time. In the case of the ANDI-SC, the CS (blue) shape is far from ideal. It seems that, on top of the fast OCT modulation, due to the optical path difference within the interferometer, another modulation with slower frequency and much larger amplitude is imprinted on the CS. This slow frequency modulation is due to the time varying amplitude of the source. The amplitude of source is varying because of the previously mentioned instability of the pump laser and coupling of light into the HNLF. The non-optimal spectral shape is an issue and creates distortion of the PSF shape in the z-domain.

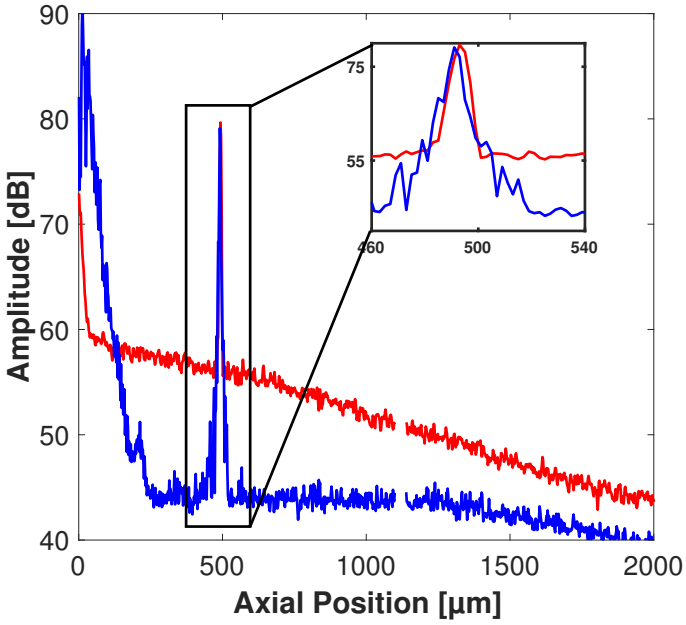

FIGURE 6.10: Example of A-scan profiles, for the ZDW-ASC (red) and ANDI-SC (blue), measured with a mirror at an axial position of 500 µm.

The following step in the OCT processing procedure is the FFT of the CS. The FFT is used for identifying the different frequency components imprinted into the CS. Then, the real part of the complex signal provides the so-called A-scan, which is a characterization of the depth reflectivity profile of the sample. Figure 6.10 displays a A-scans obtained by FFT of the two processed CSs of Figure 6.9. There, the sample is a mirror located at an axial position of 500 µm. The ZDW-SC curve (red) is a typical plot from an OCT system which source presents relatively high RIN [6, 15] . The particularity here is that the noise floor is not completely flat but with a negative slope while the axial position increases. This is an illustration of the source RIN, which creates a higher noise floor at shallow axial positions [6, 15]. In the case of the ANDI-SC, the first point to observe is the previously mentioned corruption described in Section 6.4. This means that even though the spectrum of Figure 6.6 (d) is not showing significant fringes effects from SPM, the reduction of its impact is not perfect. However, the corruption stops after 200 µm which left sufficient imaging range for OCT. After this corrupted

part of the imaging range, the ANDI-SC based noise floor is almost completely flat with a difference of up to 15 dB, at shallow axial positions, compared to the ZDW-SC. This noise floor flatness is similar to the one obtained for an SLD, which operates at shot noise limited detection [6].

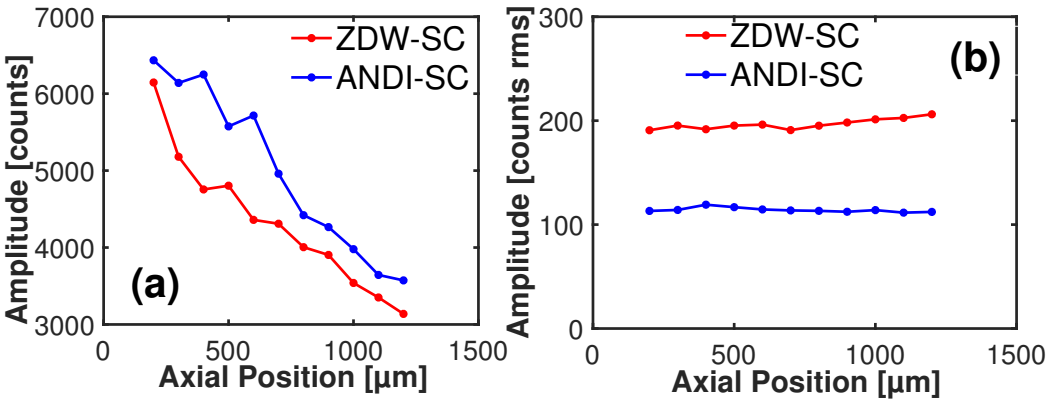

FIGURE 6.11: (a) Evolution of the maximum values of the A-scan peak similar to Figure 6.10 for the ZDW-SC and for the ANDI-SC versus depth. (b) Evaluation of the rms noise versus depth measured within the noise floor of the A-scans, similar to Figure 6.10, for the ZDW-SC and for the ANDI-SC.

A similar measurement, compared to Figure 6.10, has been done while the axial position is varied from 200 µm to 1200 µm. For each point on Figure 6.11(a), the maximum of the A-scan peak is extracted. The power on the mirror in the sample arm is around 4 mW with an attenuation of 20 dB (Neutral Density Filter with Optical Density of 2 placed in the sample arm of the interferometer) in order to avoid camera saturation. The power in the reference arm of the interferometer is similar for the two SC sources, generating a signal covering 60-70 % of the dynamic range of the spectrometer. For both the ZDW-SC and the ANDI-SC, the maximum peak value starts around 6000 counts with a slope of around -3000 counts/mm, which is expected due to the spectrometer decay (see Section 2.6.3). However, Figure 6.11 (b) is showing a quite different behaviour. Even though the signal on the sample arm and reference arm has been maintained as close as possible for each source, the ANDI-SC rms noise signal (measured within the noise

floor of the A-scan) is almost all the time half of the one of the ZDW-SC. Figure 6.12 compiles those two results into one with the calculation of the SNR. The ANDI-SC shows a SNR higher by 5-6 dB compared to the ZDW-SC. Such an improvement in the SNR can affect significantly the overall image quality of an OCT system and will be discussed in the next part of the chapter.

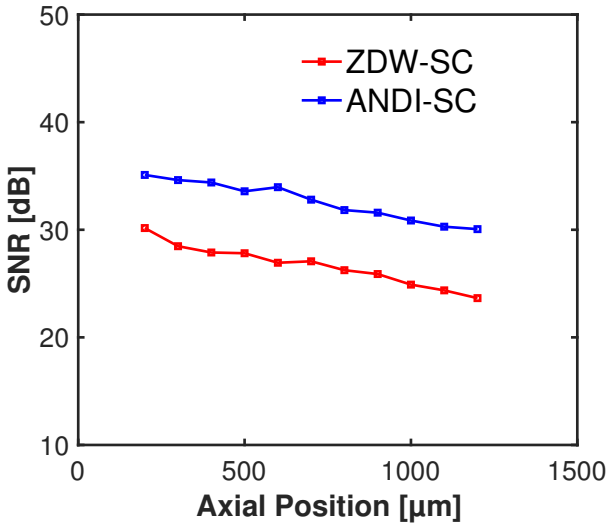

FIGURE 6.12: Evolution of the SNR versus depth for the ZDW-SC and the ANDI-SC.

6.7 B-scans comparison

In order to investigate the usefulness of a low noise SC source for UHR-OCT, a set of B-scans acquired *in-vivo* from the hand palm of a healthy volunteer is presented on Figure 6.13. The system used is an UHR-OCT system with a central wavelength of 1270 nm with a total bandwidth of 400 nm. The power used on sample is 2 mW, the signal on the reference arm of the interferometer is set to 3000 counts, representing 75 % of the camera dynamic range. Such high signal on the reference arm of the interferometer placed the OCT system in a regime where RIN is for sure influencing the noise properties of the system if a ZDW-SC is used. Then, this help to observe if

the noise improvement bring by the ANDI-SC is actually changing the image quality achievable. Each image is made of 500 A-scans and each A-scan is acquired at an exposure time of 20 µs. Such exposure time corresponds to a fast camera line rate of 42 kHz.

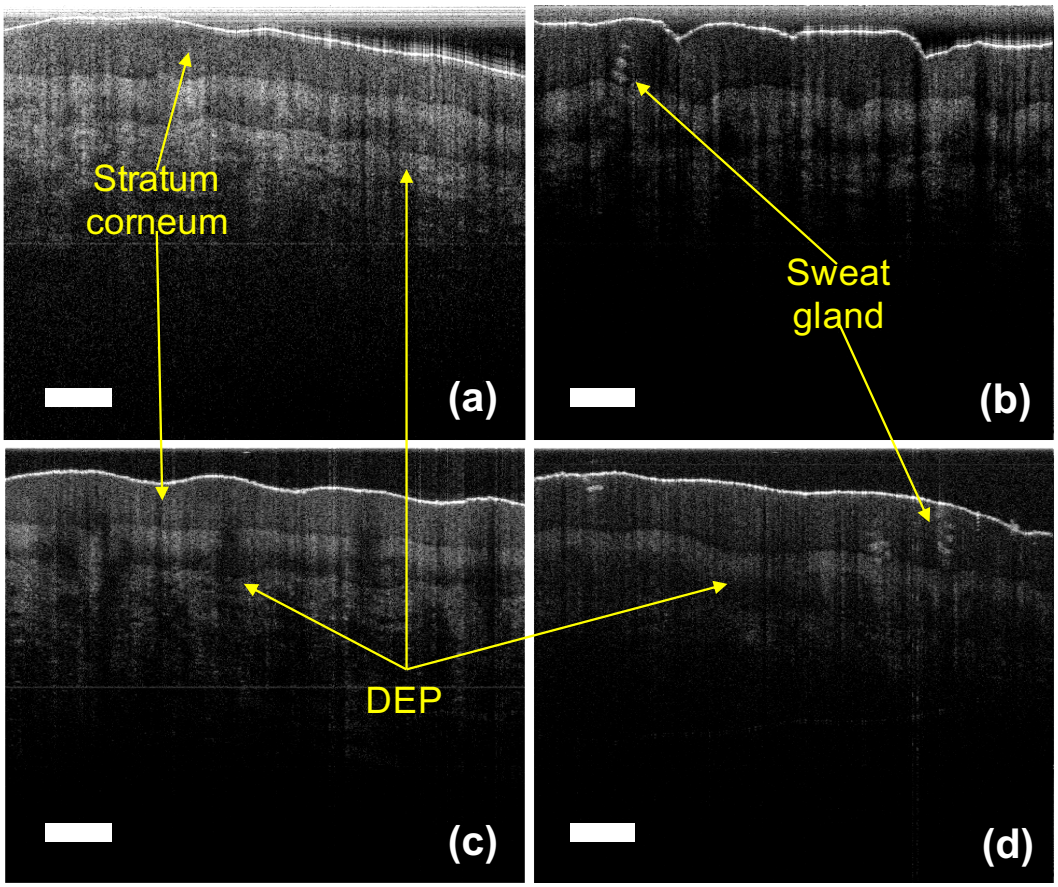

FIGURE 6.13: *In-vivo* B-scans acquired from the hand palm of a healthy volunteer using an optical power of 2 mW. (a-b) ANDI-SC based B-scans (c-d) ZDW-SC based B-scans (scale bar 500 µm).

Figure 6.13(a-b) are the ANDI-SC based images and Figure 6.13(c-d) are ZDW-SC based images acquired from a similar skin location for comparison. As a first point to notice is the effect of the SPM corruption previously mentioned. The very upper parts of the ANDI-SC based images Figure 6.13(a-b) are whiter than the images backgrounds. This is due to the SPM corruption. As explained earlier this is due to the remaining SPM effects, whose modulation frequency falls within the OCT fringes frequencies.

However, the part of the images concerned with this corruption is limited and does not prevent the use of ANDI-SC for OCT. All four images show similar structural information such as the stratum corneum, some sweat glands or the demo-epidermal junction (DEP). The background of the ZDW-SC images are whiter compared to the ANDI-SC as expected due to the increasing noise floor of the axial profile shown in Figure 6.10. Finally, the stratum corneum of the ANDI-SC based images seems blurred and not well defined. This issue might come from the slow variation of the DC part of the interference signal. Common OCT processing relies on removing a previously recorded DC spectrum from the interference fringes signal, but in the present case this correction is not perfect as the DC is constantly varying in time. It is assumed that this random time fluctuation is certainly due to thermal instability within the fibre as the peak power used for generating a broad smooth spectrum is close to the damage threshold of the fibre (see Section 6.4).

6.8 Discussion

The idea behind this study was to confirm the effective noise improvement obtained from an ANDI-SC source compared to a ZDW-SC source. The progress in terms of noise from the source is obtained by replacing the conventional HNLF, which possesses a dispersion within both the normal and anomalous regime, by a fibre with all-normal dispersion. Also, the ps pump is replaced by a laser with a shorter pulse, within the fs regime. This two changes are done in order to generate a SC with completely different non-linear effects. However, the maximal pulse length to not exceed for operating with SPM and OWB instead of MI and solitons, was not clear in the literature. Two reports [11, 12] stated that below 300 fs should be short enough for the pulse length but not evidence was provided.

The choice has been made in this study to build this new SC source using only commercially available components. This choice was motivated by two reasons. The first one was to keep the SC source design as close as possible to those described in the literature [8, 9]. This means that during the study no particular care has been taken to improve the assembly made of an

ANDI fibre/femtosecond laser presented. The second reason was the components involved. The femtosecond laser and the ANDI fibre are individually very complex technologies. Therefore, it would not be possible within the time frame of the project, to design and assemble from scratch a reliable femtosecond laser and an efficient ANDI fibre. Then, the specifications of the chosen components were not ideal. Indeed, due to the parameters of the femtosecond laser used (shortest pulse length of 170 fs and repetition rate of 80 MHz), the power within the HNLF was extremely high ($P_{average}$ = 1 W - P_{peak} = 55 kW) when sufficient peak power was reached for broad SC generation. This high power, especially considering the small Mode Field Diameter of the HNLF, leads to instability of the coupling through thermal effects. Complete deterioration of the fibre has been observed several times along the project.

It should be considered for the comparison that the repetition rates of the two SC sources used in the study are different. Indeed, the ZDW-SC operates at a pulse repetition rate of 320 MHz while the ANDI-SC operates at a lower rate of 80 MHz. During the OCT experiments, the exposure time of the spectrometer camera is maintained constant (20 µs). Then, the higher the repetition rate of the source, the higher the averaging of any intensity noise arising from the source itself. A complete study of the SC repetition rate influence on the noise into the OCT is done on Chapter 5 of this thesis. This averaging can be approximated, assuming that the noise follows a normal distribution, as the square root of the ratio of repetition rates. In this case, the repetition rate is the number of events creating a normal distribution. A difference of 3 dB ($(320/80)^{1/2}$) is to be expected between the two SC sources. Then, the difference between the two SC sources will not be 5-6 dB as shown by Figure 6.13 but 8-9 dB.

As mentioned above, the ANDI-SC presented was assembled by putting together a commercially available femtosecond laser and a HNLF will normal dispersion profile. It is then obvious to see a lot of possible paths for improving such a SC source. One of the main problem observed was the large instability of the SC source due to thermal effect into the HNLF. This was largely due to the high average power in the fibre. Two possible solutions can be proposed for this issue. First, a reduction of the repetition rate

of the pump laser can be done in order to divide the average power. However, this might reduce the averaging effect of intensity fluctuations that can lead to a higher noise in the OCT system. The second solution which could reduce the instability problem is to use a shorter optical pulse (< 100 fs) for the pump laser together with a smaller repetition rate. A shorter pulse can offer a similar or higher peak power compared to the current one but at a lower pulse energy. This average power reduction does not impair the usefulness of the SC source for UHR-OCT as the current average power of the source is within the range of several hundreds of mW. Several reports exist on using optical pulses shorter than 100 fs at 1064 nm [16] as well as a commercial product [17].

Finally, the coupling of light from the femtosecond laser into the HNLF was based only on conventional optics such as lenses and mirrors. In addition, the HNLF used was a piece of bare fibre, then the coupling of light from bulk optics into the very small core (2 µm) of the fibre was in that case not optimal. A possible improvement would be to consider a system with fibre connection from the femtosecond laser to the HNLF. Such connection can be done by working with a femtosecond laser with fibre based output or to work with a fibre based compression instead of bulk compression. An injection back in an optical fibre back before splicing to the HNLF might be a possible path, however the control of the pulse width will be challenging. Indeed, the pulse from the pump has to be ultra-short so any propagation into a dispersive material might broaden the peak in time.

6.9 Conclusion

In this chapter, a SC source with low noise properties is proposed. The usefulness of such a source is analysed and also a comparison with a SC source dedicated to OCT is presented. First, the concept of the source is presented. The new SC source is based a pumping of a HNLF, with an all-normal dispersion profile, with a short pulse (hundreds of fs pulse width). This source design changes the non-linear effects involved for SC generation from MI and Solitons to SPM and OWB. This is key for low noise operation as the first two effects are very noisy while the last two are fully

deterministic and coherent. However, during the source development several drawbacks have been pointed out. First, the low noise source relies on an assembly of commercial products which provides a non-optimal source design. Mainly the pulse length used in this experiment is too long when considering the balance of peak power and averaged power into the HNLF. The peak power required for a broad SC generation using the current ANDI-SC design leads to a high power ($P_{average}$=1 W - P_{peak} = 55 kW). This high power is close to the damage threshold of the HNLF. Also, the femtosecond laser used has a collimated output, due to the bulk compression. Such a non-fibre based output is problematic as the HNLF has a core diameter of 2 µm, making the injection of light potentially dangerous for the fibre. Indeed, bad coupling of light with such a small focused beam creates damages to the fibre facet. However, even though the current SC source is far from optimal, very interesting noise improvement have been observed for the ANDI-SC. Even more, the ANDI SC source already offers better noise properties regardless of the repetition rate advantage of the ZDW-SC.

References

[1] K. Bizheva, B. Tan, B. MacLellan, Z. Hosseinaee, E. Mason, D. Hileeto, and L. Sorbara. In-vivo imaging of the palisades of vogt and the limbal crypts with sub-micrometer axial resolution optical coherence tomography. *Biomed. Opt. Express*, 8(9):4141–4151, Sep 2017. doi: 10.1364/BOE.8.004141. URL http://www.osapublishing.org/boe/abstract.cfm?URI=boe-8-9-4141.

[2] Q.Cui, Z. Chen, Q. Liu, Z. Zhang, Q. Luo, and L. Fu. Visible continuum pulses based on enhanced dispersive wave generation for endogenous fluorescence imaging. *Biomed. Opt. Express*, 8(9):4026–4036, Sep 2017. doi: 10.1364/BOE.8.004026. URL http://www.osapublishing.org/boe/abstract.cfm?URI=boe-8-9-4026.

[3] K. Bizheva, B. Tan, B. MacLelan, O. Kralj, M. Hajialamdari, D. Hileeto, and L. Sorbara. Sub-micrometer axial resolution oct for in-vivo imaging of the cellular structure of healthy and keratoconic human corneas.

Biomed. Opt. Express, 8(2):800–812, Feb 2017. doi: 10.1364/BOE.8.000800. URL http://www.osapublishing.org/boe/abstract.cfm?URI=boe-8-2-800.

[4] L. An, J. Qin, and R. K. Wang. Ultrahigh sensitive optical microangiography for in vivo imaging of microcirculations within human skin tissue beds. *Opt. Express*, 18(8):8220–8228, Apr 2010. doi: 10.1364/OE.18.008220. URL http://www.opticsexpress.org/abstract.cfm?URI=oe-18-8-8220.

[5] U. Møller, S. T. Sørensen, C. Jakobsen, J. Johansen, P. M. Moselund, C. L. Thomsen, and O. Bang. Power dependence of supercontinuum noise in uniform and tapered pcfs. *Opt. Express*, 20(3):2851–2857, Jan 2012. doi: 10.1364/OE.20.002851. URL http://www.opticsexpress.org/abstract.cfm?URI=oe-20-3-2851.

[6] W. J. Brown, S. Kim, and A. Wax. Noise characterization of supercontinuum sources for low-coherence interferometry applications. *J. Opt. Soc. Am. A*, 31(12):2703–2710, Dec 2014. doi: 10.1364/JOSAA.31.002703. URL http://josaa.osa.org/abstract.cfm?URI=josaa-31-12-2703.

[7] M. Maria, I. B. Gonzalo, M. Bondu, R. D. Engelsholm, T. Feuchter, P. M. Moselund, L. Leick, O. Bang, and A. Podoleanu. A comparative study of noise in supercontinuum light sources for ultra-high resolution optical coherence tomography. volume 10056, pages 100560O–100560O–6, 2017. doi: 10.1117/12.2251500. URL http://dx.doi.org/10.1117/12.2251500.

[8] A. M. Heidt. Pulse preserving flat-top supercontinuum generation in all-normal dispersion photonic crystal fibers. *J. Opt. Soc. Am. B*, 27(3):550–559, Mar 2010. doi: 10.1364/JOSAB.27.000550. URL http://josab.osa.org/abstract.cfm?URI=josab-27-3-550.

[9] A. M. Heidt, A. Hartung, G. W. Bosman, P. Krok, E. G. Rohwer, H. Schwoerer, and H. Bartelt. Coherent octave spanning near-infrared

and visible supercontinuum generation in all-normal dispersion photonic crystal fibers. *Opt. Express*, 19(4):3775–3787, Feb 2011. doi: 10.1364/OE.19.003775. URL http://www.opticsexpress.org/abstract.cfm?URI=oe-19-4-3775.

[10] J.M. Dudley and J.R. Taylor. Non-linear fibre optics overview. In *Supercontinuum generation in optical fibres*, chapter 3, pages 32–51. Cambridge University Press, 2010.

[11] C. Finot, B. Kibler, L. Provost, and S. Wabnitz. Beneficial impact of wave-breaking for coherent continuum formation in normally dispersive nonlinear fibers. *J. Opt. Soc. Am. B*, 25(11):1938–1948, Nov 2008. doi: 10.1364/JOSAB.25.001938. URL http://josab.osa.org/abstract.cfm?URI=josab-25-11-1938.

[12] M. Klimczak, G. Soboń, R. Kasztelanic, K. M. Abramski, and R. Buczyński. Direct comparison of shot-to-shot noise performance of all normal dispersion and anomalous dispersion supercontinuum pumped with sub-picosecond pulse fiber-based laser. 6:19284 EP –, 01 2016. URL http://dx.doi.org/10.1038/srep19284.

[13] H. Saghaei, V. Heidari, M. Ebnali-Heidari, and M. R. Yazdani. A systematic study of linear and nonlinear properties of photonic crystal fibers. *Optik - International Journal for Light and Electron Optics*, 127 (24):11938 – 11947, 2016. ISSN 0030-4026. doi: https://doi.org/10.1016/j.ijleo.2016.09.111. URL http://www.sciencedirect.com/science/article/pii/S0030402616311378.

[14] P. M. Moselund. *Long-pulse Supercontinuum Light Sources*. PhD thesis, 9 2009.

[15] X. Yao, Y. Gan, C. C. Marboe, and C. P. Hendon. Myocardial imaging using ultrahigh-resolution spectral domain optical coherence tomography. *Journal of Biomedical Optics*, 21:21 – 21 – 13, 2016. doi: 10.1117/1.JBO.21.6.061006. URL http://dx.doi.org/10.1117/1.JBO.21.6.061006.

[16] H. Liu, S. Cao, W. Wang, B. Lin, W. Lu, and Z. Fang. A 1μm laser output based on an er-doped fiber femtosecond laser. *Optics Communications*, 397(Supplement C):161 – 165, 2017. ISSN 0030-4018. doi: https://doi.org/10.1016/j.optcom.2017.03.078. URL http://www.sciencedirect.com/science/article/pii/S0030401817302596.

[17] Datasheet onefive fs laser. http://www.onefive.com/products/origami_HP/. Accessed: 2017-09-20.

Chapter 7

Q-switch pumped SC source for UHR-OCT – A low-cost alternative

7.1 Introduction

Optical coherence tomography is without any doubt one of the technological area where academic research and companies are working almost at equivalent pace. Numerous efforts are done to continuously improve the capability of the technique, offering more and more features such as functional OCT [1, 2] or combination of modalities [3, 4]. In addition, a tremendous work is performed to provide components specifically dedicated to OCT applications.

A clear example of those efforts is the Supercontinuum (SC) source. Supercontinuum light sources have been considered useful to OCT from the very early days of OCT development, as their available bandwidth is much larger than that of any other optical source. However, the initial attempt to use them showed quite noisy images, noise interpreted as due to large pulse to pulse fluctuations. In the last 10 years, several companies and research groups have investigated principles of low noise SC sources. Solutions such as tapering of the non-linear fibre or increasing the pump repetition rate have been proposed [5]. Nowadays, SC sources are considered as reliable and stable enough for UHR-OCT for visible OCT [1] and NIR OCT in the 800 nm and 1300 nm [6] wavelength ranges. Since the stability issue has been solved, a new trend in SC sources is the need of cost reduction. Supercontinuum sources are already of lower cost than other broadband light sources, such as titanium sapphire lasers for example. Their cost still remains high

and contributes largely to the high cost of the overall OCT system. A large proportion of the high cost of the SC sources is due to the pumping laser that need to pump a Highly Non-Linear Fibre (HNLF). Most of the time, when considering SC design for OCT, a Mode-Locked (ML) laser is used. Mode-Locked laser provides short optical pulses according to different principles that increase the overall laser cost also they need to be largely amplified to reach the peak power required for SC generation. All together this concept of SC generation required many optical and electronics components, leading to an increase of the total cost of the source.

Mode-locked lasers are not the only type of laser used for pumping the HNLF in the SC generation. Q-switched (QS) lasers are often used in non-imaging application [7]. Due to their high peak power and relative simplicity, a QS-SC could be very interesting to reduce the cost of the SC source and therefore of the OCT system. In this chapter, a comparison of two SC sources regarding their noise properties is proposed. The two SC sources differ from the laser type used as the pump. The first one is a ML pump laser commonly used in SC generation while the second one is a QS pump laser allowing a much lower SC final cost. First, a pulse to pulse stability comparison is shown followed by an OCT noise impact study.

7.2 Supercontinuum pumping using a Q-switched laser

The Q-switched technique is one of the two main techniques used to obtain a pulsed laser. It can be seen as an energy storing technique where the cavity of the laser is disturbed, meaning that the cavity losses are very high, by an active or passive component [8]. After a time, the cavity properties are changed to reach very low losses. A giant laser pulse is then generated, with a pulse length ranging from ns to µs. Q-switched lasers present high energy per pulse up to several mJ [9]. Typically, repetition rates within the hundreds of kHz are achievable and even a few MHz rates have been obtained.

The main advantage of the Q-switched laser technology is its relative low cost and simplicity to reach sufficiently high peak power for SC generation. By providing directly long and high energy per pulse, no further amplification is required for SC generation, reducing dramatically the cost of optics and electronics components. However, depending on the method used for Q-switching, several drawbacks can be pointed out especially when considering it for SC generation. The principal point of concern, which is common to any Q-switched laser, is the low repetition rate. The OCT has progressed to fast reading systems; therefore, several pulses are necessary per each camera readout. In terms of noise, the OCT system is highly sensitive to pulse to pulse fluctuations within the SC sources [5]. Therefore, a high repetition rate is necessary for averaging out any excessive fluctuations [6]. Though, it is still interesting to investigate the potential used of such a source for OCT.

7.3 Supercontinuum pumping using a Mode-locked laser

Mode-locked lasers are used when very short optical pulses are needed, as they can deliver pulse length in the ps and fs regime [10]. Mode-locking is a technique which relies on the concept of phase synchronization of longitudinal modes oscillating within the laser cavity. Any laser output is made of a series of modes oscillating within the laser cavity [8]. Each mode oscillates within the cavity with a particular frequency and possesses its own phase which can varies randomly. Mode-Locking consists of using passive or active means to create a phase relationship between a number of modes as large as possible. This phase relation allows to obtain a train of ultrashort pulses [8]. When the laser cavity is short, a ML laser can pulsate at rate from MHz to GHz rate [10]. However, ML lasers show low energy when compared to a QS lasers. Then, when considering for SC generation, an amplification stage is required to reach the necessary high pulse peak power [11] to drive the HNLF. This amplification requirement is one of the reason why the cost of a ML-SC tends to be higher than that of a QS-SC.

7.4 Supercontinuum light sources

Two SC sources are used in this study, they are both available as commercial product through the company NKT Photonics A/S (Denmark).

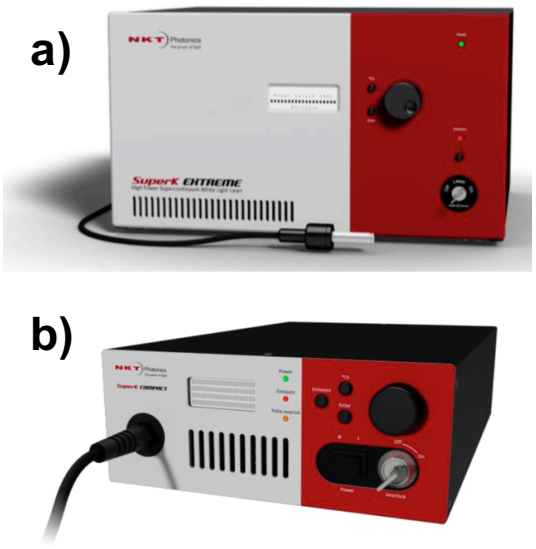

FIGURE 7.1: Pictures of the two SC sources: (a) SuperK Extreme (ML-SC), (b) SuperK Compact (QS-SC).

The first SC source is a SuperK Extreme, labelled as EXR-9 [12], recommended for OCT. This source is based on a principle described on section **??** where a ps long pulse is used to pump a HNLF close to the zero dispersion wavelength situated at a wavelength around 1040 nm. The pump used is a ML laser operating at a wavelength of 1064 nm with a pulse length of 7-10 ps and a repetition rate of 320 MHz. A fibre amplification is used to reach an average power of 5 W at the input of the HNLF. The generated SC has a blue edge around 600 nm and a red edge at 2000 nm. The total output power in the OCT wavelength range, from 1070 nm to 1470 nm, is about 1 W. A picture of the SC is shown in Figure 7.1 (a) and the source spectral shape is presented in Figure 7.2.

The second SC source is a SuperK Compact [13], which is a low-cost SC source with a total cost of around 10 % of the selling price of the firstly described SC source. This SC generation is also based on pumping of a PCF by a long optical pulse (pulse length of 1.6 ns). The pump is based

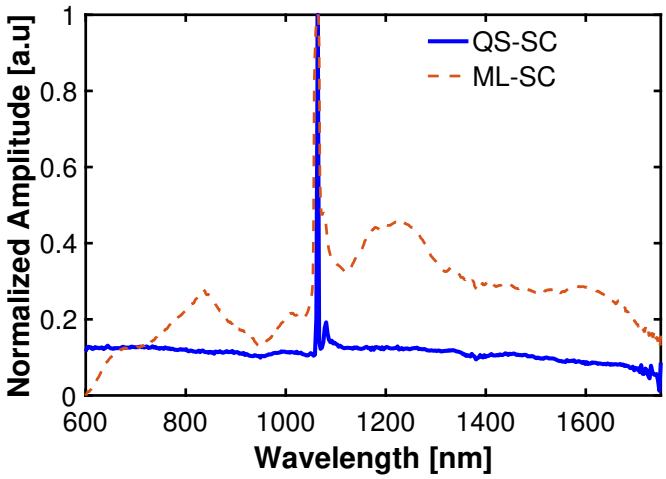

FIGURE 7.2: Normalized Power Spectral Density (Power versus Wavelength) of the QS-SC (blue solid) and of the ML-SC (red dashed) sources. Both spectra were measured using an Optical Spectrum Analyser at the output of an Integrating Sphere.

on a Q-switched architecture, more precisely a passive Q-switching using a Cr4+: YAG crystal as saturable absorber. The repetition rate can be varied from 1 Hz to 22.222 kHz, though as a drawback of passive Q-switching the average power of the SC scales with the repetition rate [8]. At the highest repetition rate of 22.222 kHz, the total output power is about 125 mW with a power within the OCT wavelength range of around 30 mW. Similarly, to the previous description, a picture of this SC source is shown in Figure 7.1 (b) and the spectral shape is presented in Figure 7.2. Later in this chapter, the Q-switched based SC will be denoted as QS-SC and the mode-locked based SC as ML-SC.

7.5 Noise characterization using pulse to pulse measurements

Supercontinuum light sources used in biomedical applications are often pulsed sources. Their repetition rate limits the reading rate in the OCT system. At least one pulse per readout is required. In addition, amplitude fluctuations from pulse to pulse limit the achievable Signal to Noise Ratio

(SNR) and therefore the image quality [6]. A straightforward method for characterizing pulse to pulse stability of an optical source consists in using a fast photodiode (GHz) connected to an integrating sphere and an oscilloscope. If the detector is fast enough, the recorded voltage signal, for each pulse, is proportional to its peak power [5]. The Relative intensity noise (RIN) of the optical source is then calculated as

$$RIN = \frac{\sigma_M}{\mu_M}, \tag{7.1}$$

where σ_M is the standard deviation of the time series of local maximum intensities within the pulse train and μ_M is the average of the times series of local maximum intensities within the pulse train. Figure 7.3 and Figure 7.4 describe the statistical properties of the pulse trains measured for the ML-SC and the QS-SC respectively. Figure 7.3 (a-b) show the pulse train, measured for the ML-SC at a wavelength of 1100 nm and 1450 nm, over a time of 0.2 µs, corresponding to a train of 64 pulses. At a wavelength of 1100 nm, the pulse train looks relatively stable, as shown in Figure 7.3 (c), which is a histogram plot of the time series of the local maximum of the pulse train (indicated by red dots in Figure 7.3 (a-b) or Figure 7.4 (a-b)). Indeed, Figure 7.3 (c) presents a normal distribution for the pulse train maximum intensity time series, which is usually an indication of low RIN [14]. In opposition, at a wavelength of 1450 nm, the pulse train is unstable with amplitude fluctuations almost equal to the full amplitude of the pulse train. This high instability is confirmed by the histogram plot, shown by Figure 7.3 (d), where the distribution is not anymore normal but looks more like a non-symmetric Gaussian. This distribution asymmetry is an indication of high RIN in SC source emission [14].

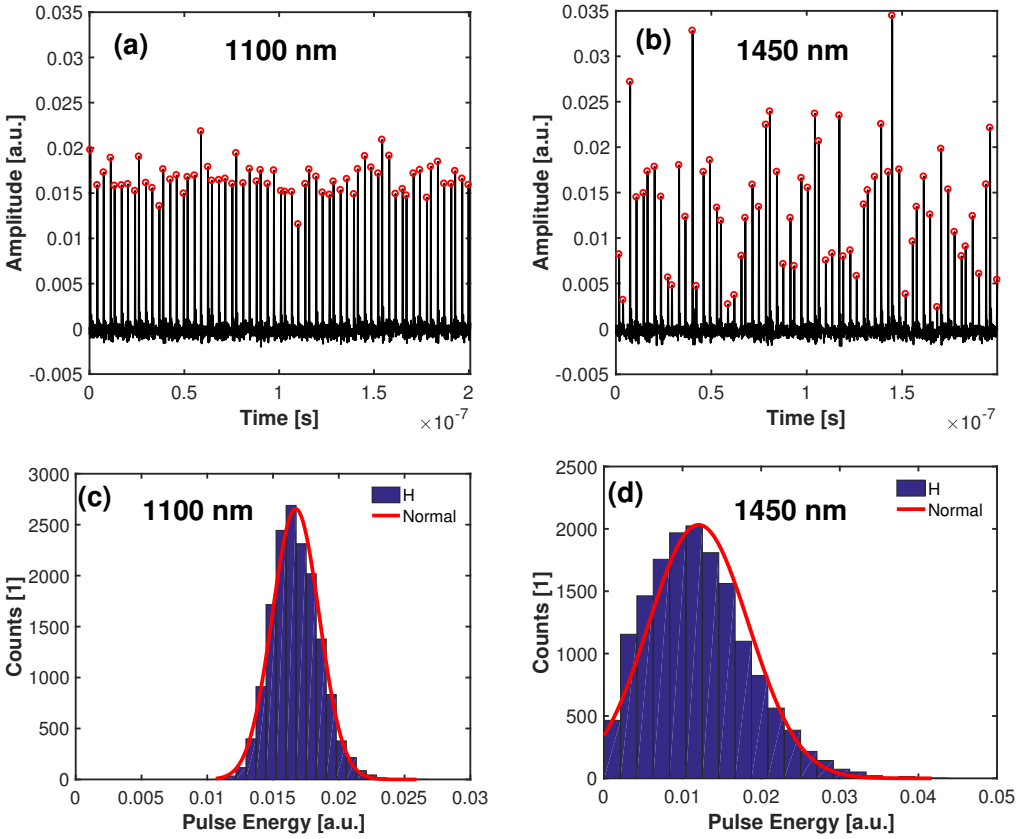

FIGURE 7.3: Pulse to pulse noise measurements of the ML-SC. (a-b): Example of pulse trains measured at central wavelengths of 1100 nm and 1450 nm respectively using a 10 nm bandpass filter. (c-d): Histograms of the maximum pulse train data series built from a 0.2 µs long pulse train. The wavelength bands are selected using 10 nm bandpass filters.

In the case of the QS-SC source, the pulse to pulse measurements show a different behaviour. Figure 7.4 (a-b) display examples of pulse trains, similarly to Figure 7.3 (a-b), recorded over a time of 2 ms (45 pulses) for a central wavelength of 1100 nm and 1450 nm respectively. Both wavelength pulse trains exhibit relative good intensity stability. Figure 7.4 (c-d) confirm this stable operation with a clear normal distribution. The sparse character of the histogram plots shown in Figure 7.4 (c-d) is due to the lack of pulses within the pulse train used for the histogram plot. The low repetition rate of the QS-SC does not allow long records of data due to the maximum 2 ms length setting of the available oscilloscope for reasonably small data size.

Using similar measurements presented in Figure 7.3 and Figure 7.4, and by covering the entire wavelength range of the OCT system a pulse to pulse stability comparison can be obtained between the two sources. To do so, the RIN is calculated using Equation 7.1 for the two SC sources. Figure 7.5 is a summary of the RIN measured over the OCT wavelength range. As shown by the pulse train analysis, the QS-SC source is much more stable than the ML-SC source. Indeed, the QS-SC exhibits an almost flat RIN from 1100 nm to 1450 nm, whilst the ML-SC exhibits a constantly increasing RIN with wavelength reaching values as high as 45 % at 1450 nm.

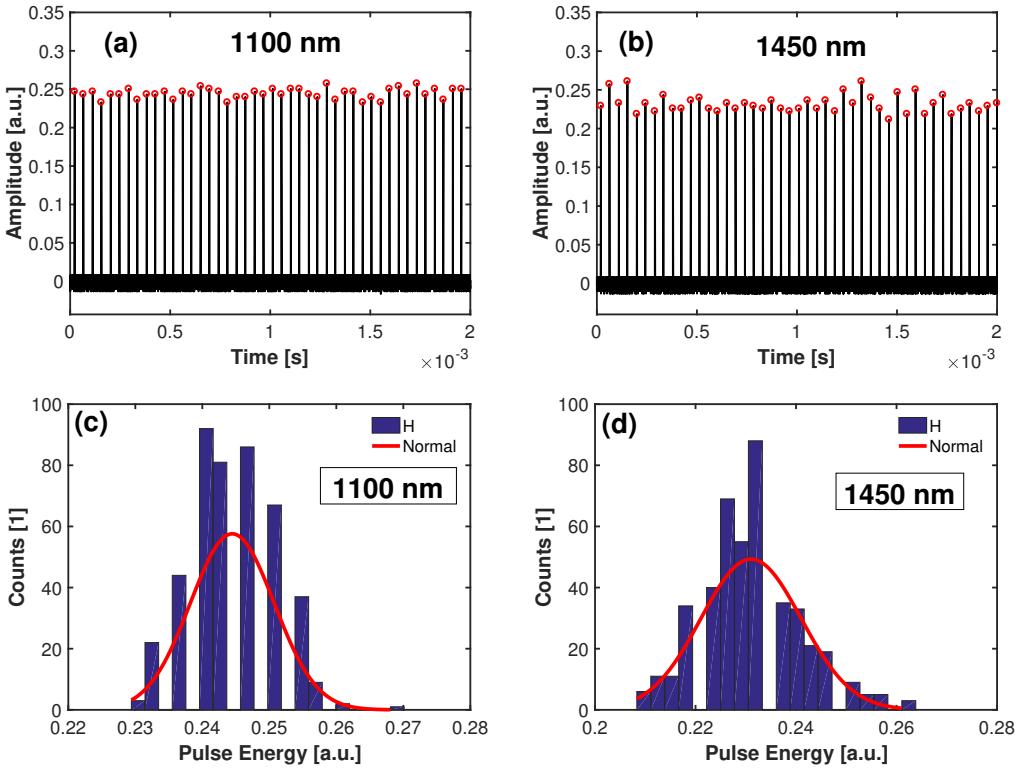

FIGURE 7.4: Pulse to pulse noise measurements of the QS-SC. (a-b): Examples of pulse trains measured at central wavelengths of 1100 nm and 1450 nm respectively using a 10 nm bandpass filters. (c-d): Histogram of the maximum pulse train data series built from a 2 ms long pulse train. The wavelength bands are selected using 10 nm bandpass filters.

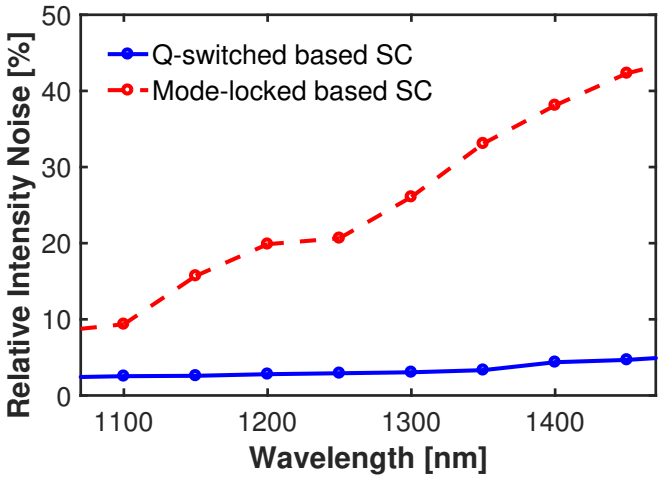

FIGURE 7.5: RIN versus wavelength measured along the spectrometer range for both QS- SC (blue solid) and ML- SC (red dashed).

Nevertheless, as mentioned above in this chapter, the ML laser and the QS laser operate at different repetition rates. This difference needs to be taken into account when operating into the OCT system. Indeed, it will determine the number of pulses per readout of the camera and obviously, at least a pulse is necessary per each readout. This demand adding the information in Table 7.1 to that in Figure 7.5, which shows the number of pulses per readout of the camera (close to the inverse of the camera frequency C_L) for the two considered SC sources. Whilst the ML-SC operates with thousands of pulses, for instance of up to 64000 pulses per $150\ \mu s$ exposure time, the QS-SC emits a few pulses only in the same time interval. This very large difference in the number of pulses per readout can somehow contradict the initial RIN versus wavelength measurement presented in Figure 7.5. The effect of pulse to pulse stability is directly observable in the OCT image and will be discussed in the next part of this chapter.

TABLE 7.1: Calculated number of pulses per camera readout for different exposure times (T_{exp}) for the ML-SC and QS-SC sources. C_L represents the camera reading rate.

SC Type	T_{exp} [μs]	C_L [kHz]	Pulses per Readout
ML	20	41.7	6400
ML	40	20.8	12800
ML	100	9.6	32000
ML	150	6.4	48000
QS	20	41.7	< 1
QS	40	20.8	< 1
QS	100	9.6	2.3
QS	150	6.4	4.6

7.6 Effects of SC noise on the OCT images

B-scan OCT images are built by assembling depth reflectivity profiles, called A-scans, acquired by scanning the sample along a given lateral direction. Then, saying that the SC source noise affects the image quality of an OCT system corresponds actually to the fact that the source noise disturbs the reflectivity profile measurements. An A-scan is built by applying a Fast Fourier Transform (FFT) operation to Channelled Spectrum (CS) acquired by the spectrometer. An A-scan is then characterized by its peaks amplitude, peaks width and its noise floor. It is common in the OCT community to assume that the peak amplitude is dependent on the amplitude of the modulation envelope contained into the CS. In opposition, the noise floor is dependent only on the signal returning back from the mirror of the reference path of the interferometer. This assumption is justified as the signal coming back from the sample is orders of magnitude smaller than the signal coming back from the reference mirror. Then, it is possible to investigate how noisy is an optical source by observing the noise floor obtained for a given signal in the reference path of the interferometer.

Figure 7.6 shows the noise floor for both SC sources and four different exposure times. Each of the 500 noise floors is a readout of the spectrometer, processed with dark signal and background subtraction, normalization, resampling, windowing and finally subject to a FFT operation. When varying

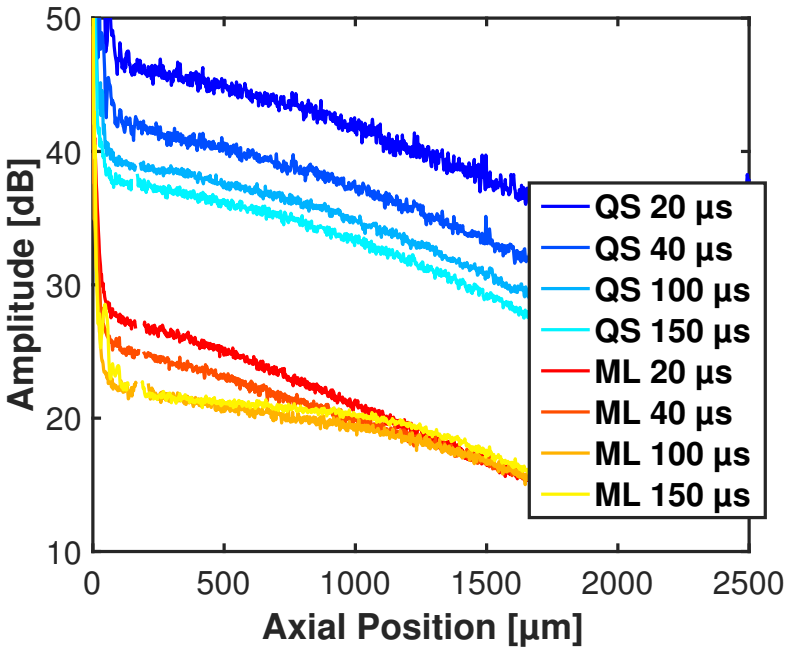

FIGURE 7.6: Noise floor of depth reflectivity profile, measured with the sample arm of the interferometer blocked, using both ML-SC and QS-SC sources at exposure times of 20 µs, 40 µs, 100 µs and 150 µs.

the exposure time the signal is kept at a similar level on the camera corresponding to 50 % of the dynamic range (2000 counts). A few pixels from the noise floor of Figure 7.6 are discarded, at an axial position of 180 µm, as they correspond to interference between the fibre-end reflection in the sample path and the reference path. A first observation is that the two groups of curves in Figure 7.6, for the QS-SC and the ML-SC, are separated by around 20 dB. In the case of the ML-SC, due to the averaging over a high number of pulses, the system is within the shot noise limited regime at around 100 µs (no improvement is seen in the noise floor from 100 µs to 150 µs exposure time). For the QS-SC, the larger the exposure time the lower the noise floor, suggesting that there is an influence of RIN in the OCT system. This initial observation is confirmed by the sensitivity plots presented in Figure 7.7. The two groups of curves show a sensitivity difference of 20 dB, which might seem important, especially considering the higher RIN of the ML-SC

compared to the QS-SC. But again, the large difference in pulses per read-out between the two sources gives the advantage to the ML-SC source when considering OCT applications. Using the sensitivity formula in [15], theoretical shot noise limited sensitivity values of 100, 103, 107, and 109 dB are obtained for exposure times of 20, 40, 100, and 150 µs, respectively, for 4 mW power on the sample. These values assume a coupling back into the fibre of 70 % of the light returning from the sample and a spectrometer efficiency of 80 % (estimated, as we use a commercial spectrometer). The 100 and 150 µs exposure time cases for the ML-SC source are close to the theoretical shot noise limited sensitivity values as expected. The QS-SC sensitivity curves lie 20-25 dB below the shot noise limited regime. An extrapolation of the obtained data suggests that a shot noise limited regime could be foreseen with the QS-SC for an exposure time of around 600 µs. However, too long exposure time clearly impairs the system frame-rate. It is noticeable that the 150 µs QS-SC lies only a few dB below the 20 µs ML-SC case. At 20 µs exposure time the camera line rate is around 40 kHz which is a common readout speed reported in recent literature using InGaAs line-scan camera [16].

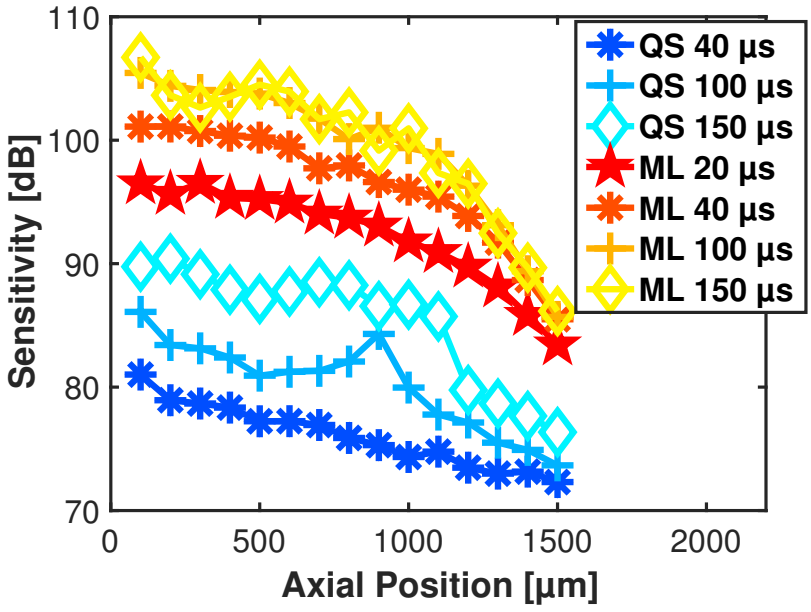

FIGURE 7.7: Sensitivity decay with depth using both ML-SC and QS-SC sources at exposure times of 20 µs, 40 µs, 100 µs and 150 µs and considering 4 mW power on sample.

Conventionally, OCT systems operate with an exposure time shorter than 100 µs in order to minimize the effect of sample motion, common values of few tens of µs can be found in the literature [17, 18]. Then, it is interesting to compare the long exposure time noise behaviour of the QS-SC with the ML-SC noise profile operating with short exposure time. This noise floor difference in that case is less than 10 dB, which is an acceptable difference. A drop of SNR is to be expected (10 dB) while using the QS-SC. Then, it seems possible to use the QS-SC for UHR-OCT with long exposure time. As a comparison of the effect of this 10 dB difference in SNR, the spectrometer decay with depth observed with any SD-OCT system is often comprised between 5-10 dB/mm but still acceptable contrast is obtained at axial positions larger than 1 mm.

7.7 Axial resolution characterization

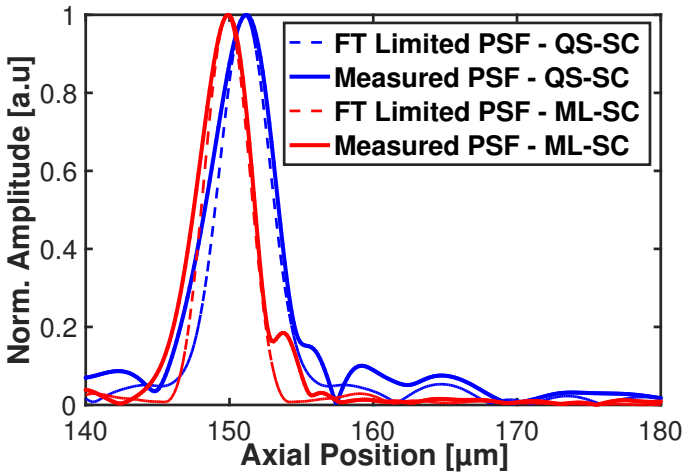

FIGURE 7.8: Normalized Point Spread Functions (PSFs), measured with a mirror in a sample arm of the interferometer at an axial position of 150 µm, for both the ML-SC and the QS-SC.

The main characteristic of SC sources is their ultra-broad spectrum covering easily several hundred of nm. This point is of importance for OCT application as it will define the axial resolution achievable by the system as described in section 2.5.2. The two sources used in this chapter offer an optical

bandwidth much larger than the spectrometer bandwidth. So, in both cases the achievable axial resolution is mainly determined by the limited bandwidth of the spectrometer and less dependent on the source spectrum itself. Figure 7.8 is an example of normalized Point Spread Functions (PSFs), measured at an axial position of 150 µm, using the ML-SC and QS-SC sources. The two PSFs show a Full Width at Half Maximum close to 5 µm (in air).

7.8 Example of Images - Non-Destructive Testing

From the results presented earlier in this chapter, it could be inferred that the QS-SC source is suitable for OCT in cases where the exposure time can be extended to values over 100 µs. Non-Destructive Testing (NDT) is a field of OCT application where scanning speed is not necessarily the main parameter. However, NDT sometimes requires UHR-OCT resolution or longer central wavelength [19]. A source like the QS-SC is ideal for such applications, as it provides exactly the same axial resolution than a conventional SC source but at a much lower cost. To illustrate this point, Figure 7.9 presents a set of 8 images (B-scans) measured from an Infra-red Card (IR – Card), which can be found in any optics laboratory. All images have been displayed with identical coding for the grey-level conversion making the visual quality comparison fair. First, an obvious difference can be seen between Figure 7.9 (a) and Figure 7.9 (e), which are the B-scans acquired using an exposure time of 20 µs. Figure 7.9 (e) presents a poor image quality with vertical black stripes all along the image. Those stripes correspond to readout of the camera where no optical pulse have been measured. Indeed, at an exposure time of 20 µs, the linerate of the camera is 41.7 kHz, which is more than twice the repetition rate of the QS-SC. The ML-SC shows a good image quality with clear structural information distinguishable in Figure 7.9 (a). A similar observation can be done for the exposure time of 40 µs. However, the QS-SC image is improved. When considering long exposure time such as 100 µs or 150 µs, the images produced by the two sources become similar, with more background noise when using the QS-SC.

An interesting tool for investigating the influence of the background noise of the OCT image in the visual quality is the Michelson contrast C_M.

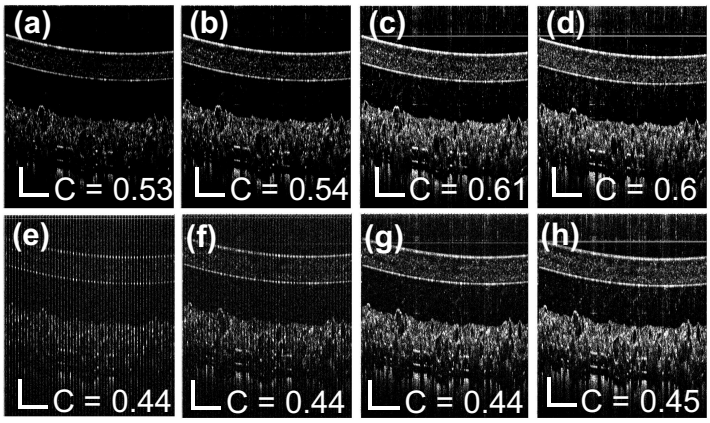

FIGURE 7.9: 1 mm x 2.4 mm B-scans of an IR card using a power on the sample of 1.3 mW with exposure times of 20 µs, 40 µs, 100 µs and 150 µs in each respective column: (a-d) ML-SC based and (e-h) QS-SC based B-scans. (scale bar 150 µm depth – 400 µm lateral)

The Michelson contrast can be calculated using the Equation 7.2,

$$C_M = \frac{I_{max} - I_{min}}{I_{max} + I_{min}}, \tag{7.2}$$

where I is the intensity signal of each pixel within the image, and where I_{max} and I_{min} are calculated as an average of the 50 first highest and respectively 50 first lowest intensity pixels within the image. This contrast calculation differs slightly from the original Michelson contrast in terms of the minimum and maximum intensity calculation. This adaptation is necessary, if not, taking directly the real minimum and maximum values of the image leads to a very high contrast of 0.99 in all the cases. From the calculated contrast which values are indicated on the corresponding images it can be seen that relatively small contrast variations are observable from QS-SC to ML-SC images. In the worst case scenario, comparing the largest contrast to the lowest lead to a variation of 20-25 %

7.9 Example of Images - Hand palm skin

So far, we have tested the QS-SC for non destructive investigation based on UHR-OCT. However, biomedical application is the main target for OCT. Figures 7.10 and Figure 7.11 are examples of skin images acquired *in-vivo* from the hand-palm of a healthy volunteer using 4 mW on the sample. The volume dimensions are 500 (A-scans) by 500 (B-scans) by 1024 (depth points). These are acquired in 37.5 s for the longest exposure time (150 µs) considered. This time is too long for imaging to be applied to samples in motion, as it is the case with imaging the eye, heart or even skin. For such long exposures, motion correction processing would be required before any volume averaging or any other advanced processing. Using the shortest exposure time of 20 µs, a volume acquisition can be finalized in 5 s, this is however still long for biomedical imaging of organs. Here, to compensate for eventual movement in x and y directions, we have used a hand-held probe, which is in contact with the sample except for a small aperture reserved for the optical beam scanning. This restricts the motion along the depth direction only, as the sample is maintained stationary in respect to

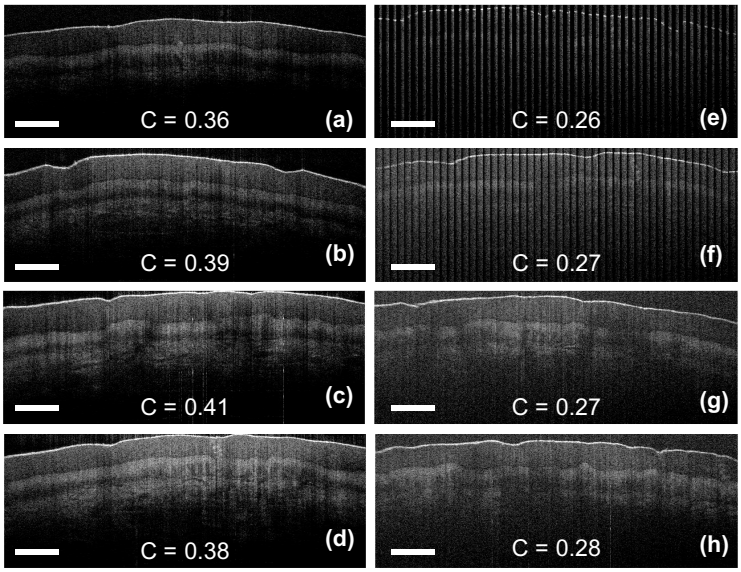

FIGURE 7.10: Example B-scans from a healthy volunteer hand palm skin of 1.6 mm x 4 mm, obtained using: (a-d) ML-SC; (e-h) QS-SC. Exposure time in each row: 20 µs, 40 µs, 100 µs and 150 µs, respectively (scale bar 450 µm).

the x and y directions. Then, the remaining motion in the z-direction can be compensated through conventional algorithms, if further volume processing would be considered. In terms of image quality, conclusions can be drawn similar to those from imaging the IR card above. Figures 7.10 and 7.11 confirm that 20 µs and 40 µs are too short exposure times and during such intervals the number of pulses is less than one. As soon as there are a few more pulses per readout, the QS-SC reaches similar image quality compared to the ML-SC. A difference of 20 % is obtained in the contrast. In the case of the en-face display of Figure 7.11, the problem of black stripes due to readouts containing no pulses is very important. The images acquired at 20 µs and 40 µs show almost no structural information.

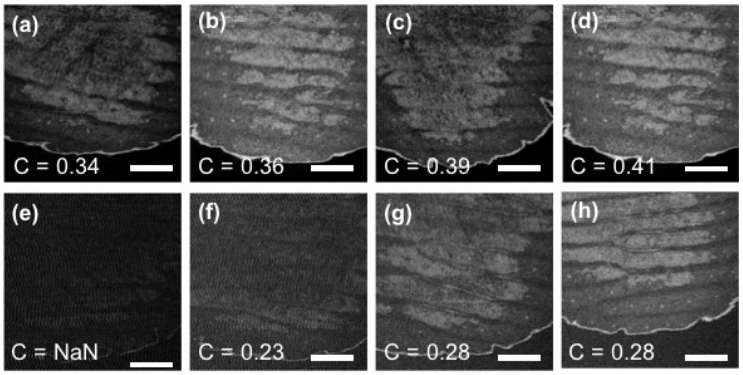

FIGURE 7.11: Example of 4 mm x 4 mm C-scans extracted from a volume acquired from a healthy volunteer hand palm skin. (a-d): ML-SC based C-scans and(e-h): QS-SC based C-scans. Exposure times 20 µs, 40 µs, 100 µs and 150 µs. (scale bar 1 mm) – (NaN means that the contrast cannot be calculated for the 20 µs QS-SC image due to lack of signal).

7.10 Conclusion

In this chapter, a QS-SC have been used for UHR-OCT in the wavelength range of 1300 nm. First, it is shown that the QS-SC shows much more stable behaviour compared to the ML-SC. This is of importance for OCT in order to reduce the pulse to pulse fluctuations causing very high RIN. Though, this stability is to be considered together with the repetition

rate of each SC source. Indeed, the QS-SC operates at a much lower repetition rate compared to the ML-SC. Then, an analysis of OCT A-scan noise floor showed that the QS-SC exhibits noise much higher than the ML-SC if long exposure time are considered, differences up to 20 dB are observed. However, the QS-SC noise level is comparable, within 10 dB, to the ML-SC used with short exposure time of 20 µs. Finally, two examples of images are presented where it is shown that the QS-SC can obtain acceptable image quality, similar to the ML-SC, at long exposure time. In addition to the demonstrated operation in the 1300 nm range, the QS-SC source is suitable for operation either at shorter wavelengths (800 nm range) or even at longer wavelengths (1700 nm, 2000 nm range). In conclusion, the QS-SC looks to be a very interesting alternative SC source offering identical extremely broad spectrum to that of a ML-SC but at a much lower cost.

References

[1] J. Yi, Q. Wei, W. Liu, V. Backman, and H. F. Zhang. Visible-light optical coherence tomography for retinal oximetry. *Opt. Lett.*, 38(11):1796–1798, Jun 2013. doi: 10.1364/OL.38.001796. URL http://ol.osa.org/abstract.cfm?URI=ol-38-11-1796.

[2] J. Kim, W. Brown, J. R. Maher, H. Levinson, and A. Wax. Functional optical coherence tomography: Principles and progress. *Physics in medicine and biology*, 60(10):R211–R237, 05 2015. doi: 10.1088/0031-9155/60/10/R211. URL http://www.ncbi.nlm.nih.gov/pmc/articles/PMC4448140/.

[3] M. J. Marques, A. Bradu, and A. Podoleanu. Towards simultaneous talbot bands based optical coherence tomography and scanning laser ophthalmoscopy imaging. *Biomed. Opt. Express*, 5(5):1428–1444, May 2014. doi: 10.1364/BOE.5.001428. URL http://www.osapublishing.org/boe/abstract.cfm?URI=boe-5-5-1428.

[4] X. Shu, M. Bondu, B. Dong, A. Podoleanu, L. Leick, and H. F. Zhang. Single all-fiber-based nanosecond-pulsed supercontinuum

source for multispectral photoacoustic microscopy and optical coherence tomography. *Opt. Lett.*, 41(12):2743–2746, Jun 2016. doi: 10.1364/OL.41.002743. URL http://ol.osa.org/abstract.cfm?URI=ol-41-12-2743.

[5] U. Møller, S. T. Sørensen, C. Jakobsen, J. Johansen, P. M. Moselund, C. L. Thomsen, and O. Bang. Power dependence of supercontinuum noise in uniform and tapered pcfs. *Opt. Express*, 20(3):2851–2857, Jan 2012. doi: 10.1364/OE.20.002851. URL http://www.opticsexpress.org/abstract.cfm?URI=oe-20-3-2851.

[6] M. Maria, I. B. Gonzalo, M. Bondu, R. D. Engelsholm, T. Feuchter, P. M. Moselund, L. Leick, O. Bang, and A. Podoleanu. A comparative study of noise in supercontinuum light sources for ultra-high resolution optical coherence tomography. volume 10056, pages 100560O–100560O–6, 2017. doi: 10.1117/12.2251500. URL http://dx.doi.org/10.1117/12.2251500.

[7] T. Werblinski, S. R. Engel, R. Engelbrecht, L. Zigan, and S. Will. Temperature and multi-species measurements by supercontinuum absorption spectroscopy for ic engine applications. *Opt. Express*, 21(11):13656–13667, Jun 2013. doi: 10.1364/OE.21.013656. URL http://www.opticsexpress.org/abstract.cfm?URI=oe-21-11-13656.

[8] W. T. Silfvast. Special laser cavity and cavity effects. In *Laser Fundamentals*, chapter 13, pages 434–488. Cambridge, 2008.

[9] O. Schmidt, J. Rothhardt, F. Röser, S. Linke, T. Schreiber, K. Rademaker, J. Limpert, S. Ermeneux, P. Yvernault, F. Salin, and A. Tünnermann. Millijoule pulse energy q-switched short-length fiber laser. *Opt. Lett.*, 32(11):1551–1553, Jun 2007. doi: 10.1364/OL.32.001551. URL http://ol.osa.org/abstract.cfm?URI=ol-32-11-1551.

[10] H. A. Haus. Mode-locking of lasers. *IEEE Journal of Selected Topics in Quantum Electronics*, 6(6):1173–1185, Nov 2000. ISSN 1077-260X. doi: 10.1109/2944.902165.

[11] P. C. Teh, Y. H. Ho, C. E. Ong, S. C. Lee, and P. S. Teh. Compact, all fiber picosecond mopa for supercontinuum generation. In *2016 IEEE 6th International Conference on Photonics (ICP)*, pages 1–3, March 2016. doi: 10.1109/ICP.2016.7510019.

[12] Datasheet SuperK Extreme. http://www.nktphotonics.com/lasers-fibers/product/superk-extreme-supercontinuum-lasers/, . Accessed: 2017-07-31.

[13] Datasheet SuperK Compact. http://www.nktphotonics.com/lasers-fibers/product/superk-compact-supercontinuum-lasers/, . Accessed: 2017-07-31.

[14] A. Kudlinski, B. Barviau, A. Leray, C. Spriet, L. Héliot, and A. Mussot. Control of pulse-to-pulse fluctuations in visible supercontinuum. *Opt. Express*, 18(26):27445–27454, Dec 2010. doi: 10.1364/OE.18.027445. URL http://www.opticsexpress.org/abstract.cfm?URI=oe-18-26-27445.

[15] W. Drexler and J. G. Fujimoto. In *Optical Coherence Tomography - Technology and Applications*, chapter 5. Springer, 2015.

[16] X. Yao, Y. Gan, C. C. Marboe, and C. P. Hendon. Myocardial imaging using ultrahigh-resolution spectral domain optical coherence tomography. *Journal of Biomedical Optics*, 21(6):061006, 2016. doi: 10.1117/1.JBO.21.6.061006. URL http://dx.doi.org/10.1117/1.JBO.21.6.061006.

[17] S. H. Yun, G. J. Tearney, B. E. Bouma, B. H. Park, and J. F. de Boer. High-speed spectral-domain optical coherence tomography at 1.3 μm wavelength. *Opt. Express*, 11(26):3598–3604, Dec 2003. doi: 10.1364/OE.11.003598. URL http://www.opticsexpress.org/abstract.cfm?URI=oe-11-26-3598.

[18] X. Yu, X. Liu, S. Chen, Y. Luo, X. Wang, and L. Liu. High-resolution extended source optical coherence tomography. *Opt.*

Express, 23(20):26399–26413, Oct 2015. doi: 10.1364/OE.23.026399. URL http://www.opticsexpress.org/abstract.cfm?URI=oe-23-20-26399.

[19] C. S. Cheung, M. Tokurakawa, J. M. O. Daniel, W. A. Clarkson, and H. Liang. Long wavelength optical coherence tomography for painted objects. volume 8790, pages 87900J–87900J–5, 2013. doi: 10.1117/12.2021700. URL http://dx.doi.org/10.1117/12.2021700.

Chapter 8

Conclusion and future work

As proposed in the introduction Chapter, two main topics have been discussed in the thesis. The first topic was the problem of signal processing in Optical Coherence Tomography (OCT) and Ultra-High Resolution-OCT (UHR-OCT). The second topic was the impact of noise due to Supercontinuum (SC) light sources in Spectral Domain-OCT (SD-OCT).

8.1 Complex Master/Slave Interferometry related topics

Signal processing is an important part of the work required in order to produce an OCT image. As described in Chapter 4, some of the processing steps are compulsory and common to any OCT technique. Such steps are detector noise correction, background subtraction or conversion to logarithmic scale. Different procedures can be applied for analysing the frequency content of the interference fringes. If considering conventional FD-OCT, resampling and dispersion compensation are compulsory for achieving an accurate depth reflectivity profile. Otherwise, if Complex Master Slave Interferometry (CMSI) is used, no resampling nor dispersion compensation are needed to infer a correct depth reflectivity profile. Within this thesis, processing dedicated to both conventional OCT and CMSI have been presented in detail. Several conclusions can be drawn regarding the alternative CMSI based OCT compared to FFT based OCT. First, CMSI effectively allows to measure a depth reflectivity profile using a comparison scheme of spectral shapes and pre-generated signals called Masks. With no FFT and

hence no resampling neither dispersion compensation, CMSI measures accurately the same information as a fully corrected FFT based OCT procedure. The second conclusion relates to the sensitivity achievable with the CMSI. If comparing CMSI based and FFT based sensitivity values obtained from the exact same data set, no differences have been observed. This tells us that the two methods are behaving similarly in terms of the noise properties when considering Low Coherent Interferometry principle. Regarding axial resolution consideration, some small advantage was noticed when using the FFT based algorithm which included resampling and dispersion compensation. Even though this advantage was small, this suggests that the CMSI procedure presented in the thesis was not optimal. However, the results reported in the thesis have been obtained based on the work done during the first half of the PhD (March 2014 – September 2015). Since then, the CMSI method was further sophisticated and now no difference is observed in the axial resolution between FFT based and CMSI based OCT.

Master-Slave Interferometry is a relatively new principle (2013). Even more, the method presented in this thesis, CMSI is only 2 years old. This means that the method is relatively young and that multiple future avenues can be pursued. However, only a few will be mentioned here. One of the most interesting would certainly be a study on live updating the Masks during the very imaging step in order to compensate for sample dispersion and then reach transform limited point spread function at any depth within the sample. Still within the topic of dispersion in OCT, due to the insensitivity to dispersion effects arising from the system, CMSI seems well suited for spectroscopic applications. Indeed, any remaining dispersive effects detected while using the CMSI procedure can come only from the sample itself. Then, a measure of those dispersive effects can be turned into information. Also, another advantage of the CMSI technique is that some preprocessing steps can be performed during the generation of Masks. Processing steps such as normalization and apodization are usually done after the readout acquisition in a FFT based scheme. Such a processing procedure is not time efficient. Using CMSI, those steps could be computed within the Masks generation step with the direct consequence of speeding up the imaging step.

8.2 Noise from SC source and OCT

The second topic and also the main topic discussed during the thesis is the impact of noise from SC sources in a SD-OCT system. Three Chapters of the thesis have been dedicated to this discussion.

The study of Chapter 5 relies on the current generation of commercial SC sources based on pumping a Photonic Crystal Fibre (PCF) close to its Zero Dispersion Wavelength (ZDW). In this chapter, it is shown that increasing the source repetition rate can lead to reduction of the extension of the Relative Intensity Noise (RIN) dominated regime over the dynamic range of the spectrometer camera. Using a repetition rate of 320 MHz, a shot noise dominated regime is achievable between 10 % and 25-30 % of the dynamic range of the camera considering exposure time in the range of 20 µs. Operating under shot noise limited regime for the OCT system leads to an increase of the Signal to Noise Ratio (SNR) of about 3-4 dB compared to the RIN dominated regime. Also, by extrapolating on the current data, a SC source operating at a repetition rate of 800 MHz to 1 GHz should enable an almost complete reduction of the source RIN impact into the OCT system. More accurately, it should reduce the RIN impact to a value smaller than the shot noise one and hence it could lead to a maximized SNR. Such a source could be assembled by playing with the balance of peak power versus average power of the SC source pump. The SC sources used in Chapter 5 have shown a spectral extension much larger than what is required for OCT in the 1300 nm region. Therefore, a decrease of the SC pump peak power can be implemented in order to reduce the average power without impairing the overall spectral bandwidth necessary for the OCT. This lower average power condition can be used in order to increase the repetition rate of the source without any risk of damaging the PCF. This peak power reduction together with an increase of repetition rate for noise reduction is possible only because the impact of both parameters on the total noise in the OCT system is different. Repetition rate increase is much more efficient than peak power increase. For example, from Chapter 5, a peak power drop of 50 % still leaves the system with large enough spectral bandwidth but also offers the possibility of doubling the pump repetition rate. Such improvement will

increase the SNR by almost 3 dB, placing the OCT system in a regime very close to shot noise dominated regime over the entire camera dynamic range.

The second study conducted regarding noise and OCT was presented in Chapter 6. In this study, the SC source design has been changed from long pulse to ultra-short pulse for the SC pump. Also, the PCF have been changed so that the fibre dispersion profile is all-normal ($D < 0$ ps.nm^{-1}.km^{-1}) instead of both anomalous ($D > 0$ ps.nm^{-1}.km^{-1}) and normal depending on the wavelength considered. By changing the SC source design from the previously described one (ps pumped close to the fibre ZDW) to the proposed one (fs pumped with all-normal dispersion fibre), the SC generation is based on deterministic non-linear effects such as Self-Phase Modulation and Optical Wave Breaking. This new concept is in opposition to the SC source design used in Chapter 5, based on non-linear effects such as Modulation Instability and Solitons. The new SC source has been assembled and tested into an SD-OCT system operating within the 1300 nm wavelength region. After SC generation, the spectrum covered a spectral region from 700 nm to 1400 nm. For the SD-OCT, the red side of the SC is used and it covered almost the entire spectral range of the spectrometer (from 1070 nm up to 1470 nm). The new SC source was used for SD-OCT imaging of skin where similar image quality was obtained compared to the conventional SC source design, with the additional advantage of less RIN level. It is shown that the deterministic SC source has a noise profile similar to a SLD source but with larger bandwidth and higher power. Nevertheless, the source built during this project was a simple proof of concept and several points need to be improved. The most important problem encountered during this project was the temporal source stability. The femtosecond laser used a compression block in bulk and therefore provided a free space collimated beam. Then, a free space to fibre coupling of light was required for injection into the PCF. This coupling was extremely unstable due to the high average power from the laser and the small core of the PCF. This critical point leads to high thermal effects at the fibre facet and inside the fibre. Several instances when the fibre was destroyed have been observed during the project. An interesting improvement for the source would be to consider a fibre based connection

between the source and the PCF. Also, during the study a commercial femtosecond source was used. A minimal pulse length of 170 fs and a repetition rate of 80 MHz lead to a high average power into the fibre however necessary to achieve a smooth SC spectrum. A shorter optical pulse could achieve a smooth spectrum for a lower average power into the fibre and then a minimal risk of fibre destruction.

The last chapter of the thesis is dedicated to a demonstration of a low-cost SC source for OCT imaging. Such SC source could be used if considering longer exposure times compared to the exposure times of current fast OCT systems. The current high cost of SD-OCT technology is to be attributed mainly to the laser cost and the spectrometer cost. In this chapter, it is proposed to use a SC source based on Q-switch technology for the SC pump instead of the conventional Mode-locked technology. The advantage of using a Q-switched-pump is its much lower cost compared to the Mode-locked one. A large technical difference between both lasers types is their repetition rate of operation. While Mode-Locked lasers can achieve hundreds of MHz and even GHz repetition rate, Q-switched lasers are limited to the kHz regime (a few tens to a few hundreds of kHz). This parameter affects the SNR of the SD-OCT system as the source RIN impact is modified by the number of pulses detected during an exposure time of the camera. However, we have shown that a QS based SC (QS-SC) source shows a much more stable pulse-to-pulse behaviour compared to a ML based SC (ML-SC). Then, the QS-SC source can be used for OCT at the only cost of increasing the exposure time of the camera to value in the range of 100 µs. Doing so, the images obtained with the QS-SC are comparable to the images obtained with the ML-SC source. Also, the OCT systems considered in this study operates in the 1300 nm region. Nevertheless, the QS-SC source presents a flat spectrum covering from 600 nm to 2400 nm. It would be interesting to investigate the usefulness of such a SC source at other wavelength range than 800 nm or 1700-2000 nm. Such a source can be a first step towards lowering the cost of SD-OCT system. Its current cost is less than 10 % compared to the cost of the ML-SC commonly used for OCT.

In a more general view and as a final conclusion, fibre-based SC sources are by far one of the most interesting optical source for SD-OCT. Due to their

ultra-broad spectrum, their high spatial coherence and large average power, they are one of the very few options available for driving OCT systems (from visible to far Infra-Red). Over the years, considerable work has been devoted to ameliorate the issue related to the high RIN that limits their usefulness in OCT. Nowadays, fibre-based SC sources have spread among most of the research groups working on SD-OCT. Essential for further progress is for academia to liaise with industry and enhance the utility of SC source. An example in this direction was the launch of the UBAPHODESA Marie Curie collaborative training school involving a leading research group in high resolution optical medical imaging (Applied Optics Group – University of Kent) and the world leader in SC source manufacturing (NKT Photonics A/S). This collaboration has led to numerous results in applications such as Microscopy, Photo-acoustic imaging and SD-OCT.

Appendix A

Complex Master-Slave Interferometry

- A. Bradu, **M. Maria** , and A. Podoleanu, "Demonstration of tolerance to dispersion of master/slave interferometry," Opt. Express 23, 14148-14161 (2015). https://www.osapublishing.org/oe/abstract.cfm?uri=oe-23-11-14148

Complex master slave interferometry

Sylvain Rivet,[1,2,*] Michael Maria,[1,3] Adrian Bradu,[1] Thomas Feuchter,[3] Lasse Leick,[3] and Adrian Podoleanu[1]

[1]*Applied Optics Group, School of Physical Sciences, University of Kent, Canterbury CT2 7NH, UK*
[2]*Université de Bretagne Occidentale, EA 938 Laboratoire de Spectrométrie et Optique Laser, 6 avenue Le Gorgeu, C.S. 93837, 29238 Brest Cedex 3, France*
[3]*NKT Photonics A/S, Blokken 84, DK-3460 Birkerod, Denmark*
[*]*sylvain.rivet@univ-brest.fr*

Abstract: A general theoretical model is developed to improve the novel Spectral Domain Interferometry method denoted as Master/Slave (MS) Interferometry. In this model, two functions, *g* and *h* are introduced to describe the modulation chirp of the channeled spectrum signal due to nonlinearities in the decoding process from wavenumber to time and due to dispersion in the interferometer. The utilization of these two functions brings two major improvements to previous implementations of the MS method. A first improvement consists in reducing the number of channeled spectra necessary to be collected at Master stage. In previous MSI implementation, the number of channeled spectra at the Master stage equated the number of depths where information was selected from at the Slave stage. The paper demonstrates that two experimental channeled spectra only acquired at Master stage suffice to produce A-scans from any number of resolved depths at the Slave stage. A second improvement is the utilization of complex signal processing. Previous MSI implementations discarded the phase. Complex processing of the electrical signal determined by the channeled spectrum allows phase processing that opens several novel avenues. A first consequence of such signal processing is reduction in the random component of the phase without affecting the axial resolution. In previous MSI implementations, phase instabilities were reduced by an average over the wavenumber that led to reduction in the axial resolution.

OCIS codes: (110.4500) Optical coherence tomography; (120.3890) Medical optics instrumentation; (110.4190) Multiple imaging; (170.4460) Ophthalmic optics and devices.

References and links

1. J. G. Fujimoto, "Optical coherence tomography for ultrahigh resolution in vivo imaging," Nat. Biotechnol. **21**(11), 1361–1367 (2003).
2. D. Huang, E. A. Swanson, C. P. Lin, J. S. Schuman, W. G. Stinson, W. Chang, M. R. Hee, T. Flotte, K. Gregory, C. A. Puliafito, and J. G. Fujimoto, "Optical coherence tomography," Science **254**(5035), 1178–1181 (1991).
3. Z. Hu and A. M. Rollins, "Fourier domain optical coherence tomography with a linear-in-wavenumber spectrometer," Opt. Lett. **32**(24), 3525–3527 (2007).
4. V. M. Gelikonov, G. V. Gelikonov, and P. A. Shilyagin, "Linear-wavenumber spectrometer for high-speed spectral-domain optical coherence tomography," Opt. Spectrosc. **106**(3), 459–465 (2009).
5. A. Payne and A. G. Podoleanu, "Direct electronic linearization for camera-based spectral domain optical coherence tomography," Opt. Lett. **37**(12), 2424–2426 (2012).
6. M. Wojtkowski, V. Srinivasan, T. Ko, J. Fujimoto, A. Kowalczyk, and J. Duker, "Ultrahigh-resolution, high-speed, Fourier domain optical coherence tomography and methods for dispersion compensation," Opt. Express **12**(11), 2404–2422 (2004).
7. C. C. Rosa, J. Rogers, and A. G. Podoleanu, "Fast scanning transmissive delay line for optical coherence tomography," Opt. Lett. **30**(24), 3263–3265 (2005).
8. C. Yang, S. Yazdanfar, and J. A. Izatt, "Fast scanning, dispersion-adjustable reference delay for OCT using fiber Bragg gratings," Proc. SPIE **5140**, 53–59 (2003).

#255422 Received 9 Dec 2015; revised 20 Jan 2016; accepted 27 Jan 2016; published 4 Feb 2016

9. Y. Yasuno, V. D. Madjarova, S. Makita, M. Akiba, A. Morosawa, C. Chong, T. Sakai, K.-P. Chan, M. Itoh, and T. Yatagai, "Three-dimensional and high-speed swept-source optical coherence tomography for in vivo investigation of human anterior eye segments," Opt. Express **13**(26), 10652–10664 (2005).
10. N. Lippok, S. Coen, P. Nielsen, and F. Vanholsbeeck, "Dispersion compensation in Fourier domain optical coherence tomography using the fractional Fourier transform," Opt. Express **20**(21), 23398–23413 (2012).
11. K. K. H. Chan and S. Tang, "High-speed spectral domain optical coherence tomography using non-uniform fast Fourier transform," Biomed. Opt. Express **1**(5), 1309–1319 (2010).
12. B. Hofer, B. Povazay, B. Hermann, A. Unterhuber, G. Matz, F. Hlawatsch, and W. Drexler, "Signal post processing in frequency domain OCT and OCM using a filter bank approach," Proc. SPIE **6443**, 64430O (2007).
13. A. Yang, F. Vanholsbeeck, S. Coen, and J. Schroeder, "Chromatic dispersion compensation of an OCT system with a programmable spectral filter," Proc. SPIE **8091**, 809125 (2011).
14. Y. Watanabe and T. Itagaki, "Real-time display SD-OCT using a linear-in-wavenumber spectrometer and a graphics processing unit," Proc. SPIE **7554**, 75542S (2010).
15. A. G. Podoleanu and A. Bradu, "Master-slave interferometry for parallel spectral domain interferometry sensing and versatile 3D optical coherence tomography," Opt. Express **21**(16), 19324–19338 (2013).
16. A. Bradu and A. G. Podoleanu, "Calibration-free B-scan images produced by master/slave optical coherence tomography," Opt. Lett. **39**(3), 450–453 (2014).
17. A. Bradu, K. Kapinchev, F. Barnes, and A. Podoleanu, "Master slave *en-face* OCT/SLO," Biomed. Opt. Express **6**(9), 3655–3669 (2015).
18. A. Bradu, K. Kapinchev, F. Barnes, and A. Podoleanu, "On the possibility of producing true real-time retinal cross-sectional images using a graphics processing unit enhanced master-slave optical coherence tomography system," J. Biomed. Opt. **20**(7), 076008 (2015).
19. A. Bradu, M. Maria, and A. G. Podoleanu, "Demonstration of tolerance to dispersion of master/slave interferometry," Opt. Express **23**(11), 14148–14161 (2015).
20. A. Bradu and A. G. Podoleanu, "Imaging the eye fundus with real-time en-face spectral domain optical coherence tomography," Biomed. Opt. Express **5**(4), 1233–1249 (2014).
21. J. Wang, A. Bradu, G. Dobre, and A. Podoleanu, "Full-field swept source master slave optical coherence tomography," IEEE Photonics J. **7**(4), 1943 (2015).

1. Introduction

Spectral (or Fourier) domain Interferometry (SDI) is widely spread in many fields of biomedical optics, especially in Optical Coherence Tomography (OCT) [1,2]. SDI encodes distances, thicknesses, scattering properties or refractive indices onto the density of modulation of the optical spectrum, *i.e.* channeled spectrum, at the interferometer output.

To decode the channeled spectrum, SDI uses a Fourier Transform (FT) operation that translates the modulation density into a distance measurement. SDI principles can be applied to systems employing either a broadband optical source (spectrometer based, Sp) or a tunable optical source (swept source, SS). In the case of a Sp system, the channeled spectrum at the interferometer output is read by a camera incorporated within the spectrometer. This channeled spectrum is chirped due to a nonlinear dependence of the pixel position in the camera versus the optical frequency. When a SS system is employed, the temporal signal read by a photodetector at the interferometer output presents a chirp mainly due to non-linear frequency sweeping. We will refer to these chirping effects as due to the decoding process from channeled spectrum. In addition to the chirp due to spectrum decoding, unbalanced dispersion in the interferometer arms also affects the regularity of maxima and minima in the readout channeled spectrum. For a strictly periodic modulation (no chirp) of the channeled spectrum, a FT returns a well-defined peak. The chirp in the spectrum modulation translates into an enlargement and reduction in the amplitude of such a peak, worsening the axial resolution and sensitivity.

In order to correct the chirping before FT, hardware and software methods have been reported. In terms of hardware solutions, a spectrometer using a prism after the diffraction grating [3,4], or chirped sampling using an analogue line scan camera [5] were proposed. Several solutions have also been proposed to compensate for dispersion, using matched lengths of glass [6], spectral delay line [7], fiber Bragg gratings [8]. In terms of software solutions, several methods have also been developed to resample and organize the data linearly along the optical frequency axis, or wavenumber, prior to the FT. Common corrections are based on the interpolation of the phase in order to obtain linearity in k-space

#255422 Received 9 Dec 2015; revised 20 Jan 2016; accepted 27 Jan 2016; published 4 Feb 2016

[9]. More complex techniques based on fractional Fourier transforms [10], non-uniform Fourier Transformation [11], or advanced computational algorithms [12–14] provide a posteriori data resampling.

Master-Slave Interferometry (MSI) is a new approach to SDI to eliminate the chirp effects [15]. The MSI proceeds in two stages. In a first stage (Master), a mirror is used as an object and experimental channeled spectra (CS_{exp}) are measured and stored, for a number P of different values of the optical path difference (OPD) in the interferometer. In a second stage (Slave), the object replaces the mirror and the channeled spectrum is compared with every CS_{exp} saved in the memory block and used as a mask. The comparison operation of each mask with the channeled spectrum was implemented via correlation [15–19] or by simplified dot product procedures for faster implementation of correlation for argument zero [20,21]. The maximum value of each comparison (correlation) is selected to provide the depth information profile (A-scan) at each OPD value selected during the Master stage.

MSI presents several advantages compared to conventional SDI. The process of data resampling performed during measurements is replaced by data storage at the Master stage, which shortens processing time while performing measurements. The quality of data resampling for the conventional FT-based method affects the axial resolution. Advantageously, MSI exhibits a constant resolution over the OPD range which recommends it as a useful tool for metrology and imaging. Each CS_{exp} provides direct access to measurements from that OPD value used at the Master stage to produce it, conferring advantage to MSI in terms of production of *en-face* OCT images. Recently, its tolerance to dispersion in the interferometer has also been demonstrated [19].

Nevertheless, the implementation of MSI reported in previous reports presents some shortcomings, such as:

(i) Typically, a large number of CS_{exp} need to be recorded at the Master stage, a problem especially when using large bandwidth sources. The sampling of the A-scans in depth is determined by the number of CS_{exp} recorded for incremental depths.

(ii) MSI is characterized by a trade-off between phase instability and axial resolution. The phase in the interferometer varies between the step of recording the CS_{exp} and the step of scanning the object to be imaged, considered here as a random phase shift j_{rand}. As the phase is discarded, it is not possible to eliminate its effects. To reduce the effect of the random phase shift, the correlation function is averaged over several lags [15–19] that leads to some deterioration of the axial resolution.

In this paper, an improved method is presented that addresses the above shortcomings. This method, Complex Master Slave Interferometry (CMSI), does not directly use CS_{exp} as masks, contrary to [15–21], but develops a procedure to infer any number of masks from a reduced number of CS_{exp} acquired. Additionally, the masks generated are complex in order to conserve the phase information.

This paper is organized into three theoretical sections and an experimental section. The theoretical sections describe the interferometric signal in a SDI set-up unbalanced from the point of view of dispersion and equipped with a chirped decoder, obtained in conventional MSI [15–21] and in the novel CMSI presented here. The chirp affecting the channeled spectrum at the interferometer output is modeled by two functions g and h. Based on these functions, a procedure of inferring a number of Q channeled spectra (masks) at the Slave stage from a variable number P of CS_{exp}, with $Q>>P$ is then presented. The experimental section demonstrates the conservation of axial resolution over depth for both spectrometer and swept source based SDI methods.

#255422 Received 9 Dec 2015; revised 20 Jan 2016; accepted 27 Jan 2016; published 4 Feb 2016

2. Chirped decoder and interferometer with unbalanced dispersion

2.1. General description of an SDI experimental set-up

In Fig. 1, a SDI schematic diagram is shown, made of two main components, an interferometer and a decoder. The interferometer includes a splitter (shown as a directional coupler), a reference mirror (M), an interface optics that conveys light towards an object (O) subject to tests or imaging. In case the application is spectral domain OCT, the interface optics contains a lateral or transversal galvo-scanner. The decoder block translates the channeled spectrum shape at the interferometer output into an electrical signal. For a spectrometer-based configuration, the source is broadband and the decoder is a spectrometer. For a swept source configuration, the optical source is a swept source laser and the decoder is a fast photodetector.

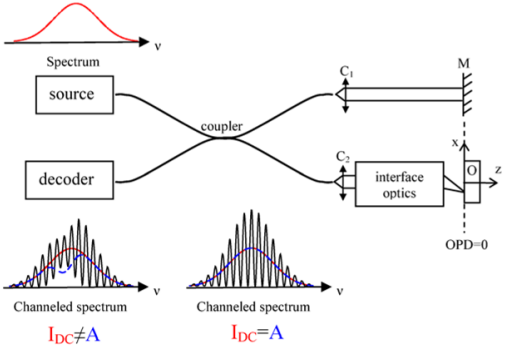

Fig. 1. Block diagram for a spectral domain OCT system. C1 and C2, collimators; M, reference mirror; O, object. Two channeled spectra are shown underneath, for a mirror as a sample. I_{DC} represents the power spectrum of the optical source, shown by the red Gaussian shape solid line. The A shape is shown by the dashed blue line, determined by the interference contrast of the modulating signal proportional to the channeled spectrum. On the left, the usual case in practice is shown when I_{DC}≠A. Here, the interference contrast *A* is deliberately shown smaller on the left side of the spectrum. In this case, A varies below I_{DC} on the left hand side and regains the I_{DC} value on the right. The channeled spectrum on the right shows the ideal case, when I_{DC} = A, i.e. when the contrast profile A and the I_{DC} profile are superposed on each other.

In the following, a mathematical expression of the electrical signal at the output of the interferometer shown in Fig. 1 is obtained, where the decoder performs nonlinearly and dispersion is left unbalanced between the arms of the interferometer.

2.2. Fourier transform of the channeled spectrum

Let us consider a non-uniform distribution of frequencies $\tilde{\nu}$ along the pixels of the line array detector when using a spectrometer, or along time when using a tunable laser. The relationship between the optical frequency n and $\tilde{\nu}$ is given by the function $g(\tilde{\nu})$ = n.

The unbalanced dispersion between the arms of the interferometer can be described by a function *d*(n):

$$d(\nu)=\frac{2\pi}{c}\nu\left[\left(n_2(\nu)-n_2(\nu_0)\right)e_2-\left(n_1(\nu)-n_1(\nu_0)\right)e_1\right], \qquad (1)$$

#255422 Received 9 Dec 2015; revised 20 Jan 2016; accepted 27 Jan 2016; published 4 Feb 2016

where n_1, and n_2 are the refractive indices of the dispersive parts in the reference and in the object arm respectively, e_1 and e_2 their thicknesses and n_0 the central optical frequency of the source.

The electrical signal $I(\tilde{\nu})$ delivered by a non-ideal decoder is a chirped signal according to $\tilde{\nu}$ and can be written as a superposition of a DC term, I_{DC}, and a complex exponential form of a periodic function $I(\tilde{\nu})$ as follows

$$I(\tilde{\nu}) = I_{DC}(g(\tilde{\nu})) + \frac{1}{2}\left(\underline{I}(\tilde{\nu}) + \underline{I}^{*}(\tilde{\nu})\right), \tag{2}$$

where g takes into account the decoding procedure chirp and * corresponds to its complex conjugate. I_{DC} follows the shape of the power spectrum of the optical source (in spectrometer-based configurations and to the tuning bandwidth in swept source configurations).

Considering r the complex reflectivity of the object varying with depth r, the complex electrical signal $I(\tilde{\nu})$ corresponding to the decoded channeled spectrum can be written as a continuous summation of modulations

$$\underline{I}(\tilde{\nu}) = \int r(\rho) A\left(g(\tilde{\nu})\right) Exp\left[i\left(\frac{2\pi}{c} g(\tilde{\nu}) 2\rho + h(\tilde{\nu}) \right)\right] d\rho, \tag{3}$$

where c is the speed of light, $h(\tilde{\nu}) = d(g(\tilde{\nu}))$ is a function depending on the unbalanced dispersion in the interferometer and the nonlinear dependence on $\tilde{\nu}$. The depth r = 0 corresponds to the OPD = 0 in the interferometer. A(n) represents the interference contrast. In practice, A(n) is different from the power spectrum of the optical source, I_{DC}(n) as shown by the left channeled spectrum in Fig. 1. This is due to several additional effects such as polarization mismatching of reference light and object light fields or due to chromatic aberrations introduced by optical components, factors that reduce the axial resolution. Although the amount of unbalanced dispersion due to the object can be incorporated into the overall unbalanced dispersion present within the system, we restrict h to describe the dispersion in the interferometer only. Equation (3) presents the most general expression for the channeled spectrum, which includes the nonlinear dependence on $\tilde{\nu}$ and the dispersion effects.

If the decoder is linear ($g(\tilde{\nu}) = \tilde{\nu} = n$) and the interferometer is perfectly balanced for dispersion ($d \equiv 0$), the inverse Fourier transform of I is directly related to the complex reflectivity r in depth z of the object (A-scan) via the following expression as detailed in Appendix A:

$$\hat{I}\left(\frac{2z}{c}\right) = \hat{I}_{DC}\left(\frac{2z}{c}\right) + \frac{1}{2} r(z) \otimes P_0\left(\frac{2z}{c}\right) + \frac{1}{2} r(-z)^{*} \otimes P_0\left(-\frac{2z}{c}\right)^{*}, \tag{4}$$

where $\hat{I}$ and $\hat{I}_{DC}$ are the inverse FT of I and I_{DC} respectively, $\otimes$ is the convolution operation and P_0 is the axial Point Spread Function (PSF) of the system defined by

$$P_0(t) = FT^{-1}\left[A(\nu)\right]. \tag{5}$$

As shown by Eq. (5), the axial resolution (the width of P_0) does not vary with depth, being only determined by the interference contrast, A(n). This happens in the case of a perfectly dispersion-balanced interferometer interrogated by an ideal decoder (either spectrometer or tuning laser).

In the paper the refractive index and the dispersion of the sample are ignored to simplify the study. All distances are measured in air. In the common practice of conventional FT based OCT methods, the depth in the sample was inferred by dividing the axial depth interval, after

#255422 Received 9 Dec 2015; revised 20 Jan 2016; accepted 27 Jan 2016; published 4 Feb 2016

FT, by the index of refraction of the sample. To compensate sample dispersion, a slab of similar material in the reference arm or a numerical compensation should be used. Similarly, the axial intervals associated to each mask of CMSI are measured in air, therefore they correspond to a depth in the sample obtained by their division to an average index of refraction. As far as sample dispersion is concerned, CMSI should also be used with a slab of similar material in the reference arm or with masks modified by the amount of dispersion to be compensated at each depth.

3. Theory of master-slave interferometry

3.1 Master slave signal

In contrast to conventional spectral (Fourier) domain interferometry, MSI delivers a signal from a single depth, *z*, within the object to be investigated. Initially, for the comparison operation required by the MSI method, correlation was used [15–19]. To improve on the calculation speed, a modified correlation operation was proposed [20,21], reduced to the correlation calculation in lag $\tilde{N} = 0$. This delivers the value of an A-scan at depth *z*, the MSI signal, according to

$$MSI(z) = \left[C(\tilde{N}, z) \right]_{\tilde{N}=0} = \left[\int CS_{\exp}\left(\tilde{\nu} + \tilde{N}, z\right) I\left(\tilde{\nu}\right) d\tilde{\nu} \right]_{\tilde{N}=0}, \tag{6}$$

where *C* is the correlation operation between the channeled spectrum *I* collected when the object is placed in the object arm (Slave stage), and the mask corresponding to the channeled spectrum CS_{exp} collected at the Master stage for an OPD = 2*z*, when the mirror is used as an object.

3.2. Limitations in the MSI practice due to using the CS_{exp} as masks

The experimental channeled spectra $CS_{exp}(z)$ can be written according to

(i) a random phase shift $\varphi_{rand}(z)$ induced by the fluctuations of the OPD between the step of acquiring the channeled spectra to be used as masks and the step of measuring the channeled spectrum *I* associated to the object,

(ii) a coefficient $\alpha(z)$ describing the variation with OPD of the strength of the CS_{exp} collected. This is due for instance to the variation of the amount of light injected into single mode fibers when altering the OPD in the interferometer,

(iii) a complex-valued channeled spectrum *CS*, not affected by the random phase shift. The channeled spectrum *CS* is only affected by the specific modality of decoding the spectrum into an output electric signal, and the dispersion in the interferometer as follows:

$$\underline{CS}(\tilde{\nu}, z) = A\left(g\left(\tilde{\nu}\right)\right) Exp\left[i\left(\frac{2\pi}{c} g\left(\tilde{\nu}\right) 2z + h\left(\tilde{\nu}\right) \right) \right]. \tag{7}$$

According to the considerations (i), (ii) and (iii) above, the experimental channeled spectrum is described by

$$CS_{\exp}\left(\tilde{\nu}, z\right) = \frac{1}{2}\alpha\left(z\right) \underline{CS}\left(\tilde{\nu}, z\right) e^{i\varphi_{rand}(z)} + \frac{1}{2}\alpha\left(z\right) \underline{CS}\left(\tilde{\nu}, z\right)^{*} e^{-i\varphi_{rand}(z)}. \tag{8}$$

Note that no DC component appears in Eq. (8) because a high-pass filter is applied on each saved CS_{exp}.

Combining Eqs. (6)-(8), the MSI signal can be written as

#255422 Received 9 Dec 2015; revised 20 Jan 2016; accepted 27 Jan 2016; published 4 Feb 2016

$$MSI(z)=\frac{1}{2}\alpha(z)e^{-i\varphi_{rand}(z)}\int \underline{CS}(\tilde{\nu},z)^{*}\ \underline{I}(\tilde{\nu})d\tilde{\nu}+CC, \tag{9}$$

where CC stands for Complex Conjugate, or using the complex exponential form of I (Appendix B), as

$$MSI(z)=\frac{1}{2}\Re e\left\{\alpha(z)e^{-i\varphi_{rand}(z)}\int \underline{CS}(\tilde{\nu},z)^{*}\ \underline{I}(\tilde{\nu})d\tilde{\nu}\right\}, \tag{10}$$

where $Re\{\}$ denotes the real part of the complex function within the curly brackets. Equation (10) is valid for an object positioned outside OPD = 0 (Appendix B).

In order to present the relationship between the MSI signal and the reflectivity r of the object, a complex function $\gamma(z)$ is defined by

$$\gamma(z)=\int \underline{CS}(\tilde{\nu},z)^{*}\ \underline{I}(\tilde{\nu})d\tilde{\nu}. \tag{11}$$

Using the expression of the CS given by Eq. (7) and the expression of the complex channeled spectrum I given by Eq. (3), $\gamma(z)$ can be expressed as

$$\gamma(z)=\iint r(\rho)\ \left|A\left(g(\tilde{\nu})\right)\right|^{2}\ Exp\left[-i\left(\frac{2\pi}{c}g(\tilde{\nu})\times 2(z-\rho)\right)\right]d\rho\, d\tilde{\nu}. \tag{12}$$

As the same amount of unbalanced dispersion $h(\tilde{\nu})$ is present in both CS_{exp} and I, (and consequently in their complex forms CS_{exp} and I), the effect of unbalanced dispersion is totally eliminated in Eq. (12). A change of variable, $\delta = z\text{-}r$, allows us to rewrite Eq. (12) as

$$\gamma(z)=\iint r(z-\delta)\ \left|A\left(g(\tilde{\nu})\right)\right|^{2}\ exp\left[-i\left(\frac{2\pi}{c}g(\tilde{\nu})2\delta\right)\right]d\delta\, d\tilde{\nu}. \tag{13}$$

Let us denote P_1 as

$$P_1(t)=\int\left|A\left(g(\tilde{\nu})\right)\right|^{2}\ Exp\left[-i\,2\pi\, g(\tilde{\nu})t\right]d\tilde{\nu}. \tag{14}$$

In case $g(\tilde{\nu})=\tilde{\nu}=$ n, we recognize $P_1(t)$ as the axial PSF of the system, similar to Eq. (5). Here the power of the interference contrast A is squared because both the masks CS_{exp} and I depend on A. Using Eq. (14) in Eq. (13), $\gamma(z)$ can be expressed as a convolution product between the complex reflectivity profile of the object $r(z)$ and the function $P_1(2z/c)$:

$$\gamma(z)=\int r(z-\delta)\,P_1(2\delta/c)\,d\delta=r(z)\otimes P_1(2z/c), \tag{15}$$

Let us consider G as the inverse function of g, $G(g)\equiv 1$. Using a change of variable $g(\tilde{\nu})=$ n, the function P_1 can be expressed as follows

$$P_1(t)=\int\left|A(\nu)\right|^{2}\ Exp\left[-i\,\nu\, t\right]G'(\nu)\,d\nu, \tag{16a}$$

where G'(n) is the derivative of G(n) in respect to n. Via a Fourier transform, Eq. (16a) can be written as

$$P_1(t)=FT^{-1}\left[\left|A(\nu)\right|^{2}G'(\nu)\right]. \tag{16b}$$

As a more general description for the MSI operation, the MSI signal for OPD = 2z can be expressed as the convolution product between the depth-resolved complex reflectivity r and the axial PSF $P_{1,}$ defined in Eq. (16b), by

#255422 Received 9 Dec 2015; revised 20 Jan 2016; accepted 27 Jan 2016; published 4 Feb 2016

$$MSI(z)=\frac{\alpha(z)}{2}\Re\mathrm{e}\left\{e^{i\varphi_{rand}(z)}\left(r(z)\otimes P_1(2z/c)\right)\right\}. \tag{17}$$

Equation (17) shows that the reflectivity of the sample measured via the MSI method is independent of the amount of dispersion left unbalanced, meaning that the axial resolution is not affected. This property has already been demonstrated in [19]. Additionally, as the decoding non-linearity described by *G'* is the same at all OPD values, the axial resolution is also independent on *z* but it is not optimal, as Eq. (16b) involves the square of A than simply A in Eq. (5). For instance if *A* has a Gaussian shape, the axial resolution is $\sqrt{2}$ poorer than the axial resolution obtained with the FT method without any unbalanced dispersion and nonlinearities. An improvement in the practice of MSI would be to eliminate the shape of *A* from the masks in Eq. (10) as suggested by the theoretical model in [19] but not done in [15–18,20,21]. Equation (17) also shows that combination of phase in the complex r with the random phase impedes the recovery of the complex r.

In order to address this problem, we propose to use complex masks, as we describe in the next section.

4. Complex master-slave interferometry

The main idea of CMSI is to generate, during the Master stage, a complex function incorporating two phenomena: (i) the non-uniform distribution along the axis, $\tilde{\nu}$, of the detector (pixel for spectrometer or time slot for swept source) due to the nonlinearities in the decoder, function *g*, and (ii) the unbalanced dispersion of the interferometer, function *h*. The masks to be used in CMSI at the Slave stage are then to be obtained from this complex function, evaluated in as many OPD = 2*z* values as the user requires, independently from the OPD values used to measure the CS_{exp}.

4.1 Extraction of the functions g($\tilde{\nu}$) and h($\tilde{\nu}$) at the master stage

In CMSI, it is possible to infer the masks from a Mask function M_{built} created by calculating the functions $g(\tilde{\nu})$ and $h(\tilde{\nu})$ from data acquired in the Master stage, when a number *P* of CS_{exp} are recorded for *P* OPD values. These experimental channeled spectra are then extended into their complex exponential form CS_{exp} according to a procedure described in Appendix C. Their corresponding phases $\mathrm{f}^{\exp}(\tilde{\nu}, z)$ are obtained by extracting the arguments of CS_{exp}. The phase $\mathrm{f}^{\exp}(\tilde{\nu}, z)$ is expressed according to

$$\phi^{\exp}(\tilde{\nu},z)=\frac{2\pi}{c}g(\tilde{\nu})\,2z+h(\tilde{\nu})+\varphi_{rand}(z). \tag{18}$$

A partial derivative of Eq. (18) in respect to $\tilde{\nu}$ removes the random phase and leads to

$$\frac{\partial}{\partial\tilde{\nu}}\phi^{\exp}(\tilde{\nu},z)=\frac{2\pi}{c}g'(\tilde{\nu})\,2z+h'(\tilde{\nu}), \tag{19}$$

where $g'(\tilde{\nu})$ and $h'(\tilde{\nu})$ are the derivatives of $g(\tilde{\nu})$ and $h(\tilde{\nu})$.

A linear regression according to *z* permits to retrieve the slope $4\pi g'(\tilde{\nu}_i)/c$ and the y-intercept $h'(\tilde{\nu}_i)$ for each $\tilde{\nu}_i$ of the channeled spectrum, and build $4\pi g'(\tilde{\nu})/c$ and $h'(\tilde{\nu})$ along the spectral coordinate $\tilde{\nu}$. Then an indefinite integration is used to infer $4\pi g(\tilde{\nu})/c$ and $h(\tilde{\nu})$. Figure 2 describes the step by step procedure of obtaining the set of functions *g* and *h* from an experimental set of CS_{exp}, and then the Mask function M_{built}.

#255422 Received 9 Dec 2015; revised 20 Jan 2016; accepted 27 Jan 2016; published 4 Feb 2016

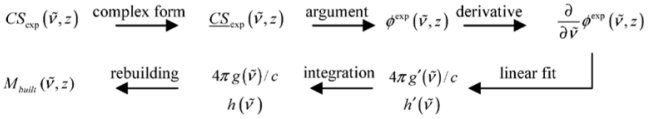

Fig. 2. Step by step procedure to infer the Mask function from a reduced set of experimentally measured channeled spectra.

By retaining the phase of the CS_{exp} only, the spectral amplitude of the Mask functions M_{built} is flat. The elimination of the spectral dependence of the masks used by CMSI leads to an optimum axial resolution related to $FT^{-1}[A]$ as it will be demonstrated in Section 4.3 below.

4.2 Complex MSI signal

The Mask function M_{built} to be used by the CMSI, is defined at the OPD = 2z as

$$M_{built}(\tilde{\nu},z) = g'(\tilde{\nu})\ Exp\left[i\left(\frac{2\pi}{c}g(\tilde{\nu})2z + h(\tilde{\nu})\right)\right], \tag{20}$$

where $g'(\tilde{\nu})$ is the derivative of $g(\tilde{\nu})$. CMSI signal is defined similarly to Eq. (6) by the following integral

$$\mathrm{CMSI}(z) = \int M^{*}_{built}(\tilde{\nu},z)\ I(\tilde{\nu})\,d\tilde{\nu}. \tag{21}$$

CMSI involves a similar definition to the MSI except that the CS_{exp} used as masks are replaced by a complex function with the adjustable parameter z. CMSI is valid for an object set outside OPD = 0, *i.e.* 2z should be larger than the coherence length L_c of the light source (inverse proportional to the bandwidth of the optical source in Sp-OCT and to the tuning bandwidth in SS-OCT).

4.3 Relation between CMSI and reflectivity r in depth

By using the complex exponential form of I, CMSI can be written as follows (Appendix D)

$$\mathrm{CMSI}(z) = \frac{1}{2}\int M^{*}_{built}(\tilde{\nu},z)\ \underline{I}(\tilde{\nu})\,d\tilde{\nu}, \tag{22}$$

and the operation of the CMSI can be described by

$$\mathrm{CMSI}(z) = \frac{1}{2}\iint r(\rho)\,A(g(\tilde{\nu}))\ \ Exp\left[-i\left(\frac{2\pi}{c}g(\tilde{\nu})\times 2(z-\rho)\right)\right] g'(\tilde{\nu})\,d\tilde{\nu}\,d\rho, \tag{23}$$

according to Eq. (20) and Eq. (3). Changes of variable n = $g(\tilde{\nu})$ and $\delta = z$-r are carried out in Eq. (23) leading to

$$\mathrm{CMSI}(z) = \frac{1}{2}\iint r(z-\delta)\,A(\nu)\,Exp\left[-i\frac{2\pi}{c}\nu 2\delta\right] d\nu\,d\delta. \tag{24}$$

Equation (24) can be rewritten as a convolution product between the complex reflectivity profile $r(z)$ and the point spread function P_0

$$\mathrm{CMSI}(z) = \frac{1}{2}r(z)\otimes P_0(2z/c), \tag{25}$$

#255422 Received 9 Dec 2015; revised 20 Jan 2016; accepted 27 Jan 2016; published 4 Feb 2016

for $2z>L_c$ where P_0 is the axial PSF defined by Eq. (5) and equal to $FT^{-1}[A]$.

Again, depth information profile is extracted and expressed as a convolution product between a complex reflectivity function and the ideal PSF of the system, which leads to a constant axial resolution in depth irrespective of the non-linearity of the decoder and irrespective of the amount of the unbalanced dispersion in the interferometer.

The drawbacks of the previous implementations of MSI addressed by CMSI are: (i) the depth points of the A-scan are now determined by a sampling parameter z, independent of the OPD values used to acquire the CS_{exp} in the Master stage, (ii) CMSI operation returns a complex signal, hence phase of r is conserved. Moreover, the building of the Mask function does not depend on the random phase shift as it will be shown in Section 5, which eliminates the need for averaging over an interval of lag wavenumbers (window in [15–19], practiced in previous MSI reports). (iii) The axial resolution is related to $FT^{-1}[A]$, as for a perfect interferometer.

5. Experimental results

5.1 Discrete formulation of the CMSI operation

As with the MSI, CMSI has been described above by continuous variables, however practical implementations involve digital processing. Let $M_{built}(n, q)$ be the complex mask inferred at the Master stage, where n = 1 to N corresponds to the sampling along the pixels in the spectrometer line camera or along the time slots within the sweeping time for a swept source and where q = 1 to Q corresponds to the different OPDs required by the user independently from the P number of CS_{exp}. In these conditions, Eq. (20) becomes

$$M_{built}(n,q) = g'(n)\, Exp\left[i\left(\frac{2\pi}{c} g(n) q \Delta OPD + h(n) \right) \right], \tag{26}$$

where DOPD defined by the user is, in practice, at least half of the coherence length of the optical source, and Eq. (21) can be re-written as

$$\mathrm{CMSI}(q) = \sum_{n=1}^{N} M^{*}_{built}(n,q)\, I(n), \tag{27}$$

as an upgrade of the dot product introduced in [19]. In this way, an A-scan can be assembled from CMSI signals evaluated at Q depths, given by the number of Q masks inferred from the number P of the CS_{exp} acquired at the Master stage.

The operation of the CMSI is demonstrated below on two versions of the set-ups described in Fig. 1, in Section 5.2 using a broadband source and a spectrometer and in Section 5.3 using a swept source and a photodetector.

5.2 A-scan with a spectrometer-based OCT

The experimental set-up is similar to that shown in [16,19]. The broadband source is a super Luminescent Diode (SLD) with a Gaussian spectrum centered at 1306 ± 2 nm and a bandwidth of 28 ± 1nm. The detection part includes a home-built spectrometer equipped with an InGaAs linear camera (Goodrich SUI, Princeton, New-Jersey, model SU-LDH, 1024 pixels, 14-Bit). Data obtained from the system are directly processed by the CMSI procedure with no resampling.

At the Master stage, experimental channeled spectra are recorded for different values of the OPD. After the extraction of the experimental phases (procedure presented in Section 4.1), the variation of $\partial\phi^{\exp}/\partial\tilde{\nu}$ according to the position of the mirror, looks like the one presented at the center of the spectrum $\tilde{\nu}_c$ (Fig. 3).

#255422 Received 9 Dec 2015; revised 20 Jan 2016; accepted 27 Jan 2016; published 4 Feb 2016

The linear regression on the derivative of the experimental phase for each value of $\tilde{\nu}$ permits to extract the functions $g(\tilde{\nu})$ and $h(\tilde{\nu})$. The integration constant has been chosen so that $g(\tilde{\nu})$ and $h(\tilde{\nu})$ are equal to zero at the center of the spectrum.

Figures 4(a) and 4(b) show $g(\tilde{\nu})$ and $h(\tilde{\nu})$ calculated from three sets of limited number P of CS_{exp}. These sets correspond to P = 2, P = 11 and P = 71 of CS_{exp} recorded from z = 140 µm to z = 1540 µm at the Master stage. The accuracy of determining g and h depends on the noise of the experimental phase measurement and the number of points, *i.e.* the number P of CS_{exp}, used for the linear regression. In the case of this experiment, the functions g and h inferred are quite similar for the three sets of CS_{exp}, as shown in Fig. 4. The instabilities shown at the edges of the spectrometer do not count in practice, as the optical spectrum is almost zero there, shown in solid line.

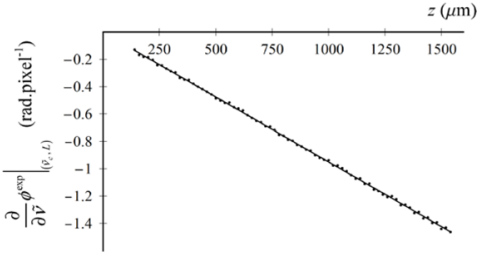

Fig. 3. Derivative of the experimental phase with respect to $\tilde{\nu}$ for different positions of the reference mirror M in Fig. 1 (black dots) adjusting the OPD = 2z. The derivative phase is evaluated at the center of the spectrum $\tilde{\nu}_c$. Continuous line, linear fit of experimental measurements.

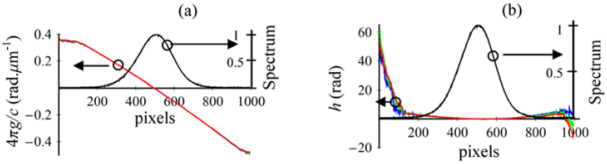

Fig. 4. The functions g (a) and h (b) versus the pixels of the spectrometer according to the number P of CS_{exp} acquired in the Master stage. Blue line, P = 2. Green line, P = 11. Red line, P = 71. Black line, normalized channeled spectrum at the Master stage for OPD = 0.

At the Slave stage, channeled spectra have been recorded for 3 positions of the reference mirror (220 µm, 720 µm and 1320 µm measured from OPD = 0). Figure 5 shows the axial reflectance profile based on Fourier Transform (black line) and CMSI according to the three sets of CS_{exp} (blue line for P = 2, green line for P = 11 and red line for P = 71). An axial sampling of 2 mm was chosen for CMSI to perform good sampling of the A-scan peaks, *i.e.* using Q = 771 masks in the range [0, 1540 mm]. The Fourier transformation of the channeled spectrum for 3 positions of the reference mirror is calculated to demonstrate the existence of chirp in the channelled spectra.

#255422 Received 9 Dec 2015; revised 20 Jan 2016; accepted 27 Jan 2016; published 4 Feb 2016

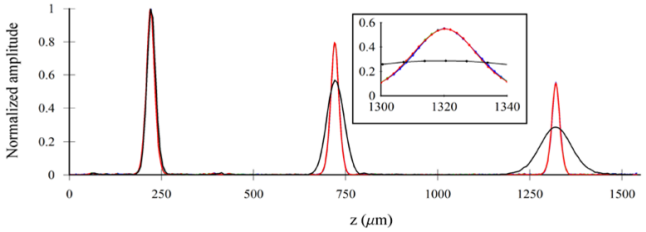

Fig. 5. A-scans for 3 OPD = 2z values (z = 220 μm, 720 μm and 1320 μm measured from OPD = 0). Black line, A-scan peaks obtained using FT. Blue line, A-scans obtained using CMSI with P = 2 CS_{exp} in the Master stage. Green line, A-scans obtained using CMSI with P = 11. Red line, A-scans obtained using CMSI with P = 71. All peaks are normalized with respect to the first peaks at z = 220 μm. The inset shows a zoom in the peaks around 1320 μm.

Although FT peaks broaden with OPD due to the dispersion induced by the interferometer and the non-linearity of spectral conversion in the spectrometer, the peak width of CMSI does not change with depth. Moreover, the reflectance profiles are identical irrespective of the number of CS_{exp} used for inferring the Mask function M_{built}. The graphs in Fig. 5 show that high resolution A-scans are achievable with a mask M_{built} obtained from P = 2 CS_{exp} only. Lastly, the inset of Fig. 5 shows details in the peaks around 1320 μm and the fact that the profiles for P = 2, 11 and 77 are identical.

Obviously, if a resampling method would be used, then the FT profile would be narrowed and in principle, if such resampling/linearization would be done to perfection, the ideal shape of A-scan peaks should be obtained as well. We do not show such graphs here as they have been presented in numerous reports on the conventional FT based OCT and such corrections are not the subject of this study.

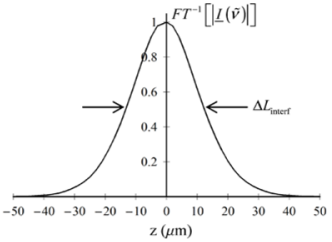

Fig. 6. PSF corresponding to the channeled spectrum I for the OPD at position 3 (z = 1340 mm) in Fig. 5. The PSF is obtained by calculating $FT^{-1}[|I(\tilde{\nu})|]$ that is equal to $FT^{-1}[|A(g(\tilde{\nu}))|]$. The complex form I has been calculated in Appendix C. $FT^{-1}[|I(\tilde{\nu})|]$ corresponds to the Fourier transformation of a channeled spectrum with no chirp.

It is important to distinguish two modalities to evaluate the axial resolution: 1) ΔL_{DC} equal to the full width at half maximum (FWHM) of the $FT^{-1}[I_{DC}(g(\tilde{\nu}))]$ profile. For a Gaussian spectrum shape the axial resolution is mathematically described by $\Delta L_{DC} = (2\text{Ln}2)/\pi \times \lambda_c^2/\Delta\lambda = 27 \pm 1$ μm, which represents the ideal axial resolution, determined by the source bandwidth only. 2) ΔL_{interf} is equal to the FWHM of the $FT^{-1}[|I(\tilde{\nu})|] = FT^{-1}[|A(g(\tilde{\nu}))|]$ profile (Fig. 6). In

#255422 Received 9 Dec 2015; revised 20 Jan 2016; accepted 27 Jan 2016; published 4 Feb 2016

this case, the axial resolution depends on a combination of factors including the spectrum shape of the source, polarization effects and injection coupling in fibers that exhibits spectral behavior due to chromatic aberrations. Not all spectral components under the optical source envelope contribute to interference, and therefore ΔL_{interf} is expected to be larger than ΔL_{DC}. ΔL_{interf} is defined as the *achievable* experimental resolution of the interferometer. In practice, ΔL_{interf} is obtained by selecting one of the CS_{exp}, $I(\tilde{\nu})$, calculating its complex form $I(\tilde{\nu})$ by using Appendix C, and Fourier transforming the absolute value $\left|\underline{I}(\ )\right|$.

As shown in Table 1, the resolution of CMSI is equal to the experimental resolution of the interferometer for the three peaks, ΔL_{interf}, which confirms our theoretical approach.

Table 1. Axial resolution according to the position of the reference mirror M in Fig. 1 (determining the optical path difference value) and the numerical tool used. ΔL_{DC} is the width of the peak $FT^{-1}[I_{DC}(g(\tilde{\nu}))]$. ΔL_{interf} is the width of the peak $FT^{-1}[|I(\tilde{\nu})|]$. All widths are evaluated via a Gaussian fit.

	ΔL_{DC} (µm)	ΔL_{interf} (µm)	FT (µm)	CMSI (µm)
Position 1 240 µm	26 ± 1	27.0 ± 0.7	28.0 ± 0.3	27.0 ± 0.2
Position 2 740 µm	26 ± 1	27.0 ± 0.7	56.0 ± 0.4	27.0 ± 0.2
Position 3 1340 µm	26 ± 1	26.1 ± 0.7	104.5 ± 0.9	26.2 ± 0.2

MSI and CMSI are not sensitive to the deviation of the channeled spectrum modulation from a regular periodicity modulation [19], *i.e.* to the chirp coming from the nonlinearity of the decoder and from the unbalanced dispersion of the interferometer. Therefore there is no need for any compensation procedure as data resampling employed in the conventional FT based OCT practice.

5.3 A-scan with a swept source-based OCT without k-clock

The experimental set-up is similar to that presented in [15,17,18,20,21], where a swept source (Axsun Technologies, Billerica, MA), central wavelength 1060 nm, sweeping range 106 nm (quoted at 10 dB) and 100 kHz line rate is used. The interferometric signal from a balance detection receiver (Thorlabs, Newton, New Jersey, model PDB460C) is sent to one of the two inputs of a dual input digitizer (Alazartech, Quebec, Canada, model ATS9350, 500 MB/s). Although the SS used for our experiments was equipped with a k-clock, to fully demonstrate the benefits of the MSI, we did not take advantage of this facility. At the Master stage, three sets of *P*-channeled spectra CS_{exp} have been recorded, $P = 2$, $P = 11$ and $P = 491$, from $z = 143$ µm to $z = 2833$ µm.

#255422 Received 9 Dec 2015; revised 20 Jan 2016; accepted 27 Jan 2016; published 4 Feb 2016

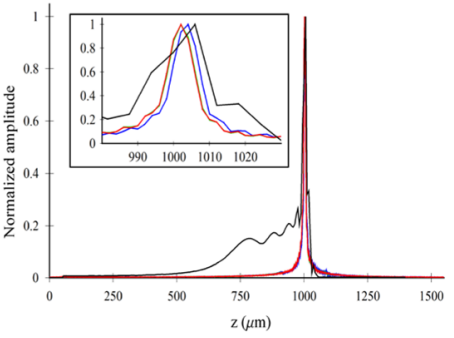

Fig. 7. A-scan for z = 1001 μm. Black line, A scan obtained with FT. The other three graphs are A-scan peaks obtained using the CMSI method with Q = 776, evaluated from different numbers of P-CS_{exp} used at the Master stage. Blue line, P = 2. Green line, P = 11. Red line, P = 491. Inset, details of the A-scans from 980 μm to 1030 μm.

At the Slave stage, a channeled spectrum has been recorded for a reference mirror positioned at 1001 μm measured from OPD = 0. Figure 7 shows the reflectance profile in depth based on Fourier Transform (black line) and on the CMSI method according to the three sets of CS_{exp} (blue line for P = 2, green line for P = 11 and red line for P = 491). Here again the Fourier transformation of the channeled spectrum corresponding to the reference mirror positioned at 1001 μm is calculated to demonstrate the existence of chirp in the channeled spectrum.

A depth sampling interval of 2 mm was chosen for CMSI to perform good sampling of the A-scan peaks, *i.e.* using Q = 776 masks for the range [0, 1550 mm]. The FT peak broadens due to the non-linearity of sweeping, as expected. The *achievable* experimental resolution of the interferometer ΔL_{interf} is equal to the FWHM of the $FT^{-1}[|I(\tilde{\nu})|] = FT^{-1}[|A(g(\tilde{\nu}))|]$ profile, which is estimated to be 9.0 ± 0.2 μm (Fig. 8) for the three sets of P-CS_{exp}. Lastly, in the inset of Fig. 7, the reflectance profiles are identical for P = 11 and P = 491, i.e. the green line overlaps the red line. For P = 2 (blue line), the A-scan displays a similar resolution but presents a slight shift of 2 μm and more noise on the edge of the peak.

#255422 Received 9 Dec 2015; revised 20 Jan 2016; accepted 27 Jan 2016; published 4 Feb 2016

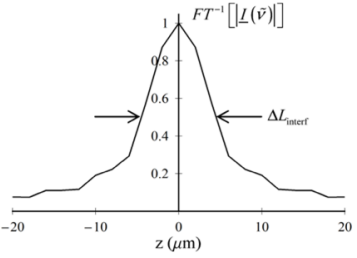

Fig. 8. PSF corresponding to the channeled spectrum I for an OPD = 2z, where z = 1001 mm. The complex form I has been calculated in Appendix C. $FT^{-1}[|I(\tilde{\nu})|]$ corresponds to the Fourier transformation of a channeled spectrum with no chirp.

5.4 Stability study and signal drop-off in depth: comparison between MSI and CMSI

In order to illustrate the insensitivity of CMSI to the random phase shift of channeled spectra acquired at the Master stage, several A-scans have been recorded over time while imaging a flat mirror. The interferometer used in this experiment is the same as in Section 5.3, *i.e.* a swept source without k-clock. The sampling in depth is chosen equal to 0.4 mm, much denser than the sampling obtained with the FT based method, estimated at 6.1 mm by measuring the displacement of the peak in Fourier domain according to the displacement of the reference mirror. This massive oversampling is implemented in order to determine a well-defined reflectance profile, to accurately measure the peak width (9.0 ± 0.2 µm here).

The MSI signal has been calculated using Eq. (6) on data collected every 2 seconds and displayed in Fig. 9(a). To perform the calculation, 100 CS_{exp} have been recorded at the Master stage from OPD = 500 mm to 540 mm. These 100 CS_{exp} are used as masks. As shown in Fig. 9(a) and by the corresponding reflectance profile for a particular time in Fig. 9(c), the reflectance profiles are noisy. We interpret this as result of fluctuations in the phase of the channeled spectrum collected during measurement (Slave stage) combined with much larger phase fluctuations cumulated during the acquisition of the CS_{exp} channeled spectra during the Master stage.

In Fig. 9(b), the absolute value of CMSI signal has been calculated from the same raw data previously used for the MSI. To perform the calculation, the Mask function M_{built} has been calculated using P = 2 CS_{exp} measured at OPD = 500 mm and 540 mm and used to generate Q = 100 masks distanced at 0.4 mm. As shown in Fig. 9(b) and by the blue profile in Fig. 9(c) the CMSI reflectance profiles do not present significant fluctuations. This demonstrates the superiority of using masks generated theoretically, deprived from the random phase affecting the phase of experimentally collected channeled spectra. More quantification of this behavior represents the subject of future more rigorous experiments, for the limited study here we evaluated that the standard deviation of the random phase shift in the set-up was 0.27 rad per second. This still affects the resulting image in Fig. 9(b).

#255422 Received 9 Dec 2015; revised 20 Jan 2016; accepted 27 Jan 2016; published 4 Feb 2016

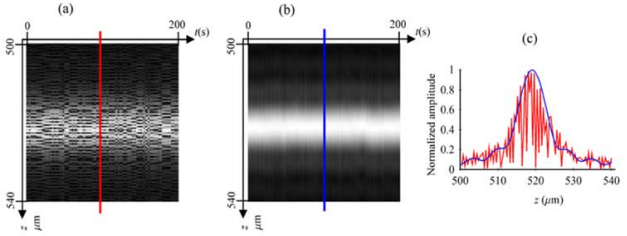

Fig. 9. (a) A-scans (vertical axis) for a mirror as object, represented in time (horizontal axis) calculated with MSI and $P = 100\ CS_{exp}$ utilized as masks. (b) A-scans (vertical axis) for a mirror as object represented in time (horizontal axis) calculated with CMSI using $Q = 100$ masks obtained from $P = 2\ CS_{exp}$. (c) Reflectance profiles calculated by MSI (red) and CMSI (blue) for $t = 100$ s in each respective image.

Another important parameter to be compared between MSI and CMSI is the signal drop-off with optical path difference. To illustrate this, B-scans of the anterior chamber of a human eye have been obtained using CMSI (Fig. 10(a)) and MSI (Fig. 10(b)). The interferometer used in this experiment is the same as in Section 5.3, *i.e.* a swept source without k-clock. The sampling interval in depth is chosen equal to 5 mm. Both images are normalized to 1 according to the maximum of each of them.

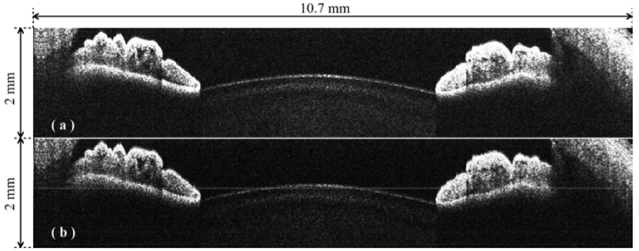

Fig. 10. (a) B-scan of the lens and the iris of a human eye with CMSI. (b) B-scan of the same raw data as in (a) but with MSI. Both images are normalized according to the maximum of each of them. To demonstrate the slight improvement in contrast at large depths of the CMSI image, we display their bottom only, showing the lens and the iris. The 2 mm-axial range of the B-scans is considered in air.

The sensitivity for both MSI and CMSI is measured as 101.3 dB close to OPD = 0 with a power equal to 1.7 mW on the sample, using the procedure detailed in [15]. The images are quite similar except for the drop-off in depth that is slightly larger for the MSI than for the CMSI. This is because in previous reports [15–21], MSI was implemented using the product between the raw channelled spectra and experimental masks, all affected by a decrease in their interference contrast with OPD. In CMSI, all masks have the same amplitude, hence an improvement in the decay of sensitivity with depth. This improvement can only be seen at large depths, therefore we have truncated the images to display large OPD values only, where some improvement can be seen in the CMSI image. The expected improvement is anticipated by the difference between Eqs. (16b) and (25).

#255422 Received 9 Dec 2015; revised 20 Jan 2016; accepted 27 Jan 2016; published 4 Feb 2016

6. Conclusions

CMSI employs a Mask function to generate any number Q of masks, where each mask is used in the second stage, Slave measurement, to obtain the reflectivity of the object from a selected depth, characteristic for each mask. In previous implementations of MSI, the only depths addressed were those for which CS_{exp} were initially acquired at the Master stage. CMSI can create any number of intermediate masks between the depths where CS_{exp} were initially acquired from. This represents a major improvement in comparison with the implementations in [15–21], as CMSI requires fewer experimental measurements while allowing for much denser sampling in depth. This feature is especially important for high axial resolution OCT, where a large number of masks are needed to accurately construct an A-scan.

As with the correlation-based MSI method, there is no need for organizing the data in equally spaced frequency slots. The Mask function incorporates both the non-linearity of reading the channeled spectrum as well as the dispersion of the interferometer in the same way as the experimentally collected masks in the MSI Therefore, MSI and CMSI can work directly in the non-uniform distribution $\tilde{\nu}$ space in opposition to the conventional FT based spectral (Fourier) domain systems. In addition, as demonstrated here, CMSI can reach the expected theoretical resolution. MSI could equally achieve such resolution if the spectral envelope imprinted by the optical source spectrum is eliminated, procedure much improved in the CMSI, as shown in building Mask functions in Fig. 2. In the FT based OCT, achieving the best axial resolution depends on how good the resampling/linearization method is. Several methods have been developed to address this issue that allowed FT-based OCT methods to achieve axial resolutions close to the theoretical axial resolution. However, these procedures are performed in the very moment of data acquisition before displaying the results, involve extra computation resources and are time consuming. In MSI and CMSI the experimental masks and respectively the Mask function and derived masks are obtained at the Master stage, *i.e*. prior to measurement. The Master stage procedure can be considered as the equivalent to the resampling/linearization procedure in the FT-based OCT method. However, MSI and CMSI are radically different in output from the FT-based OCT methods. MSI and CMSI perform a procedure for each depth of interest while the FT-based methods deliver a full A-scan in a single step. Although this may look disadvantageous, MSI and CMSI allow a more direct production of *en-face* views, as there is no need, like in FT-based OCT method, to split the A-scan into its depth components.

In terms of time required by the CMSI in comparison with the MSI method, the main gain is at the Master Stage. While MSI would have required a tedious repetition of experimental collection of hundreds of channelled spectra subsequently used as masks, the CMSI presented here requires a much reduced number of channelled spectra to be experimentally collected at the Master stage, which can then be processed theoretically into as many masks needed.

In terms of calculation at the Slave stage, the only difference is that CMSI requires the operator for the core operation [21] to be implemented in complex, so the calculations at the Slave stage for the same number of masks require slightly more than the double the time of the MSI. This disadvantage may be eliminated by using graphic cards [18]. In terms of comparison of the time required by the core operator of the MSI with the time required by conventional FT based method, with or without resampling, this is benchmarked in Fig. 3 in [21]. Similarly, the improvement in the timing of the core operation using graphic cards detailed in [18] for the MSI can be extrapolated here for the CMSI method.

Finally, it has been shown that the theoretical expression for the operation of the CMSI is identical to the Fourier transform of channeled spectra for a perfect interferometer (no dispersion) and perfect decoder, such as either a spectrometer linear in wavenumber or a linearly tunable swept source, however with the difference that the CMSI delivers a complex signal without random phase shift. This allows CMSI to eliminate the process of window integration practiced in the MSI, integration that has lead to worsening the axial resolution.

#255422 Received 9 Dec 2015; revised 20 Jan 2016; accepted 27 Jan 2016; published 4 Feb 2016

Having access to the phase, CMSI method can be further explored to measure the phase of signal acquired from the object. The recovery of phase has not been employed here, however it is expected that this will trigger future developments in polarization and flow measurements.

Appendix A: demonstration of Eq. (4)

Let the Fourier transform (FT) and its inverse (FT^{-1}) be defined by the following expressions

$$FT\left[\hat{f}(t)\right]=\int \hat{f}(t)\,Exp\left[i\,2\pi\,t\,\nu\right]dt, \tag{28}$$

$$FT^{-1}\left[f(\nu)\right]=\int f(\nu)\,Exp\left[-i\,2\pi\,t\,\nu\right]d\nu. \tag{29}$$

The decoder is considered linear ($g(\tilde{\nu})=\tilde{\nu}=\mathrm{n}$) and the interferometer perfectly balanced for dispersion ($\mathrm{d}\equiv 0$). According to (28), the inverse Fourier transform of I in (2), denoted as $\hat{I}$, is equal to

$$\hat{I}(t)=\hat{I}_{DC}(t)+\frac{1}{2}\hat{\underline{I}}(t)+\frac{1}{2}\hat{\underline{I}}(-t)^{*}, \tag{30}$$

where $\hat{I}_{DC}$ and $\hat{I}$ are the inverse FT of I_{DC} and I, and where for the last term the usual property of the Fourier transform was used

$$FT^{-1}\left[f(\nu)^{*}\right]=\hat{f}(-t)^{*}. \tag{31}$$

Equation (30) can be evaluated for $t = 2z/c$ and becomes

$$\hat{I}(2z/c)=\hat{I}_{DC}(2z/c)+\frac{1}{2}\hat{\underline{I}}(2z/c)+\frac{1}{2}\hat{\underline{I}}(-2z/c)^{*}. \tag{32}$$

Moreover, for $g(\tilde{\nu})=\tilde{\nu}=\mathrm{n}$, Eq. (3) can be written as follows

$$\underline{I}(\nu)=\int r(\rho)A(\nu)\,Exp\left[i\frac{2\pi}{c}\nu\,2\rho\right]d\rho, \tag{33}$$

and its inverse FT evaluated for $t = 2z/c$ is equal to

$$\hat{\underline{I}}(t=2z/c)=\iint r(\rho)A(\nu)\,Exp\left[-i\frac{2\pi}{c}\nu\,2(z-\rho)\right]d\rho\,d\nu, \tag{34}$$

that can be written as follows

$$\hat{\underline{I}}(2z/c)=\int \hat{A}\left(\frac{2}{c}(z-\rho)\right)r(\rho)\,d\rho=\hat{A}(2z/c)\otimes r(z), \tag{35}$$

for which $\hat{A}(t)=FT^{-1}[A(\mathrm{n})]$.

Appendix B: demonstration of Eq. (10)

Eq. (9) can be written in the Fourier domain using a variable $\tilde{t}$, pair conjugate to $\tilde{\nu}$ as follows

$$MSI(z)=\frac{1}{2}\alpha(z)e^{-i\varphi_{rand}(z)}\int\widehat{\underline{CS}}(\tilde{t},z)^{*}\,\hat{I}(\tilde{t})\,d\tilde{t}+CC, \tag{36}$$

by using the Plancherel-Parceval theorem defined by

#255422 Received 9 Dec 2015; revised 20 Jan 2016; accepted 27 Jan 2016; published 4 Feb 2016

$$\int f_1^*(\tilde{\nu})\, f_2(\tilde{\nu})\, d\tilde{\nu} = \int \hat{f}_1^*(\tilde{t})\, \hat{f}_2(\tilde{t})\, d\tilde{t}, \tag{37}$$

for which $f_1 = FT\left[\hat{f}_1\right]$ and $f_2 = FT\left[\hat{f}_2\right]$.

Similar to (30), the inverse Fourier transform of the channeled spectrum I is equal to

$$\hat{I}(\tilde{t}) = \hat{I}_{DC}(\tilde{t}) + \frac{1}{2}\underline{\hat{I}}(\tilde{t}) + \frac{1}{2}\underline{\hat{I}}(-\tilde{t})^*. \tag{38}$$

For an object placed axially in respect to the OCT system, in such a way as the OPD = 0 is placed outside of the object, the product $\underline{\widehat{CS}}^* \times \hat{I}$ is only equal to $1/2\,\underline{\widehat{CS}}^* \times \underline{\hat{I}}$. Indeed the position of the peak $\underline{\widehat{CS}}$ depends on z that is defined for $z>2L_c$ only, condition that avoids the peak $\underline{\widehat{CS}}$ to overlap the peak $\hat{I}_{DC}$ (see Fig. 11).

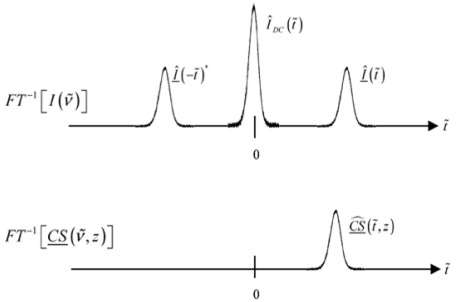

Fig. 11. Schematic representation of the peaks obtained by calculating the inverse FT of I (top) and CS (bottom) for a single layer object. The OPD is chosen so that $\hat{I}$ does not overlap $\hat{I}_{DC}$.

Then we have

$$\int \underline{\widehat{CS}}(\tilde{t},z)^*\, \hat{I}(\tilde{t})\, d\tilde{t} = \frac{1}{2}\int \underline{\widehat{CS}}(\tilde{t},z)^*\, \underline{\hat{I}}(\tilde{t})\, d\tilde{t}. \tag{39}$$

By using the Plancherel-Parseval theorem, Eq. (39) is written as follows

$$\int \underline{\widehat{CS}}(\tilde{t},z)^*\, \hat{I}(\tilde{t})\, d\tilde{t} = \frac{1}{2}\int \underline{CS}(\tilde{\nu},z)^*\, \underline{I}(\tilde{\nu})\, d\tilde{\nu}, \tag{40}$$

and the expression of MSI(z) is equal to

$$MSI(z) = \frac{1}{2}\alpha(z)\,\Re e\left\{e^{-i\varphi_{rand}(z)} \int \underline{CS}(\tilde{\nu},z)^*\, \underline{I}(\tilde{\nu})\, d\tilde{\nu}\right\}, \tag{41}$$

where Re{} means the real part of a complex function.

Appendix C: complex exponential form of a real sinusoidal function

Let f(n) be a real sinusoidal function modulated at a and defined by the following expression

#255422 Received 9 Dec 2015; revised 20 Jan 2016; accepted 27 Jan 2016; published 4 Feb 2016

$$f(\nu) = I_{DC}(\nu) + \frac{1}{2}\underline{I}(\nu)e^{i\,a\,2\pi\nu} + \frac{1}{2}\underline{I}(\nu)^{*}e^{-i\,a\,2\pi\nu}. \quad (42)$$

The complex form *f*(n) of *f*(n) is then equal to $\underline{I}(\nu)e^{i\,a\,2\pi\nu}$ and can be retrieved using (29) and the steps shown in Fig. 12.

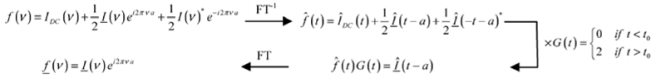

Fig. 12. Diagram explaining the process of changing a real sinusoidal function into a complex form. The parameter t_0 is chosen to eliminate the DC component of the real sinusoidal function.

Appendix D: demonstration of Eq. (22)

Eq. (22) can be written in the Fourier domain by using the Plancherel-Parseval theorem as follows

$$CMSI(z) = \int \hat{M}_{built}(\tilde{t}, z)^{*}\,\hat{I}(\tilde{t})\,d\tilde{t}. \quad (43)$$

For an OPD = 0 placed outside of the object, only the product $1/2\,\hat{M}_{built}^{*} \times \hat{\underline{I}}$ is different from 0, according to similar reasoning used in Fig. 10 in Appendix B. Therefore, the CMSI signal can be written, after using the Plancherel-Parseval theorem, as follows

$$CMSI(z) = \frac{1}{2}\int M_{built}(\tilde{\nu}, z)^{*}\,\underline{I}(\tilde{\nu})\,d\tilde{\nu}. \quad (44)$$

Acknowledgments

S. Rivet acknowledges the Marie-Curie Intra-European Fellowship for Career Development, No. 625509. M. Maria, T. Feuchter, L. Leick and A. Podoleanu acknowledge the UBAPHODESA Marie Curie European Industrial Doctorate 607627. A. Bradu and A. Podoleanu acknowledge the support of ERC (http://erc.europa.eu) COGATIMABIO 249889. A. Podoleanu is also supported by the NIHR Biomedical Research Centre at Moorfields Eye Hospital NHS Foundation Trust and the UCL Institute of Ophthalmology.